Intersubband transitions in low-dimensional nanostructures

Many-body effects in quantum wells and quantum dots

Vorgelegt von Diplom-Physikerin

Thi Uyen-Khanh Dang

aus Erlangen

von der Fakultät II – Mathematik und Naturwissenschaften
der Technischen Universität Berlin

zur Erlangung des akademischen Grades

Doktor der Naturwissenschaften

— Dr. rer. nat. —

Genehmigte Dissertation

Promotionsausschuss

Vorsitzende	:	Prof. Dr. rer. nat. Birgit Kanngießer, TU Berlin
1. Gutachter	:	Prof. Dr. rer. nat. Andreas Knorr, TU Berlin
2. Gutachter	:	Prof. Dr. rer. nat. Manfred Helm, HZ Dresden

Tag der wissenschaftlichen Aussprache: 16. November 2012

Berlin, 2012
D 83

Zusammenfassung

Die vorliegende Arbeit befasst sich mit der Intersubband-Dynamik in niederdimensionalen Halbleitersystemen. Mit Hilfe der Heisenbergschen Bewegungsgleichung werden verschiedene Vielteilchen-Effekte untersucht, insbesondere die Elektron-Elektron- und die Elektron-Phonon Wechselwirkung. Die Untersuchungen beinhalten Intersubbandübergange in Quantenfilmen, die Volumen-Oberflächendynamik in Silizium, sowie Intersublevelübergänge in einem Quantenpunkt.

Zunächst wird ein *n*-dotierter GaAs/AlGaAs Quantenfilm im thermischen Gleichgewicht betrachtet und der Einfluss der Coulomb-Wechselwirkung der Ladungsträger auf das System im Grundzustand berechnet. Dazu wird die sonst übliche Markov Näherung in zweiter Ordnung störungstheoretisch erweitert, so dass Gedächtniseffekte erster Ordnung mitgenommen werden. Diese führen zu Coulomb-induzierten Korrelationen zwischen den Ladungsträgern im Grundzustand, welche eine Renormierung der elektronischen Gleichgewichtsverteilung bewirken. Der Effekt zeigt sich im Absorptionsspektrum als spektrale Verbreiterung der Linienbreite für tiefe Temperaturen ($T < 50$ K).

Als nächstes werden Nichtgleichgewichtsprozesse behandelt. Mit dem Augenmerk auf geeignete Detektionsschemata wird hier eine leistungsfähige Methode für die Detektion von ultraschnellen Prozessen in Intersubband Quantenfilmen vorgestellt, die zweidimensionale Fourierspektroskopie. Durch eine Folge von Pulsanregungen wird das resultierende Signal einer Probe bezüglich zweier Zeiten fouriertransformiert. Das daraus ermittelte zweidimensionale Frequenzspektrum beinhaltet Informationen über verschiedene Prozesse die in der Probe ablaufen. Um diese physikalischen Prozesse, welche von den Pulsfolgen und deren Phase abhängig sind, zu verstehen und zu separieren, wird hier eine diagrammatische Technik zur Betrachtung der makroskopischen Polarisation eingeführt, die sogenannten doppelseitigen Feynmandiagramme. Am Beispiel von Elektron-Phonon-induzierter Relaxationsdynamik wird das zweidimensionale Photon-Echo Signal des Intersubbandsystems berechnet. Hier zeigt sich, dass die zweidimensionalen Spektren detaillierte Informationen im Bezug auf korrelierte Frequenzen und somit auf die Verteilung im Impulsraum liefern.

Eine quasi “natürliche” zweidimensionale Struktur ist die Oberfläche eines beliebigen Volumenhalbleiters. In dieser Arbeit wird die Volumen-Oberflächendynamik in Silizium unter dem Einfluss der Elektron-Elektron-, sowie Elektron-Phonon Wechselwirkung berechnet. Aufgrund der numerisch nicht durchführbaren Behandlung der vollen Quantenkinetik, werden von dieser ausgehend Relaxationsratengleichungen abgeleitet, welche allgemein für Langzeitdynamiken, z.B. in Lasern, genutzt werden. Im Gegensatz dazu wird die Dynamik longitudinal optischer Phononen mit Hilfe der reduzierten Peierls Gleichung berechnet, welche noch quantenkinetische Effekte enthält. Die numerischen Ergebnisse werden mit experimentellen Daten verglichen, woraus hervorgeht, dass die Kopplung der Elektronen an die dominante longitudinal optische Phononmode zu einer verlängerten Lebenszeit heißer Ladungsträger führt.

Die Restriktion der Ladungsträgerbewegung in drei Dimensionen führt zu Quantenpunkten. Hier liegt das Hauptaugenmerk auf den Intersublevelübergängen im Leitungsband unter dem Einfluss longitudinal optischer Phononen auf die Elektronen. Aufgrund der starken nichtdiagonalen Kopplung zwischen Elektronen und Phononen kann hier keine störungstheoretische Methode angewendet werden. Stattdessen wird eine Induktionsmethode für die Berechnung der Bewegungsgleichungen verwendet, welche die Elektron-Phonon Kopplung in beliebig hoher Ordnung behandelt. Die Richtigkeit des Modells wird zunächst an den Grenzfällen bekannter analytischer Modelle geprüft. Anschließend werden

Absorptionsspektren berechnet, welche deutliche Signaturen von diagonaler und nicht-diagonaler starker Kopplung aufweisen.

Abstract

This work is focused on the intersubband dynamics in low-dimensional semiconductor nanostructures. Using the Heisenberg equation of motion approach, theoretical investigations are made about the influence of many-particle interactions on the carrier dynamics. In particular, the role of the electron-electron- and electron-phonon interaction is studied in intersubband quantum wells, bulk-surface dynamics and intersublevel quantum dots.

In an *n*-doped GaAs/AlGaAs quantum well system, the effect of the electron-electron interaction on the equilibrium distribution function is examined. Going beyond the second-order Markov approximation, it can be seen that Coulomb-induced correlations in the ground state lead to a renormalization of the equilibrium function, visible as a spectral broadening of the intersubband absorption spectra for low temperatures ($T < 50$ K).

Next, the non-equilibrium dynamics in intersubband quantum wells is investigated. First, focusing on appropriate detection schemes for ultrafast processes, a useful technique for the investigation of nonlinear dynamics, the two-dimensional Fourier transform spectroscopy, is proposed. After exciting the sample with a series of strong pulses, its response is visualized in a two-dimensional frequency spectrum as a function of the Fourier-transformed delay times of the pulses. To fully understand the physical processes that are invoked by the different pulse sequences, a diagrammatic method, the so-called double-sided Feynman diagrams, will be used to interpret the complex material response. In a next step the electron-phonon interaction is included. It is demonstrated that the two-dimensional photon echo signal of the non-equilibrium system reveals detailed information about the intersubband carrier relaxation.

A quasi "natural" two-dimensional structure is the surface of a bulk. Within this thesis, the bulk-surface dynamics of silicon including the electron-electron- and electron-phonon interaction is calculated. Here, the longitudinal optical phonon dynamics is treated with a reduced Peierls equation derived from a full quantum kinetic model. To ease the immense numerical effort, an appropriate set of rate equations for the carrier dynamics is derived from the same model. The results are compared with recent experiments, where it will be seen that the coupling to the dominant longitudinal optical phonons leads to a prolonged lifetime of heated carriers.

Restricting the material in three dimensions, the intersublevel dynamics of a single quantum dot is investigated with the focus on electron-phonon interaction. Due to the strong non-diagonal coupling between electrons and longitudinal optical phonons, a perturbative approach of the dynamics is not possible. Instead, the electron-phonon interaction is included up to an arbitrary order using an inductive method. The calculations of the absorption spectra are benchmarked on analytical models and show signatures of the diagonal as well as the strong non-diagonal electron-phonon coupling.

Contents

List of Figures

List of Tables

Part I

Prologue

Chapter 1

Introduction

Today's technology is mainly based on semiconductor nanomaterials, be it for microelectronic devices, for radiation sources or in the solar cell industry. The first mesoscopic heterostructures where constructed in the early seventies [DWH74]. Nowadays, the advances of growth techniques allow for the design of various low-dimensional nanostructures with a confinement not only in one, but up to all three dimensions, enabling the control of optical and electrical properties not possible in bulk materials. In principle these heterostructures introduce a potential barrier, which restricts the carriers spatially in one or more dimensions, depending on the type of structure. If the confinement length is in the order of the de Broglie wave length of the carriers, the quantum mechanical nature of the particles becomes important. For example, the reduction of the dimensionality inherently leads to a splitting of the valence and the conduction band into so-called subbands. In particular the carrier dynamics in and between these subbands, for nanostructures of different dimensionalities, will be the scope of this work.

The main focus of the thesis lies on the intersubband dynamics in single GaAs/AlGaAs quantum wells. Being one of the first semiconductor sources of terahertz radiation [FCS$^+$94], these quantum well structures have already been investigated in detail experimentally, as well as theoretically [LN03, ZHH$^+$04] and it was found that the effects of many-particle interactions are quite pronounced in this system. However, many questions are still open and we are far from having a complete understanding of all microscopic processes in such structures. For example, there has been a deficit in the explanation of the quantum well absorption line width for ultra-low temperatures. So far, theoretical models led to line widths much smaller than observed in experiments. In order to overcome this inconsistency, the Coulomb coupling among the carriers in equilibrium is considered beyond the typical second-order Markov approximation. It will be shown that by including the electronic correlations in the ground state, the carrier distribution function is renormalized, visible in the absorption spectrum as a line width broadening, especially at low temperatures [DWRK10].

Shifting the attention from stationary problems to non-equilibrium dynamics, the electron-phonon interaction is taken into account. Here, the study is more concentrated on possible detection schemes for the investigation of non-equilibrium dynamics in intersubband quantum well structures. For this purpose, a powerful tool, the two-dimensional Fourier transform spectroscopy, will be introduced. Originating from experiments on the nuclear magnetic resonance in the seventies [WE77], this spectroscopic technique was further developed and applied to correlation and relaxation dynamics in biological systems [TM93] and eventually to semiconductor structures [LZBC06]. The benefit of this method is demonstrated on electron-phonon scattering processes: By calculating the two-dimensional photon echo spectrum, the phonon-induced relaxation dynamics can be resolved in a detail, difficult to reach for other spectroscopic schemes [DWE$^+$12].

Next, the investigation of relaxation dynamics will be expanded to other semiconductor materials. In particular, a fundamental relaxation process in silicon, the major workhorse in the semiconductor industry, is studied. Here, the dynamics is calculated within the conduction band, namely between the conduction bulk band and its *D*-down surface band, a quasi "natural" two-dimensional structure.

Based on recent experimental observations [Eic10], the relaxation of hot carriers including the electron-electron and electron-phonon scattering is calculated and compared with experimental data. The results indicate a prolonged lifetime of heated carriers due to their interaction with longitudinal optical phonons.

Finally, restricting the semiconductor to a zero-dimensional object, the intersublevel transitions in a single quantum dot are investigated. Completely confining its carriers, the quantum dot has been discussed as an appropriate structure for terahertz radiation [DS08], pushing the attempts to incorporate quantum dots in intersubband quantum wells to improve the performance of quantum cascade lasers [LNC$^+$12]. Due to the strong coupling between electrons and longitudinal optical phonons, an inherent effect in quantum dots is the formation of a new quasi-particle, the polaron. Common perturbative approaches fail when studying interactions in such a strong coupling regime. Thus, an advanced theoretical method is introduced to describe the intersublevel dynamics in detail. A special emphasis is put on a separate treatment of the diagonal and non-diagonal coupling of electrons to longitudinal optical phonons. It is shown that the linear absorption spectra exhibit signatures of both coupling mechanisms.

Structure of this thesis

The thesis is organized as follows: In Part II, a short overview of the fundamental theoretical methods will be given. First, the second quantization scheme is introduced, which is the basis of the calculations done in this work. Then, tools for the description of the temporal dynamics of the system will be provided. Part III treats the intersubband dynamics in two-dimensional structures, which includes the investigations on a GaAs/AlGaAs quantum well and the bulk-surface dynamics in silicon. Then, in Part IV, the influence of the strong electron-phonon coupling on the intersublevel dynamics of a quantum dot is studied. This work concludes with an epilogue, where the main results are recapitulated and an outlook is given.

Part II

Fundamentals

Chapter 2

Microscopic solid state theory

In the last 40 years, the quantum mechanical nature of particles in solid state nanostructures gave rise to new domains in the technology of optics and electronics, for example, in the laser field [Lau93, BGH$^+$00] or in quantum computing [CPS$^+$04]. Hereby, a thorough understanding of the fundamental processes on a sub-microscopic scale is the foundation of these technological advances. Its complexity lies in the description of the interactions between different kinds of particles in the solid state, whose number can vary from a only few, e.g. in a zero-dimensional quantum dot, to about 10^{24} particles in a bulk material. Hence it is desirable to find a generalized microscopic scheme for the many-particle dynamics in a solid. A very useful theoretical approach for the treatment of many-body interactions is the second quantization scheme since it allows to investigate the quantum kinetic behavior of different particles on an equal footing. Using this formalism, the temporal evolution of relevant system observables in solid state structures can be derived in an elegant and straight forward way.

This chapter will introduce the different many-particle interaction mechanisms which are treated in this work. Starting with the microscopic description of the general system Hamiltonian in Sec. 2.1, the potentials and the particle wave functions are specified according to the periodic structure of the solid state in Sec. 2.2. The goal of this chapter is the description of many-body interactions in second quantization. The formalism is introduced in Sec. 2.3, and subsequently, the relevant interaction Hamiltonians are formulated within the second quantization scheme in Sec. 2.3.2.

2.1 The solid state Hamiltonian

The system Hamiltonian can be determined within the LAGRANGE formalism trough the principle of least action [Sch96, Nol00]. A benefit of this description is the identification of the general coordinates Φ_i and their conjugate momenta Π_i, also allowing a straight forward transition to the canonical quantization of the fields later on. The Lagrangian density in real space representation for particles in an electromagnetic field is [CT99]:[1]

$$\begin{aligned}\mathscr{L} =& \sum_i \frac{1}{2m_i}\left(\frac{\hbar}{\mathrm{i}}\nabla_{\mathbf{r}} + q_i\mathbf{A}\right)\Psi_i^*(\mathbf{r})\left(\frac{\hbar}{\mathrm{i}}\nabla_{\mathbf{r}} - q_i\mathbf{A}\right)\Psi_i(\mathbf{r}) + \sum_i \Psi_i^*(\mathbf{r})(q_i\Phi + U)\Psi_i(\mathbf{r}) \\ & - \sum_i \frac{\mathrm{i}\hbar}{2}\left(\dot{\Psi}_i^*(\mathbf{r})\Psi_i(\mathbf{r}) + \Psi_i^*(\mathbf{r})\dot{\Psi}_i(\mathbf{r})\right) + \left[\frac{\varepsilon_0}{2}\left(\nabla_{\mathbf{r}}\Phi - \dot{\mathbf{A}}\right)^2 + \frac{1}{2\mu_0}\left(\nabla_{\mathbf{r}}\times\mathbf{A}\right)^2\right], \end{aligned} \tag{2.1}$$

where the electric field E and the magnetic field B is expressed by the vector potential $\mathbf{A}$ and the scalar potential Φ: $E = -\nabla_{\mathbf{r}}\Phi - \dot{\mathbf{A}}$ and $B = \nabla \times A$. The wave function $\Psi_i(\mathbf{r})$ corresponds to a particle with mass m_i and charge q_i. The potential U represents an external potential arising e.g. from the restriction of dimensions, which will be explained in more detail in Sec. 4. The Hamiltonian density $\mathscr{H}$ can be

[1] The time dependence of the values is not explicitly written but assumed if not otherwise noted.

found by applying a Legendre transformation $\mathscr{H} = \sum_i \Pi_i^* \dot{\Phi}_i - \mathscr{L}$. Rearranging the terms in $\mathscr{L}$, the Hamiltonian $H = \int \mathrm{d}^3 r \mathscr{H}$ then reads:

$$H = \sum_i \int \mathrm{d}^3 r \Psi_i^*(\mathbf{r}) \frac{(\frac{\hbar}{\mathrm{i}} \nabla_{\mathbf{r}} - q_i \mathbf{A})^2}{2m_i} \Psi_i(\mathbf{r}) + \sum_i \frac{1}{2} \int \mathrm{d}^3 r \Psi_i^*(\mathbf{r}) q_i \Phi \Psi_i(\mathbf{r}) + \sum_i \int \mathrm{d}^3 r \Psi_i^*(\mathbf{r}) U \Psi_i(\mathbf{r}) + \int \mathrm{d}^3 r \left[\frac{\varepsilon_0}{2} \dot{\mathbf{A}}^2 + \frac{1}{2\mu_0} (\nabla_{\mathbf{r}} \times \mathbf{A})^2 \right]. \tag{2.2}$$

The first three terms represent the self-energy of the charged particles and the interaction between the particles with a potential. The last term is the self-energy of the electromagnetic field and leads in the scheme of second quantization to quantized light (photons). Within this thesis only the interaction of carriers with classical light will be investigated, hence the electromagnetic self-energy term will be neglected from now on. Equation (2.2) is also valid if an additional external electromagnetic field is considered. In this case, the potentials consist of an internal and an external part: $\mathbf{A} = \mathbf{A}_{\mathrm{int}} + \mathbf{A}_{\mathrm{ext}}$ and $\Phi = \Phi_{\mathrm{int}} + \Phi_{\mathrm{ext}}$. To reduce the degrees of freedom of the vector/scalar potential, the COULOMB gauge is used for the internal potentials: $\nabla_{\mathbf{r}} A_{\mathrm{int}} = 0$. The choice of the COULOMB gauge automatically splits the internal electromagnetic field into a longitudinal and a transverse part: $E_{\mathrm{int}} = -\nabla_{\mathbf{r}} \Phi_{\mathrm{int}} - \dot{\mathbf{A}}_{\mathrm{int}} = E_{\mathrm{long}} + E_{\mathrm{trans}}$. As another consequence of the COULOMB gauge, the internal scalar potential can be solved via the POISSON equation $\Delta_{\mathbf{r}} \Phi_{\mathrm{int}}(\mathbf{r}) = -\rho(\mathbf{r})/\varepsilon_0 = -\Psi(\mathbf{r}) q \Psi(\mathbf{r})/\varepsilon_0$, leading to following solution for the integral of the internal scalar potential in Eq. (2.2):

$$H_{\mathrm{Coul}} = \sum_{ij} \frac{1}{2} \int \mathrm{d}^3 r \Psi_i^*(\mathbf{r}) q_i \Phi_{\mathrm{int}} \Psi_i(\mathbf{r}) = \sum_{ij} \frac{1}{2} \int \mathrm{d}^3 r \int \mathrm{d}^3 r' \Psi_i^*(\mathbf{r}) \Psi_j^*(\mathbf{r}') \frac{q_i q_j}{4\pi\varepsilon_0 |\mathbf{r} - \mathbf{r}'|} \Psi_j(\mathbf{r}') \Psi_i(\mathbf{r}), \tag{2.3}$$

with the static dielectric background constant ε_0. Thus, the longitudinal part of the electromagnetic field directly results in the COULOMB Hamiltonian H_{Coul}. If the assumption is made that the internal charges are in close vicinity and thus the interaction between the particles and the transverse internal field is negligible compared to the longitudinal internal field, $\mathbf{A}_{\mathrm{int}}$ can be neglected and Eq. (2.2) becomes:

$$H = \sum_i \int \mathrm{d}^3 r \Psi_i^*(\mathbf{r}) \frac{(\frac{\hbar}{\mathrm{i}} \nabla_{\mathbf{r}} - q_i \mathbf{A}_{\mathrm{ext}})^2}{2m_i} \Psi_i(\mathbf{r}) + \sum_i \frac{1}{2} \int \mathrm{d}^3 r \Psi_i^*(\mathbf{r}) q_i \Phi_{\mathrm{ext}} \Psi_i(\mathbf{r}) + H_{\mathrm{Coul}} + \sum_i \int \mathrm{d}^3 r \Psi_i^*(\mathbf{r}) U \Psi_i(\mathbf{r}). \tag{2.4}$$

For the external electromagnetic potentials, the gauge has not been chosen yet, leaving the possibility to add a function $\chi(\mathbf{r},t)$ to the potentials without changing the physical properties: $\Phi'_{\mathrm{ext}} = \Phi_{\mathrm{ext}} - \frac{\mathrm{d}}{\mathrm{d}t} \chi(\mathbf{r},t)$ and $\mathbf{A}'_{\mathrm{ext}} = \mathbf{A}_{\mathrm{ext}} + \nabla_{\mathbf{r}} \chi(\mathbf{r},t)$. The function $\chi(\mathbf{r},t)$ will be specified in the next step.

The Electric dipole approximation - If the wave length of the external electromagnetic field is much larger than the size of the sample (here located at the position $\mathbf{r} = 0$), the spatial variation of the external potentials over the sample is very small. In the case of nano-structured material, the size of the quantum objects lies in the few nanometer (nm) range while the wave length of the external fields extends from multiple tens of nm to micrometer (μm). Therefore, the potentials can be expanded around $\mathbf{r} = 0$, where only the lowest non vanishing order is considered. Assuming charge neutrality within the system ($\sum_i \mathbf{q}_i = 0$) the external electromagnetic potentials are:

$$\mathbf{A}_{\mathrm{ext}|\mathbf{r}=0}(\mathbf{r},t) \approx \mathbf{A}_{\mathrm{ext}}(\mathbf{r},t)_{|\mathbf{r}=0} \qquad \text{and} \qquad \Phi_{\mathrm{ext}|\mathbf{r}=0}(\mathbf{r},t) \approx [\nabla_{\mathbf{r}} \Phi_{\mathrm{ext}}(\mathbf{r},t)_{|\mathbf{r}=0} \cdot] \cdot \mathbf{r} \tag{2.5}$$

Now the gauge for the external potentials is chosen: $\chi(\mathbf{r},t) = -\mathbf{r} \cdot \mathbf{A}_{\mathrm{ext}}(0,t)$. Consequently, the vector potential vanishes [$\mathbf{A}'_{\mathrm{ext}}(\mathbf{r},t) = 0$] and the term corresponding to the scalar potential simplifies to: $\Phi'_{\mathrm{ext}}(\mathbf{r},t) = [\nabla_{\mathbf{r}} \Phi_{\mathrm{ext}}(\mathbf{r},t)_{|\mathbf{r}=0} + \dot{\mathbf{A}}_{\mathrm{ext}}(0,t)] \cdot \mathbf{r} = -\mathbf{E}_{\mathrm{ext}}(0,t) \cdot \mathbf{r}$. Thus, within this long wave length approximation, the charged particles interact directly with the electromagnetic field $\mathbf{E}_{\mathrm{ext}}(0,t) \cdot \mathbf{r}$. The

transition from the vector potential- to the electromagnetic field dependence in the Hamiltonian is also known as the GÖPPERT-MAYER transformation [GM31] but the electric dipole approximation can also be achieved by choosing a unitary translation operator [CT99]. The solid state Hamiltonian in the electric dipole approximation reads:

$$H = \sum_i \int \mathrm{d}^3 r \Psi_i^*(\mathbf{r}) \left(-\frac{\hbar^2 \nabla_{\mathbf{r}}^2}{2m_i} + U(\mathbf{r}) \right) \Psi_i(\mathbf{r}) \tag{2.6}$$

$$+ \sum_i \int \mathrm{d}^3 r \Psi_i^*(\mathbf{r}) q_i \mathbf{r} \cdot \mathbf{E}_{\mathrm{ext}}(0,t) \Psi_i(\mathbf{r}) \tag{2.7}$$

$$+ \sum_{ij} \frac{1}{2} \int \mathrm{d}^3 r \int \mathrm{d}^3 r' \Psi_i^*(\mathbf{r}) \Psi_i^*(\mathbf{r}') \frac{q_i \cdot q_j}{4\pi\varepsilon_0 |\mathbf{r} - \mathbf{r}'|} \Psi_i(\mathbf{r}') \Psi_i(\mathbf{r}) \tag{2.8}$$

$$= H_0 + H_{\mathrm{em}} + H_{\mathrm{Coul}}, \tag{2.9}$$

As mentioned before the first term, Eq. (2.6), corresponds to the free carrier energy (restricted by an additional potential U). Since the electrons do not move freely within the solid state but are restricted by the potential of the lattice, some modifications of the electronic free carrier part will be made in Sec. 2.2.1. Equation (2.8) describes the COULOMB interaction between the different charged particles within the material. In Sec. 2.2.2 the term will be separated into interactions of electrons and ions. To further evaluate the different terms of the Hamiltonian, the main characteristics of a solid state are investigated in the following section.

2.2 Particles in periodic structures

2.2.1 "Free" electronic motion

At first, the free carrier Hamiltonian [Eq. (2.6)] will be studied. H_0 can be split into the kinetics of the ions and of the electrons: $H_0 = H_{0,\mathrm{ion}} + H_{0,\mathrm{el}}$. The ions itself are strongly localized around its equilibrium position. However, looking at the ions as a collective system, it is possible to describe the motion as lattice waves. This will be done in more detail in Sec. 2.3.2. In contrast, the motion of single electrons in a solid state is now investigated with the time-independent SCHRÖDINGER equation in real space representation [Mes74]:

$$\mathscr{H}_{0,\mathrm{el}} \Psi(\mathbf{r})_{\mathrm{el}} = \left(-\frac{\hbar^2 \nabla_{\mathbf{r}}^2}{2m_0} + V_{\mathrm{latt}}(\mathbf{r}) \right) \Psi_{\mathrm{el}}(\mathbf{r}) = E \Psi_{\mathrm{el}}(\mathbf{r}), \tag{2.10}$$

with the free electron mass m_0. Here, the potential $U(\mathbf{r})$ has been replaced by the lattice potential $V_{\mathrm{latt}}(\mathbf{r})$ of the periodically positioned ions. As it will be seen in the next subsection, $V_{\mathrm{latt}}(\mathbf{r})$ originates from the electron-ion COULOMB Hamiltonian. The periodic lattice potential satisfies the condition $V_{\mathrm{latt}}(\mathbf{r}) = V_{\mathrm{latt}}(\mathbf{r} + \mathbf{R}_0)$, with the lattice vector $\mathbf{R}_0$. The eigenfunctions $\Psi_{n,\mathbf{k}}(\mathbf{r})$ of Eq. (2.10) are the so-called BLOCH functions [Zim92]:

$$\Psi_{n,\mathbf{k}}(\mathbf{r}) = \frac{1}{V} \mathrm{e}^{\mathrm{i}\mathbf{k}\cdot\mathbf{r}} u_{n,\mathbf{k}}(\mathbf{r}), \tag{2.11}$$

with the bulk volume V of the material and the lattice-periodic function $u_{n,\mathbf{k}}(\mathbf{r} + \mathbf{R}_0) = u_{n,\mathbf{k}}(\mathbf{r})$. The sub-indices assign the band number n and the momentum number $\mathbf{k}$. Hence, the eigenfunctions consist of plane waves (as an envelope function), modulated with the periodicity of the lattice. The lattice-periodic function must be evaluated due to the boundary conditions of the material. In general $u_{n,\mathbf{k}}(\mathbf{r})$ can be orthonormalized over the unit volume, which leads to the orthogonality of the BLOCH functions over the bulk volume: $\int_V \mathrm{d}^3 r \, \Psi_{n,\mathbf{k}}^*(\mathbf{r}) \Psi_{n',\mathbf{k}'}(\mathbf{r}) = \delta_{n,n'} \delta_{\mathbf{k},\mathbf{k}'}$.

Inserting the BLOCH function into Eq. (2.10), a differential equation for $u_{n,\mathbf{k}}(\mathbf{r})$ is obtained. If the motion of the electrons is concentrated near the band edge the eigenenergies can be expanded around

$\mathbf{k} = 0$. This results in second order in a correction of the electronic mass [Czy04]:

$$E_{n,\mathbf{k}} = \varepsilon_{n,\mathbf{k}=0} + \frac{\hbar^2\mathbf{k}^2}{2m_{\text{eff}}} \qquad \text{with} \qquad \frac{1}{m_{\text{eff}}} = \frac{\partial^2\varepsilon_{n,\mathbf{k}}}{\hbar^2\partial\mathbf{k}^2}_{|\mathbf{k}=0}, \tag{2.12}$$

with the energy offset $\varepsilon_{n,\mathbf{k}=0}$ at the band extrema of band n. This means that for small momenta, the electrons move under the influence of a periodic lattice potential quasi-freely but with a modified, effective electron mass m_{eff}. This so-called *effective mass approximation* is a common approximation in the solid state physics and will be used within this thesis. Thus, Eq. (2.10) simplifies to: $-(\hbar^2\nabla^2_{\mathbf{r}}/2m_{\text{eff}})\Psi_{\text{el}}(\mathbf{r}) = E\Psi_{\text{el}}(\mathbf{r})$, with the lattice-periodic function around the minimal momentum: $\Psi_{n,\mathbf{k}}(\mathbf{r}) = \frac{1}{V}e^{\mathrm{i}\mathbf{k}\cdot\mathbf{r}}u_{n,\mathbf{k}\approx 0}(\mathbf{r})$.

In a nano-structured material like a quantum well the electrons will experience a restriction of their free movement due to a confinement potential U_{conf} along the growth direction of the well $\mathbf{r}_\perp$. As U_{conf} occurs in addition to the already present lattice potential, the following SCHRÖDINGER must be solved:

$$\left(-\frac{\hbar^2\nabla^2_{\mathbf{r}}}{2m_{\text{eff}}} + U_{\text{conf}}(\mathbf{r}_\perp)\right)\Psi_{\text{el}}(\mathbf{r}) = E\Psi_{\text{el}}(\mathbf{r}). \tag{2.13}$$

Since the width of the potential is on a mesoscopic scale, $U(\mathbf{r}_\perp)$ is assumed to vary only slowly over a unit cell. In this case, the plane wave function in the perpendicular direction $\mathbf{r}_\perp$ must be replaced by a quantized wave function $\zeta_l(\mathbf{r}_\perp)$ which satisfies the restriction of the potential [HK04], while along the free in-plane direction $\mathbf{r}_\parallel$ of the well the electronic motion still can be described by plane waves. The eigenfunctions $\Psi_{n,\mathbf{k}}(\mathbf{r})$ of Eq. (2.13) then additionally account for the new quantum number of the so-called subband l: [2]

$$\Psi_{n,l,\mathbf{k}}(\mathbf{r}) = \frac{1}{\sqrt{V_\parallel}}e^{\mathrm{i}\mathbf{k}\cdot\mathbf{r}_\parallel}\zeta_l(\mathbf{r}_\perp)u_{n,\mathbf{k}\approx 0}(\mathbf{r}), \tag{2.14}$$

with the "volume" of the free direction $V_\parallel$.

Explicit calculations of the eigenfunctions of lower dimensional nanostructures will be done in Sec. 4.1 for intersubband quantum wells and in Sec.9.2.2 for intersublevel quantum dots.

2.2.2 The separation of ionic and electronic degrees of freedom

Next, the COULOMB Hamiltonian, Eq. (2.8), is split into the interaction among electrons, among ions and between electrons and ions:

$$\begin{aligned} H_{\text{Coul}} = \;& H_{\text{el-el}} + H_{\text{el-ion}} + H_{\text{ion-ion}} \\ =\;& \frac{1}{2}\int \mathrm{d}^3r \int \mathrm{d}^3r' \Psi^*_{\text{el}}(\mathbf{r})\Psi^*_{\text{el}}(\mathbf{r}')\frac{e_0^2}{4\pi\varepsilon_0|\mathbf{r}-\mathbf{r}'|}\Psi_{\text{el}}(\mathbf{r}')\Psi_{\text{el}}(\mathbf{r}) && (2.15)\\ -\;& \int \mathrm{d}^3r \int \mathrm{d}^3r' \Psi^*_{\text{el}}(\mathbf{r})\Psi^*_{\text{ion}}(\mathbf{r}')\frac{e_0 q_{\text{ion}}}{4\pi\varepsilon_0|\mathbf{r}-\mathbf{r}'|}\Psi_{\text{el}}(\mathbf{r}')\Psi_{\text{ion}}(\mathbf{r}) && (2.16)\\ +\;& \frac{1}{2}\int \mathrm{d}^3r \int \mathrm{d}^3r' \Psi^*_{\text{ion}}(\mathbf{r})\Psi^*_{\text{ion}}(\mathbf{r}')\frac{q_{\text{ion}}^2}{4\pi\varepsilon_0|\mathbf{r}-\mathbf{r}'|}\Psi_{\text{ion}}(\mathbf{r}')\Psi_{\text{ion}}(\mathbf{r}), && (2.17) \end{aligned}$$

with the electron charge e_0 and the charge of the ion q_{ion}. As mentioned in the beginning of the previous subsection, the ions are localized around their equilibrium position $\mathbf{R}^0_n$. Subsequently, the density of N ions can be approximated with localized densities around the Nth ion at $\mathbf{R}_n$: $\Psi^*_{\text{ion}}(\mathbf{r})\Psi_{\text{ion}}(\mathbf{r}) = \sum_{n=1}^{N}\delta(\mathbf{r}-\mathbf{R}_n)$. $H_{\text{el-ion}}$ then equals:

$$H_{\text{el-ion}} = \int \mathrm{d}^3r \sum_n \Psi^*_{\text{el}}(\mathbf{r})W_{\text{el-ion}}(|\mathbf{r}-\mathbf{R}_n|)\Psi_{\text{el}}(\mathbf{r}). \tag{2.18}$$

[2] This equation holds if the motion is restricted in only one or two dimensions. When all three dimensions are confined, the eigenfunction is fully described by the quantized wave function $\Psi_{n,l}(\mathbf{r}) = \zeta_{n,l}(\mathbf{r})u_{n,\mathbf{k}\approx 0}(\mathbf{r})$.

with $W_{\text{el-ion}}(|\mathbf{r}-\mathbf{R}_n|) = -e_0 q_{\text{ion}}/(4\pi\varepsilon_0|\mathbf{r}-\mathbf{R}_n|)$. If the assumption is made that the temporal motion of the ions is only a small displacement $\mathbf{s}_n(t)$ from the equilibrium position, that is, $\mathbf{R}_n = \mathbf{R}_n^0 + \mathbf{s}_n(t)$, the motion can be expanded around $\mathbf{R}_n^0$, leading in first-order to the following Hamiltonian:

$$H_{\text{el-ion}} = \int \mathrm{d}^3 r \sum_n \Psi_{\text{el}}^*(\mathbf{r}) W_{\text{el-ion}}(|\mathbf{r}-\mathbf{R}_n^0|)\Psi_{\text{el}}(\mathbf{r}) + \int \mathrm{d}^3 r \sum_n \Psi_{\text{el}}^*(\mathbf{r})\mathbf{s}_n \cdot [\nabla_{\mathbf{R}_n} W_{\text{el-ion}}(|\mathbf{r}-\mathbf{R}_n|)]_{|\mathbf{R}_n^0}\Psi_{\text{el}}(\mathbf{r}) \tag{2.19}$$

$$= \int \mathrm{d}^3 r \sum_n \Psi_{\text{el}}^*(\mathbf{r}) V_{\text{latt}}(\mathbf{r})\Psi_{\text{el}}(\mathbf{r}) \qquad + H_{\text{el-ph}}, \tag{2.20}$$

with $V_{\text{latt}}(\mathbf{r}) = W_{\text{el-ion}}(|\mathbf{r}-\mathbf{R}_n^0|)$. The first term describes the motion of the electrons within a periodic potential caused by the ions which form a static potential with regard to the electrons. The lattice potential V_{latt} has already been included in advance in the free electron Hamiltonian of the former subsection. The perturbation expansion of the ionic motion in zeroth order approximates the ions as a static lattice potential and subsequently leads to a decoupling of the motion of electrons and ions, also denoted as the BORN-OPPENHEIMER approximation. As a first-order correction, $H_{\text{el-ph}}$ treats the interaction between the electrons and the small time-dependent displacements $\mathbf{s}_n(t)$ of the ions, which will result in a collective treatment in the so-called *phonons* in the scheme of the second quantization (see following section).

In the same manner, the ion-ion Hamiltonian can be expanded: $H_{\text{ion-ion}} = \frac{1}{2}\sum_{n,m} W_{\text{ion-ion}}(|\mathbf{R}_n - \mathbf{R}_m|)$, with $W_{\text{ion-ion}} = q_{\text{ion}}^2/(4\pi\varepsilon_0|\mathbf{R}_n - \mathbf{R}_m|)$. Expanding $W_{\text{ion-ion}}$ around $\mathbf{R}_n^0$ in second order, the Hamiltonian reads [Czy04]:

$$H_{\text{ion-ion}} = \frac{1}{2}\sum_{nm} W_{\text{ion-ion}}(|\mathbf{R}_n^0 - \mathbf{R}_m^0|) \tag{2.21}$$

$$+ \frac{1}{2}\sum_{nm} (\mathbf{s}_n - \mathbf{s}_m)\cdot[\nabla_{\mathbf{R}_n-\mathbf{R}_m} W_{\text{ion-ion}}(|\mathbf{R}_n - \mathbf{R}_m|)]_{|\mathbf{R}_n^0-\mathbf{R}_m^0} \tag{2.22}$$

$$+ \frac{1}{2}\sum_{nm}\sum_{\alpha\beta}\frac{1}{2}(s_n^\alpha - s_m^\alpha)(s_n^\beta - s_m^\beta)\cdot[\partial^\alpha_{\mathbf{R}_n-\mathbf{R}_m}\partial^\beta_{\mathbf{R}_n-\mathbf{R}_m} W_{\text{ion-ion}}(|\mathbf{R}_n - \mathbf{R}_m|)]_{|\mathbf{R}_n^0-\mathbf{R}_m^0} \tag{2.23}$$

with $\alpha,\beta \in \{x,y,z\}$. The first-order term equals zero since the gradient around the equilibrium position vanishes. The second-order term can be rewritten in following way: $\tilde{\mathbf{R}}_i = \mathbf{R}_n - \mathbf{R}_m$, $\tilde{\mathbf{s}}_i = \mathbf{s}_m - \mathbf{s}_n$. The Hamiltonian then obtains the form:

$$H_{\text{ion-ion}} = \frac{1}{2}\sum_{nm} W_{\text{ion-ion}}(|\mathbf{R}_n^0 - \mathbf{R}_m^0|) + \frac{1}{2}\sum_{ij}\sum_{\alpha\beta}(\tilde{s}_i^\alpha)(\tilde{s}_j^\beta)\cdot[\partial^\alpha_{\mathbf{R}_i}\partial^\beta_{\mathbf{R}_j} W_{\text{ion-ion}}(|\tilde{\mathbf{R}}|)]_{|\tilde{\mathbf{R}}^0} \tag{2.24}$$

$$= H_{\text{Coul,ion}} \qquad + H_{\text{pot,ion}}. \tag{2.25}$$

The Hamiltonian $H_{\text{Coul,ion}}$ describes the static ionic bound of the crystal. It will not be further considered since the focus lies on the motion of the electrons and the collective lattice. The second term, $H_{\text{pot,ion}}$, can be interpreted as the potential energy of the collective lattice vibrations. Combined with the Hamiltonian $H_{0,\text{ion}}$ they result in the free energy of the phonons $H_{0,\text{ph}}$ (see next section). To conclude this section, following Hamiltonians will be considered for the description of interaction processes in the solid:

$$H_{0,\text{el}},\ H_{\text{em}},\ H_{\text{el-el}},\ H_{\text{el-ph}},\ (H_{0,\text{ion}} + H_{\text{pot,ion}}). \tag{2.26}$$

2.3 The second quantization formalism

2.3.1 Quantization of the fields

The description of an N-particle state requires the discrimination of bosonic particles with symmetric wave functions and integer spin, such as phonons, and fermionic particles with an antisymmetric wave

functions and half integer spin, such as electrons. In the scheme of the first quantization the expression of a many-particle state, consisting of a superposition of symmetrical and anti-symmetrical wave functions, becomes very laborious. An elegant simplification is realized within the second quantization: While in the first quantization, the wavelike character of particles is regarded, the second quantization pronounces the particle-like character. Overviews of the second quantization scheme are given, for example, in [Hak93, Mah00]. In this section, this formalism will be shortly recapitulated.

In second quantization, the wave function of the carriers are replaced by field operators $\hat{\Psi}(\mathbf{r},t)$ and $\hat{\Psi}^\dagger(\mathbf{r},t)$, which can be expanded in an orthonormal basis. In the case of electrons, the field operators consist of a basis set of eigenfunctions $\phi_\alpha(\mathbf{r})$ (gained from the SCHRÖDINGER equation in first quantization) with operator type expansion coefficients $\hat{a}^\dagger(t)$ and $\hat{a}(t)$:

$$\Psi_{\mathrm{el}}(\mathbf{r},t) \to \hat{\Psi}_{\mathrm{el}}(\mathbf{r},t) = \sum_{\{\alpha\}} \phi_{\{\alpha\}}(\mathbf{r})\hat{a}_{\{\alpha\}}(t) \quad \text{and} \quad \Psi^*_{\mathrm{el}}(\mathbf{r},t) \to \hat{\Psi}^\dagger_{\mathrm{el}}(\mathbf{r},t) = \sum_{\{\alpha\}} \phi^*_{\{\alpha\}}(\mathbf{r})\hat{a}^\dagger_{\{\alpha\}}(t), \quad (2.27)$$

where the Greek multi-index $\{\alpha\}$ includes the band number α, the wave vector $\mathbf{k}_\alpha$ and the spin s_α. In the following the time dependence will not be written out explicitly. The operators $\hat{a}^\dagger_\alpha$ and $\hat{a}_\alpha$ are *electron creation and annihilation operators* of one electron in state $\{\alpha\}$ and obey the anti-commutator relation, following from their anti-symmetric relation:

$$\begin{aligned} [\hat{a}_\alpha, \hat{a}^\dagger_\beta]_+ &= \hat{a}_\alpha \hat{a}^\dagger_\beta + \hat{a}^\dagger_\beta \hat{a}_\alpha = \delta_{\alpha\beta}, \\ [\hat{a}_\alpha, \hat{a}_\beta]_+ &= [\hat{a}^\dagger_\alpha, \hat{a}^\dagger_\beta]_+ = 0, \end{aligned} \quad (2.28)$$

In the case of the ionic motion, the displacement functions $\mathbf{s}_n(t)$ can also be expanded in a complete basis set of their amplitudes $\mathbf{A}_n$ with operator-like coefficients $\hat{Q}(t)$:

$$\mathbf{s}(\mathbf{r},t) \to \hat{\mathbf{s}}(\mathbf{r},t) = \frac{1}{\sqrt{m_{\mathrm{ion}} N}} \sum_{\{\lambda\}} \mathbf{A}_{\{\lambda\}}(\mathbf{r}) \mathrm{e}^{\mathrm{i}(\mathbf{q}\mathbf{R}_n - \omega_{\{\lambda\}} t)} \hat{Q}_{\{\lambda\}}(t) \quad (2.29)$$

with the number of elementary cells N and the Greek multi-index $\{\lambda\}$ including the phonon branch λ and the wave vector $\mathbf{q}_\lambda$. These operator-like coefficients themselves can be expressed by the creation operators $\hat{b}^\dagger(t)$ and annihilation operators $\hat{b}(t)$ of the lattice amplitude [Czy04]:

$$\hat{Q}_{\{\lambda\}} = \sqrt{\frac{\hbar}{2\omega_{\{\lambda\}}}} (\hat{b}^\dagger_{\lambda,\mathbf{q}_\lambda} + \hat{b}_{\lambda,-\mathbf{q}_\lambda}). \quad (2.30)$$

The new operators $\hat{b}^\dagger_{\lambda,\mathbf{q}_\lambda}$ and $\hat{b}_{\lambda,\mathbf{q}_\lambda}$ are denoted as *phonon creation and annihilation operators* of one phonon of the phonon branch λ and with the momentum vector $\mathbf{q}_\lambda$. The choice of this transformation will be clear when deriving the quantized form of the free phonon Hamiltonian $H_{0,\mathrm{ph}}$ in the following subsection. The phonon operators (being bosonic particles) obey the commutator relation:

$$\begin{aligned} [\hat{b}_\alpha, \hat{b}^\dagger_\beta]_- &= \hat{b}_\alpha \hat{b}^\dagger_\beta - \hat{b}^\dagger_\beta \hat{b}_\alpha = \delta_{\alpha\beta}, \\ [\hat{b}_\alpha, \hat{b}_\beta]_- &= [\hat{b}^\dagger_\alpha, \hat{b}^\dagger_\beta]_- = 0, \end{aligned} \quad (2.31)$$

In the following, the braces $\{\}$ in the indices will not be explicitly written, but if not otherwise noted, Greek letters are used for multi-indices. Using the field operators, it is possible to express the relevant Hamiltonians in the operator formalism.

2.3.2 The relevant Hamiltonians in second quantization

The free electron Hamiltonian $\hat{H}_{0,\mathrm{el}}$ - Applying the second quantization scheme, the Hamiltonian for free electrons can be transformed into the free electron Hamilton operator:

$$\begin{aligned}\hat{H}_{0,\mathrm{el}} &= \sum_{\alpha,\beta}\left[\int \mathrm{d}^3 r \phi_\alpha^*(\mathbf{r})(-\frac{\nabla_\mathbf{r}^2}{2m_{\mathrm{eff}}}+U_{\mathrm{conf}})\phi_\beta(\mathbf{r})\right]\hat{a}_\alpha^\dagger\hat{a}_\beta \\ &= \sum_\alpha \varepsilon_\alpha \hat{a}_\alpha^\dagger\hat{a}_\alpha \end{aligned} \tag{2.32}$$

with $\varepsilon_\alpha = \sum_\beta \int \mathrm{d}^3 r \phi_\alpha^*(\mathbf{r}) \mathscr{H}_{0,\mathrm{el}}\phi_\beta(\mathbf{r}) = \sum_\beta \varepsilon_\beta \int \mathrm{d}^3 r \phi_\alpha^*(\mathbf{r})\phi_\beta(\mathbf{r}) = \sum_\beta \varepsilon_\beta \delta_{\alpha,\beta}$. The energies are the eigenvalues, obtained from the SCHRÖDINGER equation. Explicit calculations are done in the following sections. $\hat{a}_\alpha^\dagger\hat{a}_\alpha = \hat{n}_\alpha$ is also denoted as the electron number operator. Thus, summarizing over α one obtains the number of electrons in the system.

The electron-electron Hamiltonian $\hat{H}_{\text{el-el}}$ - Inserting the electronic field operators into the electron-electron (*el-el*) COULOMB Hamiltonian $H_{\text{el-el}}$, one obtains:

$$\begin{aligned}\hat{H}_{\mathrm{el,el}} &= \frac{1}{2}\sum_{\alpha\beta\gamma\delta}\left[\frac{e_0^2}{4\pi\varepsilon_0\varepsilon_{\mathrm{bg}}}\int \mathrm{d}^3 r \int \mathrm{d}^3 r' \phi_\alpha^*(\mathbf{r})\phi_\beta^*(\mathbf{r}')\frac{1}{|\mathbf{r}-\mathbf{r}'|}\phi_\gamma(\mathbf{r})\phi_\delta(\mathbf{r}')\right]\hat{a}_\alpha^\dagger\hat{a}_\beta^\dagger\hat{a}_\gamma\hat{a}_\delta \\ &= \frac{1}{2}\sum_{\alpha\beta\gamma\delta} V_{\alpha\beta\gamma\delta}\,\hat{a}_\alpha^\dagger\hat{a}_\beta^\dagger\hat{a}_\delta\hat{a}_\gamma. \end{aligned} \tag{2.33}$$

Here, an additional background dielectric constant $\varepsilon_{\mathrm{bg}}$ has been added to take into account the material of the investigated system. Equation (2.33) describes the scattering of two electrons from the states δ and γ into the states δ and γ. These processes underlie spin and momentum conservation, which will be shown for intersubband quantum wells in Sec. 4.2.2.

The semi-classical electron-light Hamiltonian $\hat{H}_{\text{em}}$ - In the same way, the electron-light Hamiltonian in dipole approximation $\hat{H}_{\mathrm{em}}$ is obtained:

$$\begin{aligned}\hat{H}_{\mathrm{em}} &= -\sum_{\alpha\beta}\left[\int \mathrm{d}^3 r \phi_\alpha^*(\mathbf{r}) e_0 \mathbf{r}\cdot\mathbf{E}_{\mathrm{ext}}(0,t)\phi_\beta(\mathbf{r})\right]\hat{a}_\alpha^\dagger\hat{a}_\beta \\ &= -E(t)\sum_{\alpha\beta} d_{\alpha\beta}\hat{a}_\alpha^\dagger\hat{a}_\beta \end{aligned} \tag{2.34}$$

with the dipole matrix element $d_{\alpha\beta} = \int \mathrm{d}^3 r \phi_\alpha^*(\mathbf{r}) e_0 \mathbf{r}\cdot\mathbf{e}_E\phi_\beta(\mathbf{r})$ in direction of the external electromagnetic field $\mathbf{E}_{\mathrm{ext}}(0,t) = E(t)\mathbf{e}_E$. It has been mentioned before that the interaction of electrons with a quantized electromagnetic field (photons) is neglected here. The interaction with photons becomes relevant in the few-photon limit. However, since the systems treated in this thesis are excited with coherent laser fields (which emit multiple tens of photons) quantum optical effects can be disregarded.

The free phonon Hamiltonian $\hat{H}_{\text{0,ph}}$ - The free phonon Hamiltonian consists of the free ion Hamilto-

nian and the potential energy of the ions:

$$H_{0,\mathrm{ph}} = H_{0,\mathrm{ion}} + H_{\mathrm{pot,ion}} = \frac{1}{2}\int \mathrm{d}^3 r \Psi^*_{\mathrm{ion}}(\mathbf{r}) \left(-\frac{\hbar^2 \nabla^2_{\mathbf{r}}}{m_{\mathrm{ion}}} \right) \Psi_{\mathrm{ion}}(\mathbf{r}) + \frac{1}{2}\sum_{ij}\sum_{\alpha\beta} \Phi^{i,j}_{\alpha,\beta} \tilde{s}^{\alpha}_i \tilde{s}^{\beta}_j . \tag{2.35}$$

with $\Phi^{i,j}_{\alpha,\beta} = [\partial^{\alpha}_{\mathbf{R}_i} \partial^{\beta}_{\mathbf{R}_j} W_{\text{ion-ion}}(|\tilde{\mathbf{R}}|)]_{|\tilde{\mathbf{R}}^0}$. Minding the localization of one ion i around its equilibrium position $\mathbf{R}_i = \mathbf{R}^0_i + \mathbf{s}_i(t)$ (see Sec. 2.2.2), $\nabla^2_{\mathbf{r}}$ in $H_{0,\mathrm{ion}}$ can be restricted to the gradient around the respective position $\mathbf{R}_i$ of the ions. i.e.

$$\frac{1}{2}\int \mathrm{d}^3 r \Psi^*_{\mathrm{ion}}(\mathbf{r}) \left(-\frac{\hbar^2 \nabla^2_{\mathbf{r}}}{m_{\mathrm{ion}}} \right) \Psi_{\mathrm{ion}}(\mathbf{r}) = \frac{1}{2}\sum_i \left(-\frac{\hbar^2 \nabla^2_{\mathbf{R}_i}}{m_{\mathrm{ion}}} \right) = \frac{1}{2}\sum_i \left(-\frac{\hbar^2 \nabla^2_{\mathbf{s}_i}}{m_{\mathrm{ion}}} \right). \tag{2.36}$$

In the quantum mechanical description, $-\frac{\hbar}{\mathrm{i}}\nabla_{\mathbf{s}_i} = \mathbf{p}_{\mathbf{s}_i}$ is the momentum operator of the displacement $\mathbf{s}_i$ in real space representation. Thus, following the LAGRANGE formalism, the time derivative of the displacement equals $\dot{\mathbf{s}}_i = -\frac{\partial \mathscr{H}}{\partial \mathbf{p}_{\mathbf{s}_i}} = m_{\mathrm{ion}} \nabla_{\mathbf{s}_i}$. If now the displacement is replaced by its field operator according to Eq. (2.29) one obtains for Eq. (2.35):

$$\hat{H}_{0,\mathrm{ph}} = 1/2(\sum_{\lambda} \dot{\hat{Q}}^*_{\lambda} \dot{\hat{Q}}_{\lambda} + \omega^2_{\lambda} \hat{Q}^*_{\lambda} \hat{Q}_{\lambda}) \tag{2.37}$$

This Hamiltonian corresponds to the equation of motion for a set of uncoupled oscillators. Similar to the solution in the first quantization formalism, where the motion of the uncoupled oscillators can be solved with the introduction of ladder operators, Eq. (2.37) is solved by expressing $\hat{Q}_i$ with creation and annihilation operators using Eq. (2.30). Thus, the free phonon Hamiltonian in operator formalism finally becomes [Hak93]:

$$\hat{H}_{0,\mathrm{ph}} = \sum_{\mathbf{q}j} \hbar\omega_{\mathbf{q}j} \hat{b}^{\dagger}_{\mathbf{q}j} \hat{b}_{\mathbf{q}j}, \tag{2.38}$$

The energy dispersion $\hbar\omega_{\mathbf{q}j}$ depends (besides the momentum vector $\mathbf{q}$) on the phonon branch j of the collective lattice wave. Solving the SCHRÖDINGER equation for the ions, the phonon branches can be divided into the motion of the phonons longitudinal (L) or transverse (T) with respect to the direction of the lattice wave. Furthermore, the branch depends on the phase of the oscillation, where the in-phase-oscillating phonons are denoted as acoustic (A) and the with opposite-in-phase oscillating phonons are called optical (O) phonons.

The electron-phonon Hamiltonian $\hat{H}_{\text{el-ph}}$ - Finally, the electron phonon Hamilton operator $\hat{H}_{\text{el-ph}}$ is expressed in the second quantization scheme by inserting the field operators for the electronic wave functions $\Psi_{\mathrm{el}}(\mathbf{r},t)$ and for the displacement $\mathbf{s}_n$:

$$H_{\text{el-ph}} = \sum_n \sum_{\alpha\beta} \left[\int \mathrm{d}^3 r \phi^*_{\alpha}(\mathbf{r}) \cdot [\nabla_{\mathbf{R}_n} W_{\text{el-ion}}(|\mathbf{r} - \mathbf{R}_n|)]_{|\mathbf{R}^0_n} \phi^*_{\beta}(\mathbf{r}) \right] \hat{a}^{\dagger}_{\alpha} \hat{\mathbf{s}}_n \hat{a}_{\beta} \tag{2.39}$$

Using again Eqs. (2.29) and (2.30), where the displacement operator $\hat{\mathbf{s}}_n$ is decomposed into the phonon operators $\hat{b}^{\dagger}_{\mathbf{q}}$, $\hat{b}_{\mathbf{q}}$, one finally obtains:

$$\hat{H}_{\mathrm{el,ph}} = \sum_{\mathbf{q}} \sum_{\alpha\beta} g^{\alpha\beta}_{\mathbf{q}} \hat{a}^{\dagger}_{\alpha} \hat{b}_{\mathbf{q}} \hat{a}_{\beta} + g^{\alpha\beta *}_{\mathbf{q}} \hat{a}^{\dagger}_{\beta} \hat{b}^{\dagger}_{\mathbf{q}} \hat{a}_{\alpha}, \tag{2.40}$$

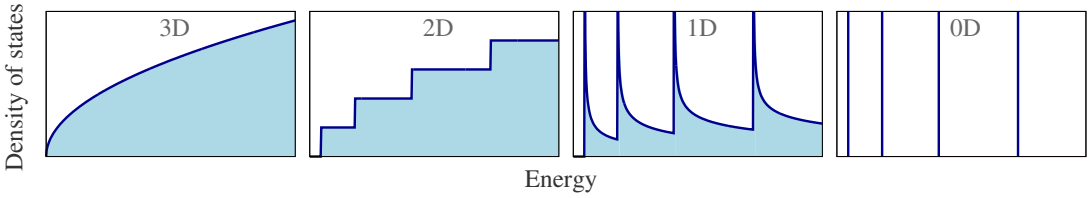

Figure 2.1 | The density of states over energy for electrons in different dimensions

with the electron-phonon (*el-ph*) matrix element $g_{\mathbf{q}}^{\alpha\beta}$. $\hat{H}_{\text{el,ph}}$ describes a phonon-assisted scattering: One electron scatters from state $\beta(\alpha)$ into the state $\alpha(\beta)$ under absorption (emission) of one phonon. For LO phonons (which will be mostly considered throughout this work), the 3D *el-ph*-interaction value is given by the FRÖHLICH coupling [Mah00]:

$$g_{\mathbf{q}}^{\text{3D}} = \mathrm{i}\left[\frac{e_0^2\hbar\omega_{\text{LO}}}{2\cdot\varepsilon_0 V}(\varepsilon_\infty^{-1}-\varepsilon_s^{-1})\right]^{\frac{1}{2}}\frac{1}{|\mathbf{q}|}. \tag{2.41}$$

Here, the LO phonons are treated in EINSTEIN approximation where the energy of the phonons is independent from their momentum, that is, $\hbar\omega_{\mathbf{q}} = \hbar\omega_{\text{LO}}$. If the dimensionality of the system is restricted along a direction $\mathbf{r}_\perp$, the *el-ph* matrix element is modified with an additional form factor: $g_{\mathbf{q}}^{\alpha\beta} = g_{\mathbf{q}}^{\text{3D}}\mathscr{F}_{\alpha\beta}$ with $\mathscr{F}_{\alpha\beta} = \int \mathrm{d}\mathbf{r}_\perp \Psi^*(\mathbf{r}_\perp)\mathrm{e}^{\mathrm{i}\mathbf{q}_\perp\mathbf{r}_\perp}\Psi(\mathbf{r}_\perp)$. The FRÖHLICH coupling matrix element is explicitly calculated for intersubband quantum wells in Sec. 4.2 and for intersublevel quantum dots in Sec. 9.2.

2.4 Restriction of dimensionality

The addition of a confinement potential in a solid not only leads to the modification of the electronic eigenfunctions and eigenenergies. Most notably, each restriction of dimensionality of the electronic motion results in the change of their *density of states* (DOS) which considers the possibility of occupying a state within a certain energy (or momentum) range. In a bulk material, where electrons can move quasi-freely in three dimensions (3D), the DOS is proportional to the square root of the energy: $\text{DOS}_{\text{3D}} \propto \sqrt{\varepsilon}$. The motion within a two-dimensional structure (2D), such as a quantum well, is limited in one direction (along the growth direction of the well), but still quasi-free in the remaining two directions (along the in-plane direction). The corresponding DOS is a step function: $\text{DOS}_{\text{2D}} \propto \Theta(\varepsilon-\varepsilon_i)$. A further restriction down to quasi-free motion in only one dimension (1D) scales with $\text{DOS}_{\text{1D}} \propto \frac{1}{\sqrt{\varepsilon}}$ while in a zero-dimensional structure (0D), such as a quantum dot, the DOS becomes discrete, that is, $\text{DOS}_{\text{0D}} \propto \delta(\varepsilon)$. The dependence of the DOS on the dimensionality is shown in Fig. 2.1.

Based on the fundamentals recapitulated in this part, different n-dimensional structures will be investigated in this work: Part III studies 2D structures (quantum wells) as well was the dynamics between 3D and 2D structures (bulk-surface dynamics). Part IV concentrates on a 0D structure (quantum dot).

Chapter 3

Tools for describing the temporal dynamics

3.1 Pictures in quantum mechanics

Now that the solid can be microscopically described by various interaction operators, a scheme for the temporal development of measurable observables must be chosen. Starting point is the well-known free carrier SCHRÖDINGER equation in a basis independent notation, which describes the time evolution of a one- or multiple particle state in the Hilbert space $\mathscr{H}$:

$$\mathrm{i}\hbar\partial_t |\Psi(t)\rangle = \hat{H}_{\mathrm{sys}} |\Psi(t)\rangle . \tag{3.1}$$

The system Hamiltonian $\hat{H}_{\mathrm{sys}}$ determines the time evolution of the wave function. In the so-called SCHRÖDINGER representation, the time development lies in the wave function while operators are generally time-independent. However, very often the time-development of the operator is the interesting value since many physical observables are found as expectation values of operators. Analogous to the classical mechanics, where the time evolution of an observable can be determined by the POISSON bracket, it is advantageous to consider a corresponding temporal evolution scheme for an operator. A change of the time dependence can be performed with the time evolution operator $\hat{U}(t,t_0)$ [GR86], which is a formal solution of the SCHRÖDINGER equation:

$$\hat{U}(t,t_0) = \hat{T}_{\leftarrow} \exp\left(-\frac{\mathrm{i}}{\hbar}\int_{t_0}^{t} \mathrm{d}\tau \hat{H}_{\mathrm{sys}}(\tau)\right), \tag{3.2}$$

$$|\Psi(t)\rangle = \hat{U}(t,t_0)\,|\Psi(t_0)\rangle , \tag{3.3}$$

with the time-order operator $\hat{T}_{\leftarrow}$, arranging the time from t_0 to t in an increasing order, i.e $t_0 < t$. Since $\hat{U}(t,t_0)$ is a unitary operator, it can be used as a transformation between different pictures for the time development of operators and wave functions without changing the mean expectation values. If $\hat{U}(t,t_0)$ is applied on $|\Psi(t_0)\rangle$ and an arbitrary operator in Hilbert space $\hat{O}$, the quantities enter the HEISENBERG picture:

$$|\Psi_{\mathrm{H}}(t_0)\rangle = \hat{U}^{\dagger}(t,t_0)\,|\Psi(t)\rangle , \tag{3.4}$$

$$\hat{O}_{\mathrm{H}}(t) = \hat{U}^{\dagger}(t,t_0)\hat{O}(t_0)\hat{U}(t,t_0), \tag{3.5}$$

where the wave functions in the HEISENBERG picture $|\Psi_{\mathrm{H}}\rangle$ become time-independent and the operators $\hat{O}_{\mathrm{H}}$ time-dependent. Taking the total time derivative of $\hat{O}_{\mathrm{H}}$, one obtains the HEISENBERG equation of

motion:

$$\frac{\mathrm{d}}{\mathrm{d}t}\hat{O}_{\mathrm{H}} = \frac{\mathrm{i}}{\hbar}\left[\hat{H}_{\mathrm{sys}}, \hat{O}_{\mathrm{H}}\right]_{-} + \left(\partial_t \hat{O}\right)_{\mathrm{H}}. \tag{3.6}$$

If the operators are not explicitly time-dependent, the last part in Eq. (3.6) vanishes. The HEISENBERG equation of motion (EOM) without explicit time dependence will be mostly used throughout this thesis to solve the microscopic dynamics.

In some cases it is useful to separate the system Hamiltonian $\hat{H}_{\mathrm{sys}}$ into a free, time-independent part $\hat{H}_0$ and a weak time-dependent part $\hat{H}'$: $\hat{H}_{\mathrm{sys}} = \hat{H}_0 + \hat{H}'(t)$. In this so-called INTERACTION picture, the time evolution operator (as well as the wave functions and common operators) is defined with respect to the unperturbed system Hamiltonian $\hat{H}_0$:

$$\hat{U}_0(t,t_0) = \hat{T}_{\leftarrow} \exp\left(-\frac{\mathrm{i}}{\hbar}\hat{H}_0(t-t_0)\right), \tag{3.7}$$

$$|\Psi_{\mathrm{I}}(t)\rangle = \hat{U}_0^{\dagger}(t,t_0)\,|\Psi(t)\rangle\,, \tag{3.8}$$

$$\hat{O}_{\mathrm{I}}(t) = \hat{U}_0^{\dagger}(t,t_0)\hat{O}\hat{U}_0(t,t_0). \tag{3.9}$$

The time dependence in the INTERACTION picture lies in both the wave vector and operator. The time evolution of these quantities is given by the following equations:

$$\frac{\mathrm{d}}{\mathrm{d}t}\hat{O}_{\mathrm{I}} = \frac{\mathrm{i}}{\hbar}\left[\hat{H}_0, \hat{O}_{\mathrm{I}}\right]_{-} + \left(\partial_t \hat{O}\right)_{\mathrm{I}} \tag{3.10}$$

$$\partial_t\,|\Psi_{\mathrm{I}}(t)\rangle = -\frac{\mathrm{i}}{\hbar}H'_{\mathrm{I}}(t)\,|\Psi_{\mathrm{I}}(t)\rangle\,. \tag{3.11}$$

It should be stressed that operators in the INTERACTION picture evolve in time with the free Hamiltonian, while the time evolution of the wave functions is given by the perturbation Hamiltonian. According to different requirements it is useful to switch between the different pictures. Their equivalence is shown in the equity of mean expectation values: $\langle\hat{O}\rangle = \sum_i \langle\Psi_i|\,\hat{O}\,|\Psi_i\rangle = \sum_i \langle\Psi_{\mathrm{H},i}|\,\hat{O}_{\mathrm{H}}\,|\Psi_{\mathrm{H},i}\rangle = \sum_i \langle\Psi_{\mathrm{I},i}|\,\hat{O}_{\mathrm{I}}\,|\Psi_{\mathrm{I},i}\rangle$.

3.2 The density operator

Facing the applicability of theoretical schemes onto experiments, one major problem originates from the fact that the preparation of the system's initial state always contain an amount indetermination. Furthermore, many experimental results are usually obtained by repeating the measurements, where it is an impossible task to prepare the system for each experiment to be in the same state. Thus, the system cannot be described by pure states. To overcome this problem, the many-particle system is expressed by a statistical average by the means of a *density operator* $\hat{\rho}$ [VN68]. The density operator considers the superposition of pure states (the so-called mixed state):

$$\hat{\rho} = \sum_i p_i\,|\Psi_i\rangle\,\langle\Psi_i| \qquad \text{with} \qquad p_i \geq 0, \text{ and } \sum_i p_i = 1, \tag{3.12}$$

with the probability p_i of the system to be in one of the possible states $|\Psi_i\rangle$. The expectation value of an operator is then given by the trace with the density operator over a basis set of eigenstates $|n_i\rangle$:

$$\langle\hat{O}\rangle = \mathrm{tr}\left(\hat{\rho}\hat{O}\right) = \sum_i \langle n_i|\,\hat{\rho}\hat{O}\,|n_i\rangle\,. \tag{3.13}$$

Using the SCHRÖDINGER equation Eq. (3.1) for $|\Psi(t)\rangle$ and its complex conjugate $\langle\Psi(t)|$, the LIOUVILLE-VON-NEUMANN equation of motion for the density operator can be derived:

$$\partial_t\hat{\rho} = -\frac{\mathrm{i}}{\hbar}\left[\hat{H}_{\mathrm{sys}}, \hat{\rho}\right]_{-}. \tag{3.14}$$

By introducing the density operator, it is also possible to describe only one part of the system, which is of interest for the investigations, for example, a system of particles in a bath. In this reduced system, one can define a *reduced* density operator, where the expectation value can be obtained via the partial trace over the basis set of the system of interest [Muk95].

To solve the differential equation for $\hat{\rho}$, the INTERACTION picture will be used. Using Eq. (3.11) and the definitions Eq. (3.7)-(3.9), the equation for the density operator in INTERACTION picture reads [Muk95]:

$$\partial_t \hat{\rho}_\mathrm{I} = -\frac{\mathrm{i}}{\hbar}\left[\hat{H}'_\mathrm{I}, \hat{\rho}_\mathrm{I}\right]_- . \tag{3.15}$$

The integration of Eq. (3.15) gives a formal solution of the density operator:

$$\hat{\rho}_\mathrm{I}(t) = \hat{\rho}_\mathrm{I}(t_0) + \left(-\frac{\mathrm{i}}{\hbar}\right)\int_{t_0}^{t} \mathrm{d}t_1 \left[\hat{H}'_\mathrm{I}(t_1), \hat{\rho}_\mathrm{I}(t_1)\right]_- . \tag{3.16}$$

By iteratively using Eq. (3.16), the density operator can be written in a NEUMANN sum: Transforming back into the SCHRÖDINGER picture, the integral expression for the density operator is obtained:

$$\begin{aligned}\hat{\rho}(t) = \rho(t_0) + \left(-\frac{\mathrm{i}}{\hbar}\right)^n \sum_n \int_{t_0}^{t} \mathrm{d}t_n \int_{t_0}^{t_n} \mathrm{d}t_{n-1} \ldots \int_{t_0}^{t_2} \mathrm{d}t_1 \times \\ \hat{U}_0(t,t_0)\left[\hat{H}'_\mathrm{I}(t_n), \left[\hat{H}'_\mathrm{I}(t_{n-1}), \ldots \left[\hat{H}'_\mathrm{I}(t_1), \rho_\mathrm{I}(t_0)\right]_- \ldots\right]_-\right]_- \hat{U}_0^\dagger(t,t_0),\end{aligned} \tag{3.17}$$

This equation nicely depicts the time evolution of the density operator under small perturbations: Beginning from t_0 the system evolves freely until the time t_1, where the system then interacts with $\hat{H}'_\mathrm{I}(t_1)$. At the time t_2 the second interaction takes place and so forth. The times in Eq. (3.17) must be chronologically ordered in time, e.g. $t_1 < \ldots < t_{n-1} < t_n < t$. This can be automatically fulfilled by including the time evolution operator $\hat{T}_\leftarrow$.

3.3 Macroscopic polarization and response function

In most optical experiments, an electromagnetic field is used to probe the material. Under field excitation the sample responds with a macroscopic polarization $P(t)$, which contains informations about, for example, the band structure or many-body interactions. Based on the strength of the incoming field, different spectroscopic methods are applied; If a weak electromagnetic field interacts with the sample, optical absorption spectra are the first choice. For excitation with strong fields nonlinearities occur and n-wave mixing spectroscopy can be performed. Thus it seems reasonable to expand the density operator in orders of the electromagnetic field as a weak perturbation $\hat{H}'(t) = E(t)\hat{\mu}$ with $\hat{\mu} = \sum_{\alpha\beta} d_{\alpha\beta}\hat{a}^\dagger_\alpha \hat{a}_\beta$ [Ham05]:

$$\hat{\rho}(t) = \hat{\rho}^{(0)}(t) + \sum_n \hat{\rho}^{(n)}(t), \qquad \text{with}$$

$$\begin{aligned}\hat{\rho}^{(n)}(t) = \left(-\frac{\mathrm{i}}{\hbar}\right)^n \int_0^\infty \mathrm{d}\tau_n \int_0^\infty \mathrm{d}\tau_{n-1} \ldots \int_0^\infty \mathrm{d}\tau_1 \, E(t-\tau_n)E(t-\tau_n-\tau_{n-1})\ldots E(t-\tau_n-\ldots-\tau_1)\prod_i \Theta(\tau_i)\times \\ \hat{U}_0(t,-\infty)\left[\hat{\mu}_\mathrm{I}(\tau_{n-1}+\tau_{n-2}+\ldots+\tau_1), \left[\hat{\mu}_\mathrm{I}(\tau_{n-2}+\ldots+\tau_1), \ldots [\hat{\mu}_\mathrm{I}(0), \rho_\mathrm{I}(-\infty)]_- \ldots\right]_-\right]_- \hat{U}_0^\dagger(t,-\infty).\end{aligned} \tag{3.18}$$

and $\hat{\rho}^{(0)}(t) = \hat{\rho}(t_0)$. In Eq. (3.18) the starting time t_0 was set to $t_0 \to -\infty$ and the time variables have been substituted with the delay times: $\tau_1 = t_2 - t_1$, $\tau_2 = t_3 - t_2$, …, $\tau_n = t - t_n$, see also Fig. 3.1.[1] Due

[1] Note that in contrast to the electromagnetic field, the time dependencies in the dipole operators have been repositioned to start with the delay time τ_1. So, the most recent time duration $t - \tau_n$ (far right in Fig. 3.1) can be expressed by all previous durations: $t - \tau_n = \tau_{n-1} + \tau_{n-2} + \ldots + \tau_1$. Hence, the dipole operators arguments can be written as $\hat{\mu}_\mathrm{I}(t-\tau_n) = \hat{\mu}_\mathrm{I}(\tau_{n-1}+\tau_{n-2}+\ldots+\tau_1)$, as well as $\hat{\mu}_\mathrm{I}(t-\tau_n-\tau_{n-1}-\ldots-\tau_1) = \hat{\mu}_\mathrm{I}(0)$.

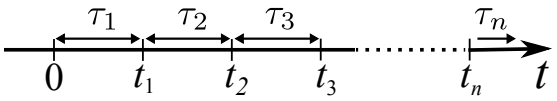

Figure 3.1 | Substitution of the time variables: $\tau_i = t_{i+1} - t_i$.

to the chronological time order, the delay times must be larger than zero, which is guaranteed by the Heaviside function $\Theta(\tau_i)$.

Now, the macroscopic polarization $P(t)$ can be expressed by the help of the density operator, which is given by the expectation value of the dipole operator:

$$P(t) = \langle \hat{\mu} \rangle = \mathrm{tr}\,(\hat{\rho}\hat{\mu}). \tag{3.19}$$

Using Eq. (3.18) for $P(t) = \sum_n P^{(n)}(t)$, one obtains for the nth-order macroscopic polarization $P^{(n)}(t)$:

$$P^{(n)}(t) = \left(-\frac{\mathrm{i}}{\hbar}\right)^n \int_0^\infty \mathrm{d}\tau_n \int_0^\infty \mathrm{d}\tau_{n-1} \ldots \int_0^\infty \mathrm{d}\tau_1\, S^{(n)}(\tau_n, \tau_{n-1}, \ldots, \tau_1) \times E(t-\tau_n)E(t-\tau_n-\tau_{n-1})\ldots E(t-\tau_n-\ldots-\tau_1), \tag{3.20}$$

with the *nth-order nonlinear response function* $S^{(n)}$:

$$S^{(n)}(\tau_n, \tau_{n-1}, \ldots, \tau_1) = \langle \hat{\mu}_\mathrm{I}(\tau_n+\tau_{n-1}+\ldots+\tau_1) \times \Big[\hat{\mu}_\mathrm{I}(\tau_{n-1}+\tau_{n-2}+\ldots+\tau_1), \big[\hat{\mu}_\mathrm{I}(\tau_{n-2}+\ldots+\tau_1), \ldots [\hat{\mu}_\mathrm{I}(0), \rho_\mathrm{I}(-\infty)]_- \ldots\big]_-\Big]_- \prod_i \Theta(\tau_i)\rangle. \tag{3.21}$$

Here, the invariance of the trace under cyclical permutation has been used: $\langle \hat{\mu}\hat{U}_0(t,-\infty)\hat{U}_0^\dagger(t,-\infty)\rangle = \langle \hat{U}_0^\dagger(t,-\infty)\hat{\mu}\hat{U}_0(t,-\infty)\rangle = \mu_\mathrm{I}(t) = \mu_\mathrm{I}(\tau_n+\tau_{n-1}+\ldots+\tau_1)$. The nth-order response function $S^{(n)}$ contains the interaction with the electromagnetic field at the distinct times τ_i. The superscript in (n) reflects the least order of interaction with the electromagnetic field. A simple expression of $P^{(n)}$ in the FOURIER space can be found with the GREENs function formalism, which describes the dynamics of free particles [Sch64, GHE01] in a compact way. However, if many-particle effects, such as *el-el-* and *el-ph* interaction are included in the dynamics, it becomes an elaborate task for obtaining the corresponding GREENs function.

Evaluating the commutators in $S^{(n)}$, the polarization of third-order already comprise multiple hundreds of terms (see also Sec. 7.2). Each term, also denoted as LIOUVILLE pathway, describes a distinct interaction between the sample and the field. Examples of different LIOUVILLE pathways will be given in Sec. 7.3.1. A common description for the evolution of the density operator is the super-operator formalism in the LIOUVILLE space [FS90, Muk95]. Although the interpretation and the resulting equations for the density operator and the macroscopic polarization are equal in the HILBERT space and in the LIOUVILLE space, the derivation of these quantities can be done in a more elegant way by using the super-operator formalism [Muk95]. A short introduction of the LIOUVILLE space description is given in Sec. 7.2.1: The macroscopic polarization will be rewritten with super-operators, since the description builds the base for a diagrammatic representation of the pathways, the so-called *double-sided Feynman diagrams* (Sec. 7.2.2). [2]

[2] These FEYNMAN diagrams will be used for the interpretation of the dynamics in Chap. 7. However, the calculations of the dynamics will be carried out in the HILBERT space description.

3.4 Optical absorption

Fundamental optical properties of a sample can already be seen in the linear optics regime, where the external electromagnetic field is so weak that the expansion of $P = \sum_n P^{(n)}$ can be approximated by $P \approx P^{(1)}$. In first order, the polarization $P^{(1)}$ reads:

$$P^{(1)}(t) = \left(-\frac{\mathrm{i}}{\hbar}\right) \int_0^\infty \mathrm{d}t_1 \, S^{(1)}(t_1) E(t-t_1) \qquad \text{with} \qquad S^{(1)}(t_1) = \langle \hat{\mu}_\mathrm{I}(t_1) \cdot [\hat{\mu}_\mathrm{I}(0), \hat{\rho}(-\infty)]_- \rangle. \quad (3.22)$$

In the frequency domain, a simple relation between the macroscopic polarization and the electromagnetic field is obtained:

$$\begin{aligned} P^{(1)}(\omega) &= -\frac{\mathrm{i}}{\hbar} \int_{-\infty}^{\infty} \mathrm{d}t \int_0^\infty \mathrm{d}t_1 \, S^{(1)}(t_1) E(t-t_1) \mathrm{e}^{\mathrm{i}\omega t} \\ &= -\frac{\mathrm{i}}{\hbar} \int_{-\infty}^{\infty} \mathrm{d}t_2 \int_0^\infty \mathrm{d}t_1 \, S^{(1)}(t_1) E(t_2) \mathrm{e}^{\mathrm{i}\omega(t_1+t_2)} \\ &= \varepsilon_0 \chi^{(1)}(\omega) E(\omega), \qquad \text{with} \qquad \varepsilon_0 \chi^{(1)} := -\frac{\mathrm{i}}{\hbar} \int_0^\infty \mathrm{d}t_1 S^{(1)}(t_1) \mathrm{e}^{\mathrm{i}\omega t_1}. \end{aligned} \quad (3.23)$$

The dielectric constant in vacuum is denoted by ε_0 and the linear susceptibility by $\chi^{(1)}(\omega)$ [Jac99]. Thus, in the frequency domain the first-order macroscopic polarization $P^{(1)}$ is proportional to the electromagnetic field. With this expression, it is possible to obtain a formula for the absorption coefficient $\alpha(\omega)$ of a sample, which is an experimentally accessible quantity. $\alpha(\omega)$ determines the intensity $I(z)$ of an electromagnetic field crossing through a sample with a thickness z, which is given by Beer's law: $I(z) = |E(z,t)E^*(z,t)| = I_0 e^{-\alpha(\omega)\Delta z}$. It can be calculated according to [SW02]:

$$\alpha(\omega) = 2\frac{\omega}{c_0} n_{bg} \mathrm{Im}\{\sqrt{1+\frac{\chi^{(1)}(\omega)}{{n_\mathrm{bg}}^2}}\} \approx \frac{\omega}{c_0 n_{bg}} \mathrm{Im}\{\chi^{(1)}\} = \frac{\omega}{c_0 \varepsilon_0 n_{bg}} \mathrm{Im}\{\frac{P^{(1)}(\omega)}{E(\omega)}\}, \quad (3.24)$$

with the speed of light c_0 and the refractive index n_bg of the surrounding medium. Since the one-particle electron expectation values correspond to the elements of the density matrix, that is, $\langle \hat{a}_i^\dagger \hat{a}_j \rangle = \rho_{ij}$, the macroscopic polarization P can be expressed by the electronic creation and annihilation operators:

$$P(t) = \mathrm{tr}\,(\hat{\rho}\hat{\mu}) = \sum_{ij} d_{ij} \langle \hat{\rho} \hat{a}_i^\dagger \hat{a}_j \rangle = \sum_{ij} d_{ij} \langle \hat{a}_i^\dagger \hat{a}_j \rangle, \qquad i,j \in \{\mathrm{v,c}\}. \quad (3.25)$$

The subindices i, j include the summation over all bands within the conduction band (c) and the valence (v) band. If the summation over the momentum number $\mathbf{k}$ is considered, the macroscopic polarization reads $P(t) = 1/V_\mathbf{k} \sum_{ij,\mathbf{k}} d_{ij} \langle \hat{a}_{i,\mathbf{k}}^\dagger \hat{a}_{j,\mathbf{k}} \rangle$, with the dimensional volume $1/V_\mathbf{k}$ corresponding to the dimension of the momentum number $\mathbf{k}$.

3.5 Overview of applied concepts

Throughout this thesis the HEISENBERG equation of motion (EOM) [Eq. (3.6)] will be used to calculate the dynamics of the relevant operators. The fundamental expectation values which are connected to measurable quantities are the microscopic densities $f_i = \langle \hat{a}_i^\dagger \hat{a}_i \rangle$ and the microscopic polarizations $p_{ij} = \langle \hat{a}_i^\dagger \hat{a}_j \rangle, i \neq j$. The advantage of the HEISENBERG-EOM, lies in the possibility to easily incorporate many-particle effects. On the other hand, the many-particle Hamiltonians lead to the so-called hierarchy problem since single-particle expectation values couple to higher-order expectation values (see part III). The solution of this problem depends on the investigating system: While for intersubband quantum well systems (Chap. 4) the correlation expansion [Kuh98] is used, in intersublevel quantum dot systems (Chap. 10) it is possible to obtain an analytical expression for a closed set of differential equations via the induction method. The schemes will be presented in the corresponding chapters. If the investigation

is focused on the long-time dynamics (neglecting quantum kinetics), the EOMs, previously obtained via HEISENBERG can also be approximated with relaxation rate equations, which will be applied in Chap. 8.

Although the second quantization scheme is used for the calculation of the overall macroscopic polarization P, the perturbative treatment via the nth-order response function $S^{(n)}$ [Eq. (3.21)] is a useful theoretical tool for a detailed analysis of the polarization: While the HEISENBERG EOM leads to a macroscopic polarization that contains all possible orders of the polarization, $P = \sum_n P^{(n)}$, the concept of $S^{(n)}$ allows the discrimination of different sets of pathways. This is of particular advantage if the interest lies in specific pathways, which will be demonstrated in Chap. 7. There, based on a perturbative treatment of $S^{(n)}$, a scheme for the interpretation (double-sided FEYNMAN diagrams) and the extraction (phase cycling) of multiple pathways will be presented.

Part III

Intersubband transitions in two-dimensional structures

Chapter 4

Intersubband quantum well model

Being the first artificially designed low-dimensional semiconductor nanostructure [DWH74], the quantum well (QW) marks the beginning of the fast technological developments of nano-scale systems in the twentieth century. A QW is created when two semiconductor compounds form a so-called double-heterostructure, where a thin layer of compound II is sandwiched between two thick layers of compound I. Such structures can be engineered using, for example, molecular beam epitaxy [VK91], where the thin layer of compound II is grown on a substrate of compound I and also coated by the same substrate. If the fundamental band gap (between the valence and conduction band) of the outer substrate is larger than the band gap of the inner layer material and the layer width is smaller than the DE BROGLIE wave length of the carriers, a confinement potential U_{conf} is formed. The confinement then restricts the motion of the carriers within the layer and splits the valence and conduction band into so-called *subbands*.

The energetic spacing of the subbands lies in the range of a few tens to hundreds of meV. Consequently, the carrier dynamics of the subbands builds the foundation of the most prominent semiconductor terahertz (THz) radiation source, the quantum cascade laser (QCL) [HEC$^+$89, FCS$^+$94, SKB$^+$98, GCSC01]. Since the THz domain covers a wide range of possible applications from the biological and medical sciences to the communication technology [Wil07], the design of high-output, room temperature-operating QCLs remains a major advance yet to be realized by the THz community [SZD$^+$04, OMOO07, FDC$^+$12]. One of the major limitations towards this goal lies in the strong many-particle interactions in ISB QWs [IR01, PLW04, WWK09]. For example, the prominent electron-phonon interaction leads to non-radiative relaxation processes which opposes the built-up of a population inversion, needed for lasing. Thus, a thorough understanding of the many-particle dynamics is crucial for the ongoing developments.

The ISB dynamics in a single QW system will be the focus of the next chapters, Chap. 4 - Chap. 7.

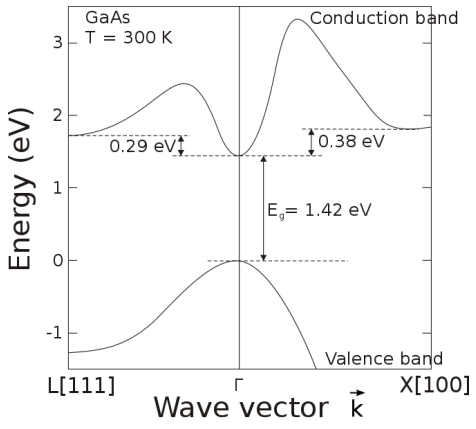

Figure 4.1 | Band structure of Gallium Arsenide (GaAs) aroung the Γ-point, taken from [oudw12]. The dynamics of the model system is focused on ISB transitions around the conduction band minimum.

In particular, a single n-doped GaAs/$Al_{0.35}Ga_{0.65}$As QW is studied (see Fig. 4.1). This double-heterostructure is favoured for the fabrication of QWs since the nearly perfect lattice matching of the two materials enables a strain-free growth of ultra-thin layers [Plo82]. In this chapter, the fundamental QW model will be introduced. After determining the eigenfunctions and the eigenenergies of this material system in Sec. 4.1, the coupling matrix elements for the electron-electron- (*el-el*) and electron-phonon (*el-ph*) interaction are derived in Sec. 4.2. Before considering the dynamics of the particles in the ISB QW via the HEISENBERG equation of motion in the following chapters, one major problem, the so-called hierarchy problem and its solution via the correlation expansion will be addressed in Sec. 4.3.

4.1 Wave functions and eigenenergies

In this section, the wave functions and the eigenenergies of the n-doped GaAs/$Al_{0.35}Ga_{0.65}$As QW are calculated. The doping with electrons leads to a partial filling of the lowest conduction subband. Thus, the ISB dynamics can be restricted to the conduction band. As previously mentioned, the double-heterostructure results in a confinement potential U_{conf} within the layer material II (GaAs). For simplicity, U_{conf} is first considered as infinitely high. Later on, in Sec. 4.1.2, a more realistic ansatz for the confinement is chosen, which modifies the eigenvalues. The infinitely deep confinement potential reads:

$$U_{\text{conf}} = \begin{cases} 0, & \text{for } |\mathbf{r}_\perp| < \frac{L}{2}, \\ \infty, & \text{for } |\mathbf{r}_\perp| > \frac{L}{2}. \end{cases} \tag{4.1}$$

The direction along the confinement is denoted as $\mathbf{r}_\perp$, whereas the direction of the free motion is $\mathbf{r}_\parallel$. To obtain the eigenenergies and eigenfunctions of the quasi-free electrons, the SCHRÖDINGER equation for the electronic wave function $\Psi_{\text{el}}(\mathbf{r},t)$ must be solved:

$$\mathrm{i}\hbar\partial_t \Psi_{\text{el}}(\mathbf{r},t) = \hat{H}\Psi_{\text{el}}(\mathbf{r},t) \qquad \text{with} \qquad \hat{H} = \left[-\frac{\hbar^2\nabla_{\mathbf{r}}^2}{2m_{\text{eff}}} + U_{\text{conf}}(\mathbf{r}_\perp)\right] \tag{4.2}$$

and the effective electron mass m_{eff} of GaAs. As the Hamiltonian is not explicitly time-dependent, a solution for $\Psi_{\text{el}}(\mathbf{r},t)$ is: $\Psi_{\text{el}}(\mathbf{r},t) = \Phi(\mathbf{r})\exp(-\frac{\mathrm{i}}{\hbar}\varepsilon t)$, which simplifies Eq. (4.2) to

$$\varepsilon\Phi(\mathbf{r}) = \left[-\frac{\hbar\nabla_{\mathbf{r}}^2}{2m_{\text{eff}}} + U_{\text{conf}}(\mathbf{r}_\perp)\right]\Phi(\mathbf{r}). \tag{4.3}$$

This equation corresponds to Eq. (2.13) in Sec. 2.2.1. The ansatz for the wave function has already been given in Eq. (2.14) as a product of the BLOCH function $\phi(r_\parallel)$ in $\mathbf{r}_\parallel$-direction and a confinement function $\zeta(\mathbf{r}_\perp)$ in $\mathbf{r}_\perp$ direction:

$$\Phi_{n,\mathbf{k}}(\mathbf{r}) = \frac{1}{\sqrt{A}}\mathrm{e}^{\mathrm{i}\mathbf{k}\cdot\mathbf{r}_\parallel}\zeta_n(\mathbf{r}_\perp)u_{c,\mathbf{k}\approx 0}(\mathbf{r}), \tag{4.4}$$

with the two-dimensional (2D) area A of the sample and the lattice periodic function of the conduction band $u_{c,\mathbf{k}\approx 0}(\mathbf{r})$. The eigenenergies of the in-plane direction can directly be written down as the free kinetic energy $\varepsilon_{\parallel,\mathbf{k}} = \hbar^2\mathbf{k}_\parallel^2/(2m_\parallel)$ (with the effective electron mass in in-plane direction $m_\parallel$). In perpendicular direction, the boundary conditions $\zeta_n(-\frac{L}{2}) = \zeta_n(\frac{L}{2}) = 0$ lead to following eigenfunctions $\zeta_n(\mathbf{r}_\perp)$ and eigenenergies $\varepsilon_{n,\perp}$:

$$\zeta_n(\mathbf{r}_\perp) = \begin{cases} \sqrt{\frac{2}{L}}\cos(k_n\mathbf{r}_\perp) & \text{for } n \text{ even}, \\ \sqrt{\frac{2}{L}}\sin(k_n\mathbf{r}_\perp) & \text{for } n \text{ odd}, \end{cases} \tag{4.5}$$

$$\varepsilon_{n,\perp} = \frac{\hbar^2\mathbf{k}_n^2}{2m_\perp} \qquad n \in \mathbb{N}\backslash\{0\}, \tag{4.6}$$

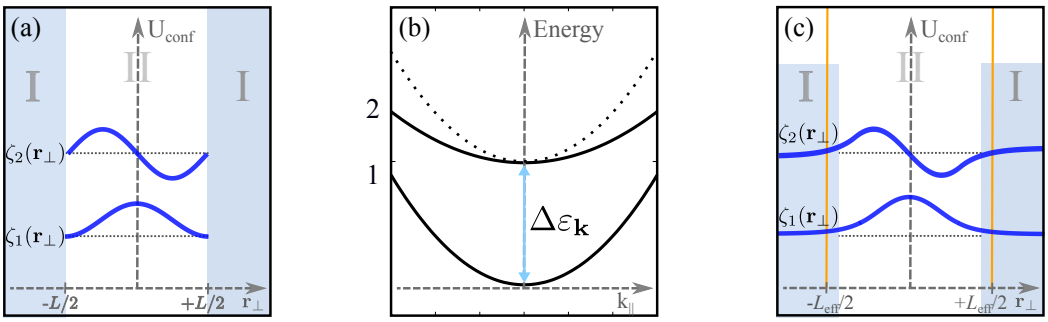

Figure 4.2 | (a) The confinement functions for the first two subbands for an infinitely deep confinement potential U_{conf}. (b) By regarding nonparabolicity effects, the gradient of subband 2 becomes smaller than the gradient of subband 1. Thus the transition energy $\Delta\varepsilon_{\mathbf{k}}$ decreases for increasing momentum number. (c) The confinement functions for a finite potential barrier U_{conf}. For calculations, an effective well width L_{eff} (orange line) and the corresponding confinement functions for an infinitely deep U_{conf} are assumed.

with $k_n = \frac{n\pi}{L}$ and the effective electron mass along the perpendicular direction $m_\perp$. The confinement functions for the lowest two subbands 1 and 2 are shown in Fig. 4.2(a). The overall single-particle eigenenergies then read:

$$\varepsilon_{n,\mathbf{k}} = \frac{\pi^2\hbar^2 n^2}{2m_\perp L^2} + \frac{\hbar^2 \mathbf{k}_\parallel^{\,2}}{2m_\parallel}, \tag{4.7}$$

with the gap energy $\varepsilon_{\text{gap}} := \varepsilon_{2,\mathbf{k}=0} - \varepsilon_{1,\mathbf{k}=0} = \frac{3\hbar^2\pi^2}{2m_\perp L^2}$ for the ISB transition between the ground state and the first excited state. Thus, the eigenenergies of each subband are parabola which are determined by the effective mass of the layer.

4.1.1 Nonparabolicity effects

So far, the perpendicular and parallel effective masses $m_\perp$ and $m_\parallel$ in Eq.(4.7) are only determined by the effective mass m_{eff} of the layer material, which is equal for each subband. But since the energy of the subbands are well above the conduction band edge, it is most probable that the effective subband masses differ from the effective mass of the layer material. The corrections of the effective mass approximation are summarized as *nonparabolicity effects* and lead to subband-dependent masses and a renormalization of the confinement energies [Bas81, MLR86]. In this thesis the subband masses are calculated according to Ekenberg [Eke89]. Starting from the bulk conduction band, higher subbands are included as a perturbation up to fourth order in $\mathbf{k}$. The subband masses then become dependent on the subband number:

$$\varepsilon_{n,\mathbf{k}} = \frac{\pi^2\hbar^2 n^2}{2m_{\perp,n} L^2} + \frac{\hbar^2 \mathbf{k}_\parallel^{\,2}}{2m_n}. \tag{4.8}$$

This nonparabolicity leads to a typical feature of the subband structure: Since the mass of the upper subband is larger than the ground state subband mass, the transition energy $\Delta\varepsilon_{\mathbf{k}}$ becomes smaller for higher momentum numbers, see Fig. 4.2(b). The calculated subband masses m_n as well as the subband gap energy ε_{gap} are given in Table A.3.

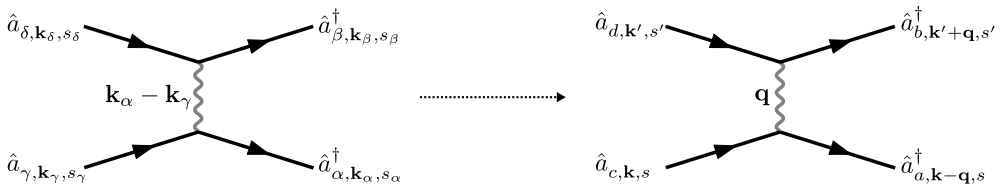

Figure 4.3 | Left: Schematic drawing of the spin and momentum conservation in *el-el* scattering events. Right: Transformation from absolute to relative momentum coordinates.

4.1.2 Effective well width approximation

Now, the more realistic case of a finite potential barrier is considered. With a finite confinement potential U_{conf}, the confinement functions $\zeta_n(\mathbf{r}_\perp)$ can penetrate the material outside of the layer, see Fig. 4.2(c). $\zeta_n(\mathbf{r}_\perp)$ must then be numerically determined by solving transcendental equations [Eke89]. However, a less numerically demanding method of taking into account the finite potential barrier is the so-called *effective well width approximation* [Liu94]: Here, the wave functions $\zeta_n(\mathbf{r}_\perp)$ for a finite confinement potential with the width L [light blue rectangles in Fig. 4.2(c)] are approximated with wave functions for an *infinitely* deep quantum well with an *effective well width* L_{eff} [vertical orange lines in Fig. 4.2(c)]. The effective well width L_{eff} is chosen in the manner that the eigenenergy of the subband ground state in an infinitely deep well is consistent with the eigenenergy $\varepsilon_{1,\mathbf{k}=0}$ calculated for a finite well.

The effective well width approximation will be used throughout this work: First, the effective subband masses and the eigenenergies are calculated for a finite quantum well according to Ekenberg [Eke89]. Then, an effective well width L_{eff} is determined to calculate the eigenfunctions $\zeta_n(\mathbf{r}_\perp)$ in Eq. (4.6).

4.2 Coupling matrix elements

After deriving the wave functions in the previous section, the coupling matrix elements for the ISB QW system can now be calculated according to Sec. 2.3.2. Without loss of generality, the direction of the confinement is assumed along the z-direction:$\mathbf{r}_\perp = z\mathbf{e}_z$. The incoming electromagnetic field shall propagate along the z-direction as well. The in-plane direction is the x-y plane: $\mathbf{r}_\parallel = x\mathbf{e}_x + y\mathbf{e}_y$.

4.2.1 Electric dipole matrix elements

Using Eq. (2.7), the optical dipole matrix element $d_{\alpha\beta}$ can be obtained through: $d_{\alpha\beta} = \int \mathrm{d}^3 r \phi^*_\alpha(\mathbf{r}) e_0 \mathbf{r} \cdot \mathbf{e}_E \phi_\beta(\mathbf{r})$. Splitting the integral into the perpendicular and in-plane direction and separating the integral into a sum of lattice and cells vectors, only the integration over the restricted domain remains: $d_{\alpha\beta}(z) = e_0 \int_{-\frac{L}{2}}^{\frac{L}{2}} \zeta^*_\alpha(z) z \zeta_\beta(z)$. This results in:

$$d_{\alpha\beta}(z) = \begin{cases} -\frac{16 e_0 L}{9\pi} & \text{for} \quad \alpha \neq \beta, \\ 0 & \text{for} \quad \alpha = \beta, \end{cases} \qquad (\alpha,\beta = 1,2) \tag{4.9}$$

i.e. the electromagnetic field can cause transitions between the subbands while transitions within the subbands are not possible.

4.2.2 Coulomb form factor

The COULOMB matrix elements of the *el-el* Hamiltonian $\hat{H}_{\text{el-el}}$, can now be determined. Starting from Eq. (2.33), the real space representation of the COULOMB matrix elements is:

$$V_{\alpha\beta\gamma\delta} = \frac{e_0^2}{4\pi\varepsilon_0\varepsilon_{\text{bg}}} \int \mathrm{d}^3 r \int \mathrm{d}^3 r' \phi_\alpha^*(\mathbf{r})\phi_\beta^*(\mathbf{r}') \frac{1}{|\mathbf{r}-\mathbf{r}'|} \phi_\delta(\mathbf{r}')\phi_\gamma(\mathbf{r}), \tag{4.10}$$

where the eigenfunctions of the previous section can now be inserted. The solution of the integral in Eq. (4.10) requires the use of the periodic lattice symmetry of the BLOCH functions. Detailed calculations are given, e.g., in [Wal02]. After solving the in-plane integral, the COULOMB matrix elements obtain following form:

$$\begin{aligned} V_{\alpha\beta\gamma\delta}^{\mathbf{k}_\alpha-\mathbf{k}_\gamma} &= \frac{e_0^2}{4\varepsilon_0\varepsilon_{bg}A} \frac{1}{|\mathbf{k}_\alpha-\mathbf{k}_\gamma|} \int \mathrm{d}z \int \mathrm{d}z' \mathrm{e}^{|\mathbf{k}_\alpha-\mathbf{k}_\gamma||z-z'|} \cdot \zeta_\alpha^*(z)\zeta_\beta^*(z')\zeta_\gamma(z)\zeta_\delta(z')\delta_{s_\alpha,s_\gamma}\delta_{s_\beta,s_\delta}\delta_{\mathbf{k}_\alpha+\mathbf{k}_\beta,\mathbf{k}_\gamma+\mathbf{k}_\delta} \\ &= \frac{e_0^2}{4\varepsilon_0\varepsilon_{bg}A|\mathbf{q}|} \mathscr{F}_{\alpha\beta\gamma\delta}^{\mathbf{q}} = V_{\text{2d}}^{\mathbf{q}} \mathscr{F}_{\alpha\beta\gamma\delta}^{\mathbf{q}}, \end{aligned} \tag{4.11}$$

with the COULOMB form factor $\mathscr{F}_{\alpha\beta\gamma\delta}^{\mathbf{q}}$ and the in-plane two-dimensional wave vector $\mathbf{q}$. The delta conditions can be automatically fulfilled with a transformation of the momenta and spins of the electron operators: $\frac{1}{2}\sum_{\alpha\beta\gamma\delta} V_{\alpha\beta\gamma\delta}^{\mathbf{k}_\alpha-\mathbf{k}_\gamma} \hat{a}_\alpha^\dagger \hat{a}_\beta^\dagger \hat{a}_\delta \hat{a}_\gamma \rightarrow \frac{1}{2}\sum_{abcd}\sum_{s,s',\mathbf{k},\mathbf{k}',\mathbf{q}} V_{abcd}^{\mathbf{q}} \hat{a}_{a,\mathbf{k}-\mathbf{q},s}^\dagger \hat{a}_{b,\mathbf{k}+\mathbf{q}',s'}^\dagger \hat{a}_{d,\mathbf{k}',s'} \hat{a}_{c,\mathbf{k},s}$. A schematic drawing of the momentum- and spin transformation in *el-el* scattering events is given in Fig. 4.3. Equation (4.11) shows that in an ISB QW system, the COULOMB potential of an ideal two-dimensional system $V_{\text{2d}}^{\mathbf{q}}$ is modified by the subband-dependent form factor $\mathscr{F}_{\alpha\beta\gamma\delta}^{\mathbf{q}}$: The motion of the electrons along the z-direction is restricted but not forbidden. In this manner, the QW is also often denoted as a "quasi-2D" system.

The matrix elements have symmetric properties considering the arrangement of the wave functions: $V_{\alpha\beta\gamma\delta} = V_{\beta\alpha\delta\gamma} = V_{\gamma\delta\alpha\beta} = V_{\delta\gamma\beta\alpha}$. Regarding the lowest two subbands, eight non-vanishing COULOMB matrix elements exist:[1]

$$\mathscr{F}_{1111}^{\mathbf{q}} = \frac{4}{L^2}\left(\frac{20L^3\pi^2|\mathbf{q}|^3 + 3L^5|\mathbf{q}|^5 - 32\pi^4(1-e^{-L|\mathbf{q}|}-L|\mathbf{q}|)}{4(4\pi^2|\mathbf{q}|+L|\mathbf{q}|^3)^2}\right), \tag{4.12}$$

$$\mathscr{F}_{2222}^{\mathbf{q}} = \frac{4}{L^2}\left(\frac{80L^3\pi^2|\mathbf{q}|^3 + 3L^5|\mathbf{q}|^5 - 512\pi^4(1-e^{-L|\mathbf{q}|}-L|\mathbf{q}|)}{4(16\pi^2|\mathbf{q}|^2+L|\mathbf{q}|^3)^2}\right), \tag{4.13}$$

$$\mathscr{F}_{1212}^{\mathbf{q}} = \frac{4}{L^2}\left(\frac{20L^3\pi^2|\mathbf{q}|^3 + L^5|\mathbf{q}|^5 - 64\pi^4(1-e^{-L|\mathbf{q}|}-L|\mathbf{q}|)}{2(64\pi^4|\mathbf{q}|^2+20L^2\pi^2|\mathbf{q}|^4+L^4|\mathbf{q}|^6)}\right), \tag{4.14}$$

$$\mathscr{F}_{2112}^{\mathbf{q}} = \frac{4}{L^2}\left(\frac{45L^3\pi^6|\mathbf{q}| + 15L^7\pi^2|\mathbf{q}|^5 + L^9|\mathbf{q}|^7 - L^4\pi^4|\mathbf{q}|^2(64+64e^{-L|\mathbf{q}|}-59L|\mathbf{q}|)}{2(9\pi^4+10L^2\pi^2|\mathbf{q}|^2+L^4|\mathbf{q}|^4)^2}\right), \tag{4.15}$$

$$\mathscr{F}_{2121}^{\mathbf{q}} = \mathscr{F}_{1212}^{\mathbf{q}}, \tag{4.16}$$

$$\mathscr{F}_{2211}^{\mathbf{q}} = \mathscr{F}_{1122}^{\mathbf{q}} = \mathscr{F}_{1221}^{\mathbf{q}} = \mathscr{F}_{2112}^{\mathbf{q}}. \tag{4.17}$$

The matrix elements V_{iiii} and V_{ijij} represent intrasubband processes, that is, electrons are scattered within its subbands, while V_{ijji} and V_{iijj} describe interactions where an electron from the upper subband scatters into the lower subband and vice versa.

Subband screening - Similar to the dielectric function of the background material, the electron plasma itself can act as a background for two interacting electrons. This so-called *screening* weakens of the

[1] Auger-type processes, corresponding to an odd number of the subband numbers 1 or 2, vanish for a symmetric quantum well as considered here.

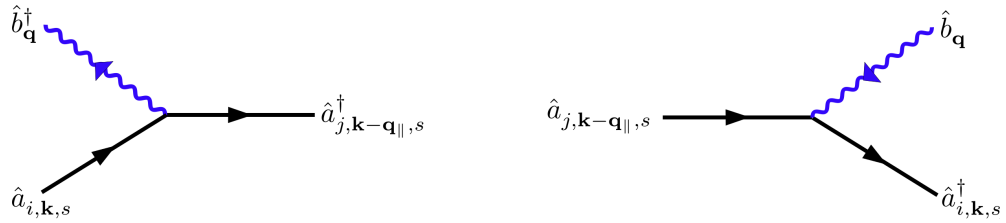

Figure 4.4 | Schematic drawing of the *el-ph* interaction regarding momentum conservation. Left shows the scattering under phonon emission and right shows the scattering under phonon absorption.

COULOMB potential, dependent on the electron density and the subband. The different subband matrix elements of the screened COULOMB potential $V^{\mathrm{scr}}_{\alpha\beta\gamma\delta}(\mathbf{q},\omega)$ are connected with a system of linear equations [LG97]:

$$V^{\mathrm{scr}}_{\alpha\beta\gamma\delta}(\mathbf{q},\omega) = V^{\mathbf{q}}_{\alpha\beta\gamma\delta} + \sum_{m,n} V^{\mathbf{q}}_{\alpha n\gamma m}\Pi^{\mathbf{q},\omega}_{mn} V^{\mathrm{scr}}_{m\beta n\delta}(\mathbf{q},\omega), \tag{4.18}$$

with $\Pi^{\mathbf{q},\omega}_{mn} = \lim_{\delta\to 0}\sum_{\mathbf{k},s}\frac{f_{\mathbf{k}-\mathbf{q},m}-f_{\mathbf{k}n}}{\varepsilon_{\mathbf{k}-\mathbf{q},m}-\varepsilon_{\mathbf{k},n}-\hbar\omega-\mathrm{i}\delta}$. Equation (4.18) can be solved analytically in the case of two subbands. If only one subband is considered, Eq. (4.18) results in the LINDHARD formula, where the screening can be expressed as a dielectric constant $\varepsilon_{\mathrm{scr}}$ [HK04].

In this work, the long wave length limit of the screened COULOMB potential $V^{\mathrm{scr}}_{\alpha\beta\gamma\delta}(\mathbf{q},0)$ is used. Regarding the dynamic equations which will be derived in the next chapters, the subband screening is applied in the following way: For scattering events with only two electrons, the COULOMB potential is unscreened. If more than two electrons are involved in the scattering process, the subband screening will be applied since the two electrons scatter under the presence of at least one "background" electron.

4.2.3 Fröhlich form factor

Next, the FRÖHLICH matrix elements $g^{ij}_{\mathbf{q}}$ for the *el-ph* interaction are evaluated. $g^{ij}_{\mathbf{q}}$ has already been introduced in Sec. 2.3.2:

$$\begin{aligned} g^{ij}_{\mathbf{q}} &= \mathrm{i}\left[\frac{e_0^2\hbar\omega_{\mathrm{LO}}}{2\varepsilon_0 V}(\varepsilon_\infty^{-1}-\varepsilon_{\mathrm{s}}^{-1})\right]^{\frac{1}{2}}\frac{1}{|\mathbf{q}|}\int \mathrm{d}z\,\zeta_i^*(z)\zeta_j(z)e^{\mathrm{i}\mathbf{q}_\perp z}\delta_{\mathbf{q}_\parallel,\mathbf{k}_i+\mathbf{k}_j} \\ &= g^{\mathrm{3D}}_{\mathbf{q}}\mathscr{F}^{\mathbf{q}_\perp}_{ij}, \end{aligned} \tag{4.19}$$

with the 3D FRÖHLICH coupling $g^{\mathrm{3D}}_{\mathbf{q}}$, the subband-dependent FRÖHLICH form factors $\mathscr{F}^{\mathbf{q}_\perp}_{ij}$ and the 3D wave vector $\mathbf{q}$. The delta condition assures the momentum conservation of scattering events where one electron and one phonon are involved. Subsequently, the difference of the electronic momenta must be equal to the in-plane momentum of the phonon. The corresponding momentum transformation of the electron-phonon scattering events is given in Fig. 4.4. The evaluated form factors are:

$$\mathscr{F}^{\mathbf{q}_\perp}_{11} = \frac{8\pi^2\sin(\frac{L\mathbf{q}_\perp}{2})}{4L\pi^2\mathbf{q}_\perp - L^3\mathbf{q}_\perp^3} \quad \text{and} \quad \mathscr{F}^{\mathbf{q}_\perp}_{22} = \frac{32\pi^2\sin(\frac{L\mathbf{q}_\perp}{2})}{16L\pi^2\mathbf{q}_\perp - L^3\mathbf{q}_\perp^3}, \tag{4.20}$$

$$\mathscr{F}^{\mathbf{q}_\perp}_{12} = \mathrm{i}\frac{16L\pi^2\cos(\frac{L\mathbf{q}_\perp}{2})\mathbf{q}_\perp}{9\pi^4 - 10L^2\pi^2\mathbf{q}_\perp^2 + L^4\mathbf{q}_\perp^4} \quad \text{and} \quad \mathscr{F}^{\mathbf{q}_\perp}_{12} = \mathscr{F}^{\mathbf{q}_\perp}_{21}. \tag{4.21}$$

The Fröhlich matrix elements for intrasubband processes which describe the diagonal coupling between one phonon and the electrons, $g^{ii}_{\mathbf{q}}$, have symmetric properties concerning $\mathbf{q}_\perp$, i.e. $g^{ii}_{\mathbf{q}_\perp} = g^{ii}_{-\mathbf{q}_\perp}$, while the intersubband matrix element (non-diagonal coupling of the phonon) are antisymmetric, $g^{ij}_{\mathbf{q}_\perp} = -g^{ij}_{-\mathbf{q}_\perp}$.

4.3 Hierarchy problem and correlation expansion

If many-body Hamiltonians such as the COULOMB interaction or the FRÖHLICH interaction are included in the equation of motion (EOM), certain difficulties can evolve. For example, if the dynamics of the electronic operators $\hat{a}^\dagger_\alpha \hat{a}_\beta$ is calculated with regard to the COULOMB interaction via the HEISENBERG EOM, following structure will occur:

$$-\mathrm{i}\hbar \frac{\mathrm{d}}{\mathrm{d}t}\langle \hat{a}^\dagger_\alpha \hat{a}_\beta \rangle_{|\text{el-el}} = \langle [\hat{H}_{\text{el-el}}, \hat{a}^\dagger_\alpha \hat{a}_\beta] \rangle = \sum_{\{123\}} V_{12\alpha 3} \langle \hat{a}^\dagger_1 \hat{a}^\dagger_2 \hat{a}_3 \hat{a}_\alpha \rangle + \cdots , \tag{4.22}$$

that is, the two-operator term $\langle \hat{a}^\dagger_\alpha \hat{a}_\beta \rangle$ couples to a four-operator term. Thus, to determine the two-operator term, the dynamics of the four-operator term has to be calculated, which itself couples to a six-operator term:

$$\begin{aligned} \frac{\mathrm{d}}{\mathrm{d}t}\langle \hat{a}^\dagger_a \hat{a}_b \rangle_{\text{el-el}} &\sim \langle \hat{a}^\dagger_c \hat{a}^\dagger_d \hat{a}_e \hat{a}_f \rangle + \cdots , \\ \frac{\mathrm{d}}{\mathrm{d}t}\langle \hat{a}^\dagger_c \hat{a}^\dagger_d \hat{a}_e \hat{a}_f \rangle_{\text{el-el}} &\sim \langle \hat{a}^\dagger_g \hat{a}^\dagger_h \hat{a}^\dagger_i \hat{a}_j \hat{a}_k \hat{a}_l \rangle + \cdots . \end{aligned} \tag{4.23}$$

This shows that the dynamics of a n-particle expectation value couples to a $(n+1)$-particle expectation value, resulting in an infinite number of coupled differential equations, also denoted as the hierarchy problem [KK06b].

A common method to truncate a system of weak coupled particles is the cluster- or correlation expansion [Fri96, KK06b], where the assumption is made that the correlation to higher many-particle states becomes less important for higher orders. The basic idea is to truncate the system in the nth-order of the EOM by splitting the n-particle expectation value into clusters from one-operator to n-operator clusters. Higher orders, that is, beginning from $(n+1)$, are neglected. The factorization of an n-particle expectation value $\langle n \rangle$ underlies the following scheme:

$$\begin{aligned} \langle 1 \rangle &= \langle 1 \rangle_S , \\ \langle 2 \rangle &= \langle 2 \rangle_S \pm \langle 2 \rangle_{\text{corr}} , \\ \langle 3 \rangle &= \langle 3 \rangle_S \pm \langle 1 \rangle_S \langle 2 \rangle_{\text{corr}} \pm \langle 3 \rangle_{\text{corr}} , \\ \langle 4 \rangle &= \langle 4 \rangle_S \pm \langle 1 \rangle_S \langle 3 \rangle_{\text{corr}} \pm \langle 2 \rangle_S \langle 2 \rangle_{\text{corr}} \pm \langle 4 \rangle_{\text{corr}} , \\ &\vdots \end{aligned} \tag{4.24}$$

The subscript "S" denotes the uncorrelated singlet contribution and the subscript "corr" denotes the correlated particles. Due to the indistinguishability of the particles, all possible permutations of the particle expectation values must be included. Considering the arrangement of the clusters, one has to distinguish between fermionic and bosonic operators: Following from their antisymmetry, the clusters which are built through the permutation of fermionic operators can be added with different signs: If the number of permutations, needed for gaining the original order of the n-particle expectation value, is odd, the expectation value obtains a $(-)$-sign. If the permutation is even, the fermionic expectation value has a $(+)$-sign. For bosonic operators, the different permutations are always added with a $(+)$-sign.

4.3.1 Coulomb coupling

If a singlet expectation value with purely fermionic operators is evaluated, the so-called *Hartree-Fock* factorization will be applied [KK06b]:

$$\langle \hat{a}^\dagger_a \ldots \hat{a}^\dagger_N \hat{a}_a \ldots \hat{a}_N \rangle_S = \langle \hat{a}^\dagger_a \ldots \hat{a}^\dagger_N \hat{a}_a \ldots \hat{a}_N \rangle_{\text{HF}} = \sum_\sigma (-1)^\sigma \Pi_{j=1}^N \langle \hat{a}^\dagger_j \hat{a}_{\sigma[j]} \rangle , \tag{4.25}$$

where $\sigma[j]$ is the number of permutations to gain the respective single-particle expectation value. Thus, the explicit expression for a two electron expectation value is:[2]

$$\langle \hat{a}_a^\dagger \hat{a}_b^\dagger \hat{a}_c \hat{a}_d \rangle = \langle \hat{a}_b^\dagger \hat{a}_c \rangle \langle \hat{a}_a^\dagger \hat{a}_d \rangle - \langle \hat{a}_a^\dagger \hat{a}_c \rangle \langle \hat{a}_b^\dagger \hat{a}_d \rangle + \langle \hat{a}_a^\dagger \hat{a}_b^\dagger \hat{a}_c \hat{a}_d \rangle_{\text{corr}}. \tag{4.26}$$

If the correlation term $\langle \hat{a}_a^\dagger \hat{a}_b^\dagger \hat{a}_c \hat{a}_d \rangle_{\text{corr}}$ is set to zero, the motion of one electron is calculated in the mean field of the other electrons and their mutual influence is neglected. This is also denoted as an HARTREE-FOCK approximation (or mean field approximation) [Hak93, Czy04].

Since also higher-order correlations will be derived in the following chapters, the HARTREE-FOCK factorization of a three-particle electron expectation value is explicitly given:

$$\begin{aligned} \langle \hat{a}_a^\dagger \hat{a}_b^\dagger \hat{a}_c^\dagger \hat{a}_d \hat{a}_e \hat{a}_f \rangle_{\text{HF}} =& \langle \hat{a}_a^\dagger \hat{a}_d \rangle \{ \langle \hat{a}_c^\dagger \hat{a}_e \rangle \langle \hat{a}_b^\dagger \hat{a}_f \rangle - \langle \hat{a}_b^\dagger \hat{a}_e \rangle \langle \hat{a}_c^\dagger \hat{a}_f \rangle \} \\ & - \langle \hat{a}_a^\dagger \hat{a}_e \rangle \{ \langle \hat{a}_c^\dagger \hat{a}_d \rangle \langle \hat{a}_b^\dagger \hat{a}_f \rangle - \langle \hat{a}_b^\dagger \hat{a}_d \rangle \langle \hat{a}_c^\dagger \hat{a}_f \rangle \} \\ & + \langle \hat{a}_a^\dagger \hat{a}_f \rangle \{ \langle \hat{a}_c^\dagger \hat{a}_d \rangle \langle \hat{a}_b^\dagger \hat{a}_e \rangle - \langle \hat{a}_b^\dagger \hat{a}_d \rangle \langle \hat{a}_c^\dagger \hat{a}_e \rangle \}. \end{aligned} \tag{4.27}$$

These expectation values occur in the calculation of the ground state correlations in Sec. 5.4 and in the BOLTZMANN scattering contributions in Sec. 5.3. Due to energy conservation, expectation values with an uneven number of electron creators or annihilators vanish.

4.3.2 Fröhlich coupling

According to Eq. (4.24), expectation values of clusters including fermionic and bosonic operators can be split into singlets as well. The expansion of a mixed electron-phonon three-particle expectation value is:[3]

$$\langle \hat{a}_\alpha^{(\dagger)} \hat{a}_\beta^{(\dagger)} \hat{b}_{\mathbf{q}}^{(\dagger)} \hat{b}_{\mathbf{p}}^{(\dagger)} \rangle = \langle \hat{a}_\alpha^{(\dagger)} \hat{a}_\beta^{(\dagger)} \rangle \langle \hat{b}_{\mathbf{q}}^{(\dagger)} \hat{b}_{\mathbf{p}}^{(\dagger)} \rangle + \langle \hat{a}_\alpha^{(\dagger)} \hat{a}_\beta^{(\dagger)} \hat{b}_{\mathbf{q}}^{(\dagger)} \hat{b}_{\mathbf{p}}^{(\dagger)} \rangle_{\text{corr}} \tag{4.28}$$

The splitting of the fermionic and bosonic densities is denoted as the BORN approximation [BW80, VWW01]. Under the assumption of a phonon bath, coherent phonon generation terms such as $\langle \hat{b}_{\mathbf{q}}^{(\dagger)} \rangle$ can be neglected, which will be used throughout this thesis. But it should be noted that for very strong electromagnetic fields, coherent phonons have to be considered [PKA10].

4.3.3 Spatial homogeneity assumption

If the expectation values are eventually split into one-particle values, it is assumed that the system observables are spatially homogeneous which is expressed by the delta condition of the momenta [SKS+96]:

$$\langle \hat{a}_{i,\mathbf{k},s}^\dagger \hat{a}_{j,\mathbf{k}',s'} \rangle = \langle \hat{a}_{i,\mathbf{k},s}^\dagger \hat{a}_{j,\mathbf{k},s} \rangle \delta_{\mathbf{k},\mathbf{k}'} \delta_{s,s'} \qquad \text{and} \qquad \langle \hat{b}_{\mathbf{q}}^\dagger \hat{b}_{\mathbf{q}'} \rangle = \langle \hat{b}_{\mathbf{q}}^\dagger \hat{b}_{\mathbf{q}} \rangle \delta_{\mathbf{q},\mathbf{q}'}. \tag{4.29}$$

For equal subband indices, the electronic one-particle expectation value $f_{i,\mathbf{k}} = \langle \hat{a}_{i,\mathbf{k}}^\dagger \hat{a}_{i,\mathbf{k}} \rangle$, that is, the distribution of the electrons in subband i in equilibrium is approximated with the FERMI function:

$$f_{i,\mathbf{k}}(\varepsilon_{\mathbf{k}}) = \frac{1}{\mathrm{e}^{-(\mu - \varepsilon_{\mathbf{k}i})/(k_{\mathrm{B}} T)} + 1}. \tag{4.30}$$

However, in the next section it will be shown that for low temperatures, the electron distribution function is modified.

[2] Note that a one-particle electron expectation value corresponds to one electron operator and one electron annihilator, that is: $\langle 1 \rangle = \langle \hat{a}^\dagger \hat{a} \rangle$.

[3] Each phonon operator corresponds to one particle.

Furthermore, if the electronic system couples only weakly to the phonons, they can be described by a set of harmonic oscillators, also denoted as a phonon bath which is unaffected by the electronic motion. The phonon distribution $\langle \hat{b}_{\mathbf{q}}^{\dagger} \hat{b}_{\mathbf{q}} \rangle = n_{\mathbf{q}}$ is then equivalent with the BOSE distribution:

$$n_{\mathbf{q}}(\hbar\omega_{\mathbf{q}}) = \frac{1}{\mathrm{e}^{\hbar\omega_{\mathbf{q}}/(k_{\mathrm{B}}T)} - 1}. \tag{4.31}$$

Chapter 5

Linear optical properties

The most fundamental optical investigation scheme is the linear absorption spectrum, where the sample is excited with a very weak pulse. When weakly exciting the system, the shape of the spectra can already give important insights into the dispersion of the material or non-equilibrium many-body processes. Many theoretical and experimental studies have already been done to determine the influence of many-particle interactions on the ISB absorption [WWFK03, PDMK08, VVA$^+$09, GWS$^+$09, HAG$^+$11]. However, especially concerning the low-temperature regime there has been a deficit in the theoretical description, predicting line widths much smaller then experimentally observed. To gain a better understanding of the ISB absorption line shape, this chapter will focus on COULOMB interaction since the spectral width is basically determined by the fastest scattering process, which is the electron-electron (*el-el*) scattering [LN04]. In the first part of this chapter, the main *el-el* scattering contributions of the microscopic polarization are revisited. Also, the processes which are responsible for the deficit of the infinitely small line width are illuminated. Then, in the second part of this chapter, a modification of the theoretical description is introduced via the COULOMB-induced *ground state correlations*. Studies about the *el-ph* interaction in the linear regime can be found, for example, in [NAK99, WFL$^+$04, SRW$^+$05, BK06].

The sections are organized as follows: Starting from the free carrier dynamics in Sec. 5.1, the first and the second-order correlation contributions of the non-diagonal elements of the density operator will be derived in Sec. 5.2 and Sec. 5.3, where also the theoretical problem of the small absorption line width is specified. Beginning from Sec. 5.4 the electronic correlations in the ground state are investigated as a possible mechanism for an intrinsic line shape broadening in the ISB absorption. They are derived in Sec. 5.4.1 as a second-order correlation contribution of the microscopic density, caused by the COULOMB interaction. The properties of the renormalized ground state distribution are examined in Sec. 5.4.2. Subsequently its influence on the absorption spectrum is investigated in Sec. 5.5, where the spectra including and neglecting ground state correlations are compared. It will be shown that correlations in the ground state yield an inherent line broadening of the absorption in the low temperature regime. The main results of this chapter have been published in [DWRK10].

5.1 Free carrier dynamics

To gain a better insight into the characteristics of ISB transitions, the absorption spectrum for free carriers is shown first. Therefore, the dynamics of the density operator $\rho_{ij,\mathbf{k}}$ is derived in second quantization formalism via the HEISENBERG EOM. The system Hamiltonian contains the semi-classical electromag-

netic electron-light Hamiltonian and the free carrier Hamiltonians:[1]

$$
\begin{aligned}
-\mathrm{i}\hbar\frac{\mathrm{d}}{\mathrm{d}t}\langle\hat{\rho}_{ij,\mathbf{k}}\rangle = -\mathrm{i}\hbar\frac{\mathrm{d}}{\mathrm{d}t}\langle\hat{a}^{\dagger}_{i,\mathbf{k}}\hat{a}_{j,\mathbf{k}}\rangle &= \langle\left[\hat{H}_{0,\mathrm{el}}+\hat{H}_{0,\mathrm{ph}}+\hat{H}_{\mathrm{em}},\hat{a}^{\dagger}_{i\mathbf{k}}\hat{a}_{j\mathbf{k}}\right]\rangle \\
&= (\varepsilon_{i,\mathbf{k}}-\varepsilon_{j,\mathbf{k}})\langle\rho_{ij,\mathbf{k}}\rangle - E(t)\left(\sum_{\alpha}d_{\alpha i}\langle\rho_{\alpha\, j,\mathbf{k}}\rangle - \sum_{\beta}d_{j,\mathbf{k}\beta}\langle\rho_{i,\mathbf{k}\,\beta}\rangle\right). \qquad (5.1)
\end{aligned}
$$

The spin index is neglected here since the equations are spin independent. The full equations for the lowest two subbands are:

$$
\begin{aligned}
\dot{f}_{1,\mathbf{k}} &= \quad \mathrm{i}\Omega_{12}(t)\mathrm{Im}\{p_{12,\mathbf{k}}\}, && (5.2)\\
\dot{f}_{2,\mathbf{k}} &= -\mathrm{i}\Omega_{12}(t)\mathrm{Im}\{p_{12,\mathbf{k}}\}, && (5.3)\\
\dot{p}_{12,\mathbf{k}} &= \mathrm{i}(\omega_{1,\mathbf{k}}-\omega_{2,\mathbf{k}})\,p_{12,\mathbf{k}} - \mathrm{i}\Omega_{12}(t)\,(f_{2,\mathbf{k}}-f_{1,\mathbf{k}}) - \gamma_{\mathrm{ph}}p_{12,\mathbf{k}}, && (5.4)
\end{aligned}
$$

with $p_{ij,\mathbf{k}} := \langle\hat{\rho}_{ij,\mathbf{k}}\rangle$ and $f_{i,\mathbf{k}} := \langle\hat{\rho}_{ii,\mathbf{k}}\rangle$ for $i \neq j$, $\omega_{i,\mathbf{k}} = \varepsilon_{i,\mathbf{k}}/\hbar$ and the Rabi frequency $\Omega_{12}(t) = E(t)d_{12}/\hbar$. To include many-body interactions on a phenomenological basis, a damping term $-\gamma_{\mathrm{ph}}p_{12,\mathbf{k}}$ has been added to Eq. (5.4). Under the assumption of a very weak pulse, Eq. (5.2) and (5.3) can be neglected, that is, the distribution in the lower and the upper subband are assumed as FERMI distribution functions. Under these assumptions, the microscopic polarization $p_{12,\mathbf{k}}$ can be solved in the FOURIER domain. For free carriers, the equation for the ISB absorption coefficient [Eq. (3.24)] is:

$$
\alpha(\omega) = -\frac{\omega}{\hbar\varepsilon_0 c_0 n_{\mathrm{bg}}}\mathrm{Im}\{\sum_{\mathbf{k}}\frac{d_{12}^2(f_{2,\mathbf{k}}-f_{1,\mathbf{k}})}{\omega-\omega_{2,\mathbf{k}}+\omega_{1,\mathbf{k}}+\mathrm{i}\gamma_{\mathrm{ph}}}+\mathrm{c.c.}\}. \qquad (5.5)
$$

Figure 5.1 shows the absorption spectra for three different temperatures and three different well widths L for a carrier density of $n_{\mathrm{d}} = 6.0\cdot 10^{11}$ cm^{-2}, fully located in the lower subband. In the upper graph [Fig. 5.1(a)], the spectra are plotted with equal subband masses, while in Fig. 5.1(b), different subband masses are included. The spectra for equal subband masses are Lorentzian and equal for different temperatures. The line width is only dependent on the phenomenological dephasing $\gamma_{\mathrm{ph}} = 320$ fs^{-1}, which is chosen in agreement with the experimentally determined value for the mean scattering [KRW$^+$01]. If different subband masses are included, the spectra become asymmetric: For higher temperatures, the spectrum is broadened along lower energies, which is more pronounced for decreasing L. This low energy tail is a result of the different subband masses: For increasing temperature, the carriers occupy higher momentum states, which are connected with lower transition energies. This is shown in Fig. 5.2(a) and (b). The more pronounced low energy tail for decreasing well width is due to the increasing difference of the slopes in the two subbands. Additionally, the maxima of the spectra including different subband masses are shifted to lower energies compared to the spectra with equal subband masses, indicated with the vertical dotted lines in Fig. 5.1, which are located at the maximum of the peaks in (a). This shift is a feature of the density of states for a 2D system: If the 2D sum in Eq. (5.5) is evaluated, the integrand is proportional to $|\mathbf{k}|\cdot(f_{2,\mathbf{k}}-f_{1,\mathbf{k}})$. This term shifts the maximum value away from $\mathbf{k} = 0$ nm^{-1} to a higher momentum number and therefore to a lower transition energy. The well-defined connection between momentum number and transition energy allows one to locate the distribution in the momentum space. This is an important feature of the ISB system which will also be used in Sec. 7. The parameters for the effective subband masses and the gap energy are given in Tab. A.3.

[1] Note that a Greek index is used as a multi-index over the subband number and the corresponding momentum vector.

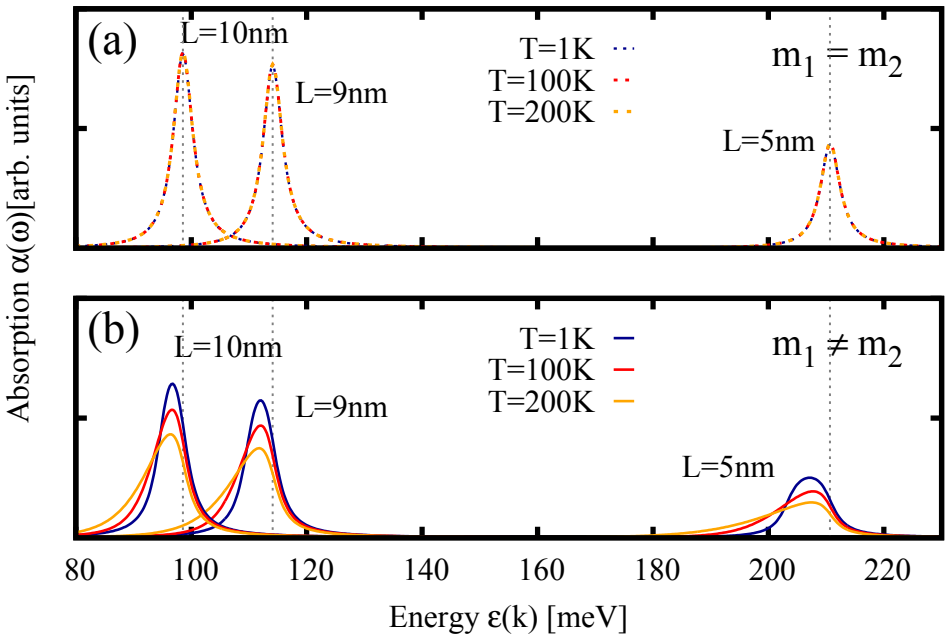

Figure 5.1 | Free carrier absorption spectra for an electron density of $n_d = 6.0 \cdot 10^{11}$ cm^{-2} with (a) equal subband masses and (b) different subband masses. The spectra are plotted for three different temperatures and for three different well widths.

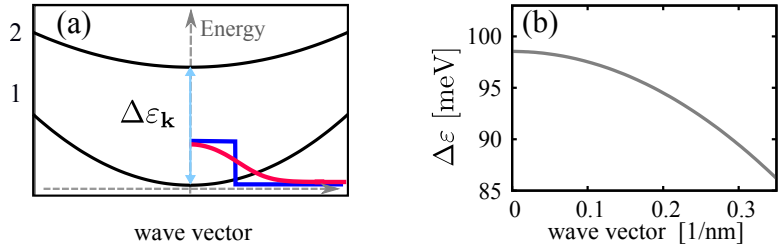

Figure 5.2 | (a) Schematic drawing of the subband dispersion and the FERMI distribution functions for $T = 1$ K (blue line) and $T = 200$ K (orange line). (b) Plot of the transition energy over the wave vector for $L = 10$ nm. The transition energy decreases for increasing momentum number.

5.2 Hartree-Fock contributions

Next, the system Hamiltonian will be expanded with the *el-el*-interaction Hamiltonian $\hat{H}_{\text{el-el}}$:

$$\begin{aligned}\frac{\mathrm{d}}{\mathrm{d}t}\langle\hat{\rho}_{12,\mathbf{k},s}\rangle &= \frac{\mathrm{i}}{\hbar}\langle\left[\hat{H}_0 + \hat{H}_{\text{em}} + \hat{H}_{\text{el-el}}, \hat{\rho}_{12,\mathbf{k},s}\right]\rangle. \\ &= \mathrm{i}\left(\omega_{1,\mathbf{k}} - \omega_{2,\mathbf{k}}\right) p_{12,\mathbf{k},s} - \mathrm{i}\Omega_{12}(t)\left(f_{2,\mathbf{k},s} - f_{1,\mathbf{k},s}\right) \qquad (5.6) \\ &\quad + \frac{\mathrm{i}}{\hbar}\sum_{\{\alpha\beta\gamma\}} V_{\alpha\beta 1\gamma}\langle\hat{a}^\dagger_\alpha\hat{a}^\dagger_\beta\hat{a}_\gamma\hat{a}_{2,\mathbf{k},s}\rangle - \frac{\mathrm{i}}{\hbar}\sum_{\{\alpha\beta\gamma\}} V_{2\alpha\beta\gamma}\langle\hat{a}^\dagger_{1,\mathbf{k},s}\hat{a}^\dagger_\alpha\hat{a}_\beta\hat{a}_\gamma\rangle. \qquad (5.7)\end{aligned}$$

Now $\langle\hat{\rho}_{12,\mathbf{k},s}\rangle$ couples to four electron operator expectation values. The coupling to higher-order correlation contributions results in the hierarchy problem as explained earlier in Sec. 4.3. As a first approximation, only the mean field term will be considered (see also Sec. 4.3.1). Hence, in first-order

correlation expansion, only the HARTREE-FOCK term, i.e. the factorization to single-particle values will be considered and the correlation term is neglected. The EOM is then:

$$\begin{aligned}\frac{\mathrm{d}}{\mathrm{d}t}p_{12,\mathbf{k},s} &= \mathrm{i}\left(\omega_{1,\mathbf{k}}-\omega_{2,\mathbf{k}}\right)p_{12,\mathbf{k},s} - \mathrm{i}\Omega_{12}(t)\left(f_{2,\mathbf{k},s}-f_{1,\mathbf{k},s}\right) - \gamma_{\mathrm{ph}}p_{12,\mathbf{k},s} \\ &+ \frac{\mathrm{i}}{\hbar}\sum_{\mathbf{q}\neq 0}\left[\left(V^{\mathbf{q}}_{2222}-V^{\mathbf{q}}_{2112}\right)f_{2,\mathbf{k}-\mathbf{q},s} - \left(V^{\mathbf{q}}_{1111}-V^{\mathbf{q}}_{2112}\right)f_{1,\mathbf{k}-\mathbf{q},s}\right]p_{12,\mathbf{k},s} \qquad (5.8)\\ &- \frac{\mathrm{i}}{\hbar}\sum_{\mathbf{q}\neq 0}\left[V^{\mathbf{q}}_{1212}p_{12,\mathbf{k}-\mathbf{q},s}+V^{\mathbf{q}}_{2211}p_{21,\mathbf{k}-\mathbf{q},s}\right]\left(f_{2,\mathbf{k},s}-f_{1,\mathbf{k},s}\right) \qquad (5.9)\\ &+ \frac{\mathrm{i}}{\hbar}V^{0}_{2112}\sum_{\mathbf{q}\neq 0,s'}\left[p_{12,\mathbf{q},s'}+p_{21,\mathbf{q},s'}\right]\left(f_{2,\mathbf{k},s}-f_{1,\mathbf{k},s}\right). \qquad (5.10)\end{aligned}$$

Higher-order correlations have been included as a dephasing constant γ_{ph}, similar to Eq. (5.4). The three mean field contributions are also denoted as *exchange* (5.8), *exciton* (5.9) and *depolarization* (5.10) terms and originate from different interplays of the COULOMB matrix elements. The influence of the HARTREE-FOCK terms have been discussed in detail, for example, in [CLSRP92, LN03, NIS99], hence only a short overview about the main effects will be given.

The first HARTREE-FOCK contribution, the *exchange term* [Eq. (5.8)], leads to a momentum dependent renormalization of the single-particle energies:

$$\begin{aligned}\mathrm{i}\left(\omega_{1,\mathbf{k}}-\omega_{2,\mathbf{k}}\right)p_{12,\mathbf{k},s} + \frac{\mathrm{i}}{\hbar}\sum_{\mathbf{q}\neq 0}\left[\left(V^{\mathbf{q}}_{2222}-V^{\mathbf{q}}_{2112}\right)f_{2,\mathbf{k}-\mathbf{q},s} - \left(V^{\mathbf{q}}_{1111}-V^{\mathbf{q}}_{2112}\right)f_{1,\mathbf{k}-\mathbf{q},s}\right]p_{12,\mathbf{k},s} \\ = \mathrm{i}\left(\tilde{\omega}_{1,\mathbf{k}}-\tilde{\omega}_{2,\mathbf{k}}\right)p_{12,\mathbf{k},s}. \qquad (5.11)\end{aligned}$$

Assuming that the subband distributions are constant in time and the carrier density being fully located in the lower subband, the exchange term causes a larger transition energy and also a softening of the nonparabolicity, i.e. the low energy tail is less pronounced compared to the free carrier spectrum. The *exciton contribution* Eq. (5.9), and the *depolarization term*, Eq. (5.10), renormalize the RABI frequency:

$$\begin{aligned}\mathrm{i}\Omega_{12}(t)\left(f_{2,\mathbf{k},s}-f_{1,\mathbf{k},s}\right) + \frac{\mathrm{i}}{\hbar}\sum_{\mathbf{q}\neq 0}\left[V^{\mathbf{q}}_{1212}p_{12,\mathbf{k}-\mathbf{q},s}+V^{\mathbf{q}}_{2211}p_{21,\mathbf{k}-\mathbf{q},s}\right]\left(f_{2,\mathbf{k},s}-f_{1,\mathbf{k},s}\right) \\ - \frac{\mathrm{i}}{\hbar}V^{0}_{2112}\sum_{\mathbf{q}\neq 0,s'}\left[p_{12,\mathbf{q},s'}+p_{21,\mathbf{q},s'}\right]\left(f_{2,\mathbf{k},s}-f_{1,\mathbf{k},s}\right) \\ = \mathrm{i}\tilde{\Omega}_{12}(t)\left(f_{2,\mathbf{k},s}-f_{1,\mathbf{k},s}\right). \qquad (5.12)\end{aligned}$$

The exciton contribution corresponds to the interaction of one electron in the upper subband with an unoccupied state in the lower subband. This resembles an excitonic interaction between an electron and an hole in interband systems [HK04] and shifts the gap energy to lower energies due to the attractive interaction. The strength of the exciton contribution increases with decreasing well width [NIBS97]. The depolarization term mainly originates from the difference between the occupied states in the lower and the upper subband. In contrast to the excitonic part, the strength of the depolarization term decreases with decreasing well width [GSKB00]. With the renormalized values, the EOM including the HARTREE-FOCK terms keeps its compact form:

$$\frac{\mathrm{d}}{\mathrm{d}t}p_{12,\mathbf{k},s} = \mathrm{i}\left(\tilde{\omega}_{1,\mathbf{k}}-\tilde{\omega}_{2,\mathbf{k}}\right)p_{12,\mathbf{k},s} - \mathrm{i}\tilde{\Omega}_{12}(t)\left(f_{2,\mathbf{k},s}-f_{1,\mathbf{k},s}\right). \qquad (5.13)$$

Comparisons with the experiment have shown that simulations for the absorption spectra including the HARTREE-FOCK terms and the phenomenological dephasing constant γ_{ph} agree very well with the experimentally measured spectra [Wal02]. However, in order to gain an overall understanding of the microscopic processes which lead to the intrinsic line width, scattering processes must also be included. For obtaining the *el-el* scattering rates, the correlation expansion will be applied in the next order (second-order correlation expansion).

5.3 Boltzmann scattering contributions

Now the correlation terms, previously neglected in Eq. (5.7), are further evaluated, that is, $\langle\hat{\rho}_{\alpha\beta\gamma 2}\rangle_{\mathrm{corr}} = \langle\hat{a}^\dagger_\alpha\hat{a}^\dagger_\beta\hat{a}_\gamma\hat{a}_{2,\mathbf{k},s}\rangle_{\mathrm{corr}}$ and $\langle\hat{\rho}_{1\alpha\beta\gamma}\rangle_{\mathrm{corr}} = \langle\hat{a}^\dagger_{1,\mathbf{k},s}\hat{a}^\dagger_\alpha\hat{a}_\beta\hat{a}_\gamma\rangle_{\mathrm{corr}}$. The full equation for $\frac{\mathrm{d}}{\mathrm{d}t}p_{12,\mathbf{k}s}$ then reads:

$$\frac{\mathrm{d}}{\mathrm{d}t}p_{12,\mathbf{k},s} = \mathrm{i}(\tilde{\omega}_{1,\mathbf{k}} - \tilde{\omega}_{2,\mathbf{k}})\,p_{12,\mathbf{k},s} - \mathrm{i}\tilde{\Omega}_{12}(t)\,(f_{2,\mathbf{k},s} - f_{1,\mathbf{k},s}) - \Gamma\{\rho_{ij,\mathbf{k},s}\}, \tag{5.14}$$

with the dephasing functional $-\Gamma\{\hat{\rho}_{ij,\mathbf{k},s}\} = \frac{\mathrm{i}}{\hbar}\sum_{\{\alpha\beta\gamma\}}V_{\alpha\beta 1\gamma}\langle\hat{\rho}_{\alpha\beta\gamma 2}\rangle_{\mathrm{corr}} - \frac{\mathrm{i}}{\hbar}\sum_{\{\alpha\beta\gamma\}}V_{2\alpha\beta\gamma}\langle\hat{\rho}_{1\alpha\beta\gamma}\rangle_{\mathrm{corr}}$. Evaluating the EOM for the four-operator correlation expectation values, these terms again couple to six-operator terms. Analogous to the previous section, the six-operator terms are split into the HARTREE-FOCK term and the correlation term, where the correlation terms are neglected. The EOM for the expectation values in second-order correlation expansion are then:

$$\begin{aligned}-\mathrm{i}\hbar\frac{\mathrm{d}}{\mathrm{d}t}\langle\hat{\rho}_{\alpha\beta\gamma 2}\rangle_{\mathrm{corr}} &= \left(\varepsilon_\alpha + \varepsilon_\beta - \varepsilon_\gamma - \varepsilon_2 - \mathrm{i}\hbar\gamma_{\mathrm{corr}}\right)\langle\hat{\rho}_{\alpha\beta\gamma 2}\rangle_{\mathrm{corr}} \\ &\quad + \sum_{\{abcd\}}\tilde{W}_{abdc}\left(\langle\hat{\rho}_{a2}\rangle\langle\hat{\rho}_{b\gamma}\rangle\langle\hat{\rho}_{\beta c}\rangle^-\langle\hat{\rho}_{\alpha d}\rangle^- - \langle\hat{\rho}_{\alpha d}\rangle\langle\hat{\rho}_{\beta c}\rangle\langle\hat{\rho}_{b\gamma}\rangle^-\langle\hat{\rho}_{a2}\rangle^-\right), \end{aligned}\tag{5.15}$$

$$\begin{aligned}-\mathrm{i}\hbar\frac{\mathrm{d}}{\mathrm{d}t}\langle\hat{\rho}_{1\alpha\gamma\beta}\rangle_{\mathrm{corr}} &= \left(\varepsilon_1 + \varepsilon_\alpha - \varepsilon_\gamma - \varepsilon_\beta - \mathrm{i}\hbar\gamma_{\mathrm{corr}}\right)\langle\hat{\rho}_{1\alpha\gamma\beta}\rangle_{\mathrm{corr}} \\ &\quad + \sum_{\{abcd\}}\tilde{W}_{abdc}\left(\langle\hat{\rho}_{a\beta}\rangle\langle\rho_{b\gamma}\rangle\langle\hat{\rho}_{\alpha c}\rangle^-\langle\hat{\rho}_{1d}\rangle^- - \langle\hat{\rho}_{1d}\rangle\langle\hat{\rho}_{\alpha c}\rangle\langle\hat{\rho}_{b\gamma}\rangle^-\langle\hat{\rho}_{a\beta}\rangle^-\right), \end{aligned}\tag{5.16}$$

with the abbreviation $\langle\hat{\rho}_{\alpha\beta}\rangle^- = \delta_{\alpha\beta} - \langle\hat{\rho}_{\alpha\beta}\rangle$ and $\tilde{W}_{abdc} = \tilde{V}_{abdc} - \tilde{V}_{badc}$. The indices a,b,c,d are multi-indices as well. A phenomenological dephasing γ_{corr} has been added, reflecting higher-order correlations. Here, the screened COULOMB potentials $\tilde{V}$ are considered.[2] Now, the equations Eq. (5.15) and (5.16) can be formally integrated. To solve them, the MARKOV approximation is applied, that is, memory effects are neglected [Kam92]. This means that the inhomogeneous parts in Eq. (5.15) and in Eq. (5.16) are assumed to be only weakly time-dependent and consequently scattering processes of particles do not contain memories of past collisions. The evolution of the MARKOV approximation leads to the following expression for $\Gamma\{\rho_{ij,\mathbf{k}}\}$:

$$\begin{aligned}\Gamma\{\hat{\rho}_{ij,\mathbf{k}}\} &= \sum_{\{\alpha\beta\gamma\}}\sum_{\{abcd\}}\{\Delta_{\alpha\beta\gamma 2}\}_{\gamma_{\mathrm{corr}}}\tilde{V}_{\alpha\beta 1\gamma}\tilde{W}_{abdc}\left(\langle\hat{\rho}_{a2}\rangle\langle\hat{\rho}_{b\gamma}\rangle\langle\hat{\rho}_{\beta c}\rangle^-\langle\hat{\rho}_{\alpha d}\rangle^- - \langle\hat{\rho}_{\alpha d}\rangle\langle\hat{\rho}_{\beta c}\rangle\langle\hat{\rho}_{b\gamma}\rangle^-\langle\hat{\rho}_{a2}\rangle^-\right) \\ &\quad - \sum_{\{\alpha\beta\gamma\}}\sum_{\{abcd\}}\{\Delta_{1\alpha\beta\gamma}\}_{\gamma_{\mathrm{corr}}}\tilde{V}_{2\alpha\beta\gamma}\tilde{W}_{abdc}\left(\langle\hat{\rho}_{a\beta}\rangle\langle\rho_{b\gamma}\rangle\langle\hat{\rho}_{\alpha c}\rangle^-\langle\hat{\rho}_{1d}\rangle^- - \langle\hat{\rho}_{1d}\rangle\langle\hat{\rho}_{\alpha c}\rangle\langle\hat{\rho}_{b\gamma}\rangle^-\langle\hat{\rho}_{a\beta}\rangle^-\right), \end{aligned}\tag{5.17}$$

where $\langle\hat{\rho}_{\mu\nu}\rangle^- = 1 - \langle\hat{\rho}_{\mu\nu}\rangle$ and

$$\{\Delta_{\alpha\beta\gamma 2}\}_{\gamma_{\mathrm{corr}}} = \frac{\gamma_{\mathrm{corr}}}{(\varepsilon_\alpha + \varepsilon_\beta - \varepsilon_\gamma - \varepsilon_2) + \hbar^2\gamma^2_{\mathrm{corr}}}. \tag{5.18}$$

Equation (5.18) is a modification of the usual expression for the BOLTZMANN scattering rates $\Gamma\{\hat{\rho}_{ij,\mathbf{k}}\}$ [LK88]: Instead of the standard, strictly energy conserving transition probability $\{\Delta_{\alpha\beta\gamma 2}\} \propto \delta(\varepsilon_\alpha + \varepsilon_\beta - \varepsilon_\gamma - \varepsilon_2)$, which can also be obtained via FERMIs golden rule [CT99], the energy conservation is softened by a Lorentzian broadening. This modification can be justified by the fact that due to the HEISENBERG uncertainty relation, a certain energy broadening of a few meV is a reasonable assumption, as long as the electron density is conserved [But07], i.e. γ_{corr} in Eq. (5.18) can also be interpreted as a softening of the delta condition due to higher-order correlations.

[2] In the HARTREE-FOCK contributions, the unscreened potential V is considered since the *el-el* scattering is not influenced by a background electron plasma, see also Sec. 4.2.2.

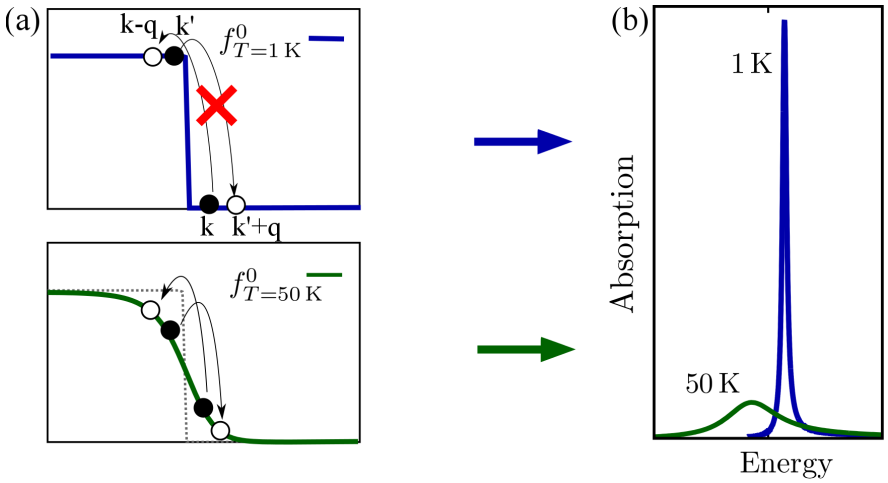

Figure 5.3 | Schematic drawing of possible scattering events for two different temperatures. The black dots represent occupied $\mathbf{k}$ states while the white dots label unoccupied $\mathbf{k}$ states. (a) For $T = 1$ K, PAULI blocking prohibits the electron-electron scattering. For $T = 50$ K, scattering channels around the FERMI edge become available. (b) The corresponding line widths of the absorption spectra show a significant broadening for higher temperatures.

Note that within this thesis, all diagonal terms (proportional to $\langle\hat{\rho}_{ij,\mathbf{k}}\rangle$) in the scattering contributions are included, while only the non-diagonal terms proportional to $\langle\hat{\rho}_{ij,\mathbf{k}-\mathbf{q}}\rangle$ are considered since these are the dominant terms counteracting the broadening of the diagonal terms. Detailed investigations considering the full scattering contributions have been made, for example, in [WFL$^+$04, WCYW06]. Taking into account the two lowest subbands, the following scattering contributions of Eq. (5.17) will be considered:

$$\Gamma\{\langle\hat{\rho}_{ij,\mathbf{k},s}\rangle\} = \sum_{\mathbf{k}',\mathbf{q},s} \Gamma_{\mathrm{diag}}\langle\hat{\rho}_{12,\mathbf{k},s}\rangle + \sum_{\mathbf{k}',\mathbf{q},s} \Gamma_{\mathrm{ndiag1}}\langle\hat{\rho}_{12,\mathbf{k}-\mathbf{q},s}\rangle + \sum_{\mathbf{k}',\mathbf{q},s} \Gamma^*_{\mathrm{ndiag1}}\langle\hat{\rho}_{21,\mathbf{k}-\mathbf{q},s}\rangle. \tag{5.19}$$

The explicit terms are given in App. B.

In past works, the inclusion of the BOLTZMANN scattering rates have led to the mentioned discrepancy between the experimentally measured and theoretically calculated ISB absorption spectra in the low temperature regime: The counteracting of the different scattering contributions leads to an intrinsic line width, which is too small compared to experimental findings. The main reason for this behavior is the PAULI blocking. This can be explained by looking e.g. at the intrasubband scattering contribution of the diagonal scattering rate, $\Gamma^{\mathrm{intra}}_{\mathrm{diag}}$:

$$\Gamma^{\mathrm{intra}}_{\mathrm{diag}} = \{\Delta_{1\mathbf{k},1\mathbf{k}',1\mathbf{k}'+\mathbf{q},1\mathbf{k}-\mathbf{q}}\}\gamma_{\mathrm{corr}}\tilde{V}^{\mathbf{q}}_{1111}(2\cdot\tilde{V}^{\mathbf{q}}_{1111} - \tilde{V}^{\mathbf{k}-\mathbf{q}-\mathbf{k}'}_{1111})\left(f_{1,\mathbf{k}',s}f^-_{1,\mathbf{k}'+\mathbf{q},s}f^-_{1,\mathbf{k}-\mathbf{q},s} + f_{1,\mathbf{k}-\mathbf{q},s}f_{1,\mathbf{k}'+\mathbf{q},s}f^-_{1,\mathbf{k}',s}\right) \tag{5.20}$$

The first term of the scattering rate consists of in- and out-scattering contributions between the states $\mathbf{k},\mathbf{k}',\mathbf{k}'+\mathbf{q},\mathbf{k}-\mathbf{q}$ and are proportional to the empty states at $\mathbf{k}'+\mathbf{q},\mathbf{k}-\mathbf{q}$ and the filled states in $\mathbf{k}'$ for one specific momentum $\mathbf{k}$. The second term is proportional to the empty states at $\mathbf{k}'$ and the filled states in $\mathbf{k}'+\mathbf{q},\mathbf{k}-\mathbf{q}$. In general, the distribution functions f are approximated as FERMI functions. For low temperatures, the FERMI distribution resembles a step function where all states below the FERMI edge are occupied and all states above the FERMI level are empty. The second term in Eq. (5.20) is cancelled by the non-diagonal term in Γ_{diag}, see App. B. The first term becomes arbitrarily small for low temperatures due to the PAULI blocking. A schematic drawing of the corresponding scattering process is shown in Fig. 5.3(a): For $T \to 0$, there exist no free states below the FERMI edge, making electron-electron scattering impossible. Consequently, the line width of the correspondent absorption spectrum

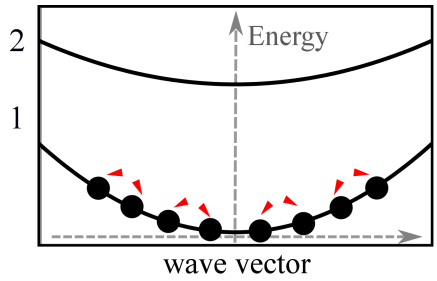

Figure 5.4 | Schematic drawing of the ground state correlations in the momentum space: The electrons (black dots) are correlated via the Coulomb coupling (red arrows). This leads to a deviation from the generally assumed FERMI distribution in the equilibrium ground state.

becomes arbitrarily small [blue line in Fig. 5.3(b)]. For higher temperatures, the states below the FERMI level are unoccupied and states above the level occupied, which allows scattering around the FERMI edge. Consequently, the absorption line width is significantly broadened [green line in Fig. 5.3(b)].

While some theoretical descriptions have included disorder corrections such as impurities [BLKW05] or interface roughness [LN04], it will be shown in the following section that by including COULOMB ground state correlations on a self-consistent level, the intrinsic line width is broadened and the former numerical instability of the line width at low temperatures can be counterbalanced even in high-quality samples.

5.4 Ground state correlations

In this section, the distribution function $f_{i,k,s}$ will be investigated in more detail. Instead of assuming a FERMI function for $f_{i,k,s}$ a deviation $\delta f_{i,k,s}$ is considered, originating from *el-el* correlations in the ground state. Similar calculations have been done in three-dimensional electron gases [GMB57, GHE01] and metals [DV60, TY91], where many-body correlations lead to a deviation of the equilibrium distribution function from the conventionally assumed FERMI distribution at low temperatures. Later on, the theoretical description has been further developed by assuming the *el-el* interaction as the responsible mechanism [LV71, Lan80]. Figure 5.4 shows a schematic drawing of the electrons, which are correlated via the COULOMB interaction (red arrows). At high temperatures the ground state correlations will play a minor role, while for low temperatures, its influence is expected to increase for the following reason: For high temperatures, the kinetic energy of the electrons will dominate over the COULOMB interaction. Going to lower temperatures, the COULOMB repulsion can be of the same order as the kinetic energy and consequently gains importance. For the derivation of the ground state correlations a perturbative ansatz for the distribution function is chosen and developed via the correlation expansion up to second order, similar to the derivation of the BOLTZMANN scattering terms in Sec. 5.3. Then, the properties of the correlated distribution function will be investigated. The influence of the ground state correlations on the absorption spectra will be demonstrated in Sec. 5.5.

5.4.1 Renormalization of the distribution function

To investigate the influence of the ground state correlations, the deviation $\delta f_{i,\mathbf{k},s} = f_{i,\mathbf{k},s} - f^0_{i,\mathbf{k},s}$ from the equilibrium FERMI distribution $f^0_{i,\mathbf{k},s}$ is determined. $\delta f_{i,\mathbf{k},s}$ is calculated with the HEISENBERG EOM, considering the free carrier Hamiltonian $\hat{H}_0$ and the COULOMB interaction Hamiltonian $\hat{H}_{\text{el-el}}$:

$$-\mathrm{i}\hbar\frac{\mathrm{d}}{\mathrm{d}t}\delta f_{i,\mathbf{k},s} = -\mathrm{i}\hbar\frac{\mathrm{d}}{\mathrm{d}t}f_{i,\mathbf{k},s} = \langle[\hat{H}_0 + \hat{H}_{\text{el-el}}, a^\dagger_{i,\mathbf{k},s}a_{i,\mathbf{k},s}]\rangle. \tag{5.21}$$

Equation (5.21) is evolved up to second order in the COULOMB coupling. In the following, the subband index i is set to 1 since in equilibrium (and for a moderate doping density) only the lower subband is occupied at low temperatures. The correlation expansion of $\delta f_{i,\mathbf{k},s}$ resembles the derivation of the HARTREE-FOCK contributions in Sec. 5.2 and the BOLTZMANN scattering contributions in Sec. 5.3 (excluding the electromagnetic field contributions). In first-order correlation, the mean field terms are

obtained, which vanish in a one subband system. Thus, the time evolution of the deviation $\delta f_{1,\mathbf{k},s}$ is only determined by the correlation terms:

$$\frac{\mathrm{d}}{\mathrm{d}t}\delta f_{1,\mathbf{k},s} = \frac{\mathrm{i}}{\hbar}\sum_{\{\alpha\beta\gamma\}} \tilde{V}_{\alpha\beta 1\gamma}\langle\hat{\rho}_{\alpha\beta\gamma 1}\rangle_{\mathrm{corr}} - \frac{\mathrm{i}}{\hbar}\sum_{\{\alpha\beta\gamma\}} \tilde{V}_{1\alpha\beta\gamma}\langle\hat{\rho}_{1\alpha\beta\gamma}\rangle_{\mathrm{corr}}. \tag{5.22}$$

The summation over $\{\alpha\beta\gamma\}$ reduces to the lower subband 1, but the different momenta have to be considered, In the following, the subband index 1 will be dropped. Developing the correlation terms, the dynamic equations until second order are:

$$\frac{\mathrm{d}}{\mathrm{d}t}\delta f_{\mathbf{k}} = \frac{\mathrm{i}}{\hbar}\sum_{\mathbf{k}',\mathbf{q}} \tilde{V}^{\mathbf{q}}\left[\langle\hat{\rho}\rangle_{\mathrm{corr},1} - \langle\hat{\rho}\rangle_{\mathrm{corr},2}\right], \tag{5.23}$$

$$\begin{aligned}\frac{\mathrm{d}}{\mathrm{d}t}\langle\hat{\rho}\rangle_{\mathrm{corr},1/2} &= \pm\frac{\mathrm{i}}{\hbar}(\varepsilon_{\mathbf{k}-\mathbf{q}} + \varepsilon_{\mathbf{k}'+\mathbf{q}} - \varepsilon_{\mathbf{k}'} - \varepsilon_{\mathbf{k}})\langle\hat{\rho}\rangle_{\mathrm{corr},1/2} - \gamma_{\mathrm{corr}}\langle\hat{\rho}\rangle_{\mathrm{corr},1/2} \\ &\quad \pm\frac{\mathrm{i}}{\hbar}\tilde{W}^{\mathbf{k},\mathbf{q},\mathbf{k}'}\left(f_{\mathbf{k}}f_{\mathbf{k}'}f^{-}_{1,\mathbf{k}'+\mathbf{q}}f^{-}_{\mathbf{k}-\mathbf{q}} + f_{\mathbf{k}-\mathbf{q}}f_{\mathbf{k}'+\mathbf{q}}f^{-}_{\mathbf{k}'}f^{-}_{\mathbf{k}}\right) \\ &= \pm\frac{\mathrm{i}}{\hbar}(\Delta\varepsilon - \mathrm{i}\hbar\gamma_{\mathrm{corr}})\langle\hat{\rho}_{\mathbf{k},\mathbf{q},\mathbf{k}'}\rangle_{\mathrm{corr},1/2} \pm \frac{\mathrm{i}}{\hbar}\tilde{W}^{\mathbf{k},\mathbf{q},\mathbf{k}'}Q(t)\end{aligned} \tag{5.24}$$

with $\tilde{W}^{\mathbf{k},\mathbf{q},\mathbf{k}'} = 2\tilde{V}^{\mathbf{q}} - \tilde{V}^{\mathbf{k}'-\mathbf{q}-\mathbf{k}}$. The dephasing γ_{corr} represents higher correlation contributions and equals the phenomenological damping γ_{corr} in the BOLTZMANN scattering terms. Furthermore, the spin index s has been dropped after evaluating the sum over the spins $\sum_{\sigma_{\alpha/\beta/\gamma}}$, that is, $\delta f_{1,\mathbf{k},s} = \delta f_{\mathbf{k}}$.

Similar to the derivation of BOLTZMANN scattering terms, the equations can be formally integrated. The memory of the inhomogeneity, $Q(t)$, is assumed to be small, but unlike the usual MARKOV approximation, where the memory in the inhomogeneity is fully neglected, $Q(t)$ is expanded in a perturbation series around the local time t: $Q(t') = Q(t) + (t-t')\dot{Q}(t)$. This means that memory effects are included in first order. The formally integrated equation with the expanded inhomogeneity reads:

$$\langle\hat{\rho}\rangle_{\mathrm{corr},1/2} = \mp\frac{\mathrm{i}}{\hbar}\int_0^\infty \mathrm{d}s\, e^{(\pm\frac{\mathrm{i}}{\hbar}\Delta\varepsilon - \gamma_{\mathrm{corr}})s}\tilde{W}^{\mathbf{k},\mathbf{q},\mathbf{k}'}\left[Q(t) + s\,\dot{Q}(t)\right]. \tag{5.25}$$

The first-order memory effects are contained in the temporal derivative of the source. Here, the substitution $s = t - t'$ according to the MARKOV approximation has already been applied. The zeroth-order term $\propto Q(t)$ yields the typical BOLTZMANN scattering contributions which are negligibly small for finite values of γ_{ph} if the FERMI distribution functions are assumed for the distribution functions $f_{\mathbf{k}}$. For $\gamma_{\mathrm{ph}} = 0$ the terms vanish. Thus, $Q(t)$ is set to zero. Under these assumptions, Eq. (5.25) can be solved:

$$\langle\hat{\rho}\rangle_{\mathrm{corr},1/2} = \mp\frac{\mathrm{i}}{\hbar}\tilde{W}^{\mathbf{k},\mathbf{q},\mathbf{k}'}\dot{Q}(t)\left[\frac{1}{(\pm\frac{i}{\hbar}\Delta\varepsilon - \gamma_{\mathrm{corr}})^2}\right], \tag{5.26}$$

which is substituted in Eq. (5.23). In a first-order iteration, the electron occupations occurring in the inhomogeneity $Q(t)$ are approximated with FERMI distribution functions f^0. The final expression for the deviation then reads:

$$\delta f_{\mathbf{k}} = 2\sum_{\mathbf{k}',\mathbf{q}} \frac{\Delta\varepsilon^2 - \hbar^2\gamma_{\mathrm{corr}}^2}{(\Delta\varepsilon^2 + \hbar^2\gamma_{\mathrm{corr}}^2)^2}\left(\tilde{V}^{\mathbf{k}'-\mathbf{q}-\mathbf{k}} - 2\tilde{V}^{\mathbf{q}}\right)\tilde{V}^{\mathbf{q}}\left[f^0_{\mathbf{k}}f^0_{\mathbf{k}'}f^-_{\mathbf{k}'+\mathbf{q}}f^-_{\mathbf{k}-\mathbf{q}} - f^0_{\mathbf{k}'+\mathbf{q}}f^0_{\mathbf{k}-\mathbf{q}}f^-_{\mathbf{k}'}f^-_{\mathbf{k}}\right], \tag{5.27}$$

The two scattering terms illustrate the interplay of the electrons: In the first term, two electrons with momentum $\mathbf{k}'+\mathbf{q}$ and $\mathbf{k}-\mathbf{q}$ are annihilated and created with the momentum numbers $\mathbf{k}'$ and $\mathbf{k}$. Thus, it is dependent on the occupied states at $\mathbf{k}$ and $\mathbf{k}'$ and the empty states at $\mathbf{k}'+\mathbf{q}$ and $\mathbf{k}-\mathbf{q}$. The second term acts vice versa. For lower temperatures, when the FERMI distribution function approximates the Heaviside function, the only possible terms for in- and out-scattering have momenta around the FERMI

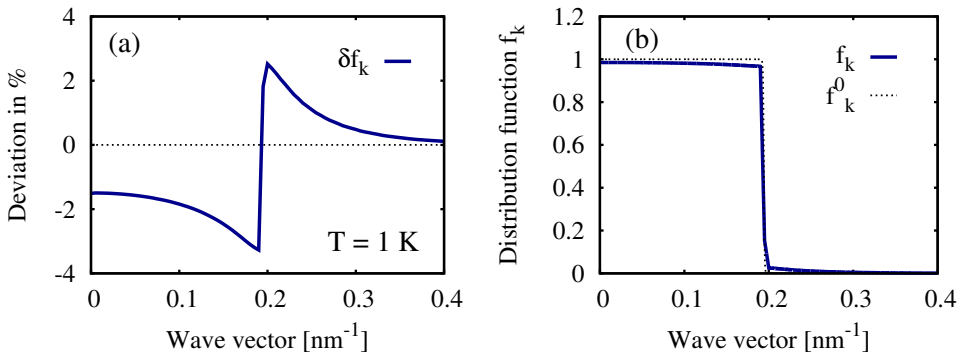

Figure 5.5 | (a) Deviation $\delta f_{\mathbf{k}}$ from a FERMI distribution for a carrier density of $n_{\mathrm{d}} = 6.0 \cdot 10^{11}$ cm^{-2} in a 5 nm quantum well at a temperature of $T = 1$ K. (b) Corresponding distribution function $f_{\mathbf{k}} = f^0_{\mathbf{k}} - \delta f_{\mathbf{k}}$ (solid blue line). The corresponding FERMI function $f^0_{\mathbf{k}}$ is shown as a dotted black line. The strongest deviation is found at the sharp edge in the distribution function (solid line) around $\mathbf{k} = 0.2$ nm $^{-1}$.

edge $\mathbf{k}_{\mathrm{F}}$, that is, $\mathbf{k} \approx \mathbf{k}' \approx \mathbf{k}_{\mathrm{F}}$ for small $\mathbf{q}$. Under these conditions, $(V^{\mathbf{k}'-\mathbf{q}-\mathbf{k}} - 2\tilde{V}^{\mathbf{q}}) < 0$. For momentum numbers $\mathbf{k}, \mathbf{k}'$ below the FERMI edge, the first scattering term predominates, giving the deviation an overall negative sign. Above the FERMI edge, the dominant second term leads to an overall positive sign.

Figure 5.5(a) shows the angle integrated deviation $\delta f_{\mathbf{k}}$ for a carrier density of $n_{\mathrm{d}} = 6.0 \cdot 10^{11}$ cm^{-2} for a 5 nm quantum well at a temperature of $T = 1$ K. The FERMI edge lies around $k_{\mathrm{F}} \approx 0.2$ nm^{-1}. The deviation $\delta f_{\mathbf{k}}$ decreases for increasing momentum number until reaching its minimal value just below the FERMI edge. Just above the FERMI edge, $\delta f_{\mathbf{k}}$ increases sharply, reaching its maximal value. Then the deviation decreases again and approaches the value zero. The maximal value of $\delta f_{\mathbf{k}}$ reaches about 3% of the absolute value of the FERMI function at $T = 1$ K. Comparing $f_{\mathbf{k}}$ [dark blue line in 5.5(b)] with the FERMI distribution [dotted line in 5.5(b)], a slight decrease of the electron distribution below the FERMI edge and a slight increase of the electron distribution above the FERMI edge is visible. The difference between the FERMI distribution $f^0_{\mathbf{k}}$ and the distribution $f_{\mathbf{k}}$, where ground state correlations are considered, is quantitatively small (since the maximal change of the value is in the order of 3%). Still, the ground state correlations are expected to play an important role, since the deviation opens up a new physical scenario in the low temperature regime: It leads to an occupation above the FERMI edge and to unoccupied states below the FERMI edge. Thus, even for $T \to 0$ K, scattering is possible, which was prohibited in the former case due to the PAULI blocking.

5.4.2 Properties of the ground state correlations

Temperature dependence - In order to gain further information about the properties of the deviation $\delta f_{\mathbf{k}}$ and its influence on the equilibrium function, the dependence of $\delta f_{\mathbf{k}}$ on different parameters will now be investigated. Figure 5.6(left) shows the deviation function for different temperatures for a carrier density of $n_{\mathrm{d}} = 6.0 \cdot 10^{11}$ cm^{-2} in a 5 nm quantum well. For $T = 1$ K, the deviation (blue line) has a sharp change of the algebraic sign around the FERMI edge. For higher temperatures (red and green lines), the deviation softens around the edge and the maximum of the deviation decreases and shifts away from the FERMI edge. This is due to the scattering terms in the deviation, which consist of products of four FERMI functions: The smoothing of $\delta f_{\mathbf{k}}$ resembles the smoothing of the FERMI function for higher temperatures. The corresponding distribution functions $f_{\mathbf{k}}$ [solid lines in Fig. 5.6(left)] show only small corrections from the FERMI distribution $f^0_{\mathbf{k}}$ (dotted). The observed differences between $f_{\mathbf{k}}$ and $f^0_{\mathbf{k}}$ for different T remain on the same order though. The influence of the ground state correlations

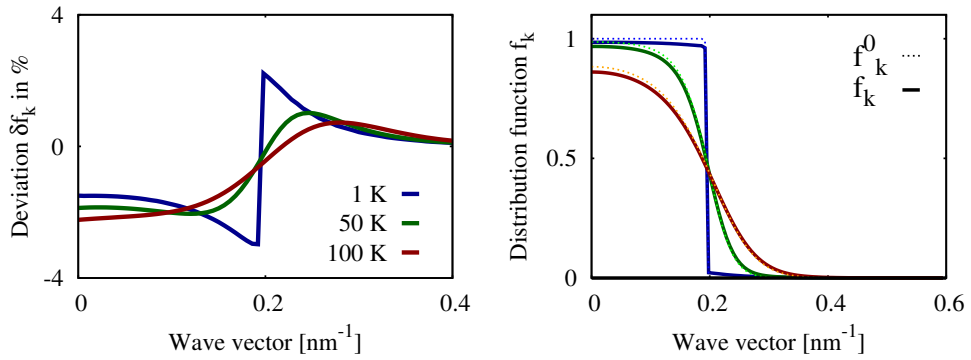

Figure 5.6 | (Left) Deviation $\delta f_{\mathbf{k}}$ for a carrier density of $n_{\mathrm{d}} = 6.0 \cdot 10^{11}$ cm^{-2} in a 5 nm quantum well for three different temperatures. For increasing temperature, the maximum of the deviation shifts away from the FERMI edge. (b) Corresponding distribution functions $f_{\mathbf{k}}$. The FERMI distribution functions $f^0_{\mathbf{k}}$ are drawn as dotted lines.

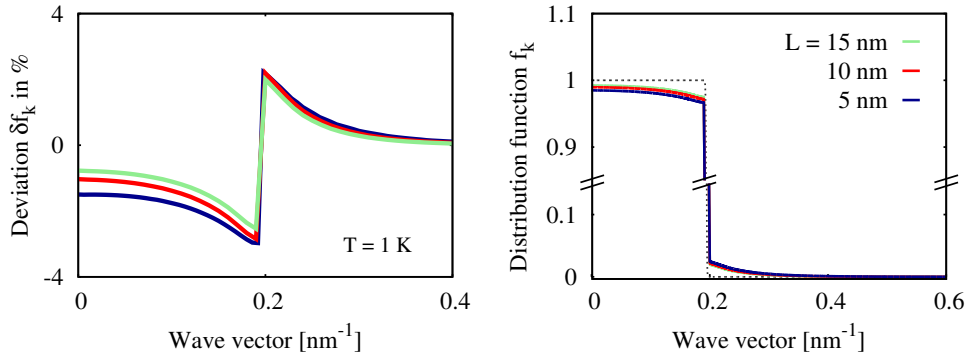

Figure 5.7 | (Left) Deviation $\delta f_{\mathbf{k}}$ for a carrier density of $n_{\mathrm{d}} = 6.0 \cdot 10^{11}$ cm^{-2} at $T = 1$ K for three different well widths. The overall value of the deviation slightly increases for decreasing well width. (Right) Distribution function $f_{\mathbf{k}}$. The difference between the different well widths is hardly visible.

is expected to decrease for increasing temperatures for the following reasons: While for $T = 1$ K the deviation allows the in-scattering to momentum states below the FERMI edge, these scattering types are already available for higher temperatures. Consequently, the relative importance of $\delta f_{\mathbf{k}}$ decreases. Furthermore, as explained above, the dominant scattering processes at low temperatures are processes around the Fermi edge, i.e. for small $\mathbf{q}$. Due to $\tilde{V}^{\mathbf{q}} \sim 1/|\mathbf{q}|$, the scattering rates are maximal for small $\mathbf{q}$. For increasing temperature, the electron scattering is less common around the FERMI edge and thus $\delta f_{\mathbf{k}}$ decreases.

Well width dependence - Besides the temperature dependence, the ground state correlations also depend on the quantum well width. The deviation is slightly stronger for decreasing well widths. This can be understood since the COULOMB form factor $\mathscr{F}_{1111}$ decreases more strongly for increasing well width L. Figure 5.7 shows the deviation $\delta f_{\mathbf{k}}$ for a carrier density of $n_{\mathrm{d}} = 6.0 \cdot 10^{11}$ cm^{-2} at $T = 1$ K for $L = 5$, 10 and 15 nm. The corresponding distribution function $f_{\mathbf{k}}$ is plotted on the right side. The

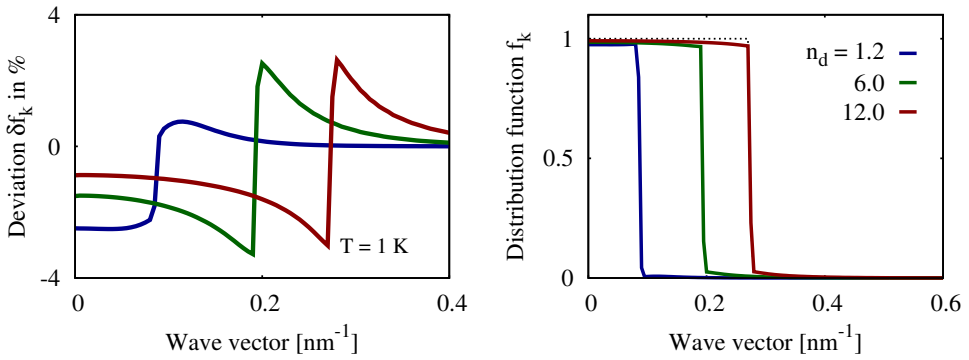

Figure 5.8 | (Left) Deviation $\delta f_{\mathbf{k}}$ of a 5 nm quantum well for $T = 1$ K, for different carrier densities $n_{\mathrm{d}} \times 10^{11}$ cm^{-2}. Due to the small density, the curve of $n_{\mathrm{d}} = 1.2$ (blue line) is already smoothed considerably. (Right) Distribution functions $f_{\mathbf{k}}$ for the different carrier densities.

difference of $f_{\mathbf{k}}$ for different well widths is hardly visible. This is again due to the dominant scattering processes around the FERMI edge, that is, for very small $\mathbf{q}$: For all well widths, the form factor starts from the value $\mathscr{F}_{1111}(\mathbf{q} = 0) = 1$. A more pronounced difference of the deviation $\delta f_{\mathbf{k}}$ can be expected for higher temperatures, since the scattering processes are possible for a broader momentum range of $\mathbf{q}$ and the COULOMB form factors of the different well widths vary more for larger $\mathbf{q}$ values. However, this is not shown here since the overall impact of the deviation $\delta f_{\mathbf{k}}$ decreases for higher temperatures.

Carrier density dependence - Additionally, the deviation function is dependent on the carrier density n_{d}. The carrier density dependence of $\delta f_{\mathbf{k}}$ is plotted in Fig. 5.8. For $n_{\mathrm{d}} = 1.2 \cdot 10^{11}$ cm^{-2} (blue line) the deviation is decreased and smoothed around the Fermi edge. The smoothing originates from the already smoothed Fermi distribution function since for smaller densities the Fermi edge is less pronounced. The decreasing height of $\delta f_{\mathbf{k}}$ for smaller densities can be explained by the short-range nature of the electronic correlations: For a larger mean-free path (Wigner-Seitz radius) r_s between the electrons [Zim92], the probability of a momentum transfer decreases. The deviation for $n_{\mathrm{d}} = 1.2 \cdot 10^{12}$ cm^{-2} (red line) above the FERMI edge is only slightly larger than for $n_{\mathrm{d}} = 6. \cdot 10^{11}$ cm^{-2} (green line). In fact, a decrease of the deviation is expected at a certain point for large densities since the kinetic energy, which goes with $1/{r_s}^2$, predominates the COULOMB interaction, going with $1/r_s$ between the electrons [Mah00]. The corresponding distribution functions $f_{\mathbf{k}}$ are plotted on the right side of Fig. 5.8. As in the other cases, the magnitude of the deviation is in the same range for the chosen densities. The difference of the FERMI distribution and the renormalized distribution including the ground state correlations can best be seen in the absorption spectra, which will be shown in the next section.

5.5 Absorption spectra

Next, the influence of the ground state correlations (GSCs) on the absorption spectra is studied. Therefore, the microscopic polarization is calculated with Eq. (5.14). To observe the differences, the spectra without GSCs, that is, where the distributions $f_{\mathbf{k}}$ in Eq. (5.14) are approximated with FERMI functions $f^0_{\mathbf{k}}$ (no GSC), will be compared with the spectra obtained by including the corrected distributions $f_{\mathbf{k}} = f^0_{\mathbf{k}} + \delta f_{\mathbf{k}}$ (with GSC).

First, the density dependence is studied. Figure 5.9 shows the 5 nm ISB QW spectrum (with a gap energy of 210 meV) for three different doping densities $n_{\mathrm{d}} = 1.2 \cdot 10^{11}$ cm^{-2} (red lines), $n_{\mathrm{d}} = 6.0 \cdot 10^{11}$ cm^{-2} (green lines) and $n_{\mathrm{d}} = 1.2 \cdot 10^{12}$ cm^{-2} (blue lines) with a temperature of T = 1 K. The solid

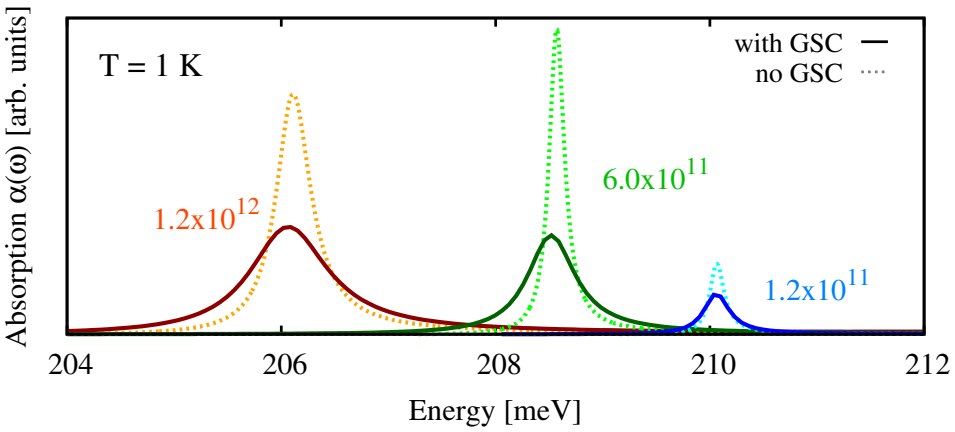

Figure 5.9 | ISB absorption spectrum of a 5 nm quantum well for a temperature of $T = 1$ K for different doping densities including (dark lines) and neglecting (light lines) the electronic ground state correlations (GSC).

dark lines are the spectra including GSCs, the spectra calculated without considering GSCs are drawn with light dotted lines. A strong shift to lower energies is visible for increasing densities. This is caused by the energetic renormalization resulting from the HARTREE-FOCK contributions [LN04, WFL$^+$04], since the exciton term leads to a smaller effective band gap between the lower and upper subband for a larger density difference between the two subbands. Comparing the spectra with and without GSCs, there is a strong broadening of the absorption line shape including GSCs compared to the spectrum neglecting GSCs. While for a doping density of $n_\mathrm{d} = 1.2 \cdot 10^{11}$ cm^{-2} (blue lines) the spectra including and neglecting GSCs differ by a factor two in the full width at half maximum (FWHM), for $n_\mathrm{d} = 6.0 \cdot 10^{11}$ cm^{-2} the FWHM of the spectra including GSCs (solid dark green line) is even three times larger than without GSCs (dotted light green line). This corroborates the argument that even small GSCs have a strong influence at low temperatures: Although the maximal change of the deviation $\delta f_\mathbf{k}$ from the FERMI function $f^0_\mathbf{k}$ for $T = 1$ K is only up to 3% around the FERMI edge, the absorption spectra show a considerable difference. This clearly demonstrates the new physical scenario if GSCs are included: The absorption line width increases due to the generation of available free(occupied) scattering states below(above) the FERMI edge, counteracting the strong PAULI blocking otherwise present for low temperatures. For the parameters used here, the difference between the absorption spectrum including and neglecting ground state correlations is maximal for a doping density of $n_\mathrm{d} = 6.0 \times 10^{11}\mathrm{cm}^{-2}$. Thus the following investigations will be restricted to a 5 nm quantum well with $n_\mathrm{d} = 6.0 \times 10^{11}\mathrm{cm}^{-2}$. But it is clear that the investigations are qualitatively similar for other carrier densities. Since there are only minor differences of the deviation $\delta f_\mathbf{k}$ for different well widths, the focus lies on a 5 nm ISB QW.

Next, the influence of the GSC on the spectra will be investigated for three different temperatures. Figure 5.10 shows the absorption spectra for the temperatures T = 1 K, 50 K and 100 K including GSCs (solid dark lines) and neglecting GSCs (dotted light lines). The absorption spectra for T=1 K correspond to the two absorption spectra in Fig. 5.9 in the middle (blue lines). A smaller energy and absorption range is shown in the inset of Fig. 5.10 to gain better insights into the absorption shapes for $T = 50$ K and 100 K. For increasing temperature, the correlation effects are of no significant relevance as discussed earlier in the temperature dependence of $\delta f_\mathbf{k}$. While the difference between the absorption spectra including (solid dark green line) and neglecting (dotted light green line) can be seen as a slight decrease of the maximum for $T = 50$ K, the difference for $T = 100$ K (see dotted and solid red lines in the inset) is hardly visible. Instead, nonparabolicity- and HARTREE-FOCK effects gain importance, leading to a shift of the maximum to lower energies for increasing temperature [WFL$^+$04].

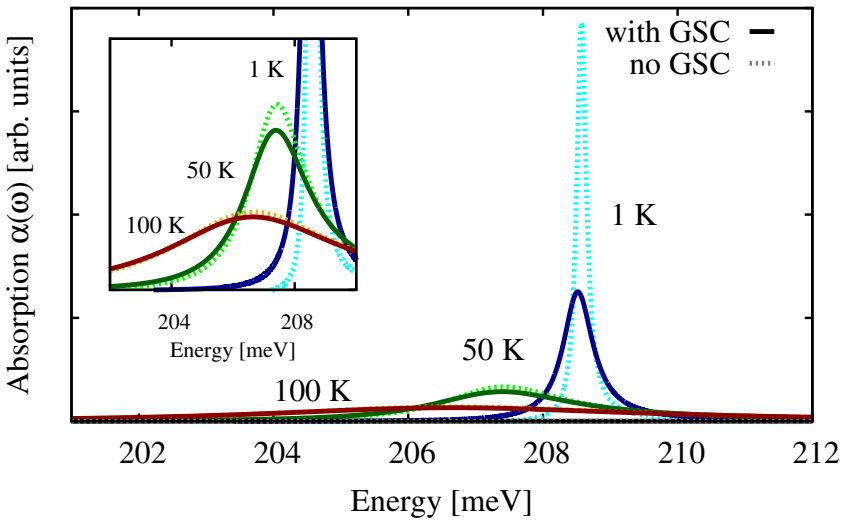

Figure 5.10 | ISB absorption spectrum of a 5 nm quantum well with $n_d = 6.0 \times 10^{11}$ cm^{-2} including (dark lines) and neglecting (light lines) the electronic ground state correlations (GSC) for different temperatures. Inset: Enlarged view of the absorption line shapes.

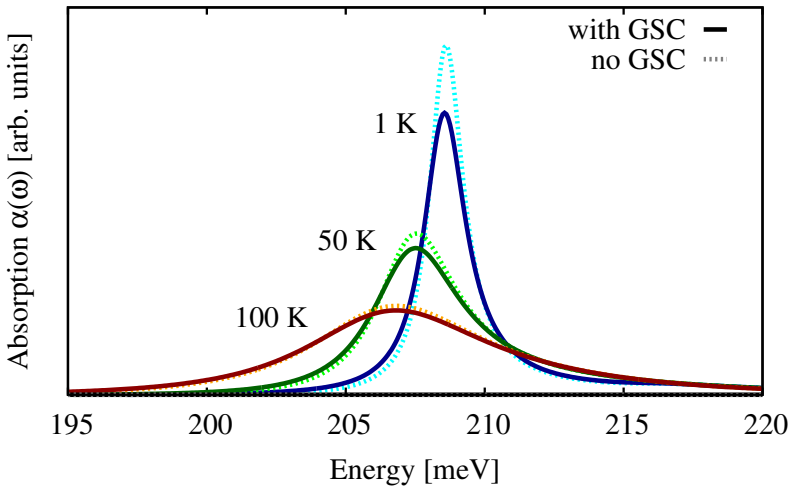

Figure 5.11 | ISB absorption spectrum of a 5 nm quantum well including (dark lines) and neglecting (light lines) the electronic ground state correlations (GSC), with microscopically calculated temperature-dependent Markovian *el-ph* scattering rates for a doping density $n_d = 6.0 \times 10^{11}$cm^{-2} for different temperatures.

The GSCs are visible as a significant broadening of the spectrum at low temperatures compared to the spectra neglecting GSCs. Still, the line width is yet strongly underestimated compared to experimental findings [Kai00, SRW$^+$05]. In order to include all important scattering processes which contribute to the absorption line shape, *el-ph* interaction should also be taken into account [LN04, WFL$^+$04]. This is assumed to be the major broadening mechanism for temperatures higher than T =100 K [BFWK04]. Even for low temperatures, spontaneous phonon emission yields a temperature-independent contribution to the line width. As a first approximation, microscopically calculated temperature-dependent

Markovian *el-ph* scattering rates are included as an additional constant dephasing contribution γ_{phon} [BFWK04]. Therefore the term $\frac{\mathrm{d}}{\mathrm{d}t} p_{12,\mathbf{k},s|\text{phonon}} = -\gamma_{\text{phon}} p_{12,\mathbf{k},s}$ is included in Eq. (5.14). The resulting calculated ISB absorption spectra are found in Fig. 5.11. The solid dark lines are calculated including GSC and the phenomenological dephasing of $\gamma_{\text{phon}} = 1/1000$ fs^{-1} while the light dotted spectra only include the dephasing contribution. Now, the influence of the GSCs is strongly masked by the phonon-induced dephasing. Still, a deviation between the absorption spectra neglecting ground state correlations (solid light line) and including ground state correlations (solid dark line) can be found for $T = 1$ K, where the spectra neglecting GSCs (dotted light blue line) show less broadening than the ones including GSCs (solid dark blue line). For T = 50 K and 100 K, the difference is hardly visible, comparable to the spectra in Fig. 5.10. Although the phonon dephasing masks the GSC induced broadening, it should be noted that a definite conclusion can only be made if the full *el-ph* scattering rates are taken into account [Wal04]: Since the *el-ph* rates also consist of multiple products of FERMI functions, the deviation could lead to a further broadening of the spectra if the *el-ph* scattering is treated consistently. This should be considered for future work on ISB spectra at low temperatures.

5.6 Conclusions

In conclusion, the linear optical properties of an intersubband quantum well system have been investigated with the focus on the COULOMB interaction. First, the free carrier dynamics was derived, revealing the asymmetric line shape for increasing temperature due to the nonparabolicity of the subbands. Then, the first- and second-order correlation terms of the microscopic polarization have been included and the different contributions of the HARTREE-FOCK terms and the BOLTZMANN terms have been discussed. In the next step, electronic ground state correlations were taken into account and their influence on the absorption spectra was investigated. The inclusion of ground state correlations leads to a significant broadening of the absorption line width for temperatures $T < 50$ K, where the full width at half maximum is increased by up to a factor three at T = 1 K. The addition of a phenomenological electron-phonon dephasing masks the impact of the ground state correlations on the spectral width. As an outlook, a more consistent treatment of both the electron-phonon- and electron-electron dephasing, including full non-Markovian effects [BK06], should be carried out to allow deeper insights into the influence of electronic ground state correlations on the system.

Chapter 6

Relaxation dynamics

In the previous chapter quantum wells (QWs) were investigated in the linear optics regime. Here, the carriers were in thermal equilibrium. Now, in this chapter the focus will shift to non-equilibrium dynamics. Under the influence of strong fields, electrons can be excited into higher momentum states. Subsequently, a redistribution of the carriers takes place via different many-particle interactions. The quantum kinetics responsible for this ultrafast relaxation have been investigated experimentally as well as theoretically in the last decades [BTR+95, ZWLF98, CAH+96]. In particular, it was found that the major relaxation mechanism in GaAs bulk semiconductors on short time scales is the scattering of electrons with LO phonons [SKM94].

This chapter will briefly revise the review the fundamental characteristics of quantum kinetic relaxation phenomena. The understanding of these fundamentals provides a basis for the discussion of more elaborate techniques to detect many-body interaction and relaxation phenomena presented in the next chapter, Chap. 7. More detailed investigations concerning electron-phonon (*el-ph*) relaxation processes can be found in e.g. [BFWK04, But07]. In order to theoretically describe relaxation processes, the equations of motion [EOMs] for the relevant microscopic quantities with focus on the electron-LO phonon (*el-LO*) interaction are derived in the next two sections. Subsequently, the dynamics will be investigated considering the relaxation within the subband (intrasubband relaxation) as well as between the two subbands (intersubband relaxation).

6.1 Equations of motion

The non-equilibrium dynamics in QWs is governed by the microscopic polarization $p_{ij,\mathbf{k}} = \langle \rho_{ij,\mathbf{k}} \rangle$ with $i \neq j$ and the occupation densities $f_{i,\mathbf{k}} = \langle \rho_{ii,\mathbf{k}} \rangle$. Their temporal evolution is obtained by evaluating the HEISENBERG EOM, Eq, (3.6). The system Hamiltonian consists of the free carrier kinetics, the electromagnetic interaction and the *el-LO* Hamiltonian:

$$\begin{aligned} -\imath\hbar\frac{\mathrm{d}}{\mathrm{d}t}\langle\hat{\rho}_{ij,\mathbf{k}}\rangle &= \langle\left[\hat{H}_{0,\mathrm{el}}+\hat{H}_{\mathrm{em}}+\hat{H}_{\text{el-ph}},\hat{a}^{\dagger}_{i\mathbf{k}}\hat{a}_{j\mathbf{k}}\right]\rangle \\ &= (\varepsilon_{i,\mathbf{k}}-\varepsilon_{j,\mathbf{k}})\langle\hat{\rho}_{ij,\mathbf{k}}\rangle - E(t)\left(\sum_{\alpha} d_{\alpha i}\langle\hat{\rho}_{\alpha j}\rangle - \sum_{\beta} d_{j\beta}\langle\hat{\rho}_{i\beta}\rangle\right) \\ &+ \sum_{o,\mathbf{q}}(g^{oi}_{\mathbf{q}}\sigma^{oj}_{\mathbf{k}+\mathbf{q}_{\parallel},\mathbf{q},\mathbf{k}} + g^{io*}_{\mathbf{q}}\sigma^{jo*}_{\mathbf{k},\mathbf{q},\mathbf{k}-\mathbf{q}_{\parallel}} - g^{jo}_{\mathbf{q}}\sigma^{io}_{\mathbf{k},\mathbf{q},\mathbf{k}-\mathbf{q}_{\parallel}} - g^{oj*}_{\mathbf{q}}\sigma^{oi*}_{\mathbf{k}+\mathbf{q}_{\parallel},\mathbf{q},\mathbf{k}}), \end{aligned} \tag{6.1}$$

with $i,j \in \{1,2\}$ and the expectation value of the phonon-assisted density matrix elements (PADs): $\sigma^{ij}_{\mathbf{k},\mathbf{q},\mathbf{k}'} = \langle\hat{a}^{\dagger}_{i,\mathbf{k}}\hat{b}_{\mathbf{q}}\hat{a}_{j,\mathbf{k}'}\rangle$ and $\sigma^{ij*}_{\mathbf{k},\mathbf{q},\mathbf{k}'} = \langle\hat{a}_{i,\mathbf{k}}\hat{b}_{\mathbf{q}}\hat{a}_{j,\mathbf{k}'}\rangle^* = \langle\hat{a}_{j,\mathbf{k}'}\hat{b}^{\dagger}_{q}\hat{a}_{i,\mathbf{k}}\rangle$. Note that while the momenta $\mathbf{k}$ and $\mathbf{k}'$ are two-dimensional, the LO phonon momentum $\mathbf{q}$ is three-dimensional. The two-dimensional in-plane projection of the LO phonon momentum is denoted as $\mathbf{q}_{\parallel}$. As already in previous chapters, the

one-particle expectation values $\langle\hat{\rho}_{ij,\mathbf{k}}\rangle$ couple to the two-particle PADs. The arising hierarchy problem is treated within the correlation expansion according to Sec. 4.3. Here, the occurring coherent term $\langle\hat{b}_{\mathbf{q}}^{(\dagger)}\rangle$ is neglected and the dynamics of the PADs correlation terms $\sigma^{ij}_{\mathbf{k},\mathbf{q},\mathbf{k}',\mathrm{corr}}$ are further derived:

$$\begin{aligned}
-\mathrm{i}\hbar\frac{\mathrm{d}}{\mathrm{d}t}\sigma^{ij}_{\mathbf{k},\mathbf{q},\mathbf{k}',\mathrm{corr}} &= (\varepsilon_{i,\mathbf{k}}-\varepsilon_{j,\mathbf{k}'}-\hbar\omega_{\mathrm{LO}}+\mathrm{i}\hbar\gamma_{\mathrm{LO}})\sigma^{ij}_{\mathbf{k},\mathbf{q},\mathbf{k}',\mathrm{corr}} \\
&\quad -\sum_{mo} g^{mo*}_{\mathbf{q}}\{(1+n_{\mathbf{q}})(\delta_{oj}-\langle\rho_{oj,\mathbf{k}'}\rangle)\langle\rho_{im,\mathbf{k}}\rangle - n_{\mathbf{q}}(\delta_{im}-\langle\rho_{im,\mathbf{k}}\rangle)\langle\rho_{oj,\mathbf{k}'}\rangle\}, \\
-\mathrm{i}\hbar\frac{\mathrm{d}}{\mathrm{d}t}\sigma^{ij*}_{\mathbf{k},\mathbf{q},\mathbf{k}',\mathrm{corr}} &= (\varepsilon_{j,\mathbf{k}}-\varepsilon_{i,\mathbf{k}'}+\hbar\omega_{\mathrm{LO}}+\mathrm{i}\hbar\gamma_{\mathrm{LO}})\sigma^{ij*}{}_{\mathbf{k},\mathbf{q},\mathbf{k}',\mathrm{corr}} \\
&\quad +\sum_{mo} g^{mo}_{\mathbf{q}}\{(1+n_{\mathbf{q}})(\delta_{jo}-\langle\rho_{jo,\mathbf{k}'}\rangle)\langle\rho_{mi,\mathbf{k}}\rangle - n_{\mathbf{q}}(\delta_{mi}-\langle\rho_{mi,\mathbf{k}}\rangle)\langle\rho_{jo,\mathbf{k}'}\rangle\}. \qquad (6.2)
\end{aligned}$$

To close the set of equations the occurring three-particle quantities have been expanded into products of single-particle quantities. In particular, the phonons are treated within a bath approximation and the Bose distribution function $\langle\hat{b}^{\dagger}_{\mathbf{q}}\hat{b}_{\mathbf{q}}\rangle = n_{\mathbf{q}}$ is introduced, see also in Sec. 4.3.2. A phenomenological dephasing γ_{LO} with $\hbar\gamma_{\mathrm{LO}} = 1$ meV has been included in the PADs, approximating higher-order *el-ph* correlations [SKM94, But07]. The explicit terms are given in App. B.2. The PADs consist of two parts: The first part describes the change of the electronic state under the emission of an LO phonon $[\propto (1+n_{\mathbf{q}})]$, while the second part describes the change under the absorption of an LO phonon $[\propto n_{\mathbf{q}}]$. With the set of EOMs closed, it is now possible to investigate the *el-ph* relaxation processes.

6.2 Phonon-induced relaxation

6.2.1 Intrasubband relaxation

First, only the dynamics in one subband, the upper band $f_{2,\mathbf{k}}$, is considered. The investigation will show, how a non-equilibrium carrier distribution will relax into a Fermi distribution by scattering with phonons, see Fig. 6.1. The model is then expanded in the next subsection, where the relaxation from the upper band $f_{2,\mathbf{k}}$ to the lower band $f_{1,\mathbf{k}}$ is included. For now, the EOMs simplify to the form

$$\begin{aligned}
-\mathrm{i}\hbar\frac{\mathrm{d}}{\mathrm{d}t}f_{2,\mathbf{k}} &= 2\sum_{\mathbf{q}} g^{22}_{\mathbf{q}}\mathrm{Re}\{\sigma^{22}_{\mathbf{k}+\mathbf{q}_{\parallel},\mathbf{q},\mathbf{k}} - \sigma^{22*}_{\mathbf{k},\mathbf{q},\mathbf{k}-\mathbf{q}_{\parallel}}\}, \\
-\mathrm{i}\hbar\dot{\sigma}^{22}_{\mathbf{k},\mathbf{q},\mathbf{k}'} &= (\varepsilon_{2,\mathbf{k}}-\varepsilon_{2,\mathbf{k}'}-\hbar\omega_{\mathrm{LO}}+\mathrm{i}\hbar\gamma_{\mathrm{LO}})\sigma^{22}_{\mathbf{k},\mathbf{q},\mathbf{k}'} \\
&\quad -g^{22*}_{\mathbf{q}}\{(1+n_{\mathbf{q}})(1-f_{2,\mathbf{k}'})f_{2,\mathbf{k}} - n_{\mathbf{q}}(1-f_{2,\mathbf{k}})f_{2,\mathbf{k}'}\}, \\
-\mathrm{i}\hbar\dot{\sigma}^{22*}_{\mathbf{k},\mathbf{q},\mathbf{k}'} &= (\varepsilon_{2,\mathbf{k}'}-\varepsilon_{2,\mathbf{k}}+\hbar\omega_{\mathrm{LO}}+\mathrm{i}\hbar\gamma_{\mathrm{LO}})\sigma^{22*}_{\mathbf{k},\mathbf{q},\mathbf{k}'} \\
&\quad -g^{22}_{\mathbf{q}}\{(1+n_{\mathbf{q}})(1-f_{2,\mathbf{k}})f_{2,\mathbf{k}'} - n_{\mathbf{q}}(1-f_{2,\mathbf{k}'})f_{2,\mathbf{k}}\}. \qquad (6.3)
\end{aligned}$$

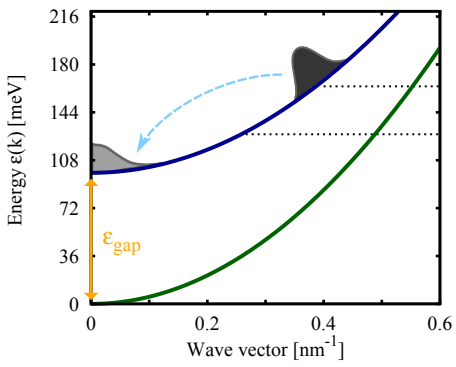

Figure 6.1 | Subband dispersion of the upper and lower subband. Shown is the relaxation process within the upper subband. Beginning from the initial Gaussian, the distribution relaxes towards the upper subband minimum. The dotted black lines are spaced with a distance of the LO phonon energy $\hbar\omega_{\mathrm{LO}} = 36$ meV.

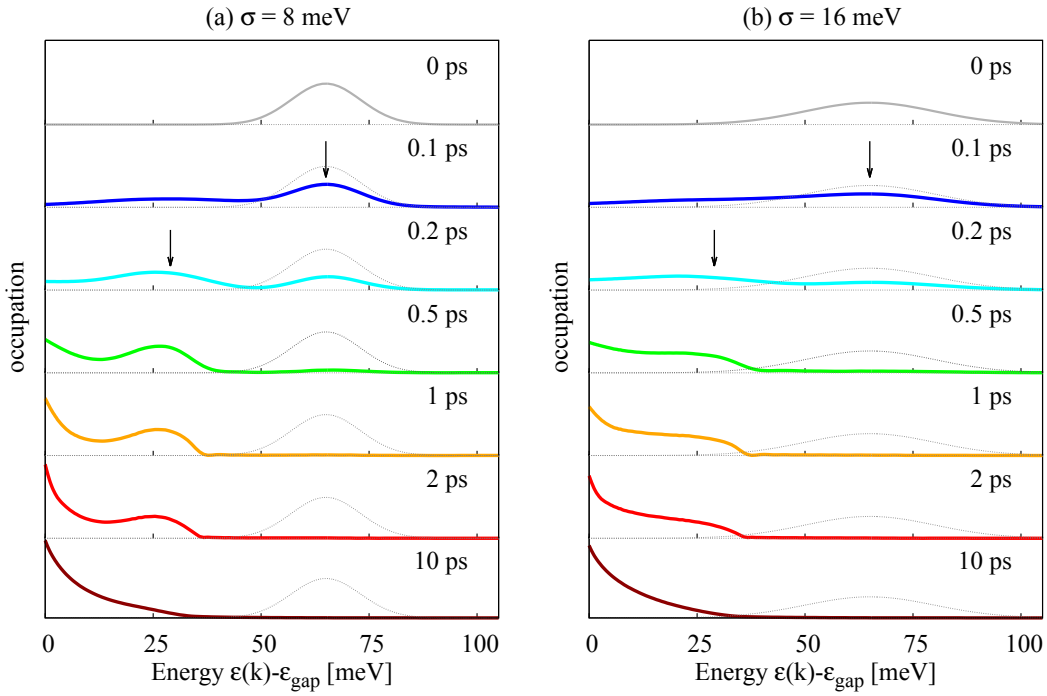

Figure 6.2 | Intrasubband relaxation under electron-phonon scattering of an initially Gaussian distribution (grey). The carrier density is $n_d = 5.0 \cdot 10^{10}$ cm^{-2} and the initial distribution has a standard deviation of (a) $\sigma = 8$ meV and (b) $\sigma = 15$ meV. The arrows are spaced with a distance of the LO phonon energy $\hbar\omega_{LO} = 36$ meV. The bath temperature is set to $T = 100$ K.

Figure 6.2(a) shows the angle integrated relaxation of an initially Gaussian distribution with a carrier density of $n_d = 5.0 \cdot 10^{10}$ cm^{-2} for increasing time from top to bottom. The Gaussian has a standard deviation of $\sigma = 8$ meV and is located 65 meV above the subband minimum. The LO phonon bath temperature is set to $T = 100$ K. For increasing time the carrier scatter towards the subband minimum. Within 10 ps the distribution has relaxed into the equilibrium FERMI distribution, where the system has reached the steady state and no further dynamics occur. A schematic drawing of the intrasubband relaxation process in the momentum space is shown in Fig. 6.1: Here, the upper subband dispersion (solid dark blue line) and the lower subband dispersion (solid dark green line) is plotted. Corresponding to the arrows in Fig. 6.2(a) which point to the phonon replica, their positions in the momentum space are displayed in Fig. 6.1 via the dotted black lines, which are spaced with one LO phonon energy.

Analysing the process in more detail, it can be seen that at 0.1 ps, the maximum is still centred around $\varepsilon(\mathbf{k}) = 65$ meV (see the black vertical arrow at 0.1 ps). Hundred femtoseconds later, the maximum of the distribution has shifted to $\varepsilon(\mathbf{k}) = 29$ meV (see the arrow at 0.2 ps). The energetic shift of the distribution corresponds to the LO phonon energy in GaAs ($\hbar\omega_{LO} = 36$ meV) and results from a phonon-assisted relaxation process: The electrons relax down to the subband minimum under emission of one LO phonon, indicated with the two arrows in Fig. 6.2(a), which are separated by one LO phonon energy. Due to renormalization effects [SKM94] the phonon replica sharpens around $\varepsilon(\mathbf{k}) = 29$ meV for increasing time until $t = 1$ ps . At the same time, the electrons scatter down to the subband minimum. However, the PADs not only include terms, where one electron scatters from momentum $\mathbf{k}$ to $\mathbf{k}'$ under LO phonon emission, but also terms accounting for a scattering from $\mathbf{k}'$ to $\mathbf{k}$ under LO phonon absorption.

In Fig. 6.2(b), the same relaxation process is shown for a broad initial distribution function, a Gaussian with a standard deviation of $\sigma = 15$ meV. The distribution also relaxes towards the subband mini-

mum. But due to the large spectral width of the initial distribution, the distribution is strongly broadened during the relaxation process and the phonon replica (indicated with the arrow at 29 meV) is hardly visible. Still, the relaxation down to the subband minimum follows the two-step LO phonon-induced relaxation, similar to the results in Fig. 6.2(a). After 10 ps, the distribution is fully located as a FERMI distribution around the subband minimum.

The final FERMI equilibrium function at the subband minimum is a result of the quantum kinetic treatment of the relaxation process: Under strict energy conservation, which would be obtained via the Born-Markov approximation, the relaxation into a FERMI function is impossible. On the other hand, if γ_{LO} is not included, the infinite memory of the system prohibits a relaxation into the FERMI distribution as well. By including γ_{LO}, the memory kernel can be truncated and the relaxation to a FERMI distribution becomes possible [But07].

6.2.2 Intersubband relaxation

Now, the full Eqs. (6.1) and (6.2) are taken into account and a more complex dynamics for the relaxation processes including two subbands occurs. Figure 6.3 depicts the involved *el-ph* scattering events: a non-equilibrium carrier distribution in the upper subband $f_{2,\mathbf{k}}$ will relax under phonon emission (i) within the upper band and (ii) into the lower subband $f_{1,\mathbf{k}}$, see black and grey arrows. For the simulation the initial distribution is again prepared as a Gaussian, located 65 meV above the upper subband minimum with a standard deviation of $\sigma = 8$ meV. The fundamental subband gap energy is set to $\varepsilon_{\mathrm{gap}} = 98.54$ meV, corresponding to a 10 nm QW.

The temporal evolution of (a)$f_{2,\mathbf{k}}$ and (b) $f_{1,\mathbf{k}}$ is displayed in Fig. 6.4 for increasing time from top to bottom. The relaxation process in the upper subband resembles the relaxation process for intrasubband scattering shown in Fig. 6.2(a) and reproduces the phonon replica at 29 meV [see the black arrows in (a)]. However, in contrast to the pure intraband relaxation of Fig. 6.2 a substantial occupation at the upper subband minimum never builds up, as carriers scatter from here into the lower subband.

Figure 6.4(b) displays the temporal evolution of the electron distribution in the lower subband. Here, the LO phonon induced relaxation shows a more complex structure, exhibiting multiple peaks during the intrasubband relaxation towards the lower subband minimum.

This behavior can be understood more clearly by looking at the subband structure of the lower and the upper subband, see Fig. 6.3. Starting point of the intersubband relaxation is the initial Gaussian distribution with the maximum 65 meV above the upper subband minimum (that is, 162 meV above the lower subband minimum). From here, electrons scatter from the upper to the lower subband under emission of one LO phonon with the constant energy of $\varepsilon_{\mathrm{LO}} = 36$ meV to a momentum corresponding to the energy of $\varepsilon(\mathbf{k}) = 125$ meV. This process is marked with the black diagonal arrow in Fig. 6.3 and corresponds to the increase of the population distribution $f_{1,\mathbf{k}}$ in Fig. 6.4(b) for 0.1 ps and 0.2 ps (see the black arrow for 0.2 ps). The successive relaxation under the emission of LO phonons towards the lower subband minimum is indicated with the black arrows in Fig. 6.4(b) from 0.2 ps to 2 ps. Analogous, the corresponding positions of the phonon replica in the momentum space are displayed in the subband

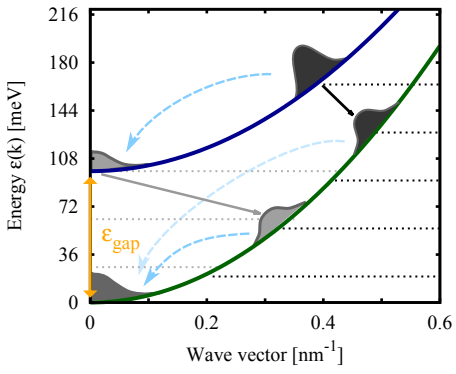

Figure 6.3 | The relaxation processes into the lower subband: The first intersubband process starts from the initial Gaussian, indicated with the black arrow. The second process originates from the distribution at the upper subband minimum (grey arrow). The dotted black and grey lines are spaced with a distance of the LO phonon energy $\hbar\omega_{\mathrm{LO}} = 36$ meV, respectively.

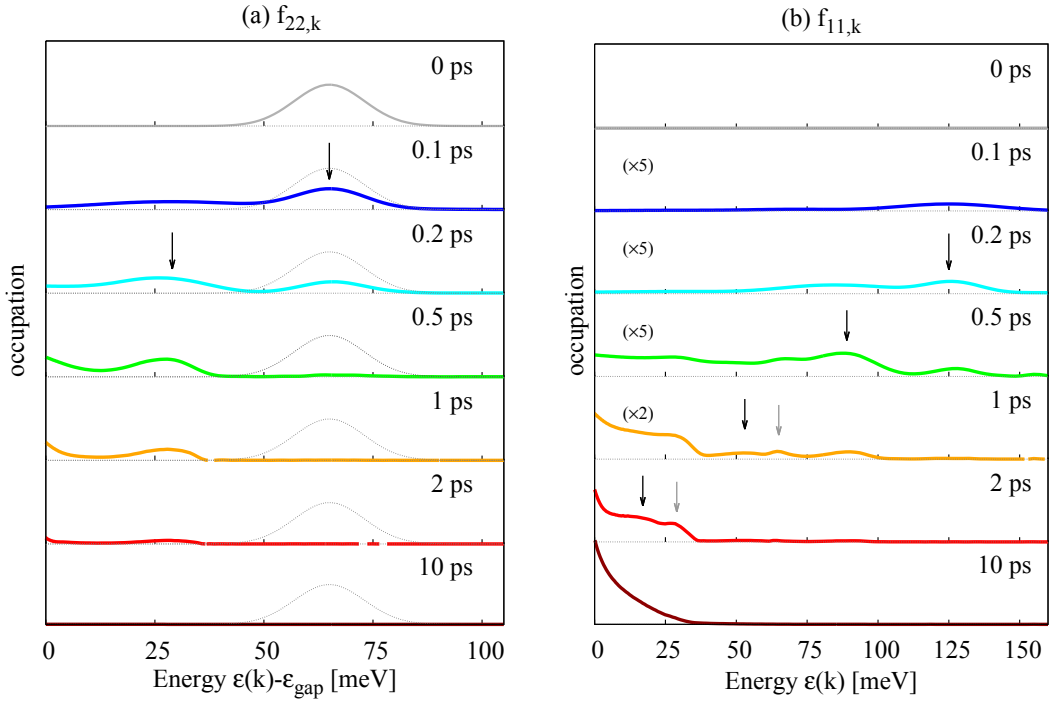

Figure 6.4 | Inter- and Intrasubband relaxation of an initially Gaussian distribution in the upper subband $f_{2,\mathbf{k}}$. The carrier density is $n_\mathrm{d} = 5.0 \cdot 10^{10}$ cm^{-2} and the initial distribution has a standard deviation of (a) $\sigma = 8$ meV. Shown is (a) the relaxation in the upper subband and (b) the dynamics in the lower subband. The black arrows are spaced with a distance of the LO phonon energy $\hbar\omega_\mathrm{LO} = 36$ meV. The grey arrows are also spaced with $\hbar\omega_\mathrm{LO} = 36$ meV. The bath temperature is set to $T = 100$ K.

scheme in Fig. 6.3 via the dotted black lines, which are spaced with one LO phonon energy.

Besides the phonon replica originating from the relaxation of the initial Gaussian distribution, other local maxima can be seen in the population distribution $f_{1,\mathbf{k}}$ in Fig. 6.4(b): For $t = 0.5$ ps [green line in (b)], another phonon replica begins to form up slightly below the main replica at 88 meV. For $t = 1$ ps, this local maximum at 62 meV is clearly visible (grey arrow pointing to the orange line) and arises from the intersubband scattering of the population distribution located at the upper subband minimum. The process is displayed in Fig. 6.3 as a grey diagonal arrow. Again, the successive intrasubband relaxation towards the lower subband minimum with the constant LO phonon energy is shown as dotted grey lines, respectively in Fig. 6.4(b) as grey arrows.

6.3 Conclusions

In conclusion, the relaxation processes under the influence of the electron-LO phonon interaction in an intersubband quantum well system have been investigated. It was demonstrated that the scattering with LO phonons leads to replica during the intrasubband relaxation. The spectral width of the replica depends on the width of the initial distribution. While for an initial Gaussian distribution with a standard deviation of $\sigma = 8$ meV the replica are clearly distinguishable, for $\sigma = 16$ meV the replica are broadened in such a way that they cannot be clearly determined. In addition to intrasubband processes, the electrons can also relax from the upper to the lower subband. Since the intersubband relaxation originates from various electrons in the upper subband, the distribution in the lower subband exhibits multiple phonon

replica, where the main down-scattering channel results from the initial Gaussian distribution at $\varepsilon(\mathbf{k}) - \varepsilon_{\mathrm{gap}} = 65$ meV and from the scattering around the upper subband minimum.

The next chapter will expand on the considerations and fundamental processes presented here. It will investigate a similar system but is focusing on how these relaxation processes can be measured in experiments using nonlinear optics. Therefore an elaborate framework is used to implement numerical simulations of such experiments. The insights into the electron-LO phonon scattering processes which have been provided this chapter will be valuable to interpret the results in Chap. 7.

Chapter 7

Two-dimensional spectroscopy on quantum well intersubband systems

Recapitulating the previous chapters it becomes clear that many-body interactions in quantum well ISB system are quite pronounced. The investigation of the electron-electron (*el-el*) and electron-phonon (*el-ph*) interaction in the linear regime is straight forward by using common absorption spectra: The sample is excited with a very weak pulse, which "probes" the system without changing the electronic distribution in either bands. For the detection of effects in the nonlinear regime, such as relaxation processes and dephasing times, the system must be strongly excited, that means the carrier distribution is in a non-equilibrium state. Since the dynamics and interactions in semiconductors take place on picosecond (ps) to femtosecond (fs) time scales, they can be tracked through a series of ultrafast pulses, Thus, a large variety of coherent spectroscopy schemes, for example, pump-probe or four wave mixing experiments, have been used to investigate complex many-body interactions in the nonlinear regime [AK04]. In standard transient experiments, the ultrafast dynamics are observed as a change of transmission or absorption [IKS$^+$00, WRW$^+$05, WRW$^+$06, KK06a], yielding indirect information about the electronic population at certain energies.

In the seventies a more complex access to the investigation of many-body correlations was developed in the nuclear magnetic resonance (NMR) [WE77]: The 2D NMR spectroscopy analyzes nuclei and other coupled spin systems such as molecules by detecting their change of magnetization. To extract different multiple quantum transitions (that is, pathways, which correspond to different physical or biological processes), the sample is excited with a pulse sequence, where in the experiment the time delays between the different pulses is varied. By FOURIER transformation (FT) of the time delays, more detailed information can be obtained about correlated frequencies [EBW98, Jon03]. It was not until twenty years later, with the development of ultra-short laser pulses [DJY$^+$00, BHS$^+$10], when this principle of the 2D FT spectroscopy could be transferred to electronic systems, whose interaction time scales lie in the ps to fs range. Since then, this method has already been applied to a wide range of biological systems and semiconductor nanostructures [TM93, KMCT07, KMS09, AM10, MR11, KRW$^+$11], giving access to detailed structural information and dynamics of these systems [BMSF04, Cho08, CZB$^+$09, MSN$^+$09, KGF$^+$10]. To demonstrate the potential of this method, the 2D FT spectroscopy will be applied to the quantum well ISB system with the focus on LO phonon induced relaxation, which has already been treated in the previous chapter. There, it has been shown that electron-LO phonon (*el-LO*) scattering processes lead to phonon replica during the relaxation of an excited electronic distribution. Yet, the question of appropriate detection schemes has been left unanswered.

The chapter is organized as follows: After giving an introductory example of a 2D FT spectrum in Sec. 7.1, the theoretical tools for a thorough understanding of the principles of the nonlinear optical spectroscopy are provided in Sec. 7.2. Here, it will be seen that the macroscopic polarization can be split into a sum of different quantum pathways, which correspond to different physical processes. To understand the meaning of these quantum pathways, the so-called double-sided FEYNMAN diagrams will be

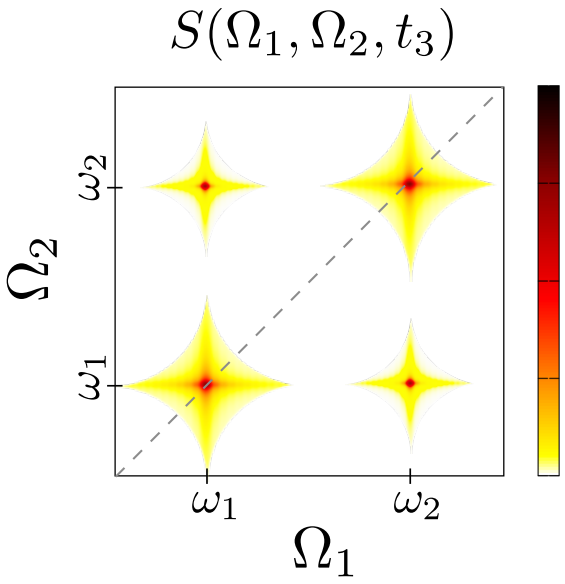

Figure 7.1 | Schematic 2D FT spectrum: The two frequency axes Ω_1 and Ω_2 are obtained via FOURIER transforming the delay times between the exciting pulses. Uncorrelated signals appear along the dashed line $\Omega_1 = \Omega_2$ (diagonal peaks) while correlations can be seen as off-diagonal elements (cross peaks).

introduced in Sec. 7.2.2. In Sec. 7.3, typical experimental setups for the detection and separation of the different outcoming signals will be recapitulated. In general, these setups enable the extraction of multiple quantum pathways, corresponding to different physical processes. Common experiments use a non-collinear setup, where incoming pulses propagate in different directions [KDT03a], detecting different signals via phase matching. Another approach is to use a collinear setup, where the superposed quantum pathways can be separated by the so-called *phase cycling* technique [SSD95, WSSD97, Tan08]. Here, the phases of the incoming time-ordered pulses are varied for each repetition of the experiment. When combining the outcoming response signals, multiple quantum pathways can be extracted, see Sec. 7.3.1. For the detection of the relaxation processes, the so-called *2D photon echo signal* will be introduced as the signal of choice in Sec. 7.4. Subsequently, its resulting spectra are interpreted in detail in the corresponding subsections Sec. 7.4.3 and Sec. 7.4.4. The main results of this chapter are published in [DWE+12].

7.1 Two-dimensional Fourier transform spectroscopy

In a 2D FT spectroscopy experiment, the sample is excited with a series of pulses with variable delay times t_i. To resolve correlations, at least two pulses must be applied, while for the detection of fully frequency resolved relaxation processes a three pulse sequence is needed [Jon03]. In general, the ability to distinguish different correlation processes increases with the number of pulses. When exciting the sample, the pulses induce a carrier coherence in the material. The resulting macroscopic polarization then emits a dipole field $S(t_i)$, which can be detected and visualized through a generic 2D FT spectrum, which shows the strength of a signal over two frequency axes. This is obtained by FOURIER transforming $S(t_i)$ with respect to two delay times, for example, $S(t_1,t_2,t_3) \rightarrow S(\Omega_1,\Omega_2,t_3)$. An exemplary contour plot of a 2D FT spectrum is shown in Fig. 7.1. The dashed line marks the diagonal $\Omega_1 = \Omega_2$ and the signal strength is indicated through the color bar.

The 2D spectrum immediately reveals correlated and uncorrelated processes: If the system is first excited with a frequency $\Omega_1 = \omega_1$, and the detected signal has the same frequency $\Omega_2 = \omega_1$ the system

is in the same state during the time duration t_3. Thus, lacking interaction or correlation processes, the signal will appear on the diagonal. But if a signal is excited with a frequency $\Omega_1 = \omega_1$ and the detection frequency differs from the excitation frequency (e.g. $\Omega_2 = \omega_2$) the system is in a new state, responding with a different frequency. In a 1D spectrum it is not possible to directly distinguish between correlated and uncorrelated processes since the signal along second axis Ω_1 is projected onto the Ω_2 axis. Thus a 2D spectrum can give additional information of the system, which will be explained in detail in the next sections.

In general, the signals shown in the 2D spectra do not correspond to the full material response, that is, the overall macroscopic polarization of the sample, but rather originate from selected *parts* of the polarization, here denoted as *directional polarizations*.[1] Each directional polarization contains different LIOUVILLE pathways and thus provides different informations about the sample. For a better understanding of these pathways, the macroscopic polarization P which has already been derived in Chap. 3 will be revisited in the following section.

7.2 Theoretical tools

7.2.1 The macroscopic polarization in the Liouville space

Starting from the expressions derived in Sec. 3.3, the macroscopic polarization $P(t)$ will be further evaluated. As stated, $P(t)$ can be written as a sum of n-order macroscopic polarizations, that is, $P(t) = \sum_n P^{(n)}(t)$, where the super-index (n) reflects the order of the electromagnetic field. For clarity, the expression for $P^{(n)}(t)$, Eq. (3.20), is recalled:

$$P^{(n)}(t) = \left(-\frac{\mathrm{i}}{\hbar}\right)^n \int_0^\infty \mathrm{d}\tau_n \int_0^\infty \mathrm{d}\tau_{n-1} \ldots \int_0^\infty \mathrm{d}\tau_1 \, S^{(n)}(\tau_n, \tau_{n-1}, \ldots, \tau_1) \times \\ E(t-\tau_n)E(t-\tau_n-\tau_{n-1})\ldots E(t-\tau_n-\ldots-t_1),$$

with the nth-order response function $S^{(n)}(\tau_n, \tau_{n-1}, \ldots, \tau_1)$:

$$S^{(n)}(\tau_n, \tau_{n-1}, \ldots, \tau_1) = \prod_i \Theta(\tau_i) \times \\ \langle \hat{\mu}_\mathrm{I}(\tau_n + \tau_{n-1} + \ldots + \tau_1) \left[\hat{\mu}_\mathrm{I}(\tau_{n-1} + \tau_{n-2} + \ldots + \tau_1), \left[\hat{\mu}_\mathrm{I}(\tau_{n-2} + \ldots + \tau_1), \ldots [\hat{\mu}_\mathrm{I}(0), \rho_\mathrm{I}(-\infty)]_- \ldots\right]_-\right]_- \rangle.$$

The nth-order response function $S^{(n)}$ has already been shortly discussed in Sec. 3.3: After the full evaluation of the commutators in $S^{(n)}$, each term corresponds to one LIOUVILLE pathway, which reflects the response of the sample due to different interactions with the fields.

To further examine the sample-field interaction, which is mainly expressed via the commutators of the dipole operator $\hat{\mu}_\mathrm{I}$ and the density operator ρ_I at a certain delay time τ_l, it is useful to switch into the LIOUVILLE space: The LIOUVILLE space provides a mathematical calculus for operators and enables a compact notation for interactions between operators. Here, so-called *super-operators* are defined as objects which act on the operators in the HILBERT space [FS90].[2] For example, defining the Liouvillian super-operator $\hat{\mathscr{L}}$ as taking the commutator with $\hat{H}$, the HEISENBERG EOM for an arbitrary operator $\hat{O}$ without explicit time dependence takes a compact form:

$$-i\hbar \frac{\mathrm{d}}{\mathrm{d}t}\hat{O} = \hat{\mathscr{L}}\hat{O} \quad \text{with} \quad \hat{\mathscr{L}}\hat{O} = \left[\hat{H}, \hat{O}\right]_- = \hat{H}\hat{O} - \hat{O}\hat{H}. \tag{7.1}$$

In order to find a more intuitive expression for the complicated form of $P^{(n)}$ the aim of this section is to describe the macroscopic polarization via the super-operators.

[1] This expression originates from the non-collinear spectroscopy setup, where different orders of the macroscopic polarization are detected in different directions, see also Sec. 7.3.

[2] For clarity, calligraphic letters are used for the super-operators.

Analogous to the interaction picture in Hilbert space (Sec. 3.1), the Liouvillian $\hat{\mathscr{L}}$ can be separated into an unperturbed, time-independent part and a small time-dependent perturbation accordingly: $\hat{\mathscr{L}} = \hat{\mathscr{L}}_0 + \hat{\mathscr{M}}(t)$. While $\hat{\mathscr{L}}_0$ acts as the commutator with the unperturbed system Hamiltonian $\hat{H}_0$, the perturbation Liouvillian $\hat{\mathscr{M}}(t)$ commutates with the dipole operator $\hat{\mu}$ and the respective electromagnetic field, i.e. $\hat{\mathscr{M}}(t)\hat{O} = E(t)\left[\hat{\mu}, \hat{O}\right]_-$, assumed as a small perturbation. Analogous to the time evolution operator $U(t,t_0)$, a unitary Liouvillian time evolution super-operator $\hat{\mathscr{U}}(t,t_0)$ can be defined as:

$$\hat{\mathscr{U}}(t,t_0)\hat{O} = \hat{U}(t,t_0)\hat{O}\hat{U}^\dagger(t,t_0) \quad \text{with} \quad \hat{\mathscr{U}}(t,t_0) = T_{\leftarrow} \mathrm{e}^{-\frac{\mathrm{i}}{\hbar}\hat{\mathscr{L}}_0(t-t_0)}. \tag{7.2}$$

The time evolution operator in the interaction picture $\hat{U}(t,t_0)$ evolves with respect to the unperturbed Hamiltonian and has already been defined in Eq. (3.7). Correspondingly, $\hat{\mathscr{U}}(t,t_0)$ in Eq. (7.2) is driven by $\hat{\mathscr{L}}_0$. With the help of the super-operators, the equation for the nth-order macroscopic polarization, Eq. (3.20), reads:

$$\begin{aligned} P^{(n)}(\tau_n, \tau_{n-1}, \ldots, \tau_1) = \left(-\frac{\mathrm{i}}{\hbar}\right)^n \int_0^\infty \mathrm{d}\tau_n \int_0^\infty \mathrm{d}\tau_{n-1} \ldots \int_0^\infty \mathrm{d}\tau_1 \times \\ \prod_i \Theta(\tau_i) \langle \hat{\mu}_\mathrm{I}(\tau_n + \ldots + \tau_1) \hat{\mathscr{M}}_\mathrm{I}(\tau_{n-1} + \ldots + \tau_1) \ldots \hat{\mathscr{M}}_\mathrm{I}(\tau_1) \hat{\mathscr{M}}_\mathrm{I}(0) \hat{\rho}_\mathrm{I}(-\infty) \rangle. \end{aligned} \tag{7.3}$$

Note that here, the electromagnetic fields $E(\tau_i)$ are contained in $\hat{\mathscr{M}}(\tau_i)$. Recalling the transformation rule for an operator $\hat{O}$ from the SCHRÖDINGER picture into the interaction picture [Eq. (3.9)], the corresponding expression in LIOUVILLE space is: $\hat{O}_\mathrm{I}(t) = \hat{\mathscr{U}}^\dagger(t,t_0)\hat{O}(t_0)$, whereas the perturbation Liouvillian in the interaction picture is transformed into the SCHRÖDINGER picture via $\hat{\mathscr{M}}_\mathrm{I}(t) = \hat{\mathscr{U}}^\dagger(t,t_0)\hat{\mathscr{M}}\hat{\mathscr{U}}(t,t_0)$. Using this rule, the interaction (super-) operators of Eq. (7.3) can be written in the SCHRÖDINGER description, where $P^{(n)}$ obtains its final description in LIOUVILLE space:

$$\begin{aligned} P^{(n)}(\tau_n, \tau_{n-1}, \ldots, \tau_1) = \left(-\frac{\mathrm{i}}{\hbar}\right)^n \int_0^\infty \mathrm{d}\tau_n \int_0^\infty \mathrm{d}\tau_{n-1} \ldots \int_0^\infty \mathrm{d}\tau_1 \prod_i \Theta(\tau_i) \times \\ \langle \hat{\mu} \hat{\mathscr{U}}(\Delta\tau_{n,n-1}) \hat{\mathscr{M}}(\tau_{n-1}) \hat{\mathscr{U}}(\Delta\tau_{n-1,n-2}) \ldots \\ \ldots \hat{\mathscr{U}}(\Delta\tau_{2,1}) \hat{\mathscr{M}}(\tau_1) \hat{\mathscr{U}}(\Delta\tau_{1,0}) \hat{\mathscr{M}}(0) \hat{\mathscr{U}}(\Delta\tau_{0,-\infty}) \hat{\rho}(-\infty) \rangle, \end{aligned} \tag{7.4}$$

with $\hat{\mathscr{U}}(\Delta\tau_{k,k-1}) = \hat{\mathscr{U}}(\tau_k + \tau_{k-1} + \ldots + \tau_1, \tau_{k-1} + \ldots + \tau_1)$. For obtaining Eq. (7.4), the algebra of the time evolution super-operator have been used, i.e. $\hat{\mathscr{U}}(\tau_k + \tau_{k-1}, \tau_1)\hat{\mathscr{U}}^\dagger(\tau_{k-1}, \tau_1) = \hat{\mathscr{U}}(\Delta\tau_{k,k-1})$. Using the LIOUVILLE super-operators, the time-ordered interaction mechanisms on the density operator $\hat{\rho}(-\infty)$ can be "read" directly from right to left in Eq. (7.4): Being in equilibrium for the initial time $t = -\infty$, the system interacts with the first perturbation at $t = 0$ via the dipole super-operator $\hat{\mathscr{M}}(0)$. After the interaction, the system evolves freely with the time evolution operator $\hat{\mathscr{U}}(\Delta\tau_{1,0})$ within the delay time τ_1. Then, after τ_1, the second interaction with $\hat{\mathscr{M}}(\tau_1)$ occurs. Afterwards, the system again evolves freely with the time evolution operator $\hat{\mathscr{U}}(\Delta\tau_{2,1})$ within the delay time τ_2 and so forth.

Corresponding to the description above, one can visualize Eq. (7.4) in a diagrammatic way with the help of the double-sided FEYNMAN diagrams. The rules for constructing the diagrams will be given in the next subsection.

7.2.2 Double-sided Feynman diagrams

The double-sided FEYNMAN diagrams are the visual analogue to "reading" Eq. (7.4) from right to left, given in Fig. 7.2(a): While the time in the equation increases from right to left, the time development

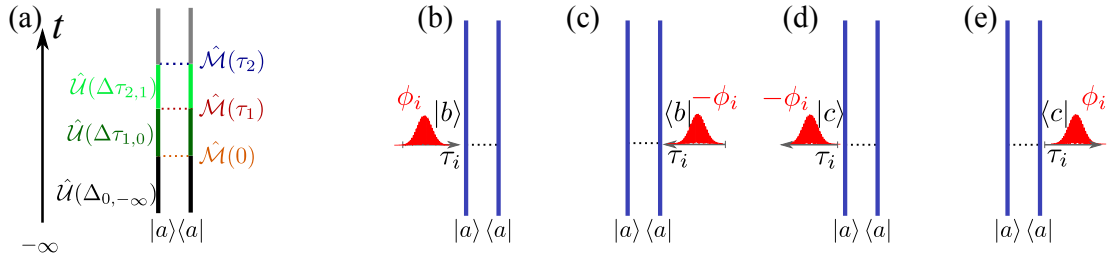

Figure 7.2 | (a) Double-sided Feynman diagram of a system which is perturbed by $\hat{\mathcal{M}}$ at different delay times $\sum_i \tau_i$. The vertical lines represent the time evolution from bottom to top. (b)-(e) The double-sided Feynman diagrams for a system interacting with one incoming electromagnetic field, drawn as a horizontal arrow. Four different interactions are possible.

in the diagram is drawn from bottom to top. Starting point of the diagram is the initial system in equilibrium at $t = -\infty$, where $|a\rangle$ is the equilibrium ket state and $\langle a|$ its Hermitian conjugate. The time evolution of the system, determined by the time evolution super-operator $\hat{\mathcal{U}}$, is symbolized with two vertical lines [the two lines arise from the fact that in the HILBERT space $\hat{\mathcal{U}}$ corresponds to two time evolution operators, see Eq. (7.2)]. The horizontal dotted lines mark the time point where the system is perturbed. Hence, one can fully recover the description of the previous subsection in Fig. 7.2(a): At the bottom is the equilibrium state $|a\rangle\langle a|$. The first time evolution super-operator $\hat{\mathcal{U}}(\Delta\tau_{0,-\infty})$ which propagates the initial system is given by the two black lines at the bottom. The first perturbation at $t = 0$ with $\hat{\mathcal{M}}(0)$ (yellow colored) corresponds to the first horizontal dotted line. Then, the consecutive time propagation $\hat{\mathcal{U}}(\Delta\tau_{1,0})$ during τ_1 is given by the dark green lines. Consequently, the second perturbation after τ_1 follows with $\hat{\mathcal{M}}(\tau_1)$ (red colored) and so forth. For clarity, the lines in Fig. 7.2(a) have been drawn with different colors, but in general, the lines have the same color.

The perturbation can be further specified, since the interaction with electromagnetic pulses is regarded. For simplicity, it is assumed that the incoming field $E(t)$ can be cast into two oppositely rotating parts, centred at the delay time τ_i : $E(t) = \tilde{E}(t-\tau_i)\mathrm{e}^{-\mathrm{i}[\omega_i(t-\tau_i)-\phi_i]} + \text{c.c.}$. The carrier frequency ω_i is considered to be in resonance with the system. The super-operator $\hat{\mathcal{M}}$ and hence the incoming electromagnetic field can either interact with the bra or the ket in the expectation value of $P^{(n)}$, changing the state of the system. The field perturbation is drawn as a horizontal arrow. Hereby, the incoming field interacts with the system in different ways: If the arrow points towards the vertical line, the initial state $|a\rangle\,(\langle a|)$ changes into a higher excited state $|b\rangle\,(\langle b|)$, see Fig. 7.2(b), (c). An arrow pointing away from the vertical line makes a transition to a lower excited state $|c\rangle\,(\langle c|)$, Fig. 7.2(d), (e). If the arrow points to the right (and is marked with the positive phase ϕ_i), the density operator interacts with the first term of the electromagnetic field $\tilde{E}(t-\tau_i)\mathrm{e}^{-\mathrm{i}\omega_i(t-\tau_i)+\mathrm{i}\phi_i}$, see Fig. 7.2(b), (d), while pointing to the left (and marked with the positive phase ϕ_i) indicates the interaction with the complex conjugate part $\tilde{E}(t-\tau_i)\mathrm{e}^{\mathrm{i}\omega_i(t-\tau_i)-\mathrm{i}\phi_i}$, see Fig. 7.2(c), (e). Thus, there exist four diagrams for the interaction of the system with one incoming electromagnetic pulse.[3] After interacting with all pulses, the density operator (that is, the ket and the bra) must be in the same state. Otherwise the expectation value is zero.[4] The overall sign of the double-sided Feynman diagrams correspond to $(-1)^n$, where n is the number of interactions on the bra. A detailed description for the application of double-sided FEYNMAN diagrams is given in Ref. [APV+09, Muk95].

The double sided FEYNMAN diagrams can now be used to interpret the different pathways without explicitly calculating the whole macroscopic polarization $P(t)$. This is of a great advantage especially if the investigations are concentrated on certain physical processes and hence on a small subset of all possible LIOUVILLE pathways. For the purpose of this chapter, where its aim is the resolution of

[3] For obtaining the four diagrams, the rotating wave approximation has been applied, that is off-resonant processes were neglected.

[4] In general, the last interaction, originating from the dipole operator $\hat{\mu}$ brings the system back into a diagonal state. Since this transition is not due to an incoming pulses, this interaction is marked with a different color, see Fig. 7.6.

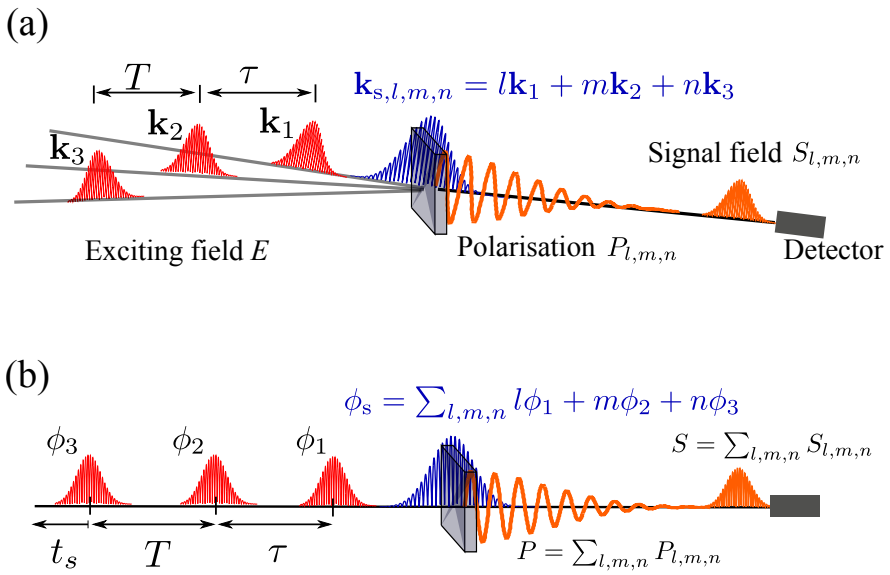

Figure 7.3 | (a) Non-collinear pulse setup: The exciting incoming pulses and the signal radiate in different directions $\mathbf{k}_i$. The different orders of the field interaction are spatially separated. (b) Collinear pulse setup: The incoming pulses propagate in the same direction, but differ in their phases ϕ_i. Consequently, the detected signal is a superposition of all interactions with the pulses. The resulting polarization P contains multiple orders of the field interaction.

relaxation processes, the pathways will be selected which contribute to the so-called *2D photon echo* signal. The corresponding FEYNMAN diagrams are given in Sec. 7.4. But before investigating the 2D photon echo signal in detail, the two most common experimental schemes for the extraction of the LIOUVILLE pathways will be explained in the following section.

7.3 Experimental detection schemes

The most prevailed geometric detection scheme is a non-collinear setup where the three pulses of a sequence come from different directions but still excite the sample at the same point [BMSF04]. The incoming electromagnetic field pulse sequence [TKSW03] is:

$$E(t) = \sum_{n=1}^{3} E_n(t) = \frac{1}{2}\sum_{n=1}^{3} \tilde{E}(t-\tau_n)\mathrm{e}^{-\mathrm{i}[\omega_n(t-\tau_n)-\phi_n]} + \text{c.c.}. \tag{7.5}$$

Here, the Gaussian envelope function $\tilde{E}(t-\tau_n) = A_0/\sigma \exp[-(t-\tau_n)^2/2\sigma^2]$ is centred around τ_n, the carrier frequencies ω_n and the phases $\phi_n = \mathbf{k}_n \cdot \mathbf{r}$. Since the 2D FT spectra show the FOURIER transform of the delay times, the electric field is rewritten as a function with respect to the different delay times between the pulses: $E(t) \to E(\tau, T, t_s)$, with $\tau = \tau_2 - \tau_1$, $T = \tau_3 - \tau_2$, $t_s = \tau_s - \tau_3$ [KT01, YT09].

The first and the second pulse are separated by the delay time τ, the second and third one by the waiting time T. The time after the third incoming pulse is denoted as the signal time t_s. A schematic of the non-collinear setup is given in 7.3(a). The pulse excitation induces a directional polarization $\mathbf{P}_{l,m,n}(t)$ of the sample, which radiates multiple signal fields $S_{l,m,n}$ in different directions $\mathbf{k}_s = l\mathbf{k}_1 + m\mathbf{k}_2 + n\mathbf{k}_3$, which is advantageous for the detection of the signal.

In another setup, the so-called collinear setup, the pulses propagate in the same direction. To experimentally distinguish the pulses, they are marked with different phases ϕ_n. The outcoming signal field is an overlay of all signals $\phi_s = \sum_{l,m,n} l\phi_1 + m\phi_2 + n\phi_3$ and consequently cannot be spatially separated.

Hence, the macroscopic polarization P and also the signal S are a superposition of all directional values: $(P/S) = \sum_{l,m,n}(P/S)_{l,m,n}$. In both setups it is common to apply a phase sensitive (heterodyne) detection scheme since the phase gives additional information about the system. Hence a local oscillator pulse E_{loc} is added to the fields in Eq. (7.5), allowing to separate the real and imaginary part of the signal [LCJ95]. By superposing the local oscillator with the outcoming polarization of the sample, an intensity can be measured which depends on the phase between E_{loc} and $P_{(l,m,n)}(t)$. Hence, by successively varying the phase of E_{loc}, the phase of the signal can be determined. The heterodyne signal S (respectively $S_{l,m,n}$) is then given by [APV+09]:

$$S_{(l,m,n)}(\tau,T,t_{\mathrm{s}}) = \int_{-\infty}^{\infty} \mathrm{d}t\, P_{(l,m,n)}(t) E^{*}_{\mathrm{loc}}(t-\tau_s)\mathrm{e}^{i\omega_s(t-\tau_s)}, \tag{7.6}$$

with E_{loc} at the signal time τ_s, the frequency ω_s and the emitted nonlinear polarization $P(t)$ (respectively $P_{l,m,n}(t)$).

As indicated in Fig. 7.3, the signal field can consist of multiple combinations of $l\mathbf{k}_1$, $m\mathbf{k}_2$ and $n\mathbf{k}_3$ or $l\phi_1$, $m\phi_2$, $n\phi_3$, respectively. These combinations originate from different orders of interaction with the incoming pulse sequence, where the sum of the absolute values of $l,m,n \in \mathbb{Z}$ display the least order of interaction with the respective pulses. Hence the sub-indices of $P_{l,m,n}$ reflect the order n of the directional polarization, for example, $P_{2,0,-1}(t)$ is at least enclosed in the third-order polarization $P^{(3)}$, since $|2|+|0|+|-1| = 3$. Each combination contains different sets of LIOUVILLE pathways, whose number of terms strongly increase with the order of the macroscopic polarization. Thus, it is desirable to reduce the number of pathways.

The simplest way to restrict the polarization to a certain order is by choosing a certain electromagnetic field strength. For the following investigations, it is sufficient to investigate the polarization until third-order $P^{(3)}(t)$. The corresponding equation in the LIOUVILLE formalism reads:

$$\begin{aligned} P^{(3)}(\tau_3,\tau_2,\tau_1) = \left(-\frac{\mathbb{i}}{\hbar}\right)^3 \int_0^{\infty}\mathrm{d}\tau_3 \int_0^{\infty}\mathrm{d}\tau_3 \int_0^{\infty}\mathrm{d}\tau_1 \prod_{i=1}^{3}\Theta(\tau_i)\times \\ \langle \hat{\mu}\hat{\mathscr{U}}(\Delta\tau_{3,2})\hat{\mathscr{M}}(\tau_2)\hat{\mathscr{U}}(\Delta\tau_{2,1})\hat{\mathscr{M}}(\tau_1)\hat{\mathscr{U}}(\Delta\tau_{1,0})\hat{\mathscr{M}}(0)\hat{\mathscr{U}}(\Delta\tau_{0,-\infty})\hat{\rho}(-\infty)\rangle, \end{aligned} \tag{7.7}$$

The evaluated third-order polarization consists of more than 800 terms,[5] that is, LIOUVILLE pathways, which represent different interactions of the sample with the pulse sequence. To further restrict the number of pathways of $P^{(3)}(t)$, time ordering is considered. This means that the incoming pulses are ordered in time and assumed to not overlap in the time domain, which corresponds to a small standard deviation of the envelope pulses $E(t-\tau_n)$ of the exciting pulse sequence in Eq. (7.5). This considerably reduces the number of pathways to 32 since the time-ordered fields consist of two terms.

Considering the collinear setup, the question arises how the directional polarizations can be selectively detected, since they propagate in the same direction. Here, to separate the signals, a technique called *phase cycling* (PC) is applied. This - at first sight more cumbersome - detection scheme has the advantage that the collinear phase cycling is not restricted by the size of the sample and that the amount of required data can be considerably reduced [TKSW03]. The details of the PC technique will be explained in the following section.

7.3.1 Phase cycling

As already discussed in Sec. 7.3, the directional polarizations $P_{l,m,n}$ can be automatically selected in a non-collinear setup through phase matching, while in a collinear setup, where the directional polarizations all propagate in the same direction, see also Fig. 7.3(b). Compared to the theoretical framework, the collinear setup corresponds to the derivation of the macroscopic polarization via the HEISENBERG

[5] One can verify it by inserting the pulse sequence in Eq.(7.5), which consists of six terms, into Eq.(7.7): Evaluating the commutator in Eq.(7.7), which lies in the super-operator $\hat{\mathscr{M}}$, there are eight terms. Since four terms are the conjugate complex of the other four terms, that is, correspond to the same physical processes, four terms remain. Multiplying these terms with the electromagnetic fields, where each one consists of six terms, equals $6\cdot6\cdot6\cdot4 = 864$ terms.

EOM, since here the resulting polarization contains all directional polarizations as well. Hence, to extract the directional polarizations in the collinear setup and in the numerics, phase cycling must be applied. The corresponding procedure is as follows: To select one specific directional polarization, the sample must be excited with a series of pulse sequences with different sets of phases on the three exciting pulses $\Phi_s = (\phi_{1s}, \phi_{2s}, \phi_{3s})$.

The overall nonlinear polarization $P(\tilde{t})$ ($\tilde{t} := \tau, T, t_s$), can be written as a superposition of all directional polarizations $P_{l,m,n}(\tilde{t})$ in the following way [ME00]:

$$\begin{aligned} P(\tilde{t}, \phi_1, \phi_2, \phi_3) &= \sum_{l,m,n} P_{l,m,n}(\tilde{t}) \mathrm{e}^{i(l\phi_1 + m\phi_2 + n\phi_3)} + \text{c.c.} \\ &= \mathscr{P}(\tilde{t}, \phi_1, \phi_2, \phi_3) + \mathscr{P}^*(\tilde{t}, \phi_1, \phi_2, \phi_3), \end{aligned} \tag{7.8}$$

with the particular phases of ϕ_i originating from the exciting three pulse sequence, see Fig. 7.3(b). The idea is now to create a system of N linearly independent equations for Eq. (7.8), with the number N of all possible combinations of l, m, n, which corresponds to repeating the experiment N-times. Hence, to retain the linear independence of the equations in Eq. (7.8), the set of phase combinations $\Phi_s = (\phi_{1s}, \phi_{2s}, \phi_{3s})$ must be varied for each experiment. The first index of ϕ_{is} indicates the phase of the ith pulse E_i and the second index denotes the s-th experiment. The N linear equations read:

$$\begin{aligned} \mathscr{P}(\tilde{t}, \Phi_1) &= \sum_{\{l,m,n\}=1}^{N} P_{l,m,n}(\tilde{t}) \mathrm{e}^{\mathrm{i}(l\phi_{11} + m\phi_{21} + n\phi_{31})} \\ \mathscr{P}(\tilde{t}, \Phi_2) &= \sum_{\{l,m,n\}=1}^{N} P_{l,m,n}(\tilde{t}) \mathrm{e}^{\mathrm{i}(l\phi_{12} + m\phi_{22} + n\phi_{32})} \\ &\vdots \end{aligned} \tag{7.9}$$

$$\mathscr{P}(\tilde{t}, \Phi_N) = \sum_{\{l,m,n\}=1}^{N} P_{l,m,n}(\tilde{t}) \mathrm{e}^{\mathrm{i}(l\phi_{13} + m\phi_{23} + n\phi_{33})} \tag{7.10}$$

For clarity, it is sufficient to display the unconjugated, positive part of the polarization $\mathscr{P}$. Using the abbreviation $c_{s,u} = \mathrm{e}^{\mathrm{i}\Phi_s \cdot \mathbf{u}}$ with $\mathbf{u} = (l, m, n)^T$ and $\Phi_s = (\phi_{1s}, \phi_{2s}, \phi_{3s})^{\mathrm{T}}$, the set of equations in Eq. (7.10) can be cast into a matrix [ME00]:

$$\begin{pmatrix} c_{1,1} & c_{1,2} & \dots & c_{1,N} \\ c_{2,1} & c_{2,2} & \dots & c_{2,N} \\ \vdots & \vdots & \ddots & \vdots \\ c_{N,1} & c_{N,2} & \dots & c_{N,N} \end{pmatrix} \begin{pmatrix} P_{\{1\}}(\tilde{t}) \\ P_{\{2\}}(\tilde{t}) \\ \dots \\ \dots \\ P_{\{N\}}(\tilde{t}) \end{pmatrix} = \begin{pmatrix} \mathscr{P}(\tilde{t}, \Phi_1) \\ \mathscr{P}(\tilde{t}, \Phi_2) \\ \dots \\ \dots \\ \mathscr{P}(\tilde{t}, \Phi_N) \end{pmatrix}, \tag{7.11}$$

where $\{u\}$ in $P_{\{u\}}$ is a specific combination of l, m, n. The combination of phases Φ_s can be chosen arbitrarily under the prerequisite that the determinant of the matrix in Eq. (7.11) must not be zero. By inverting the matrix in Eq. (7.11), the directional polarizations can now be expressed as a linear combination of the phase-dependent macroscopic polarizations:

$$P_{l,m,n}(\tilde{t}) = \sum_{i=1}^{N} c^*_{i,\{l,m,n\}} \mathscr{P}(\tilde{t}, \Phi_i), \tag{7.12}$$

with the elements of the inverted matrix $c^*_{i,\{l,m,n\}}$. The number of possible combinations N is limited by the respective orders in the excitation fields E_n. As within this thesis the response is restricted to the third-order. Furthermore, if the dipole selection rules of our system are regarded, interactions of even order vanish, that is, $P^{(0)} = P^{(2)} = 0$. This leads to 22 combinations of $\{l, m, n\}$, which are given in App. C. Accordingly, 22 sets of phase combinations are needed. One possible choice for sets of phase

s	1	2	3	4	5	6	7	8	9	10	11
ϕ_{1s}	0	0	0.5	0.5	1	1	1.5	0	0	0.5	1.5
ϕ_{2s}	0	0	0	0	0	0	0	0	0	0	0
ϕ_{3s}	0	0.5	1	0.5	0	0.5	1.5	1.5	1	1.5	1

s	12	13	14	15	16	17	18	19	20	21	22
ϕ_{1s}	1.5	0	0	0.5	1	1	1.5	0	0	0.5	1.5
ϕ_{2s}	0	1.5	0.5	0.5	0.5	0.5	0.5	0.5	0.5	0.5	0.5
ϕ_{3s}	0.5	0	0.5	1	0	0.5	1.5	1.5	1	1.5	1

Table 7.1 | One possible choice for the set of phase combinations of the exciting field (to be multiplied by π).

combinations is presented in Table 7.1. They are also used for the calculations of the following 2D spectra. The resulting inverse of the matrix is given in App. C. As shown in Eq. (7.12), the directional polarizations $P_{l,m,n}$ consist of different linear combinations of $P(\tilde{t},\Phi_i)$, with the analytically calculated prefactors $c^*_{i,\{l,m,n\}}$. Hence, if all macroscopic polarizations $P(\tilde{t},\Phi_i)$ are recorded, all 22 directional polarizations can be calculated at once through phase cycling and the corresponding 2D can then be obtained by FOURIER transformation of two delay times.

Fig. 7.4 shows four 2D spectra of a two-level system (2LS), obtained by the same numerical (or experimental) set according to Table (7.1). In Fig. 7.4 top left, the 2D FOURIER transformation of the overall macroscopic polarization with a phase set of $\Phi = \{0,0,0\}$ (i.e. without PC) is given. Clockwise displayed are other exemplary spectra of the FOURIER transformed directional third-order polarizations $P_{1,-1,1}(\tau,T=0,t_s)$, $P_{-1,1,1}(\tau,T=0,t_s)$ and $P_{1,1,-1}(\tau,T=0,t_s)$. All spectra are FOURIER transformed with respect to the delay times τ and t_s. The choice of these distinct delay times will be explained in the next section. The different prefactors $c^*_{i,\{l,m,n\}}$, needed for the construction of the corresponding combination of $\{l,m,n\}$, can be found with the matrix in App. C. For the 2D spectra in Fig. 7.4, the system has been excited with spectrally broad 0.1π pulses with a standard deviation of $\sigma = 20$ fs. The gap energy has been set to $\varepsilon_{\text{gap}} = 98.54$ meV. The comparison between the 2D spectrum of the overall polarization and the spectra obtained with PC shows that the signatures of the directional third-order polarizations cannot be resolved within the overall 2D spectrum, since the strength of third-order signals is considerably weaker then the overall signal. Thus, the PC technique enables the extraction of even weak signatures.

7.4 Two-dimensional photon echo signal

In Chap. 6, the LO phonon induced relaxation process has already been investigated but have remained on a theoretical basis since no experimental detection scheme has been presented for tracking the relaxation dynamics. Hereby, a common setup is the pump-probe setup, which detects the change of transmission of the population distribution for different times with a probe pulse with one specific frequency. The change of the distribution is then displayed as 1D curves in difference transmission spectra (DTS) [MMF$^+$92, BTR$^+$95]. In comparison, the 2D spectrum can give additional information: On one hand, the two frequency axes extend the change of the population distribution on a whole frequency range. In principle, this could also be realized in the DTS by varying the probe frequency for each experiment. On the other hand, the mapping the two frequency axes enables the *correlation* of the involved frequencies, which cannot be resolved in an 1D spectrum. This will be explained in detail in the corresponding 2D spectra in Sec. 7.1. Considering the 2D spectrum, the question remains which directional polarization $P_{l,m,n}$ is to be considered for the detection of relaxation processes.

Here, the double-sided FEYNMAN diagrams give the answer: Analysing the corresponding diagrams, it can be seen that the nonlinear third-order directional polarization $P_{-1,1,1}$, whose 2D FOURIER

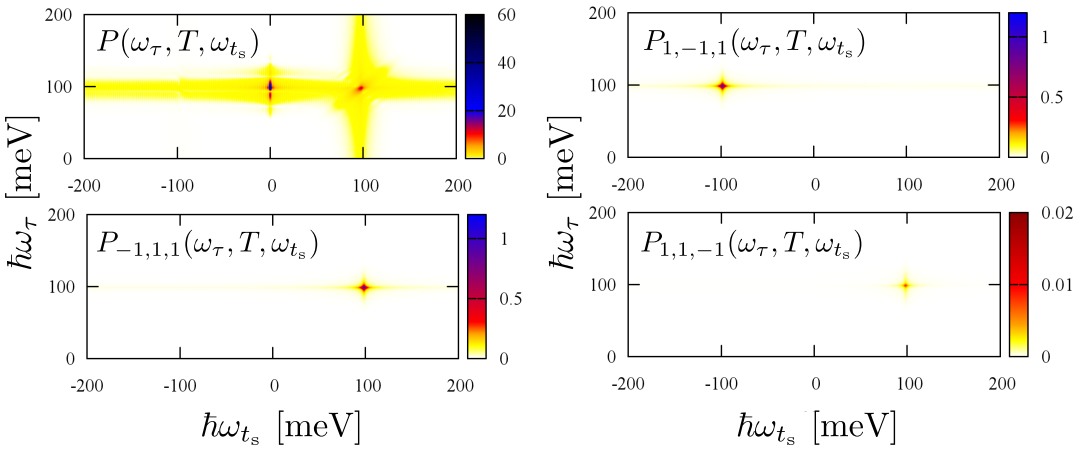

Figure 7.4 | 2D spectra of a two-level system. Top left is the FOURIER transformation of the overall macroscopic polarization $P(\tau,T,t_s)$ with a phase set of $\Phi = \{0,0,0\}$. Clockwise displayed are other 2D spectra of the (with respect to the delay times τ and t_s) FOURIER transformed directional third-order polarizations $P_{1,-1,1}(\tau,T,t_s)$, $P_{-1,1,1}(\tau,T,t_s)$ and $P_{1,1,-1}(\tau,T,t_s)$. The waiting time T has been set to $T = 100$ fs. The signal strength of the third-order spectra is considerably weaker than the signal strength of the overall polarization.

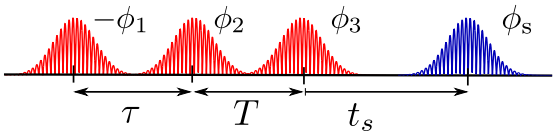

Figure 7.5 | Pulse sequence with the phase combination needed for the 2D photon echo signal.

transformation is also denoted as *2D photon echo signal*, can resolve relaxation processes [APV+09]. The corresponding phase sequence is $\Phi_I = -\phi_1 + \phi_2 + \phi_3$, shown in Fig. 7.5. The double-sided FEYNMAN diagrams of $P_{-1,1,1}$ are given in the next subsection. For an accurate interpretation of the 2D photon echo signal, the LO phonon induced relaxation is investigated in one dimension first (analogous to Chap. 6). This will be done in Sec. 7.4.2. Finally, the 2D photon echo spectra are presented in the last two subsections Sec. 7.4.3 and Sec. 7.4.4 with an in-depth interpretation and discussion of the results.

7.4.1 Relevant pathways

In the third-order limit, three possible sets of many-particle states exist: No excitation of the system ground states (g), single excitation (e) and double excitation (f) of the many-particle system. These different configurations are visualized in Fig.7.6(a). Using the method of the double-sided FEYNMAN diagrams, the pathways for the photon echo signal can be evaluated. The state of the density operator can be read at each point of time by looking at the composition of the bra and ket. For example, diagonal states such $|g\rangle\langle g|$ denote the population distribution in the ground state, while non-diagonal states, such as $|e\rangle\langle g|$, are a coherence between the excited state and the ground state. Here, the three incoming pulses are marked with red-colored phases, while the fourth pulse, the signal pulse with the signal phase ϕ_s is the pulse which brings the system back into a diagonal state, corresponding to the last interaction with the dipole operator $\hat{\mu}$ on the left side of the expectation value in $P^{(n)}$, Eq. (7.4). In addition to the previously introduced symbols in the double-sided Feynman diagrams, the solid vertical lines are

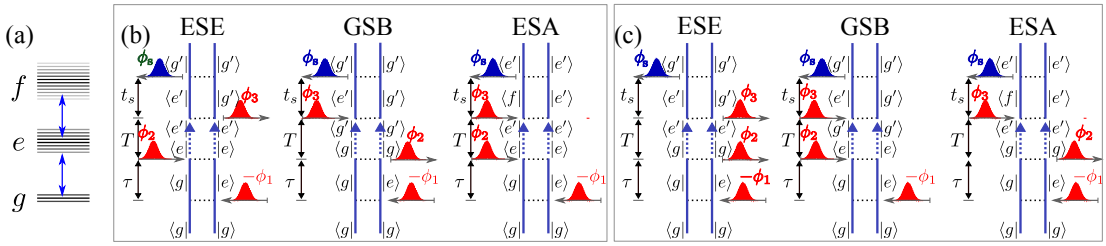

Figure 7.6 | (a) Schematic band diagram of the many-particle state in the 3rd order limit: ground state g, first excited state e, double excited state f. The arrows indicate the allowed dipole transitions between the states. (b),(c): Relevant double-sided Feynman diagrams for the photon echo signal: (b) Intrasubband and (c) intersubband processes for ESE (excited state emission), GSB (ground state bleaching) and ESA (excited state absorption). The dotted arrows represent the evolution of the densities due to relaxation processes.

connected via dashed vertical arrows. These arrows represent relaxation processes during that time period.

Six resonant LIOUVILLE pathways contribute to the photon echo signal $P_{-1,1,1}$, shown in Fig. 7.6(b) and Fig. 7.6(c). [6] The characterisation of the processes is done at the time of the third incoming pulse (after T): If the pulse changes the system from an excited state density $|e'\rangle\langle e'|$ to a coherence between ground and excited state $|e'\rangle\langle g'|$, this process is called excited state emission (ESE) since the coherence is created under the emission of one photon. In the same manner the excited state absorption (ESA) corresponds to a process, where after the third pulse a coherence is created under absorption of one photon. The change of the ground state into a coherence under absorption of one photon is called ground state bleaching (GSB). The six pathways can be split into two groups: Pathways with intrasubband relaxation during the waiting time T [Fig. 7.6(b)], i.e. the density relaxes within the subband $|g\rangle\langle g| \rightarrow |g'\rangle\langle g'|$, respectively $|e\rangle\langle e| \rightarrow |e'\rangle\langle e'|$). And pathways with intersubband (ISB) relaxation during T, where the system changes from $|e\rangle\langle e|$ to $|g'\rangle\langle g'|$ or vice versa [Fig. 7.6(c)]. A third possible intersubband process is the so-called double excited state absorption, that is, a transition from $|e\rangle\langle e|$ to $|f\rangle\langle f|$ during the waiting time T. Although included in the theoretical model, this excitation is lightly unlikely and hence not depicted in Fig. 7.6.

In all six pathways, the pulses interact with the sample in a similar fashion. The corresponding processes in reciprocal space are depicted in Fig. 7.7: The first pulse with the phase $-\phi_1$ creates a coherence between the ground state and the first excited state (a). After the delay time τ, the second incoming pulse with the phase ϕ_2 can create a density (or population distribution) either in the ground or in the excited subband (b). During the waiting time T, the population distribution changes due to the *el-ph* interaction, indicated in (c) as the change between the dotted and blue distributions. Then, the third pulse with the positive phase ϕ_3 again creates a coherence in the system (c). Finally, the signal pulse brings the density operator back into a diagonal state. By FOURIER transforming the first delay time τ and the signal time t_s, it is possible to track the frequencies and hence states which are involved in the first and the second coherence. This mapping of the frequencies then allows conclusions to the time evolution of the population distribution during T: If the population distribution has not changed during T [dotted lines in Fig. 7.7(c)] the same transition frequencies are involved in the first and the second coherence [indicated as light blue arrows in Fig. 7.7(a) and (c)]. If the system has changed during T [dark blue lines in Fig. 7.7(c)], different transition frequencies will occur in the second coherence [additional light orange arrows in Fig. 7.7(a) and (c)]. Hence, in order to observe relaxation processes in the ISB model system, the 2D photon echo spectra of the signal $P_{-1,1,1}(\omega_\tau, T, \omega_{t_s})$ has to be investigated for different waiting times T.

[6] Coherent processes such as $|g\rangle\langle g'|$ are neglected since spatial homogeneity is assumed.

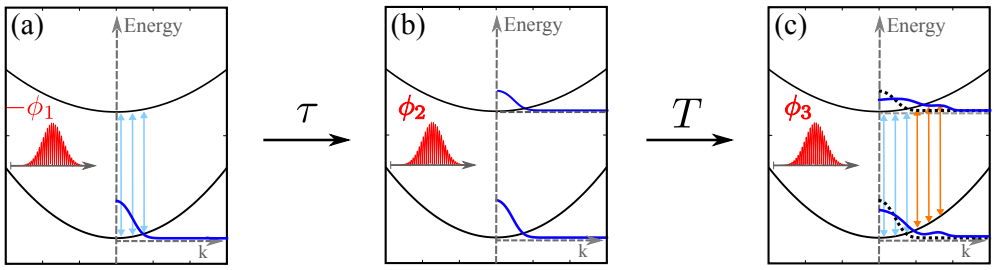

Figure 7.7 | Schematic drawing of the processes induced by the photon echo pulse sequence. (a) The first pulse creates a coherence (light blue arrows), (b) the second pulse creates a density (two dark blue lines) and (c) the third pulse induces a coherence again (light blue and orange arrows). If the distribution relaxes during T [solid blue lines in (c)], the first and the second coherence exhibit different frequencies.

7.4.2 Intersubband relaxation under a two-pulse excitation

Before the 2D spectra are presented, it is useful to analyze the ISB relaxation under excitation of this specific pulse sequence. The ISB QW under consideration has a width of $L = 10$ nm with a fundamental subband gap energy of $\varepsilon_{\text{gap}} = 98.54$ meV. The electronic doping density is $n_{\text{d}} = 5.0 \cdot 10^{10}$ cm^{-2}. The sample is excited with three Gaussian 0.1π pulses with $\sigma = 20$ fs. The frequency is centred around the gap energy $\omega_{\text{L}} = \omega_{\text{gap}}$. The calculation for the dynamics are done with the inclusion In the simulation of the dynamics the *el-ph* interaction is taken into account in second-order BORN where the temperature of the phonon bath is assumed to be $T = 100$ K. As already explained in the previous subsection, the third pulse creates a coherence, sampling the frequencies of the population distribution at the waiting time T. Thus, to analyze the corresponding population dynamics, only the first two pulses are applied, separated by a delay time of $\tau = 0.1$ ps. This is shown in Fig. 7.8, where the angle-integrated population distribution is plotted for different waiting times T after the second pulse. In this picture, only one specific delay time, namely $\tau = 0.1$ ps, is shown. To get a full 2D photon echo spectrum, the delay time τ is varied. Thus, Fig. 7.8 only shows one possible arrangement of the population, while the 2D photon echo spectrum will show the overall population distribution probability.

The upper graph in Fig. 7.8(a) shows the population distribution of the upper subband $f_{2,\mathbf{k}}$ for three different waiting times T. The population distribution $f_{1,\mathbf{k}}$ does not change considerably for different waiting times since only about 1/20 of the initial distribution is excited by the weak 0.1π pulse. Hence, instead of showing $f_{1,\mathbf{k}}$, the *difference* between the population distribution in the lower subband $f_{1,\mathbf{k}}$ and the distribution before pulse excitation $\rho^0_{11,\mathbf{k}}$ is a more meaningful quantity and shown in the lower plot, i.e. $(\rho_{11,\mathbf{k}} - \rho^0_{11,\mathbf{k}})$. In both graphs, the x-axis is labelled with to different tics: The Energy(k_i) of the subband i and the corresponding momentum state k_i in subband i, with Energy(k_i) $= \hbar^2\mathrm{k}^2/2m_i$, which differ due to the nonparabolicity.

After excitation with the first two pulses, which create an electron distribution in the upper subband $f_{2,\mathbf{k}}$, the distribution $f_{2,\mathbf{k}}$ decreases for increasing waiting times from the upper to the lower subband via LO phonon emission. By looking at the band diagram of the two subbands in Fig. 7.8(b), the *el-ph* processes which lead to the differential distribution in the lower subband $(\rho_{11,\mathbf{k}} - \rho^0_{11,\mathbf{k}})$ can be clearly identified. The dark blue line is the energy dispersion of the upper subband 2 and the dark green line is the energy dispersion of the lower subband 1. The horizontal dotted lines are spaced with a LO phonon energy of 36 meV. Shortly after excitation, the electrons around the upper subband minimum relax to the lower subband under emission of one LO phonon. The process is indicated as a dark grey arrow in Fig. 7.8(b). When using the LO phonon energy of 36 meV to bridge the subband gap, the electrons must relax into a state in the lower subband with a high momentum of about $k \approx 0.35$ nm^{-1}. This leads to the broad, slight increase of the occupation $\rho_{11,\mathbf{k}\approx 0.35\ \text{nm}^{-1}}$ in Fig. 7.8(a) for $T = 0.5$ ps. Then the electrons at $\rho_{11,\mathbf{k}\approx 0.35\ \text{nm}^{-1}}$ can further relax towards the lower subband minimum under emission of

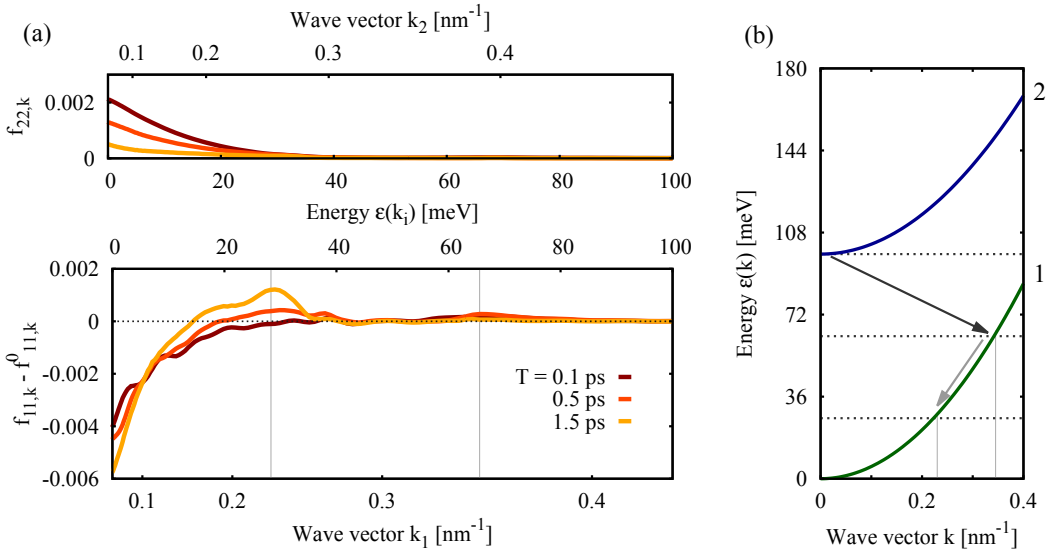

Figure 7.8 | (a) Population distribution of the angle-integrated upper subband $f_{2,\mathbf{k}}$ (upper graph) and differential population distribution of the lower subband $f_{1,\mathbf{k}} - f^0_{1,\mathbf{k}}$ (lower graph) for three different waiting times T. $f^0_{1,\mathbf{k}}$ is the initial FERMI ground state distribution before the pulse excitation. The distributions are excited with the first two pulses with a delay time of $\tau = 0.1$ ps. (b) Band dispersion of the lower subband 1 and the upper subband 2. The grey arrows mark the electron relaxation processes under emission of one LO phonon. The dotted lines are spaced with a distance of one LO phonon energy $\hbar\omega_{\mathrm{LO}} = 36$ meV.

one LO phonon energy, which corresponds to the momentum state $k \approx 0.23$ nm^{-1} (light grey arrow in Fig. 7.8(b)). This eventually leads to the strongly increased occupation $\rho_{11,\mathbf{k}\approx 0.35\ \mathrm{nm}^{-1}}$ in Fig. 7.8(a) for $T = 1.5$ ps. The momentum state $k \approx 0.22$ nm^{-1} is less than one LO phonon energy above the lower subband minimum as can bee seen in Fig. 7.8(b). Hence, lacking *el-el* interaction to further redistribute the carrier momentum, the population at $\rho_{11,\mathbf{k}\approx 0.22\ \mathrm{nm}^{-1}}$ will continue to increase for higher waiting times T. Due to the broad spectral pulses (FWHM ≈ 77 meV), the phonon replica are not as pronounced as the ones in Chap. 6. Still, this increased occupation in the lower subband at $\rho_{11,\mathbf{k}\approx 0.35\ \mathrm{nm}^{-1}}$ should be visible in the 2D spectrum.

7.4.3 Photon echo spectra for free carriers

As the detected signal field is proportional to the macroscopic polarization in the FOURIER space [BMSF04], i.e. $S(\omega_\tau, T, \omega_{t_s}) \propto P(\omega_\tau, T, \omega_{t_s})$, it is sufficient to consider $P_{-1,1,1}(\omega_\tau, T, \omega_{t_s})$ in the following 2D spectra. The directional polarization $P_{-1,1,1}(\tau, T, t_s)$ is extracted from the overall macroscopic polarization P via the phase cycling protocol, explained in Sec. 7.3.1. The free carrier spectrum of $P_{-1,1,1}(\hbar\omega_\tau, T = 0.5\ \mathrm{ps}, \hbar\omega_{t_s})$ is shown in Figure 7.9 for a system with equal (left column) and different subband masses (right column). Their imaginary, real and absolute parts are shown from top to bottom. The color bar displays the signal strength. Along the horizontal axis is the FOURIER transform of the delay time, $\hbar\omega_\tau$. The label of this axis is also referred as the *excitation frequency* since the first incoming pulse excites the system. $\hbar\omega_{t_s}$ is plotted along the vertical axis and is denoted as the *response frequency*, since the system "responds" with these frequencies due to the time evolution of the distributions. The different signs of the horizontal and vertical axis originate from the opposing phases of the first and the third incoming pulse (the first phase is negative while the third phase is positive). The 2D spec-

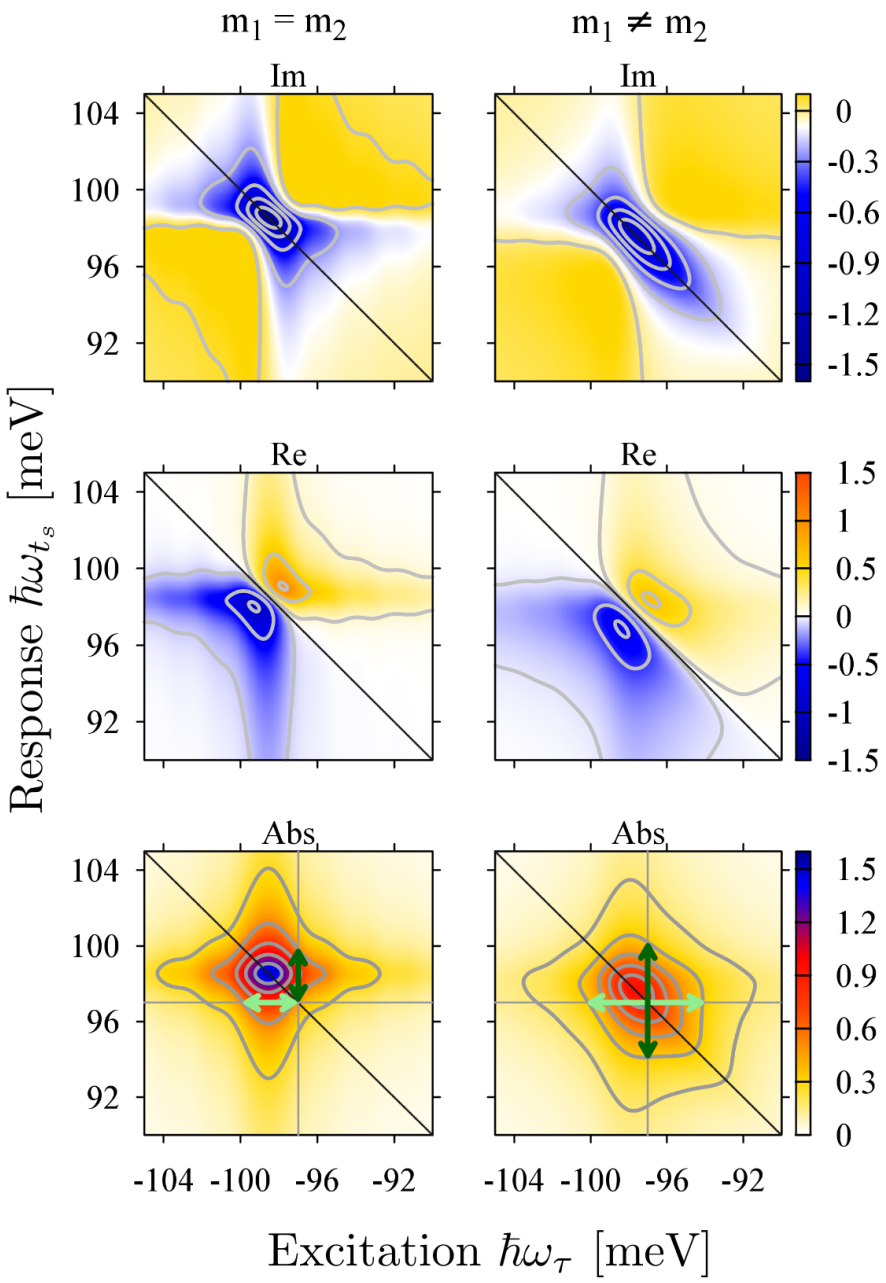

Figure 7.9 | 2D free carrier spectra of the photon echo signal $P_{-1,1,1}$ in a 10 nm ISB QW using (left column) equal and (right column) different subband masses for $T = 0.5$ ps. From top to bottom shown are the imaginary, real and absolute parts of the signal. The contour lines of the absolute parts are equally spaced with a distance of 1/6 of the maximum signal strength.

trum maps each excitation and response energy which allows one to detect changes between excitation and response. In standard 1D photon echo spectra, the response is directly projected on the excitation frequency [Muk95].

The free carrier spectrum, calculated via Eq. (5.4) with equal subband masses, is shown in Fig. 7.9

(left). The bow-tie shaped imaginary part of $P_{-1,1,1}$ is located around the gap energy $\varepsilon_{\text{gap}} = 98.54$ meV. Its form is symmetric along the diagonal and even symmetric along the anti-diagonal (top). The real part $P_{-1,1,1}$ is point-symmetric along the diagonal (see the sign change of the signal strength) and also symmetric along the anti-diagonal (middle). The absolute value is diamond shaped (bottom) and symmetric along the diagonal and the anti-diagonal. The signal with equal subband masses resembles the 2D spectrum of a homogeneously broadened two-level system [KDT03b], which can be intuitively understood since for equal subband masses, all transition energies equal the gap energy. Thus, the width of the absolute spectrum solely depends on the phenomenological dephasing γ_{ph} in Eq. (5.4). The imaginary, real and absolute spectra for different subband masses (Fig. 7.9, right column), become asymmetric perpendicular to the diagonal: Their form is stretched along the diagonal towards lower energies. This low-energy tail is the result of the different subband masses and has already been observed in the 1D absorption spectra in Sec. 5.1. However, the symmetry along the diagonal is retained for the 2D spectra including different subband masses. The maximum of the signal strength is shifted towards lower energies, well-known from the linear absorption spectra in Sec. 5.1 Additionally, typical features of the photon echo signal can be observed [Muk00]: The width of the absolute signal along $\hbar\omega_{t_s} = \text{const.}$ is determined by the homogeneous line width while the width along $-\hbar\omega_\tau = \hbar\omega_{t_s}$ is inhomogeneously broadened by the possible transition energies due to the subband population distributions.

In terms of the double-sided Feynman diagrams, the symmetric shape of the 2D free carrier spectra along the diagonal are the result of the interaction-free system, where the diagonal states do not alter during the waiting time T. The first pulse samples the available transition energies of the equilibrium system [cf. the blue line in Fig. 7.7(a)]. These available transition energies are drawn along the horizontal axis in Fig. 7.9. The second pulse creates a density in the excited state. Since there is no momentum exchange through the excitation (and since the pulses have a large spectral width), the distribution,lifted into the upper subband, resembles the distribution in the lower subband. Thus, if the subband distributions do not relax during T [cf. dotted black lines in Fig. 7.7(c)], the third pulse samples the same transition energies, which are drawn along the vertical axis in Fig. 7.9. To give an explicit example, one excitation frequency will be compared with the corresponding response frequency: Here, the occupation probability along $\hbar\omega_\tau = -97$ meV is compared with the one at $\hbar\omega_{t_s} = 97$ meV at the contour of 1/3 of the signal strength, see arrows in Fig. 7.9 bottom left: In the spectrum including equal subband masses, the response occupation probability along one excitation energy (dark vertical arrow) is equal to the excitation occupation probability along the corresponding response energy (light horizontal arrow). This also holds for the free carrier spectrum including different subband masses (arrows in Fig. 7.9 bottom right). Note that the spectra show the difference of the momentary population at the time $t = \tau + T$ to the initial ground state distribution $|g\rangle\langle g|$ at the time $t = \tau$ [Muk00]. But since the differential population, i.e. mainly the excited state distribution, resembles initial ground state distribution in form and momentum state occupation, the same transition energies are sampled.

To conclude: Due to the lack of many-body interactions, no relaxation processes can take place. Consequently, the 2D spectra, revealing the difference of the distribution upon excitation as an asymmetry, are symmetric in the free carrier case.

7.4.4 Photon echo spectra including the electron-phonon interaction

In the next step, the el-LO phonon interaction is included in the dynamics. Now, when a density is created by the second pulse, the coupling to the phonon bath will lead to a dephasing of the coherence and a relaxation of the non-equilibrium distribution. The dynamics of these processes will be accessible via the 2D photon echo spectra. In the left column of Fig. 7.10, the absolute $P_{-1,1,1}$ 2D spectra including el-LO phonon interaction are shown for three different waiting times of $T = 0.1$, 0.5 and 1.5 ps from top to bottom. To better follow the development of the population distribution for the different waiting times, the response signal is additionally displayed as 1D cuts for three different excitation energies at $\hbar\omega_\tau =$ a) -99 meV, b) -97.5 meV, and c) -96 meV. The strength of the 1D signals of Fig. 7.10, right column is color-coded similar to the 2D spectra. For comparison the corresponding 1D cuts of the 2D free carrier spectra including different subband masses were also added, taken from Fig. 7.9, bottom

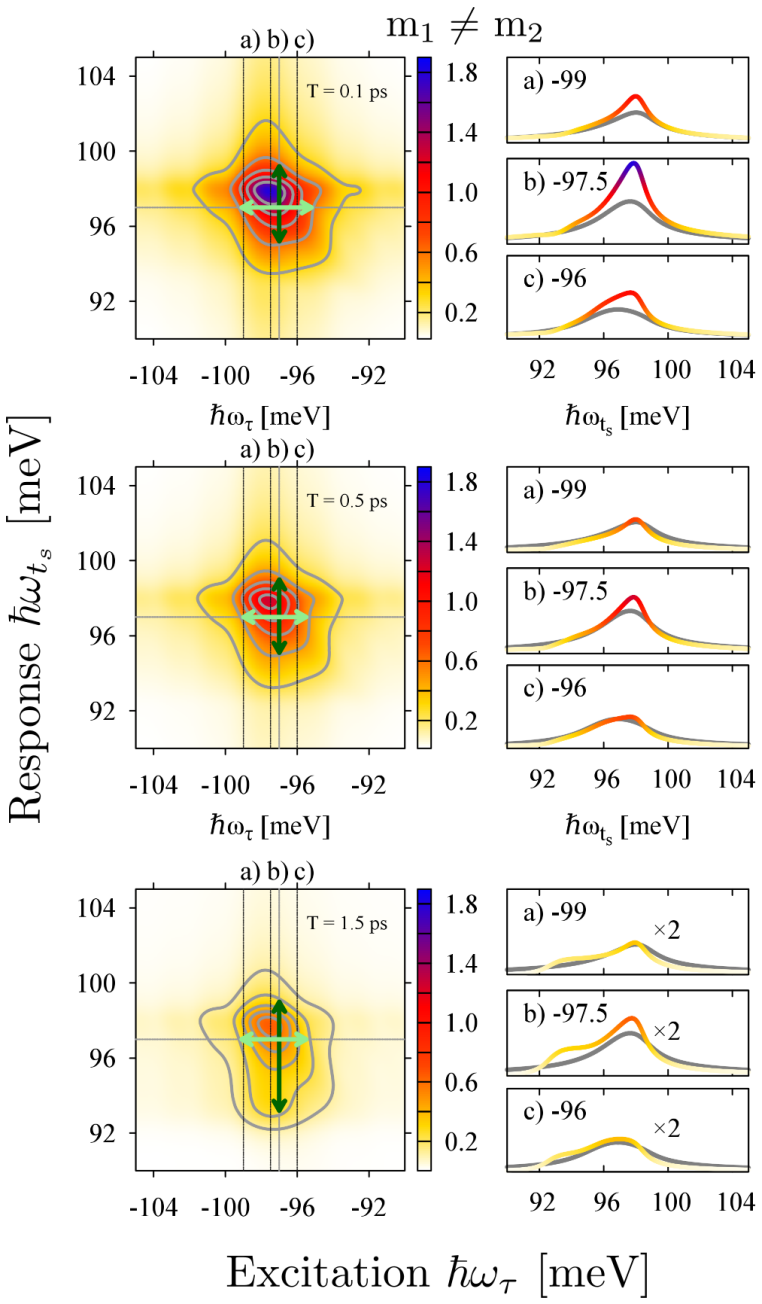

Figure 7.10 | Left column: Absolute 2D photon echo spectra including electron-LO phonon interaction for three different waiting times, showing the mapping of excitation and response energy for top: $T = 0.1$ ps, middle: $T = 0.5$ ps, bottom: $T = 1.5$ ps. Right column: Occupation probability (colored cuts) of the response energy for three different excitation energies (along the dotted lines in the 2D spectra). The grey lines in the right column are the appropriate cuts for the non-interacting system. For longer waiting times, electron relaxation takes place, visible as an increasing signal at $\hbar\omega_{t_s} \approx 94$ meV. The contour lines are equally spaced with a distance of 1/6 of the maximum strength.

right. The free carrier cuts are shown as grey lines in the right column of Fig. 7.10. The phases of the refractive (Re) and the absorptive (Im) signal are not shown since they do not considerably change in sign for different T. This indicates that relaxation processes related to varying T are phase insensitive.

The 2D spectra strongly alter for different T: Looking from top to bottom, the signal becomes asymmetric for increasing waiting time, shifting to lower response energies. In the following, the 2D spectra will be examined in greater detail for different waiting times T. The increasing asymmetry of the spectra for different T approve that the el-LO phonon scattering time lie in the well-known ps range [RR90]. Furthermore, note that the signal strength decreases. However, the homogeneous line width along $\hbar\omega_{t_s} = \text{const.}$ though is similar in all three 2D spectra, since it is determined by the T_2 time, induced by *el-ph* interaction.

Similar to the 2D free carrier spectrum with different subband masses in (Fig. 7.9, bottom right), the *el-ph* 2D signal for $T = 0.1$ ps (Fig. 7.10, top left) is quite symmetric and stretched along the diagonal towards lower energies. The low energy tail in the corresponding 1D cuts (top right) is also visible but not as pronounced as along the diagonal of the 2D spectrum. Comparing again the exemplary energy of $(-)97$meV along the horizontal and vertical axis (dark and light green arrows), the response occupation probability along one excitation energy (dark vertical arrow) is nearly equal to the excitation occupation probability along the appropriate response energy (light horizontal arrow). The symmetry of the 2D spectrum indicates that during the waiting time $T = 0.1$ ps almost no relaxation occurred.

If the spectrum for $T = 0.1$ ps (Fig. 7.10, top) is compared with the spectrum for $T = 0.5$ ps (Fig. 7.10, middle), a reduction of the signal strength is visible. This can best be seen via the height of the corresponding 1D cuts on the right side. Here, ISB relaxation from the upper to the lower subband has already taken place, which has already been analyzed in Fig. 7.8(a). For $T = 0.5$ ps (Fig. 7.10, middle), a small low energy shift along the response energy $\hbar\omega_{t_s}$ axis is visible, leading to a slightly asymmetric shape of the spectrum: The comparison of response and the excitation probability for the respective energies does not lead to the same occupation probability (cf. the different lengths of the dark and light arrow in Fig. 7.10, middle).

For $T = 1.5$ ps, the asymmetry of the 2D spectrum (Fig. 7.10, bottom left) further increases since the shift along the response energy $\hbar\omega_{t_s}$ is strongly pronounced. This clear difference between the excitation and response occupation probabilities can be seen by comparing the light and dark arrows: The range of response energies for one specific excitation energy is considerably larger than the range of the respective excitation energy for one response energy. The 1D plots for $T = 1.5$ ps (Fig. 7.10, bottom right) show an increased signal plateau around the energy of $\hbar\omega_{t_s} \approx 94$ meV, which has not been present for smaller waiting times. This transition energy corresponds to the electron momentum $k \approx 0.22$ nm^{-1}. This characteristic momentum originates from the ISB relaxation process from the upper to the lower subband, shown in the lower graph of Fig. 7.8(a). The momentum conservation leads to the increased occupation probability at $f_{11,\mathrm{k}\approx 0.22\ \mathrm{nm}^{-1}}$. However, it should be noted that the increased occupation is due to the absent *el-el* interaction, which should lead to a further redistribution for increasing waiting times.

The comparison of the three 2D spectra nicely demonstrate the benefit of the 2D FT spectroscopy: Although the increased occupation probability at $f_{11,\mathrm{k}\approx 0.22\ \mathrm{nm}^{-1}}$ is small compared to the absolute population distribution (lying in the single-digit percentage range), this scattering channel can be clearly resolved since the 2D photon echo samples the *change* of the distribution compared to the initial distribution (before pulse excitation). The results confirm that the presented technique is very well suited for the detection of many-body interactions in ISB systems.

7.5 Conclusions

In conclusion, the 2D photon echo signal was investigated for a single intersubband quantum well. Analogous to an experimental collinear setup with a three pulse excitation, the numerically obtained macroscopic polarization was derived and a phase cycling protocol was applied to extract different quantum pathways, contributing to the so-called Φ_I-signal. In order to resolve phonon-induced relax-

ation processes, the 2D photon echo signal was analyzed in more detail. The signal of the intersubband system was FOURIER transformed into the frequency domain for different waiting times T. The comparison between the different 2D spectra gives direct information about the temporal evolution of the occupation probability. The analysis of the free carrier spectra shows that without many-body interaction, the 2D frequency spectra are symmetric along the diagonal. The inclusion of the electron-phonon interaction breaks the symmetry for increasing waiting times. While for $T = 0.1$ ps the spectrum is still quite symmetric along the diagonal, the spectrum for $T = 0.5$ ps already suggests a slight shift to lower response energies, indicating the beginning of the carrier relaxation. For $T = 1.5$ ps, the 2D spectrum shows strong asymmetries along the diagonal of the excitation and response frequency, particularly visible in an increased signal at a response energy of $\hbar\omega_{t_s} \approx 94$ meV. This result corresponds to the two-step relaxation process due to the scattering with LO phonons, which eventually leads to an increased occupation in the lower subband at $\mathbf{k} \approx 0.22$ nm^{-1}.

Overall, with the presented technique, it is possible to map excitation and response frequencies independently and thus to get accurate informations about the dynamics of the electronic occupation probability. The simulations demonstrate that the 2D FOURIER spectroscopy is a powerful tool for the detection of many-body correlations and electronic dynamics. As a further aspect, the technique is capable to extract other signals, such as the anti-photon echo and double quantum coherence by choosing a different set out of the possible quantum pathways. The prior calculated microscopic polarization can be used and the necessary adaptation of the phase cycling protocol is straight forward. The study of these signals will be a very interesting aspect for future investigations.

Chapter 8

Bulk - surface dynamics in silicon

The previous chapters investigated 2D systems where the restriction of their dimensionality originated from an artificial combination of different semiconductor compounds. Another naturally occurring quasi-2D structure is the surface of 3D bulk systems, exhibiting additional bands and carrier dynamics [Hai95] between bulk and surface. A very prominent material is silicon due to its wide application in electronic devices, for example, for microelectronic circuits or in solar cells [HTDF96, Ree08, KNR$^+$09].

Here, the relaxation of hot carriers through the electron-phonon (*el-ph*) interaction is of particular interest [vD79, PLL$^+$07]. The subsequent heating of the lattice often results in a reduction of the electrical conductivity and hence to a less efficient performance of the electronic devices. Therefore, studies about the dynamics of hot carriers in silicon have been and still are of large scientific and technological interest [SPD98, IT09]. In recent experiments on silicon, it was observed that hot carriers which are excited to the conduction band have a prolonged lifetime at high temperatures [Eic10]. It is assumed that the main mechanism for the heated temperature is the coupling to longitudinal optical (LO) phonons. To support the experimental observations, the bulk-surface dynamics regarding electron-LO phonon (*el-LO*) interaction will be investigated in this chapter.

Silicon is an indirect band gap semiconductor (see Fig. 8.1) and as such a challenge for the theoretical description concerning band structure- and surface simulations. One accurate method to calculate the band structure and the matrix elements is to combine the density matrix and density functional theory [BKSK07, BKSK08]. However, the calculation of absorption spectra or even relaxation dynamics of the silicon surface requires simulations with a high numerical effort. The extension to bulk-surface dynamics would become an unbearable task considering the computational capacity [Bue08]. In this chapter, the numerical effort is by approximating the bulk-surface dynamics in silicon with rate equations. The phonon bath is treated on a more fundamental level, based on a quantum kinetic model. In the first section, Sec. 8.1, the full quantum kinetic equations for the Si(100) model system are derived.

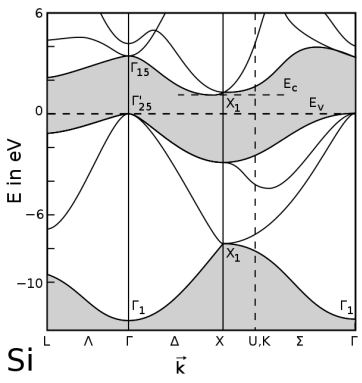

Figure 8.1 | Band structure of silicon taken from [koudw12]. The indirect band gap is indicated with dashed horizontal lines.

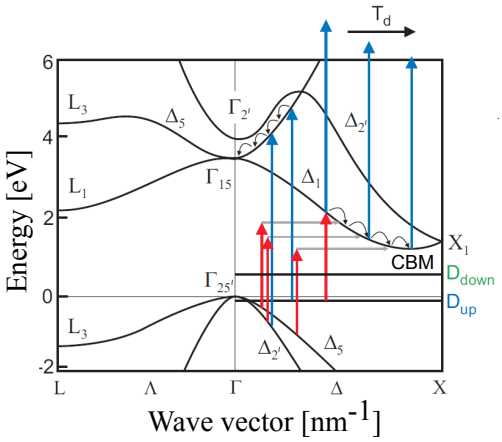

Figure 8.2 | Schematic drawing of the 2PPE spectroscopy process, taken from [Eic10]. The carriers are excited with a strong pump pulse from the valence band to the conduction band X valley. The dynamics of the hot carriers are tracked with a probe pulse in the X-valley around the conduction band minimum (CBM).

Then, in Sec. 8.2, assumptions are made to reduce the complexity of the description. This leads to the reduced BLOCH BOLTZMANN PEIERLS equations in Sec. 8.2.3. Section 8.3 presents the numerical results, which are also compared with the experimental data. This chapter concludes with a discussion of the experimentally and theoretically obtained results in Sec. 8.4.

8.1 Modelling the dynamics in silicon

8.1.1 Experimental observations

The detection of the relaxation processes in silicon (Si) requires a very high temporal resolution of ultrafast timescales, since the many-particle interactions take place on a femtosecond (fs) scale. In experiments, these ultrafast processes are typically resolved with a fs pump-probe spectroscopy [GP94, WKFR04, IT09]: With the two-photon photoemission (2PPE), electrons are excited from the valence band along the Gamma point to the conduction band with a strong pump pulse. A probe pulse then tracks the electron dynamics in the X-valley of the conduction band (CB). The 2PPE process is shown in Fig. 8.2. Parallel to the relaxation of the carriers towards the CB minimum (CBM), electrons scatter into the unoccupied surface band D_{down} via surface recombination.

Recent 2PPE experiments on Si were made by Eickhoff et al. [Eic10], generating a hot carrier distribution in the CB with a temperature of $T_{\text{el}} > 4000$ K. To study the subsequent relaxation, energy distribution curves (EDCs) were measured for different time delays between the pump and the probe pulse, explained in more detail in Sec. 8.3.3. The extraction of the bulk temperature via the EDCs indicated an increased temperature of the electron distribution even after a time of more than 8 ps. It is assumed that the reason for the increased carrier temperature is the interplay of the excited hot carrier distribution with LO phonons during the relaxation towards the CBM. To model the essential features of the system, the *el-el-* as well as the *el-ph* interaction has to be taken into account. Additionally, the dynamics of the phonons is considered. The equations of motion (EOM) for the carriers and the LO phonons are presented in the next subsection.

8.1.2 The Bloch-Boltzmann-Peierls equations

In the previous chapters, the phonons were treated as a bath of harmonic oscillators, where the mean phonon number is given by a BOSE distribution function $n_{\mathbf{q}}(\hbar\omega_{\mathbf{q}})$. Correspondingly, $n_{\mathbf{q}}$ and the lattice temperature T_{latt} were no dynamic quantities. The scenario of the 2PPE experiment requires a different approach. Here, electrons are heated to a temperature of a few thousand Kelvin and the hot carriers couple back during their relaxation, heating the phonons in turn. As previously mentioned, the emphasis lies on the coupling of the electrons to the LO phonons. The other phonon branches are assumed to play

a minor role. To have an adequate description of the system, the dynamics include not only the EOM for the bulk and the surface electron density, but also the (now time-dependent) LO phonon occupation number $n_{\mathbf{q}}(t)$.

First, the phonon-induced dynamics is considered. The calculations of the bulk and the surface dynamics are done in a similar way as in Chap. 6, where the relaxation of carriers via the *el-LO* interaction was investigated. Hence, the EOM for the electronic expectation values reads (cf. Eq. (6.1)):

$$-\mathrm{i}\hbar\frac{\mathrm{d}}{\mathrm{d}t}\langle\hat{\rho}_{ij,\mathbf{k}}\rangle_{|\text{el-LO}} = \sum_{o,\mathbf{q}}(g_{\mathbf{q}}^{oi}\sigma_{\mathbf{k}+\mathbf{q},\mathbf{q},\mathbf{k}}^{oj} + g_{\mathbf{q}}^{io*}\sigma^{jo*}{}_{\mathbf{k},\mathbf{q},\mathbf{k}-\mathbf{q}} - g_{\mathbf{q}}^{jo}\sigma_{\mathbf{k},\mathbf{q},\mathbf{k}-\mathbf{q}}^{io} - g_{\mathbf{q}}^{oj*}\sigma^{oi*}{}_{\mathbf{k}+\mathbf{q},\mathbf{q},\mathbf{k}}), \tag{8.1}$$

with the phonon assisted density matrix elements (PADs) $\sigma^{ab(*)}{}_{\mathbf{k},\mathbf{q},\mathbf{k}'}$. In Chap. 6, the differential equations of the PADs [Eq. (6.2)] have been directly solved numerically. Now, instead of calculating the temporal evolution of the PADs, the PADs are solved via the MARKOV approximation [Kuh98], that is, memory effects are neglected. This leads to the following equation for the electronic densities $\langle\hat{\rho}_{ii,\mathbf{k}}\rangle = f_{i,\mathbf{k}}$

$$\begin{aligned}\frac{\mathrm{d}}{\mathrm{d}t}f_{i,\mathbf{k},|\text{el-LO}} = \frac{2\pi}{\hbar}\sum_{j,\mathbf{q}}|g_{\mathbf{q}}^{ji}|^2\delta(\varepsilon_{j,\mathbf{k}+\mathbf{q}}-\varepsilon_{i,\mathbf{k}}-\hbar\omega_{\text{LO}})\left(n_{\mathbf{q}}^{+}f_{j,\mathbf{k}+\mathbf{q}}f_{i,\mathbf{k}}^{-}-n_{\mathbf{q}}f_{j,\mathbf{k}+\mathbf{q}}^{-}f_{i,\mathbf{k}}\right)\\ -|g_{\mathbf{q}}^{ij}|^2\delta(\varepsilon_{j,\mathbf{k}+\mathbf{q}}-\varepsilon_{i,\mathbf{k}}+\hbar\omega_{\text{LO}})\left(n_{\mathbf{q}}^{+}f_{i,\mathbf{k}}f_{j,\mathbf{k}+\mathbf{q}}^{-}-n_{\mathbf{q}}f_{i,\mathbf{k}}^{-}f_{j,\mathbf{k}+\mathbf{q}}\right),\end{aligned} \tag{8.2}$$

with $f^{-}=(1-f)$ and $n^{+}=(1+n)$. The different contributions can be interpreted in the following manner: The scattering of the electrons can contain the emission [[$\sim n^{+}$]] or the absorption [[$\sim n$]] of a phonon. Due to the delta function, these processes are energy and momentum conserving. A scattering process from $\mathbf{k}+\mathbf{q}$ to $\mathbf{k}$ (under phonon emission) depends on the electronic occupation $f_{\mathbf{k}+\mathbf{q},j}$ and on the available, empty states $f_{\mathbf{k},i}^{-}$ to scatter into.[1] Hence, the terms which are proportional to $f_{i,\mathbf{k}}^{-}$ can also be combined and denoted as an out-scattering rate $\Gamma_{\text{out}}^{\text{el-LO}}(\mathbf{k},\mathbf{q},j)$, while the terms proportional to $f_{i,\mathbf{k}}$ are denoted as an in-scattering rate $\Gamma_{\text{in}}^{\text{el-LO}}(\mathbf{k},\mathbf{q},j)$. This gives Eq. (8.2) the simple form:

$$\frac{\mathrm{d}}{\mathrm{d}t}f_{i,\mathbf{k},|\text{el-LO}} = \Gamma_{\text{in}}^{\text{el-LO}}(\mathbf{k},\mathbf{q},j)f_{i,\mathbf{k}}^{-} - \Gamma_{\text{out}}^{\text{el-LO}}(\mathbf{k},\mathbf{q},j)f_{i,\mathbf{k}}. \tag{8.3}$$

Next, the phonon occupation number $\langle\hat{b}_{\mathbf{q}}^{\dagger}\hat{b}_{\mathbf{q}}\rangle = n_{\mathbf{q}}$ is evaluated. The temporal evolution is also obtained via the HEISENBERG EOM until second-order correlation expansion. Applying again the MARKOV approximation, an equation similar to Eq. (8.2) is obtained [BMH+07]:

$$\frac{\mathrm{d}}{\mathrm{d}t}n_{\mathbf{q}} = -\frac{n_{\mathbf{q}}-n_0}{\tau_{\text{LO}}} + \frac{2\pi}{\hbar}\sum_{i,\mathbf{k}}|g_{\mathbf{q}}^{ii}|^2\delta(\varepsilon_{i,\mathbf{k}+\mathbf{q}}-\varepsilon_{i,\mathbf{k}}-\hbar\omega_{\text{LO}})\left[n_{\mathbf{q}}^{+}f_{i,\mathbf{k}+\mathbf{q}}f_{i,\mathbf{k}}^{-}-n_{\mathbf{q}}f_{i,\mathbf{k}+\mathbf{q}}^{-}f_{i,\mathbf{k}}\right]. \tag{8.4}$$

The equations (8.3) and (8.4) are also denoted as BLOCH-BOLTZMANN-PEIERLS equations [All87]. The decay of the LO phonons $[-(n_{\mathbf{q}}-n_0)/\tau_{\text{LO}}]$ is included phenomenologically and accounts for the phonon-phonon interaction: Due to the finite lifetime of the LO phonons τ_{LO}, the phonon modes will eventually decay into the equilibrium function n_0, where n_0 is the BOSE distribution with the equilibrium temperature T_0. The heating of the LO phonons is determined by the scattering of one electron from $\mathbf{k}+\mathbf{q}$ to $\mathbf{k}$ under emission of one phonon and by the scattering of one electron from $\mathbf{k}$ to $\mathbf{k}+\mathbf{q}$ under absorption of one phonon, similar to the dynamics of Eq. (6.2).

8.1.3 The Coulomb-induced Boltzmann equation

Next, the electron-electron (*el-el*) interaction is included, which results in the COULOMB-induced BOLTZMANN equations via second-order correlation expansion and HARTREE-FOCK factorization. Their derivation has been done in a similar fashion in Sec. 5.3 for the microscopic polarization. Here, the EOM

[1] The microscopic polarization is not regarded since the relaxation processes are investigated *after* the excitation with the pump pulse.

under COULOMB interaction is calculated for the microscopic densities $f_{i,\mathbf{k}}$. Applying the MARKOV approximation, the equation reads [cf. Eqs. (5.14)-(5.17)]:

$$\frac{\mathrm{d}}{\mathrm{d}t} f_{i,\mathbf{k}|\text{el-el}} = -\frac{2\pi}{\hbar} \sum_{\{\alpha\beta\gamma\}} \delta(\varepsilon_\alpha + \varepsilon_\beta - \varepsilon_\gamma - \varepsilon_{i,\mathbf{k}}) \times \\ \tilde{V}_{\alpha\beta i\gamma} \tilde{W}_{1\gamma\alpha\beta} \left(\langle \hat{\rho}_{a1,\mathbf{k}} \rangle \langle \hat{\rho}_{b\gamma} \rangle \langle \hat{\rho}_{\beta c} \rangle^- \langle \hat{\rho}_{\alpha d} \rangle^- - \langle \hat{\rho}_{\alpha d} \rangle \langle \hat{\rho}_{\beta c} \rangle \langle \hat{\rho}_{b\gamma} \rangle^- \langle \hat{\rho}_{ai,\mathbf{k}} \rangle^- \right), \quad (8.5)$$

with the multi-indices $\{a,b,c,d\}$ (where the multi-index a includes the band number a, the momentum vector $\mathbf{k}_a$ and the spin s_a) and the abbreviations $\langle \hat{\rho}_{\alpha\beta} \rangle^- = \delta_{\alpha\beta} - \langle \hat{\rho}_{\alpha\beta} \rangle$ and $\tilde{W}_{abdc} = \tilde{V}_{abdc} - \tilde{V}_{badc}$.[2] Disregarding the microscopic polarizations, the terms proportional to $f_{i,\mathbf{k}}$ can now also be combined in an out-scattering rate $\Gamma^{\text{el-el}}_{\text{out}}(\mathbf{k},\mathbf{q},j)$ and the terms proportional to $f^-_{i,\mathbf{k}}$ can be combined in-scattering rate $\Gamma^{\text{el-el}}_{\text{in}}(\mathbf{k},\mathbf{q},j)$, similar to Eq. (8.2). The COULOMB-induced BOLTZMANN scattering equation than reads [LK88]:

$$\frac{\mathrm{d}}{\mathrm{d}t} f_{i,\mathbf{k},|\text{el-el}} = \Gamma^{\text{el-el}}_{\text{in}}(\mathbf{k},\mathbf{q},j) f^-_{i,\mathbf{k}} - \Gamma^{\text{el-el}}_{\text{out}}(\mathbf{k},\mathbf{q},j) f_{i,\mathbf{k}}. \quad (8.6)$$

To model the full dynamics in Si, the full equations include the COULOMB-induced BOLTZMANN equation and the BLOCH-BOLTZMANN-PEIERLS equations. The numerical effort connected with the calculation of the full quantum kinetics is beyond the capacities of this work. Hence, in the next section, some assumptions are made to reduce the numerical .complexity of the system.

8.2 Reduction of complexity

8.2.1 Relaxation rate approximation

To reduce the numerical effort of the dynamics, the EOMs are treated more qualitatively and the quantum kinetics is neglected. The simplification of the *el-el-* and *el-ph* scattering equations is done within the relaxation rate approximation, which is a well established technique in the microscopic laser theory [Lau93, CK05]. In this approximation, the focus lies on the long time limit of the dynamics, where the system is close to its equilibrium. Hence, the actual distribution $f_\mathbf{k}$ differs from the equilibrium function f^0 by a small deviation δf: $f = f^0 + \delta f$, with the equilibrium FERMI distribution function f^0. The overall scattering terms then read:

$$\frac{\mathrm{d}}{\mathrm{d}t} f_{\mathbf{k}|\text{scatt}} = \Gamma_{\text{in}}(1 - f^0_\mathbf{k} - \delta f_\mathbf{k}) - \Gamma_{\text{out}}(f^0_\mathbf{k} + \delta f_\mathbf{k}). \quad (8.7)$$

Applied to the equation for the *el-ph* scattering rate, Eq. (8.3) can be simplified:

$$\frac{\mathrm{d}}{\mathrm{d}t} f_{i,\mathbf{k},|\text{el-el}} = \Gamma^{\text{el-LO}}_{\text{in}}(\mathbf{k},\mathbf{q},j)(1 - f^0_{i\mathbf{k}} - \delta f_{i,\mathbf{k}}) - \Gamma^{\text{el-LO}}_{\text{out}}(\mathbf{k},\mathbf{q},j)(f^0_{i,\mathbf{k}} + \delta f_{i,\mathbf{k}}) \\ = -(\Gamma^{\text{el-LO}}_{\text{in}}(\mathbf{k},\mathbf{q},j) + \Gamma^{\text{el-LO}}_{\text{out}}(\mathbf{k},\mathbf{q},j)\delta f_{i,\mathbf{k}} \sim -\frac{1}{\tau^{\text{intra}}_{\text{el-LO}}} \delta f_{i,\mathbf{k}} = -\frac{f_{i,\mathbf{k}} - f^0_{i,\mathbf{k}}}{\tau^{\text{intra}}_{\text{el-LO}}}, \quad (8.8)$$

with the intraband *el-LO* scattering time $\tau^{\text{intra}}_{\text{el-LO}}$. More detailed calculations can be found in App. D.1. In the second step the condition was used that, in equilibrium, the overall in- and out-scattering contributions are equal: $\Gamma_{\text{in}}(1 - f^0_{i,\mathbf{k}}) = \Gamma_{\text{out}} f^0_{i,\mathbf{k}}$. Furthermore, the dependence on the momenta is neglected. Hence, the scattering time $\tau_{\text{el-LO}}$ can be interpreted as a mean value of the different momentum-dependent scattering contributions.[3] In the same manner, the BOLTZMANN scattering terms for *el-el* in-

[2] Here, the screened COULOMB potentials $\tilde{V}$ are considered.

[3] It should be noted that in principal, the scattering times τ can be determined microscopically through its relation $\tau^{\text{intra}}_{\text{el-LO}} = (\Gamma^{\text{el-LO}}_{\text{in}}(\mathbf{k},\mathbf{q},j) + \Gamma^{\text{el-LO}}_{\text{out}}(\mathbf{k},\mathbf{q},j)^{-1}$. But to ease the numerical effort, mean values will be chosen for the scattering times.

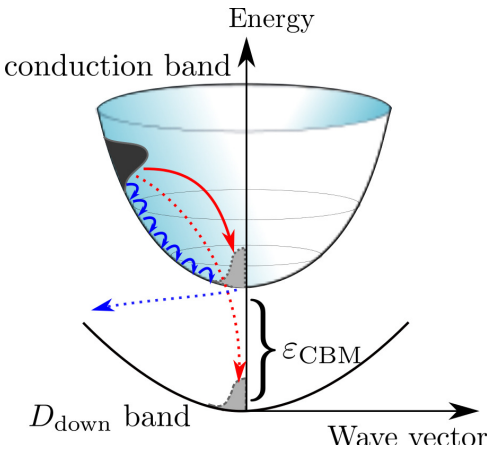

Figure 8.3 | Schematic drawing of the different many-body processes including *el-el*- (red arrows) and *el-ph* scattering processes (blue arrows) within the band (solid arrows) and between the CB and the D_{down} surface band (dashed arrows) during the relaxation of the initial distribution (dark grey Gaussian). The LO phonon dynamics is only considered in the conduction band (solid blue arrows).

teraction in Markov approximation are simplified to a rate equation:

$$\begin{aligned}\frac{\mathrm{d}}{\mathrm{d}t} f_{i,\mathbf{k},|\text{el-el}} &= \Gamma^{\text{el-el}}_{\text{in}}(\mathbf{k},\mathbf{q},j)(1-f^0_{i\mathbf{k}}-\delta f_{i,\mathbf{k}}) - \Gamma^{\text{el-el}}_{\text{out}}(\mathbf{k},\mathbf{q},j)(f^0_{i,\mathbf{k}}+\delta f_{i,\mathbf{k}}) \\ &\sim -\frac{1}{\tau_{\text{el-lel}}}\delta f_{i,\mathbf{k}} = -\frac{f_{i,\mathbf{k}}-f^0_{i,\mathbf{k}}}{\tau^{\text{intra}}_{\text{el-el}}}.\end{aligned} \tag{8.9}$$

It is obvious that the relaxation rate approximation is a quite coarse approximation since the investigated system is in a high non-equilibrium state shortly after the pulse excitation. But since the aim is to model the long lifetime behavior of hot electrons, the quantum kinetic behavior, normally pronounced at shorter time scales, can be neglected in the simulations. A detailed discussion is done in Sec. 8.4.

8.2.2 Reduced Peierls equation

Next, the PEIERLS equation is modified. It is assumed that the lattice heating is mainly influenced by the hot carriers in the bulk conduction band. Thus, Eq. (8.4) only includes the summation over the momentum-independent CB distribution f_{CB}. Furthermore, the different $\mathbf{q}$-modes of the LO phonons are treated within the EINSTEIN model with equal coupling elements. Since the emission and absorption of phonons play an important role for the carrier heating, the relaxation rate approximation is applied in a reduced manner: Only the FRÖHLICH form factors and the delta condition are included in the relaxation rate $\tau_{\text{el-LO}}$, leading to the reduced PEIERLS equation:

$$\frac{\mathrm{d}}{\mathrm{d}t} n = -\frac{n-n_0}{\tau_{\mathrm{LO}}} + \frac{1}{\tau^{\text{intra}}_{\text{el-LO}}} \frac{\sqrt{2m^3_{\mathrm{bulk}}}}{\hbar^3} \int_0^\infty \mathrm{d}\varepsilon \sqrt{\varepsilon} \left[n^+ f_{\mathrm{CB}}(t,\varepsilon+\varepsilon_{\mathrm{LO}}) f^-_{\mathrm{CB}}(t,\varepsilon) - n f_{\mathrm{CB}}(t,\varepsilon) f^-_{\mathrm{CB}}(t,\varepsilon+\varepsilon_{\mathrm{LO}}) \right], \tag{8.10}$$

with the bulk effective mass m_{bulk} of the CB and the intraband *el-LO* scattering time $\tau^{\text{intra}}_{\text{el-LO}}$. Here, the integration over the momentum has been substituted by an integral over energies and the dependence on the angles has been approximated by introducing a mean scattering time. For further details, see App. D.1.

8.2.3 Set of dynamic equations

Next, the dynamics of the Si(100) system is calculated. Applying the relaxation rate equations to the investigated system, the EOM for the 3D bulk band distribution f_{CB}, the 2D D_{down} surface band distribution $f_{D_{\mathrm{Down}}}$ and the phonon occupation number n are obtained. The dynamics of the bulk (b) and surface (s) $\mathrm{D_{down}}$ band can be divided into scattering processes towards a FERMI function within the

bands, denoted as $f^{\mathrm{b/s,intra}}$, and scattering processes into a global FERMI function between the bulk and the D_{down} band, denoted as $f^{\mathrm{b/s,inter}}$. The dynamics include the *el-el* interaction as well as the *el-LO* interaction, depicted in Fig. 8.3. The different processes will be explained further below. The assumed scattering times are chosen in order to fit the experimental data [Eic10] and are given in Table A.4. The overall equations for the dynamics read:

$$\begin{aligned}\frac{\mathrm{d}}{\mathrm{d}t}f_{\mathrm{CB}}(t,\varepsilon) = &-\frac{f_{\mathrm{CB}}(t,\varepsilon)-f^{\mathrm{b,intra}}_{\text{el-el}}[\varepsilon,T^{\mathrm{b}}_{\mathrm{el}},\mu^{\mathrm{b}}_{\mathrm{el}}]}{\tau^{\mathrm{intra}}_{\text{el-el}}(n_{\mathrm{b}})}-\frac{f_{\mathrm{CB}}(t,\varepsilon)-f^{\mathrm{b,intra}}_{\text{el-LO}}[\varepsilon,T^{\mathrm{b}}_{\mathrm{LO}},\mu^{\mathrm{b}}_{\mathrm{LO}}]}{\tau^{\mathrm{intra}}_{\text{el-LO}}}\\ &-\frac{f_{\mathrm{CB}}(t,\varepsilon)-f^{\mathrm{b,inter}}_{\text{el-el}}[\varepsilon,T^{\mathrm{tb}}_{\mathrm{el}},\mu^{\mathrm{tb}}_{\mathrm{el}}]}{\tau^{\mathrm{inter}}_{\text{el-el}}(n_{\mathrm{b}})}-\frac{f_{\mathrm{CB}}(t,\varepsilon)-f^{\mathrm{b,inter}}_{\text{el-ph}}[\varepsilon,\mu^{\mathrm{tb}}_{\mathrm{ph,300K}}]}{\tau^{\mathrm{inter}}_{\text{el-LO}}},\end{aligned} \tag{8.11}$$

$$\begin{aligned}\frac{\mathrm{d}}{\mathrm{d}t}f_{D_{\mathrm{down}}}(t,\varepsilon) = &-\frac{f_{D_{\mathrm{down}}}(t,\varepsilon)-f^{\mathrm{s,intra}}_{\text{el-el}}[\varepsilon,T^{\mathrm{s}}_{\mathrm{el}}]}{\tau^{\mathrm{intra}}_{\text{el-el}}(n_{\mathrm{s}})}-\frac{f_{D_{\mathrm{down}}}(t,\varepsilon)-f^{\mathrm{s,intra}}_{\text{el-LO}}[\varepsilon,\mu^{\mathrm{s}}_{\mathrm{LO}}]}{\tau^{\mathrm{intra}}_{\text{el-LO}}}\\ &-\frac{f_{D_{\mathrm{down}}}(t,\varepsilon)-f^{\mathrm{s,inter}}_{\text{el-el}}\left[\varepsilon,T^{\mathrm{tb}}_{\mathrm{el}},\mu^{\mathrm{tb}}_{\mathrm{el}}\right]}{\tau^{\mathrm{inter}}_{\text{el -el}}(n_{\mathrm{b}})}-\frac{f_{D_{\mathrm{down}}}(t,\varepsilon)-f^{\mathrm{s,inter}}_{\text{el-ph}}[\varepsilon,\mu^{\mathrm{tb}}_{\mathrm{ph,300K}}]}{\tau^{\mathrm{inter}}_{\text{el -LO}}}-\frac{f_{D_{\mathrm{down}}}(t,\varepsilon)}{\tau_{D_{\mathrm{down}}}},\end{aligned} \tag{8.12}$$

$$\begin{aligned}\frac{\mathrm{d}}{\mathrm{d}t}n(t) = &-\frac{n(t)-n_0}{\tau_{\mathrm{LO}}}+\frac{1}{\tau^{\mathrm{intra}}_{\text{el-LO}}}\frac{\sqrt{2m^3_{\mathrm{bulk}}}}{\hbar^3}\\ &\times\int \mathrm{d}\varepsilon\sqrt{\varepsilon}\{[n(t)+1][1-f_{\mathrm{CB}}(t,\varepsilon)]f_{\mathrm{CB}}(t,\varepsilon+\hbar\omega_{\mathrm{LO}})-n(t)[1-f_{\mathrm{CB}}(t,\varepsilon+\hbar\omega_{\mathrm{LO}})]f_{\mathrm{CB}}(t,\varepsilon)\}.\end{aligned} \tag{8.13}$$

The dynamics of the LO phonon mode $n(t)$ has already been described in Sec. 8.1.2. The phonon mode is determined by relaxation of the hot electrons in the CB $[f_{\mathrm{CB}}(t,\varepsilon)]$ under the emission$[\sim n(t)+1]$ and the absorption $[\sim n(t)]$ of one LO phonon with a phonon energy of $\hbar\omega_{\mathrm{LO}} = 65$ meV. For later times the LO phonons decay into a phonon equilibrium n_0 at room temperature $T_0 = 300$ K.

The dynamics of the electrons are described by several relaxation rate terms, originating from different many-body processes: In the first hundred femtoseconds, the most prominent process is the relaxation of the initial non-equilibrium distribution within the bulk band towards the CBM. Responsible for this fast relaxation is the *el-el* scattering ($\tau^{\mathrm{intra}}_{\text{el-el}}$), depicted as the solid red arrow in Fig. 8.3, which decreases for decreasing electron bulk density n_{b}: $[\tau^{\mathrm{intra}}_{\text{el-el}}(n_{\mathrm{b}}) = \tau^{\mathrm{intra}}_{\text{el,0}}(n_{\mathrm{init}}/n_{\mathrm{b}})]$, with the initial electron bulk density n_{init}. This drives the occupations into a local equilibrium $f^{\mathrm{b,intra}}_{\text{el-el}}[\varepsilon,T^{\mathrm{b}}_{\mathrm{el}},\mu^{\mathrm{b}}_{\mathrm{el}}]$ in the CB. Considering the density dependence, it has been shown that screening effects lead to a sub-linear density dependence [BFC$^+$88]. However, since only moderate changes at short time scales have been detected, screening is not included in the calculations. During the intraband relaxation, LO phonons are emitted (solid blue arrows in Fig. 8.3), heating the phonon reservoir, which couples back to the distribution in the bulk band $f_{\mathrm{CB}}(t,\varepsilon)$. This *el-LO* intraband term acts on a similar timescale ($\tau^{\mathrm{intra}}_{\text{el-LO}}$), leading to a phonon temperature dependent local equilibrium $f^{\mathrm{b,intra}}_{\text{el-LO}}[\varepsilon,T^{\mathrm{b}}_{\mathrm{LO}},\mu^{\mathrm{b}}_{\mathrm{LO}}]$, with the temperature of the heated reservoir $T^{\mathrm{b}}_{\mathrm{LO}}$. The same processes are applied to the D_{down} band, where the *el-el* intraband relaxation time is now dependent on the surface density $[\tau^{\mathrm{intra}}_{\text{el-el}}(n_{\mathrm{s}}) = \tau^{\mathrm{intra}}_{\text{el,0}}(n_{\mathrm{init}}L_{\mathrm{s}}/n_{\mathrm{s}})]$, with the width of the surface L_{s}.

Besides the intraband processes, the electrons scatter from the bulk band into the unoccupied D_{down} surface band. This interband process, also denoted as surface recombination, is initially driven by the Auger-type *el-el* scattering $[\tau^{\mathrm{inter}}_{\text{el-el}}(n_{\mathrm{b}}) = \tau^{\mathrm{inter}}_{\text{el,0}}(n_{\mathrm{init}}/n_{\mathrm{b}})^2]$ [Vor00], which decreases for decreasing density in the bulk (dotted red arrow in Fig. 8.3). Electron scattering can bridge large energies for high electron densities under the restriction of energy conservation, forming a global two band equilibrium between bulk and surface $f^{\mathrm{b/s,inter}}_{\text{el-el}}[\varepsilon,T^{\mathrm{tb}}_{\mathrm{el}},\mu^{\mathrm{tb}}_{\mathrm{el}}]$. For electrons near the bulk minimum, it is possible to scatter via phonons with high parallel momentum (dotted blue arrow in Fig. 8.3. This process becomes dominant (but is still small) for large times ($\tau^{\mathrm{inter}}_{\text{el-LO}}$), driving the two band distribution to a global equilibrium $f^{\mathrm{b/s,inter}}_{\text{el-ph}}[\varepsilon,\mu^{\mathrm{tb}}_{\mathrm{ph,300K}}]$ on a picosecond scale [Bue08]. The population of the surface band decays with a D_{down} lifetime $\tau_{D_{\mathrm{down}}}$.

To obtain the local and global equilibrium functions corresponding to the different many-body processes, the chemical potentials μ and temperatures T are calculated for each time step. These two values can be determined by regarding the electron density and the energy density conservation. The detailed calculations for obtaining μ and T for the local and the global equilibrium functions as well as the values for τ and L_{surf} are given in App. D.2.

8.3 Relaxation dynamics

The bulk-surface dynamics is calculated under the assumption that the optical excitation generates an initial non-thermal electron density n_{init}, which is solely located in the bulk band ($n_{\text{b},t=0} = n_{\text{init}}$) while the D_{down} surface band is unoccupied ($n_{\text{s},t=0} = 0$). The initial bulk distribution is approximated as Gaussian, located about 0.6 eV above the CBM, estimated by the experimental data. The standard deviation σ and the amplitude A_0 of the Gaussian distribution are chosen in a way that the energy density corresponds to a hot carrier bulk distribution with a temperature of $T \approx 4500$ K, estimated the experimental data ($A_0 = 0.009254$, $\sigma = 50$ meV).

8.3.1 Bulk-surface relaxation

First, the EOMs for the carrier densities Eq. (8.11) and (8.12) are investigated. The time evolution of f_{CB} and $f_{D_{\text{down}}}$ is shown in Fig. 8.4(a) and (b):[4] The theoretical simulation of the dynamics starts directly after the excitation with the probe pulse. The relaxation within the conduction band towards the CBM takes place on a femtosecond timescale mainly due to the fast *el-el* scattering time but also via slower

[4] The minimal energy ($\varepsilon = 0$) corresponds to the D_{down} band minimum.

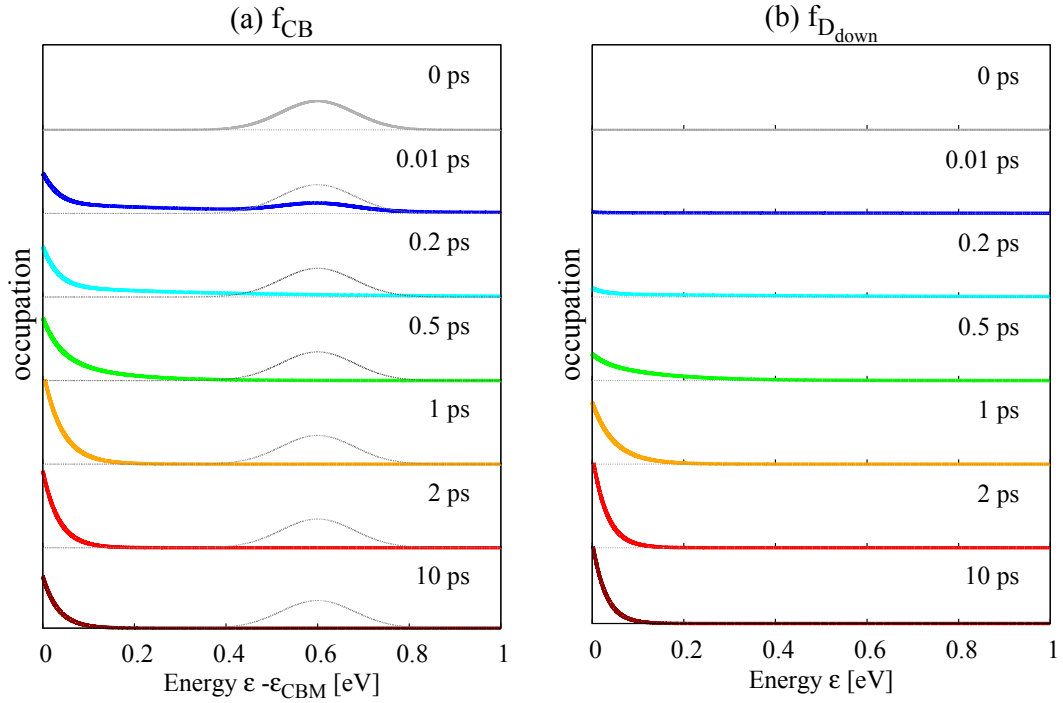

Figure 8.4 | Relaxation of an initially Gaussian distribution, located in the conduction band, in Si(100) with an initial carrier density of $n_{\text{init}} = 1.0 \cdot 10^{19}$ cm^{-3}. (a) Population distribution of the conduction band f_{CB}. (b) Population distribution of the D_{down} surface band $f_{D_{\text{down}}}$.

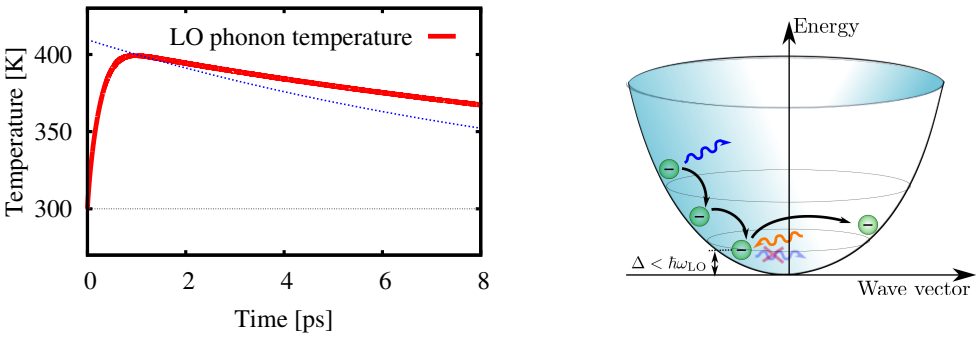

Figure 8.5 | Left: Plot of the temperature of the LO phonon mode. The dotted blue line is a fit of the temperature if the *el-ph* scattering is not taken into account. After $t = 8$ ps, the temperature of the LO phonon mode is well above room temperature (horizontal dotted grey line). Right: Schematic drawing of the electron relaxation process with LO phonons at the CBM: Reaching a momentum below the LO phonon energy, electrons cannot relax further down to the conduction band minimum.

LO phonon emission: The *el-el* scattering will thermalize the carrier distribution towards a FERMI function with a high electronic temperature $T_{el} \approx 4000$ K. However, simultaneously a relaxation via LO phonon emission takes place, but on a slower timescale. This process is accompanied by a cooling of the electronic system, as its energy dissipates to the lattice. For $t = 0.2$ ps [blue line in (a)], the signatures of the initial Gaussian distribution are no longer visible. During this time, only a few carriers have relaxed into the D_{down} band via the Auger-type *el-el* scattering, see blue lines in Fig. 8.4(b). Although the *el-ph* scattering takes places on a slower time scale, it still contributes to the equilibration of the carriers and the distribution further relaxes towards the CBM. Additionally, electrons scatter into the D_{down} band via surface recombination. The steady increase of the occupation in the D_{down} band [Fig. 8.4(b)] is visible for increasing time. Due to the fast surface recombination, the carriers mainly relax from the conduction band directly to the D_{down} band minimum. Since the calculations are done in relaxation rate approximation, the relaxation of the carrier distribution contains no quantum kinetics (such as the phonon replica in Chap. 6) but is determined by the equilibrium FERMI functions in Eq. (8.11) and Eq. (8.12).

8.3.2 Longitudinal optical phonon heating

Next, the lattice heating originating from the relaxation of the hot carriers will be investigated. To extract a temperature for the LO phonon mode, it is assumed that the LO phonon mode is in a quasi-equilibrium, described by the BOSE distribution $n(\hbar\omega_{\text{LO}})$ for each time step. Hence, the temperature T_{LO} is obtained via: $T_{\text{LO}} = \hbar\omega_{\text{LO}}/k_{\text{B}} \ln\left(1/n(\hbar\omega_{\text{LO}}) + 1\right)^{-1}$. The detailed calculation can be found in App. D.1. Figure 8.5(left) shows the LO phonon temperature for increasing time. Within the first picosecond the temperature increases up to $T_{\text{LO}} = 400$ K. This rise is due to the pronounced emission of LO phonons during the hot carrier relaxation, since an increasing temperature is directly connected to the increasing LO phonon distribution. After 1 ps the temperature decreases on a slower timescale, determined by the LO phonon lifetime τ_{LO}. The decrease of the temperature is further slowed down since the hot carriers in the conduction band are located less than one LO phonon energy ($\hbar\omega_{\text{LO}} = 65$ meV) above the CBM. A schematic drawing of this process is given in Fig. 8.5(right): After the pulse excitation, the electrons relax towards the conduction band minimum around the X-valley. During the down-scattering, LO phonons are emitted (blue wavy arrows) and the lattice is heated. Nearly reaching the CBM the relaxation slows down if the electron distribution is less than one LO-phonon energy $\hbar\omega_{\text{LO}}$ above the CBM since LO phonons cannot be further emitted. Instead, the absorption of phonons (red wavy arrows) and the successive re-emission of LO phonons becomes more likely, leading

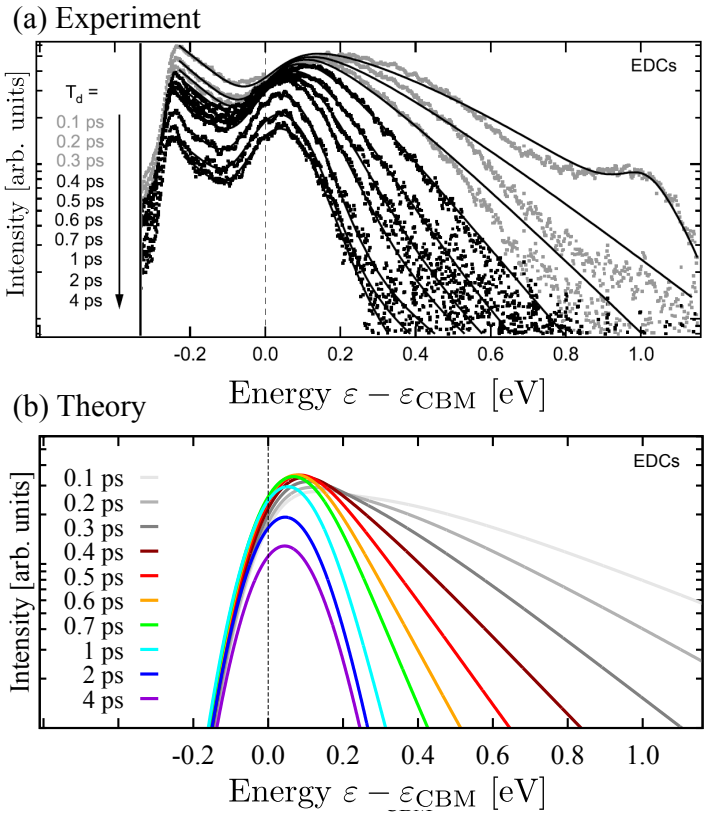

Figure 8.6 | (a) Experimentally extracted electron distribution curves (EDCs), taken from [Eic10]. The solid black lines display the best fit to the experimental data points. (b) Simulated EDCs in the CB. The CB distributions are convoluted with a Gaussian pulse.

to *el-LO* scattering processes even at longer times. Therefore, the *el-LO* scattering dynamics leads to slower temperature decrease, compared to the standard exponential decay with the LO lifetime τ_{LO} into a BOSE distribution with the normal room temperature. For comparison, the exponential decay of the temperature is plotted as dotted blue line in Fig. 8.5(left) if the scattering contributions in Eq. (8.13) are neglected, that is, if the integral equals zero. In conclusion, the relaxation of hot carriers leads to a lattice temperature which is well above the room temperature of $T_0 = 300$ K, even after 8 ps. The next subsection will show that the heated lattice couples back and influences the electronic system.

8.3.3 Comparison with the experiment

Now the numerics are compared with the experimental results of Eickhoff et al. [Eic10]. The measurements are done with an angle- and time-resolved 2PPE spectroscopy, where a pump pulse excites a high carrier concentration of $n_{\mathrm{b}} = 1 \cdot 10^{19}$ cm^{-3} from the valence band into the X-valley of the CB. The probe pulse then tracks the momentum- and energy relaxation of the hot carriers in the CB as a function of the delay time between the pulses T_{d}, by lifting electrons to states above the vacuum energy. The corresponding distribution curves of the carriers over the energy are extracted within an emission angle of $\pm 2^{\circ}$ around the maximum intensity along the energy $E - E_{\mathrm{CBM}}$.

Electronic distribution curves - The collected data points of the 2PPE measurements are shown in Fig. 8.6(a) for delay times $T_{\mathrm{d}} = 0.1 - 4$ ps. To extract the electronic distribution, the data points are

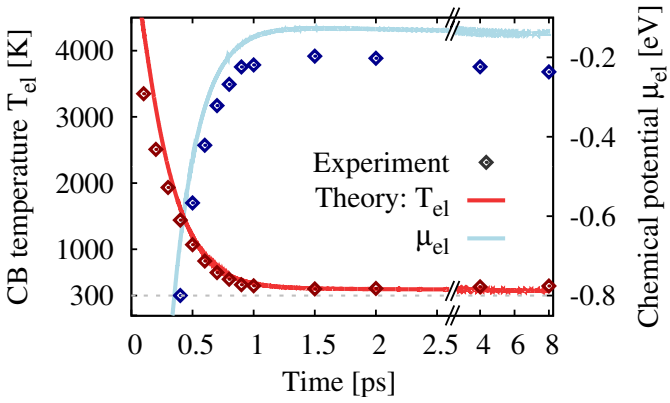

Figure 8.7 | Plot of the CB temperature T_{el} and the chemical potential μ_{el}. The graph shows the theoretical results (solid lines) and the values of the experimentally extracted EDCs in Fig. 8.6(a) (diamond shaped symbols).

approximated with electronic distribution curves (EDCs). The model of the EDCs consists of a temperature and chemical potential dependent FERMI function, multiplied with the density of states for the bulk CB ($\propto \sqrt{E-E_{\mathrm{CBM}}}$). The signal below $E-E_{\mathrm{CBM}}=0$ as well as the protrusion at $E-E_{\mathrm{CBM}}\approx 1$ eV for $T_{\mathrm{d}}=0.1$ ps does not originate from the CB distribution but arises from photoemission out of the defect states within the band gap (below $E-E_{\mathrm{CBM}}=0$) and from the ionization of the electrons in the occupied D_{up} state (protrusion at $E-E_{\mathrm{CBM}}\approx 1$ eV) [Eic10]. To model the experimental inhomogeneous broadening, the EDCs are additionally convoluted with a Gaussian with a full width at half maximum (FWHM) of 0.15 eV. The data points for a time of $T_{\mathrm{d}}=0.1-0.3$ ps cannot be properly approximated with EDCs [grey data points in Fig. 8.6(a)]. The corresponding EDCs, determined by the experiment, are depicted as solid black lines. In the same manner the EDCs of the numerical simulations obtained from Eq. (8.11) - (8.13) are extracted. For this purpose, the electronic distributions, shown for different delay times in Fig. 8.3(a), are also multiplied with the bulk density of states and convoluted with a Gaussian of 0.15 eV. The EDCs, extracted from the numerics, are shown in Fig. 8.6(b). It has been found that the shift of the maxima of the EDCs for different times strongly depend on the *el-el* scattering time. The best agreement is found for $\tau_{\mathrm{el},0}^{\mathrm{intra/inter}}=20$ fs, which unsurprisingly suggests ultrafast *el-el* scattering . In addition to the maximum shift, a signal decrease of the EDCs is visible. This is due to the scattering from the CB to the D_{down} band via surface recombination, which will be shown and discussed in Fig. 8.8.

Temperature and chemical potential - For a better comparison between experiment and theory, the CB temperature T_{el} and the chemical potential μ_{el}, which are used for the experimentally determined EDCs, are shown in Fig. 8.7 as red/blue diamond shaped symbols for $T_{\mathrm{el}}/\mu_{\mathrm{el}}$. The simulated T_{el} and μ_{el} curves are the calculated values of the temperature $T_{\mathrm{el}}^{\mathrm{b}}$ and the chemical potential $\mu_{\mathrm{el}}^{\mathrm{b}}$ of the local FERMI equilbrium function in the CB $f_{\text{el-el}}^{\mathrm{b,intra}}$ in Eq. (8.11). The comparison between experiment and theory shows good agreement. The chemical potential obtained from the experiment and from the simulation slightly differs for long times by about 0.1 eV. This could be due to the uncertainty of the chosen bulk effective mass m_{bulk} (see Table A.4). The temperature displays a strong decrease within the first ps, dropping from $T_{\mathrm{el}}>4000$ K for $t=0$ ps to $T_{\mathrm{el}}<500$ K for $t=1$ ps. After 1 ps, the bulk temperature stays well above room temperature (dotted grey line). This elevated temperature can also be found within a time interval of more than 10 ps (not shown here). Unlike in the experimental data, which suggests that the temperature even increases for 8 ps, the numerically obtained temperature slowly decreases since it is connected to the decreasing lattice temperature, shown in Fig. 8.5: The elevated temperature of the LO phonon mode couples back to the electronic bulk temperature, leading to the prolonged heating. The best agreement between experiment and theory is achieved for a LO phonon lifetime of $\tau_{\mathrm{LO}}=10$ ps, which is supported by the values reported in silicon [UAS^{+}97] and germanium [Oth98]. However, also shorter lifetimes of 2 ps have been found in [MC84].

Density dependence - As it has been stated, the intensity of the EDCs decreases for increasing time

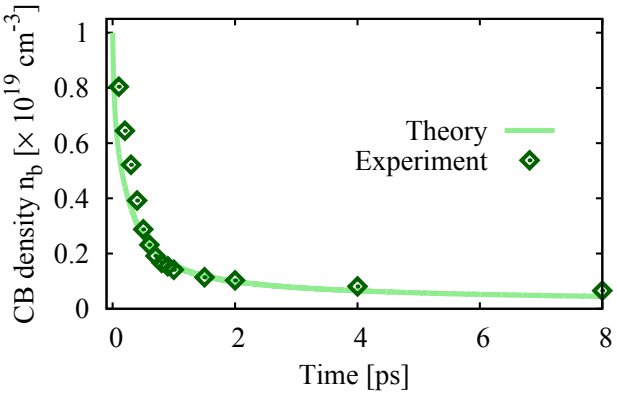

Figure 8.8 | Plot of the CB density n_b. The graph shows the theoretical results (solid line) and the experimentally obtained CB density from the integrated EDCs of Fig. 8.6(a) (diamond shaped symbols).

which is directly connected to the density decrease in the CB. The main scattering channel out of the CB is the interband scattering into the D_{down} surface band via surface recombination [WKFR04, TIT09]. Figure 8.8 shows the bulk electron density n_b. The experimental data for the density (diamond shaped symbols) is obtained by the determination of the area of the EDCs in Fig. 8.6(a). The data of the simulation is shown as a solid line. Similar to the temperature decrease, the CB electrons also exhibit a strong density decrease within the first picosecond, mainly driven by the *el-el* interband scattering. Since the *el-el* scattering time decreases with decreasing density, the scattering to the D_{down} surface is considerably slowed down after 1 ps. The further, slowed down decrease takes place under phonon emission with a high parallel momentum, see also the dotted blue arrow in Fig. 8.3. The experimental data are in very good agreement with the numerical results.

8.4 Conclusions

In conclusion, the conduction band - surface dynamics in silicon was investigated. While the bulk and surface dynamics have been treated in a relaxation rate approximation, the LO phonon dynamics was calculated with a more elaborate scheme via the reduced PEIERLS equation. Here, the dominant LO phonon mode is considered, treated within the EINSTEIN model with a momentum independent coupling strength. The comparison between experiment and theory shows very good agreement in the energy distribution curves, the curve of the bulk temperature, as well as the conduction band density. In particular, the simulations reproduce the elevated temperature of the conduction band carriers for a time of $T_d = 8$ ps. This indicates that during the relaxation of the hot carriers towards the conduction band minimum, the dominant LO phonon mode is heated. Subsequently, it couples back to the system via a heated lattice temperature. The long lasting elevated temperature of the LO mode is due to the long phonon lifetime of $\tau_{\text{LO}} = 10$ ps. Additionally, the emission of LO phonons is slowed down since electrons, which are located less than one LO phonon energy above the conduction band minimum cannot relax further down, leading to a heated electronic system compared to the normal exponential decay.

As a consequence of the approximations made in the theoretical description of the system, the model lacks quantum kinetic behavior and is mainly determined by the chosen scattering times. But it is reasonable to assume that the lack of quantum kinetics for short times only weakly affects the long-time behavior of the overall dynamics, in particular that of the hot carrier relaxation. Furthermore, since the used parameters are supported by previous measurements on silicon and germanium, appropriate scattering times have been applied for modelling the long-time dynamics in silicon. Concluding from the good agreements between experiment and theory, and since a full quantum kinetic description of the system is yet beyond numerical capacities, the theoretical model seems to be adequate for the description of the experimental observations. As a further aspect, the dominant LO phonon mode could be treated more thoroughly by regarding the momentum dependence. Also, other phonon branches should be

included. However, the feasibility of a more detailed treatment of the bulk-surface dynamics in silicon must be further discussed in future investigations.

Part IV

Intersublevel transitions in a quantum dot

Chapter 9

Intersublevel quantum dot model

9.1 Introduction

In the previous part, the main focus lay on the intersubband transitions in quantum wells. There, the subband transition energies covered a certain spectral range due to their in-plane subband dispersion. In terms of their usage in opto-electronic devices, such as lasers, this is a clear disadvantage since lasers with a narrow bandwidth are preferred. Instead, nanostructures with discrete energy levels are favourable. A possible candidate to achieve this are zero-dimensional nano-objects, so-called *quantum dots* (QDs), where the full quantization of the electronic states can be gained by restricting the electronic motion in all dimensions.

Consequently, after the successful growth of quantum wells, many efforts have been made towards forming QDs, which succeeded in the eighties [EO81, GGM$^+$85, RRA$^+$88]. Nowadays the advances in crystal growth techniques allow for a proper control of shapes and sizes of QDs [BGL99], finding its use in low-threshold laser devices [Bim05], for single-photon emitters [SAB07] or entangled-photon sources [CMD$^+$10]. The most prevailed technique is the fabrication of self-assembled quantum dots through the STRANSKI-KRASTANOV growth. Here, QDs are formed when a semiconductor material is placed on a substrate which a large lattice mismatch. The resulting strain during the growth causes a built up of small islands, the QDs.

In recent years it has also been proposed to use QDs for THz cascade lasers since it is expected that the discrete energy spacing between the QD subbands (which lies in the few meV range) and the dots low threshold should improve the performance of quantum cascade lasers (QCLs) [DS08]. Already, successful demonstrations showed how to incorporate QDs in the quantum well QCLs [LNC$^+$12].

The investigation of the intersublevel (ISL) dynamics of a quantum dot will be the subject of this part. In particular, the model is focused on a single QD with strong electron-LO phonon (*el-LO*) interaction. With the LO phonon energy being on the same order of magnitude as the ISL gap energy, the scattering with LO phonons constitutes a major relaxation channel for non-radiative intersublevel transitions. After introducing the general model system and the important interaction mechanisms in the following section, the eigenvalues and the coupling matrix elements are determined in Sec. 9.2.1 and Sec. 9.2.2. Theoretical tools for the development of the EOM are provided in Chap. 10. Subsequently, the results will be presented in Chap 11. The main work has primarily been done by Sandra Kuhn and can be found in [KSR$^+$12].

9.2 General model system

The model system consists of a single electron in a spherical QD, having a fundamental gap energy of a few eV between the valence (v) and the conduction (c) band. Each of the two bands contain two sublevels. In this chapter the interest lies in the sublevel transitions within one band. Hence, the dynamics

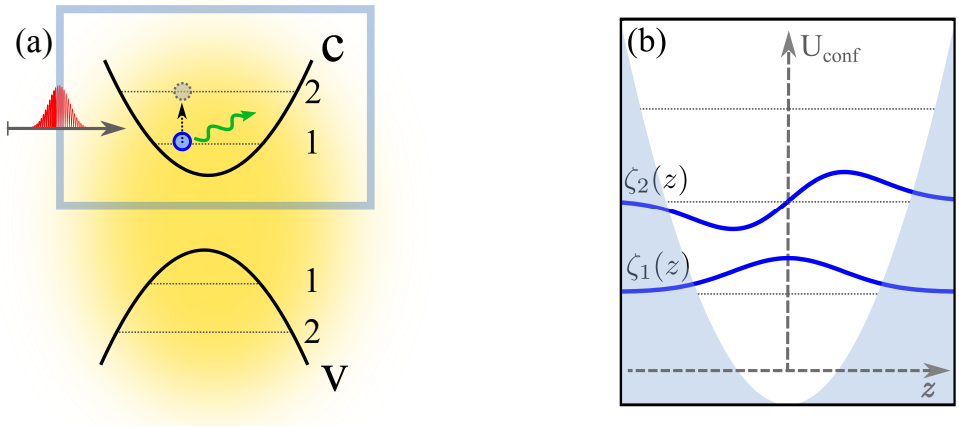

Figure 9.1 | (a): Spherical quantum dot model. The dynamics is restricted to the conduction band sublevels, where one electron (blue dot) is initially in an equilibrium position in the lower conduction sublevel. The LO phonons (green arrow) of the system are in equilibrium with an external phonon bath (yellow cloud). (b): Confinement potential and eigenfunctions for the first two sublevels along one confinement direction.

will be restricted to the conduction band. The equilibrium position of the electron is in the lower conduction band sublevel c1. A schematic of the QD model is given in Fig. 9.1(a). As already mentioned before, the interaction between electrons and LO phonons is now in the strong coupling regime and will play a major role in the ISL dynamics [HVL+97]. Thus, when excited with an electromagnetic field (drawn in the figure as a red pulse), the response of the QD is expected to exhibit distinct signatures of the strong *el-LO* coupling (green arrow). As before, the LO phonons are given in terms of the creation ($\hat{b}_{\mathbf{q}}^{\dagger}$) an annihilation operators ($\hat{b}_{\mathbf{q}}$). In the previous part, Part III, the electronic and phononic operators could be factorized ($\langle \hat{a}^{\dagger}\hat{a}\ \hat{b}^{\dagger}\hat{b}\ \rangle \approx \langle \hat{a}^{\dagger}\hat{a}\ \rangle\langle \hat{b}^{\dagger}\hat{b}\ \rangle$) and the phonons were treated as a bath, that is, $\langle \hat{b}_{\mathbf{q}}^{\dagger}\hat{b}_{\mathbf{q}}\rangle = n_{\mathbf{q}}$, with the BOSE function $n_{\mathbf{q}}$.

In the QD, the setting is very different: Due to the strong *el-LO* coupling, correlations between the carriers and the lattice vibrations cannot be neglected and a decoupling of their dynamics is impossible, see also Chap. 10. However, the specific strong-coupling scenario will exclusively effect the LO phonon mode. On the other hand, it is not the only mode present in the system. Thus, to account for the coupling of the LO phonons to other phonon modes, an external reservoir of harmonic oscillators $\langle \hat{b}_{\xi}^{(\dagger)}\rangle$ is introduced [yellow cloud in Fig. 9.1(a)]. The weak interaction provides a more realistic treatment of the coupling to the phonons, resulting in an equilibrium state of the system which depends on the temperature of the external reservoir.

For the calculation of the dynamics, the following system Hamiltonian has to be considered:

$$\hat{H}_{\text{sys}} = \hat{H}_0 + \hat{H}_{\text{el-ph}} + \hat{H}_{\text{em}} + \hat{H}_{\text{ext}} + \hat{H}_{\text{ph-ext}}, \tag{9.1}$$

with the Hamiltonian of the external phonon bath $\hat{H}_{\text{ext}} = \sum_{\xi} \varepsilon_{\xi} \hat{d}_{\xi}^{\dagger}\hat{d}_{\xi}$ and the Hamiltonian which couples the LO phonons to the external phonon bath $\hat{H}_{\text{ph-ext}} = \sum_{\xi,\mathbf{q}} A_{\xi}^{\mathbf{q}} \hat{b}_{\mathbf{q}}^{\dagger}\hat{d}_{\xi} + \sum_{\xi,\mathbf{q}} A_{\xi}^{\mathbf{q}*} \hat{d}_{\xi}^{\dagger}\hat{b}_{\mathbf{q}}$. The other Hamiltonians, that is the free-carrier Hamiltonian $\hat{H}_0 = \hat{H}_{0,\text{el}} + \hat{H}_{0,\text{ph}}$, the electron-phonon (*el-ph*) interaction Hamiltonian $\hat{H}_{\text{el-ph}}$, and the semi-classical electron-light Hamiltonian $\hat{H}_{\text{em}}$, have already been introduced in Sec. 2.3.2. The gap energy between the levels will be varied between 30 - 50 meV, which is a realistic value for ISL transition energies [ZGC+09]. To model the dynamics, the coupling parameters must be calculated. Consequently, the eigenfunctions and eigenenergies in the QD are presented in the following subsections.

9.2.1 Wave functions and eigenenergies

For the general QD model, the confinement potential U_{conf} is assumed to be parabolic:

$$U_{\text{conf}}(\mathbf{r}) = m_{\text{eff}}\omega_{\text{g}}\mathbf{r}^2, \tag{9.2}$$

with the eigenfrequency ω_{g} of the electron and the bulk effective mass m_{eff} of GaAs. The Cartesian coordinates $\{x,y,z\}$ are chosen as the real space basis set. The SCHRÖDINGER equation for the time-independent part of the electronic wave function $\Psi_{\text{el}}(\mathbf{r},t) = \Phi(\mathbf{r})\exp(-\frac{\mathrm{i}}{\hbar}\varepsilon t)$:

$$\varepsilon\Phi(\mathbf{r}) = \left[-\frac{\hbar\nabla_{\mathbf{r}}^2}{2m_{\text{eff}}} + m_{\text{eff}}\omega_{\text{g}}\mathbf{r}^2\right]\Phi(\mathbf{r}). \tag{9.3}$$

Equation (9.3) is the differential equation for a single harmonic oscillator. The corresponding eigenenergy has already been determined in Sec. 2.3.2 for the derivation of the *el-ph* Hamiltonian and reads:

$$\varepsilon_n = \hbar\omega_{\text{g}}n \qquad \text{with the sublevel gap energy} \qquad \varepsilon_{\text{gap}} = \varepsilon_2 - \varepsilon_1 = \hbar\omega_{\text{g}}. \tag{9.4}$$

Being fully confined, the electronic wave function are described by confinement functions in each direction: $\Phi_{l,m,n}(\mathbf{r}) = \zeta_l(x)\zeta_m(y)\zeta_n(z)u_{c,\mathbf{k}\approx 0}(\mathbf{r})$. The eigenfunctions of the harmonic oscillator are known as [CT99]:

$$\zeta_n(x) = \left(\frac{m_{\text{eff}}\omega_{\text{g}}}{\pi\hbar}\right)^{1/4}\frac{1}{\sqrt{2^n n!}}H_n\left(\sqrt{\frac{m_{\text{eff}}\omega_{\text{g}}}{\hbar}}x\right)\mathrm{e}^{-\frac{1}{2}\frac{m_{\text{eff}}\omega_{\text{g}}}{\hbar}x^2}, \tag{9.5}$$

with the Hermite polynomials $H_n = (-1)^n\mathrm{e}^{x^2}\frac{\partial^n}{\partial x^n}\mathrm{e}^{-x^2}$. Figure 9.1(b) shows the first and the second confinement function along one direction. The two lowest eigenfunctions then read:

$$\begin{aligned}\Phi_1(\mathbf{r}) &= \zeta_0(x)\zeta_0(y)\zeta_0(z)\\ &= \left(\frac{m_{\text{eff}}\omega_{\text{g}}}{\pi\hbar}\right)^{3/4}\mathrm{e}^{-\frac{1}{2}\frac{m_{\text{eff}}\omega_{\text{g}}}{\hbar}(x^2+y^2+z^2)}, \qquad (9.6)\\ \Phi_{2(A,B,C)}(\mathbf{r}) &= A\zeta_1(x)\zeta_0(y)\zeta_0(z) + B\zeta_0(x)\zeta_1(y)\zeta_0(z) + C\zeta_0(x)\zeta_0(y)\zeta_1(z)\\ &= \left(\frac{m_{\text{eff}}\omega_{\text{g}}}{\pi\hbar}\right)^{3/4}\left(\frac{2m_{\text{eff}}\omega_{\text{g}}}{\hbar}\right)^{1/2}(Ax+By+Cz)\mathrm{e}^{-\frac{1}{2}\frac{m_{\text{eff}}\omega_{\text{g}}}{\hbar}(x^2+y^2+z^2)}. \qquad (9.7)\end{aligned}$$

The second energy level is triply degenerated considering the eigenfunctions, where the constants A,B,C are variable factors with $|A|^2+|B|^2+|C|^2 = 1$.[1] However, in reality, the degeneracy of the second energy level is lifted by an anisotropic splitting [ZGC+09]. Thus, only one eigenfunction of the excited state has to be considered in the following calculations. Within this work, it is assumed that with an appropriate transformation scheme, two constants vanish and the third constant can be set to one. Without loss of generality, the constants are chosen in following way: $A = B = 0, C = 1$.

9.2.2 Coupling matrix elements

With the wave functions obtained in the previous subsection, the coupling matrix elements for the electromagnetic and the *el-LO* coupling can be calculated according to Sec. 2.3.2.

Electric dipole matrix elements - Analogous to the determination of the matrix elements of the ISB model, the integral of the dipole matrix element [Eq, (2.7)] can be decomposed into the lattice and

[1] For example, one possible combination of the three eigenstates is $\Phi_{2(1,0,0)}, \Phi_{2(0,1,0)}, \Phi_{2(0,0,1)}$.

cells vectors. Due to the chosen constants, only the integration of the confinement functions along the z-direction remains: $d_{\alpha\beta}(z) = e_0 \int_{-\infty}^{\infty} \zeta_\alpha^*(z) z \zeta_\beta(z)$. The dipole matrix elements then read:

$$d_{\alpha\beta}(z) = \begin{cases} e_0 \frac{\pi^{3/2}}{8\sqrt{2}} \left(\frac{m_{\text{eff}}\omega_{\text{g}}}{\pi\hbar}\right)^{3/2} \left(\frac{2m_{\text{eff}}\omega_{\text{g}}}{\hbar}\right)^{1/2} \left(\frac{1}{2}\frac{m_{\text{eff}}\omega_{\text{g}}}{\hbar}\right)^{-5/2} & \text{for} \quad \alpha \neq \beta, \\ 0 & \text{for} \quad \alpha = \beta, \qquad (\alpha, \beta = 1,2). \end{cases} \tag{9.8}$$

For other incoming directions of the electromagnetic field, the dipole matrix element equals zero due to the above chosen constants $A = B = 0$.

Fröhlich form factors - Next, the matrix elements for the *el-ph*-Hamiltonian are evaluated similar to Sec. 4.2.3. As mentioned, the interaction is considered between electrons and LO phonons. Thus, the FRÖHLICH matrix elements $g_{\mathbf{q}}^{ij}$ have to be calculated:

$$\begin{aligned} g_{\mathbf{q}}^{ij} &= \mathrm{i} \left[\frac{e^2 \hbar \omega_{\text{LO}}}{2 \cdot \varepsilon_0 V} (\varepsilon_\infty^{-1} - \varepsilon_s^{-1}) \right]^{\frac{1}{2}} \frac{1}{|\mathbf{q}|} \int \mathrm{d}\mathbf{r} e^{\mathrm{i}\mathbf{q}\mathbf{r}} \Phi_i^*(\mathbf{r}) \Phi_j(\mathbf{r}) \\ &= g_{\mathbf{q}}^{\text{3D}} \mathscr{F}_{ij}^{\mathbf{q}}, \end{aligned} \tag{9.9}$$

with the 3D FRÖHLICH coupling matrix element $g_{\mathbf{q}}^{\text{3D}}$, the sublevel dependent FRÖHLICH form factors $\mathscr{F}_{ij}^{\mathbf{q}} = \int \mathrm{d}\mathbf{r} e^{\mathrm{i}\mathbf{q}\mathbf{r}} \Phi_i^*(\mathbf{r}) \Phi_j(\mathbf{r})$ and the 3D wave vector $\mathbf{q}$. Calculating the integrals, the form factors are:

$$\begin{aligned} \mathscr{F}_{11}^{\mathbf{q}} &= \mathrm{e}^{-\frac{\hbar}{4m_{\text{eff}}\omega_{\text{g}}}|\mathbf{q}|^2} \qquad \text{and} \qquad \mathscr{F}_{22}^{\mathbf{q}} = \frac{\hbar^2 q_z - 2m_{\text{eff}}\omega_{\text{g}}}{8m_{\text{eff}}\omega_{\text{g}}} \mathrm{e}^{-\frac{\hbar}{4m_{\text{eff}}\omega_{\text{g}}}|\mathbf{q}|^2} \\ \mathscr{F}_{12}^{\mathbf{q}} &= \mathrm{i} \frac{1}{2\sqrt{2}} \left(\frac{\hbar}{m_{\text{eff}}\omega_{\text{g}}}\right)^{1/2} q_z \mathrm{e}^{-\frac{\hbar}{4m_{\text{eff}}\omega_{\text{g}}}|\mathbf{q}|^2} \qquad \text{and} \qquad \mathscr{F}_{12}^{\mathbf{q}} = \mathscr{F}_{21}^{\mathbf{q}}. \end{aligned} \tag{9.10}$$

Detailed calculations for the *el-LO* coupling matrix elements can be found in [Kuh11]. It should be noted that in this general QD model, ISL gap energy is freely chosen. That means, that the eigenfrequency ω_{g} of the confinement potential is chosen according to our needs (but within the reasonable range of 40 - 60 meV). Nonetheless, the comparison of the general model with experimental data of InAs/GaAs QDs led to good agreements considering the *el-LO* coupling strength [HVL$^+$97, ZGC$^+$09, SDW$^+$11]. Therefore, the dynamics of this model system serves as a realistic model study of the *el-LO* interaction in ISL QDs.

Chapter 10

Theoretical framework

10.1 Hierarchy problem and induction method

As already investigated in Sec. 4.3, the dynamics of n-particle operators couples to $(n+1)$-particle operators if the HEISENBERG EOM includes many-body Hamiltonians such as the FRÖHLICH interaction. Unlike in the former part, where the correlation expansion has been used to solve the hierarchy problem, this perturbative scheme cannot be applied to the ISL QD system due to the strong coupling between electrons and phonons. Instead, the so-called *induction method* will be introduced, which is an analytically exact solution of the EOMs under assumption of a fixed number of electrons in the system [CRCK10] and the coupling to only one phonon branch. If the EOMs of the electronic quantities, such as the electronic density or the microscopic polarization are evaluated for the model system, they couple in higher orders solely to phonon operators, that is:

$$\begin{aligned} \frac{\mathrm{d}}{\mathrm{d}t}\langle \hat{a}_a^\dagger \hat{a}_b \rangle_{\text{el-ph}} &\sim \langle \hat{a}_c^\dagger \hat{a}_d \hat{b}_{\mathbf{q}}^{(\dagger)} \rangle + \cdots \\ \frac{\mathrm{d}}{\mathrm{d}t}\langle \hat{a}_c^\dagger \hat{a}_d \hat{b}_{\mathbf{q}}^{(\dagger)} \rangle_{\text{el-ph}} &\sim \langle \hat{a}_g^\dagger \hat{a}_j \hat{b}_{\mathbf{q}}^{(\dagger)} \hat{b}_{\mathbf{q}}^{(\dagger)} \rangle + \cdots \end{aligned} \tag{10.1}$$

For the calculation of the EOMs, it is useful to find a general solution of the commutator of a single phonon annihilation operator $\hat{b}_{\mathbf{q}}$ with a series of phonon creation operators $\left(\hat{b}_{\mathbf{q}}^\dagger\right)^n$. This commutator is given by [AHK99]:

$$\left[\hat{b}_{\mathbf{q}'}, \left(\hat{b}_{\mathbf{q}}^\dagger\right)^n\right]_- = n\left(\hat{b}_{\mathbf{q}}^\dagger\right)^{n-1} \delta_{\mathbf{q},\mathbf{q}'} \tag{10.2}$$

Eq. (10.2) can be proven via the induction method and is also valid for the hermitian conjugate. With this relation, it is possible to calculate the commutators for an arbitrary number of phonon operators.

Note that in the HEISENBERG EOM, the dynamics considering the *el-ph* Hamiltonian will be evaluated with the induction method. In contrast, the interaction of the system with the external phonon reservoir is treated within the correlation expansion up to second order together with the bath assumption $\langle \hat{d}_\xi^\dagger \hat{d}_\xi \rangle = n_\xi$ (see Sec. 4.3) since the coupling to the external harmonic oscillators is assumed to be weak.

10.2 Equations of motion

As stated in the previous section, the electronic operators couple in higher order to a series of LO phonon creators and annihilators. Thus, it is reasonable to combine the sum of LO phonon operators by defining

a n-phonon operator $B^{l,m}_{l',m'}$, indicating different LO phonon creators and annihilators with its indices:

$$\hat{B}^{l,m}_{l',m'} = \left(\hat{B}^{\dagger}_{\mathrm{nd}}\right)^{l} \left(\hat{B}^{\dagger}_{\mathrm{d}}\right)^{m} \left(\hat{B}_{\mathrm{d}}\right)^{m'} \left(\hat{B}_{\mathrm{nd}}\right)^{l'}, \tag{10.3}$$

with the abbreviations $\hat{B}^{(\dagger)}_{\mathrm{nd}} = \sum_{\mathbf{q}} g^{21(*)}_{\mathbf{q}} \hat{b}^{(\dagger)}_{\mathbf{q}}$ and $\hat{B}^{(\dagger)}_{\mathrm{d}} = \sum_{\mathbf{q}} (g^{22(*)}_{\mathbf{q}} - g^{11(*)}_{\mathbf{q}}) \hat{b}^{(\dagger)}_{\mathbf{q}}$. Here, the operators have been split into the sum of phonons with *diagonal* coupling to the electrons ($\hat{B}^{(\dagger)}_{\mathrm{d}}$) and the sum of phonons which couple *non-diagonally* to the electronic coherence ($\hat{B}^{(\dagger)}_{\mathrm{nd}}$). Later on it will be seen that by using the n-phonon operators in the EOM, the set of dynamical equations obtain a well-arranged form.

In the same manner the electronic operators can be rewritten. In a two-level system, the pure electronic one-particle expectation values consists of three configurations: the microscopic ground state density $\langle \hat{a}^{\dagger}_1 \hat{a}_1 \rangle$, the excited state density $\langle \hat{a}^{\dagger}_2 \hat{a}_2 \rangle$ and the microscopic polarization $\langle \hat{a}^{\dagger}_1 \hat{a}_2 \rangle$ (and its complex conjugate). The three electronic configurations can also be written as an operator joined with $\hat{B}^{l,m}_{l',m'}$, leading to the phonon-assisted electronic operators:

$$\hat{G}^{l,m}_{l',m'} = \hat{a}^{\dagger}_1 \hat{a}_1 \hat{B}^{l,m}_{l',m'}, \quad \hat{E}^{l,m}_{l',m'} = \hat{a}^{\dagger}_2 \hat{a}_2 \hat{B}^{l,m}_{l',m'} \quad \hat{T}^{l,m}_{l',m'} = \hat{a}^{\dagger}_1 \hat{a}_2 \hat{B}^{l,m}_{l',m'}, \tag{10.4}$$

where $\langle \hat{G}^{0,0}_{0,0} \rangle, \langle \hat{E}^{0,0}_{0,0} \rangle, \langle \hat{T}^{0,0}_{0,0} \rangle$ are the pure electronic expectation values mentioned above. With these abbreviations, the EOMs can be written in a compact manner. Before evaluating the dynamics of the system, some further modifications are made. First, a correction of the n-particle equilibrium state is performed by the introduction of WEYL operators in the next subsection. Then, to reduce the numerical effort, the equations are calculated in the rotating frame picture, which will be explained in Sec. 10.2.2. Subsequently, the equations are shown in the last subsection.

10.2.1 Weyl transformation

Treating the motion of a single electron, the *electron picture* has been used for the description of the dynamics. But this picture results in an "anomaly" for the initial state of the system: Since the phonon operators are connected to the electronic densities, the phonon dynamics is already driven for the initial time $t = 0$ without external excitation if the EOMs for $\langle \hat{b}^{\dagger}_{\mathbf{q}} \hat{b}_{\mathbf{q}} \rangle$ are derived with the system Hamiltonian [Eq. (9.1)]. In particular, the lower sublevel which is occupied with one electron increases the phonon number for $t = 0$. Thus, the system is not in an initial equilibrium state. This unphysical behavior is a direct consequence of the electron picture since the phonon dynamics are not driven in other pictures, for example, in the *electron-hole picture* [CK99], which is widely used for systems with large transition energies. To maintain the equilibrium of the system at initial times, the phonon operators $\hat{b}^{(\dagger)}_{\mathbf{q}}$ are expressed by new, renormalized phonons $\hat{\tilde{b}}^{(\dagger)}_{\mathbf{q}}$ via a WEYL transformation [Wey25]:

$$\hat{\tilde{b}}^{(\dagger)}_{\mathbf{q}} = \hat{b}^{(\dagger)}_{\mathbf{q}} + c \qquad \text{with} \qquad c = \frac{1}{\hbar \omega_{\mathrm{LO}}} \sum_{i,\mathbf{q}} f^{(t=0)}_i g^{ii*}_{\mathbf{q}}, \tag{10.5}$$

with the transformation constant $c_{\mathbf{q}}$, which considers the electronic densities $f^{(t=0)}_i = \langle \hat{a}^{\dagger}_i \hat{a}_i \rangle (t = 0)$ for the initial time. The transformation guaranties the equilibrium at the initial time since the new operator $\hat{\tilde{b}}^{(\dagger)}_{\mathbf{q}}$ is not driven for $t = 0$. Expressing the old phonon operators by the new ones, the Hamiltonians then read:

$$\begin{aligned} &\hat{H}_{0,\mathrm{el}} + \hat{H}_{0,\mathrm{el}} + \hat{H}_{\text{el-ph}} = \sum_i \varepsilon_i \hat{a}^{\dagger}_i \hat{a}_i + \sum_{\mathbf{q}} \hbar \omega_{\mathbf{q}} \hat{b}^{\dagger}_{\mathbf{q}} \hat{b}_{\mathbf{q}} + \sum_{ij,\mathbf{q}} g^{ij}_{\mathbf{q}} \hat{a}^{\dagger}_i \hat{a}_i \, (\hat{b}^{\dagger}_{\mathbf{q}} + \hat{b}_{\mathbf{q}}) \\ \rightarrow\ &\hat{\tilde{H}}_{0,\mathrm{el}} + \hat{\tilde{H}}_{0,\mathrm{el}} + \hat{\tilde{H}}_{\text{el-ph}} = \sum_i \tilde{\varepsilon}_i \hat{a}^{\dagger}_i \hat{a}_i + \sum_{\mathbf{q}} \hbar \omega_{\mathbf{q}} \hat{\tilde{b}}^{\dagger}_{\mathbf{q}} \hat{\tilde{b}}_{\mathbf{q}} + \left(\sum_{i \neq j,\mathbf{q}} g^{ij}_{\mathbf{q}} \hat{a}^{\dagger}_i \hat{a}_i \, (\hat{\tilde{b}}^{\dagger}_{\mathbf{q}} + \hat{\tilde{b}}_{\mathbf{q}}) + \sum_{\mathbf{q}} \hat{a}^{\dagger}_2 \hat{a}_2 (g^{\mathrm{d}}_{\mathbf{q}} \hat{\tilde{b}}^{\dagger}_{\mathbf{q}} + g^{\mathrm{d}*}_{\mathbf{q}} \hat{\tilde{b}}_{\mathbf{q}}) \right), \end{aligned} \tag{10.6}$$

with $\tilde{\varepsilon}_i = \varepsilon_i - 2\sum_{\mathbf{q}} \frac{g^{ii}_{\mathbf{q}} g^{11*}_{\mathbf{q}}}{\hbar\omega_{\mathrm{LO}}}$ and $g^{\mathrm{d}(*)}_{\mathbf{q}} = (g^{22(*)}_{\mathbf{q}} - g^{11(*)}_{\mathbf{q}})$. Here, the initial conditions have been set to $f^{(t=0)}_{11} = 1 - f^{(t=0)}_{22} = 1$. The WEYL transformation leads to a renormalization of the energies, $\tilde{\varepsilon}_i$ and a modification of the *el-LO* Hamiltonian. For the sake of clarity, the transformed operators $\hat{\tilde{b}}^{(\dagger)}_{\mathbf{q}}$ are renamed to $\hat{b}^{(\dagger)}_{\mathbf{q}}$ and the calculations are performed with the WEYL operators.

10.2.2 Rotating frame picture

The next modification of the EOM is numerically motivated. Since the resolution of fast frequencies require a fine discretization of the time steps, it is often useful to change into a *rotating frame*. Here, the different phonon-assisted operators are decomposed into a slowly varying envelope part (marked with the tilde-sign) and into the fast oscillating part with the rotating frequency ω_{R}:

$$\hat{X}^{l,m}_{l',m'} = \tilde{X}^{l,m}_{l',m'} \cdot \mathrm{e}^{\mathrm{i}\omega_{\mathrm{R}(X)}t}. \tag{10.7}$$

The phonon-assisted operators are $\hat{X} = \{\hat{B}, \hat{G}, \hat{E}, \hat{T}\}$ and the corresponding rotation frequency is given by $\omega_{\mathrm{R}(B)} = \omega_{\mathrm{R}(G)} = \omega_{\mathrm{R}(E)} = (l-l')\omega_{\mathrm{LO}} + (m-m')\omega_{\mathrm{LO}}$ and $\omega_{\mathrm{R}(T)} = \omega_{\mathrm{R}(B)} - \omega_{\mathrm{gap}}$. In the following subsection, the HEISENBERG EOMs are presented for the full dynamics.[1]

10.2.3 Set of dynamic equations

Now the dynamics for the phonon-assisted expectation values can be calculated with the HEISENBERG EOM by using the induction method, Eq. (10.2). For the expectation values with an arbitrary number of phonon creators or annihilators, the EOMs then read:

$$\begin{aligned}
-\mathrm{i}\hbar\,\frac{\mathrm{d}}{\mathrm{d}t}\langle\hat{T}^{l,m}_{l',m'}\rangle =& \left[\mathrm{i}(l+l'+m+m')\gamma + \mathrm{i}D + (l-l'+m-m')\hbar\omega_{\mathrm{LO}} - \varepsilon_{\mathrm{gap}}\right]\langle\hat{T}^{l,m}_{l',m'}\rangle \\
&+ l g^2_{21}\langle\hat{E}^{l-1,m}_{l',m'}\rangle - l' g^2_{21}\langle\hat{G}^{l,m}_{l'-1,m'}\rangle - m' g^2_{\mathrm{eff}}\langle\hat{T}^{l,m}_{l',m'-1}\rangle \\
&+ \langle\hat{E}^{l,m}_{l'+1,m'}\rangle - \langle\hat{G}^{l,m}_{l'+1,m'}\rangle - \langle\hat{T}^{l,m}_{l',m'+1}\rangle - \langle\hat{T}^{l,m+1}_{l',m'}\rangle + \langle\hat{E}^{l+1,m}_{l',m'}\rangle - \langle\hat{G}^{l+1,m}_{l',m'}\rangle \\
&+ \hbar\Omega(t)\left(\langle\hat{E}^{l,m}_{l',m'}\rangle - \langle\hat{G}^{l,m}_{l',m'}\rangle\right) \\
&- \mathrm{i}\hbar\frac{\mathrm{d}}{\mathrm{d}t}\langle\hat{T}^{l,m}_{l',m'}\rangle_{|\text{ph-ext}},
\end{aligned} \tag{10.8}$$

$$\begin{aligned}
-\mathrm{i}\hbar\,\frac{\mathrm{d}}{\mathrm{d}t}\langle\hat{G}^{l,m}_{l',m'}\rangle =& \left[\mathrm{i}(l+l'+m+m')\gamma + (l-l'+m-m')\hbar\omega_{\mathrm{LO}}\right]\langle\hat{G}^{l,m}_{l',m'}\rangle \\
&+ l' g^2_{21}\langle\hat{T}^{l,m}_{l'-1,m'}\rangle + l g^2_{21}\langle\hat{T}^{l-1,m}_{l',m'}\rangle^* \\
&- \langle\hat{T}^{l+1,m}_{l',m'}\rangle + \langle\hat{T}^{l,m}_{l'+1,m'}\rangle^* + \langle\hat{T}^{l+1,m}_{l',m'}\rangle^* - \langle\hat{T}^{l,m}_{l'+1,m'}\rangle \\
&+ \hbar\Omega(t)\left(\langle\hat{T}^{l,m}_{l',m'}\rangle^* - \langle\hat{T}^{l,m}_{l',m'}\rangle\right) \\
&- \mathrm{i}\hbar\frac{\mathrm{d}}{\mathrm{d}t}\langle\hat{G}^{l,m}_{l',m'}\rangle_{|\text{ph-ext}},
\end{aligned} \tag{10.9}$$

[1] In the numerical simulations, the dynamics is only calculated for the slowly varying parts, that is $\frac{\mathrm{d}}{\mathrm{d}t}\tilde{X}^{l,m}_{l',m'}$, since their EOMs can be simulated with a less numerical effort than for the original operators. The time derivation of the original operators is then re-obtained with the relation $\frac{\mathrm{d}}{\mathrm{d}t}\hat{X}^{l,m}_{l',m'} = (\frac{\mathrm{d}}{\mathrm{d}t}\tilde{X}^{l,m}_{l',m'})\mathrm{e}^{\mathrm{i}\omega_{\mathrm{R}(X)}t} + \mathrm{i}\omega_{\mathrm{R}(X)}\tilde{X}$, which can be verified if the time derivative is applied to Eq. (10.7).

$$
\begin{aligned}
-\mathrm{i}\hbar\,\frac{\mathrm{d}}{\mathrm{d}t}\langle\hat{E}^{l,m}_{l',m'}\rangle =&[\mathrm{i}(l+l'+m+m')\gamma+(l-l'+m-m')\hbar\omega_{\mathrm{LO}}]\,\langle\hat{E}^{l,m}_{l',m'}\rangle\\
&-l'g^2_{21}\langle\hat{T}^{l,m}_{l'-1,m'}\rangle^*+lg^2_{21}\langle\hat{T}^{l-1,m}_{l',m'}\rangle+mg^2_{\mathrm{eff}}\langle\hat{E}^{l,m-1}_{l',m'}\rangle-m'g^2_{\mathrm{eff}}\langle\hat{E}^{l,m}_{l',m'-1}\rangle\\
&+\langle\hat{T}^{l+1,m}_{l',m'}\rangle-\langle\hat{T}^{l,m}_{l'+1,m'}\rangle^*-\langle\hat{T}^{l+1,m}_{l',m'}\rangle^*+\langle\hat{T}^{l,m}_{l'+1,m'}\rangle\\
&+\hbar\Omega(t)\,(\langle\hat{T}^{l,m}_{l',m'}\rangle-\langle\hat{T}^{l,m}_{l',m'}\rangle^*)\\
&-\mathrm{i}\hbar\frac{\mathrm{d}}{\mathrm{d}t}\langle\hat{E}^{l,m}_{l',m'}\rangle_{|\text{ph-ext}},
\end{aligned}
\tag{10.10}
$$

with $g^2_{\mathrm{eff}}=\sum_q|g^{22}_{\mathbf{q}}-g^{11}_{\mathbf{q}}|^2$ and $g^2_{21}=\sum_q\left(g^{21}_{\mathbf{q}}\right)^2$ and $\Omega(t)=d_{12}E(t)/\hbar$. A dephasing time of the phonons γ has been included, due to their finite lifetime. Also, a pure dephasing D of the polarization is taken into account on a phenomenological level. Due to the one-electron assumption, the EOM of the pure n-phonon operator can be obtained through the relation $\langle\hat{B}^{l,m}_{l',m'}\rangle=\langle\hat{G}^{l,m}_{l',m'}\rangle+\langle\hat{E}^{l,m}_{l',m'}\rangle$.

The differential equations for the expectation values considering the external phonon bath, that is $\frac{\mathrm{d}}{\mathrm{d}t}\langle\hat{X}^{l,m}_{l',m'}\rangle_{|\text{ph-ext}}$, are given in App. E. Due to the weak coupling of the system phonons to the external phonon reservoir, the equations are calculated via the second-order correlation expansion. The external bath equilibrates the LO phonons with the bath phonons, beginning from the time $t=0$. Hence, to correctly model the excitation dynamics, the excitation pulse must not be applied until the system has found its equilibrium state.

10.2.4 Initial conditions

To model the dynamics, initial conditions for the system must be chosen. If decomposing the expectation values of the phonon-assisted electronic operators $\langle\hat{X}^{l,m}_{l',m'}\rangle=\langle\hat{a}^\dagger_i\hat{a}^\dagger_j\rangle\langle\hat{B}^{l,m}_{l',m'}\rangle$, the initial electronic expectation values $\langle\hat{a}^\dagger_1\hat{a}_1\rangle(t_0)=\langle\hat{G}^{0,0}_{0,0}\rangle(t_0)$, $\langle\hat{a}^\dagger_2\hat{a}^\dagger_2\rangle(t_0)=\langle\hat{E}^{0,0}_{0,0}\rangle(t_0)$ and $\langle\hat{a}^\dagger_1\hat{a}^\dagger_2\rangle(t_0)=\langle\hat{T}^{0,0}_{0,0}\rangle(t_0)$ as well as the expectation value for the n-phonon operator $\langle\hat{B}^{0,0}_{0,0}\rangle(t_0)$ have to be determined. The electronic expectation values denote the probability to find the electron in the ground state ($\langle\hat{G}^{0,0}_{0,0}\rangle$) and the excited state ($\langle\hat{E}^{0,0}_{0,0}\rangle$), with a transition probability between the levels ($\langle\hat{T}^{0,0}_{0,0}\rangle$). If not otherwise noted, the initial conditions for the electronic expectation values are $\langle\hat{G}^{0,0}_{0,0}\rangle(t_0)=1-\langle\hat{E}^{0,0}_{0,0}\rangle(t_0)=1$ and $\langle\hat{T}^{0,0}_{0,0}\rangle(t_0)=0$.

For the initial conditions of $\langle\hat{B}^{l,m}_{l',m'}\rangle(t_0)$, the WICK theorem is applied, which proves that the n-phonon operator $\langle\hat{B}^{l,m}_{l',m'}\rangle(t_0)$ can be split into all possible combinations of phonon density expectation values [Mah00]. The initial condition for $\langle\hat{B}^{l,m}_{l',m'}\rangle(t_0)$ then reads:

$$
\langle\hat{B}^{l,m}_{l',m'}\rangle(t_0)=\overbrace{l!(g^2_{21})^l n^l_{\mathrm{LO}}}^{\rho_{\mathrm{t},l}}\delta_{l,l'}\overbrace{m!(g^2_{\mathrm{eff}})^m n^m_{\mathrm{LO}}}^{\rho_{\mathrm{d},m}}\delta_{m,m'}=\rho_{\mathrm{t},l}\rho_{\mathrm{d},m}\delta_{l,l'}\delta_{m,m'}. \tag{10.11}
$$

A detailed derivation for the n phonon operator statistics can be found in [Kuh11]. Accordingly, the initial conditions for the phonon-assisted electronic operators are:

$$
\langle\hat{X}^{l,m}_{l',m'}\rangle(t_0)=\langle\hat{X}^{0,0}_{0,0}\rangle(t_0)\rho_{\mathrm{t},l}\rho_{\mathrm{d},m}\delta_{l,l'}\delta_{m,m'}, \tag{10.12}
$$

with $\hat{X}=\{\hat{G},\hat{E},\hat{T}\}$. The phonon distribution for the initial time is given by the BOSE distribution function $n_{\mathrm{LO}}=n(\hbar\omega_{\mathrm{LO}})$.[2]

[2] Note, that the factorization of the electronic and the phononic expectation values is not correct: Being in the strong-coupling regime, the correlations between the electrons and the LO phonons are not negligible (see Sec. 9.2). Hence, the initial conditions do not necessarily lead to an initial equilibrium state. This deficit is fixed by the inclusion of the external phonon reservoir, which equilibrates the system.

Chapter 11

Absorption spectra

The equations Eq. (10.8) - (10.10) are analytically exact. Still, it is obvious that the solution for an infinite number of orders is numerically impossible. Instead, the EOMs are solved until an certain order n, which is determined by the convergence of the solution. To prove the accuracy of the induction method, the EOMs are compared to two exactly solvable models: The independent Boson model and the Jaynes-Cummings model. This is done in the next subsection. After benchmarking the induction method, the full dynamics of the QD model system is considered and the absorption spectrum is calculated in Sec. 11.2. A conclusion of the ISL QD model system and the obtained results is given in the last subsection.

11.1 Benchmarks

Independent Boson model - As a first benchmark, the independent Boson model (IBM) is investigated. In the IBM, a two-level system interacts with a phonon bath via the diagonal coupling [Mah00]. Thus, the non-diagonal FRÖHLICH coupling element g_{21}^2 and the indices l, l' in Eqs. (10.8)-(10.10) are set to zero. To model the same conditions as the exactly solvable IBM, the external phonon bath is neglected as well. The IBM describes the dynamics of the microscopic polarization under absorption and emission of phonons if the two-level system is excited with an electromagnetic pulse. The interplay with an emitted (absorbed) phonon can be seen in the absorption spectra as an additional peak multiple phonon energies above (below) the main peak located around the sublevel gap energy ε_{gap}, also denoted as STOKES (anti-STOKES) satellite peaks. To cover the whole energy spectrum, the electromagnetic field is assumed as a delta-like pulse. This can be simulated by setting the initial condition of the phonon-assisted transition operator to $\hat{T}_{0,0}^{0,0} = 0.5\mathbb{1}$.

Figure 11.1 shows the absorption spectrum, obtained by solving the Eqs. (10.8)-(10.10) until sixth order for a temperature of $T = 0$ K on the left side and for varying temperatures on the right side. For the calculations, GaAs parameters are used. The pure dephasing D is set to $D = 0.4$ meV (corresponding to an inverse dephasing time of 0.6 ps^{-1}). The gap energy has been set resonantly with the LO phonon energy to enhance the *el-ph* interaction effects. For $T = 0$ K (red line), the STOKES peaks are clearly visible at multiple LO phonon energies above ε_{gap}, which is for GaAs at $\hbar\omega_{\text{LO}} = 36$ meV, while the anti-STOKES peaks do not appear since no LO phonons can be absorbed at zero Kelvin. The line width of the peaks is determined by the dephasing constant D. Additionally, the inset shows a smaller energy scale around the detuned gap energy. Here, it can be seen that the main peak is shifted away from the gap energy with an energy Δ_{LO} to lower energies. This shift results from the formation of new *el-ph* quasi-particles, so-called *polarons*. The polaron shift is given by $\Delta_{\text{LO}} = g_{\text{eff}}^2/\varepsilon_{\text{LO}}$ and renormalizes the sublevel gap energy ε_{gap}. With the given parameters, the polaron shift equals $\Delta_{\text{LO}} = 0.9$ meV.

For $T = 0$ K, the proportional height of the STOKES peaks can be determined by the Poissonian distribution: $p_i = p_0 \exp(-F)F^i/i!$, with the Huang-Rhys factor $F = \Delta_{\text{LO}}/\varepsilon_{\text{LO}}$ and the height of the ith peak p_i, beginning from the main peak p_0 [MK00]. Comparing the height of maxima in Fig. 11.1

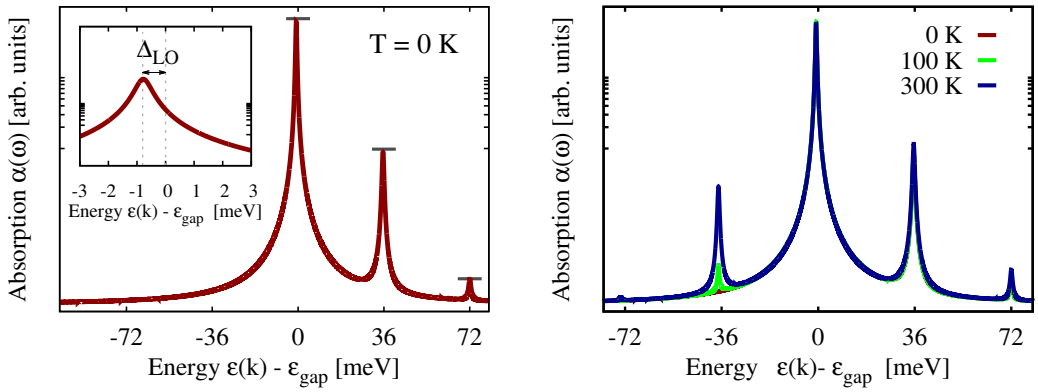

Figure 11.1 | Left: Absorption spectrum on a logarithmic scale for the ISL QD model with only diagonal coupling for $T = 0$ K, showing STOKES satellite peaks above the gap energy. Inset: the maximum of the main peak is shifted away from the gap energy with a shift of Δ_{LO}, due to the formation of polarons. Right: The same spectrum for different temperatures: The anti-STOKES peaks below the gap energy become visible for increasing temperature. The spectra reproduce features of the independent Boson model.

for $T = 0$ K (marked with grey horizontal lines), the spectrum reproduces the Poissonian distribution and leads to a Huang-Rhys factor of $F \approx 0.025$, which is in agreement with several literature values [HBG+01, SDW+11, BMS+03]. For increasing temperature, the anti-STOKES peaks become visible (blue and green line), indicating the pronounced possibility of LO phonon absorption for higher temperatures. Therefore, the equations, derived via the induction method reproduce the main features of the IBM.

Jaynes-Cummings model - Next, the Jaynes-Cummings model (JCM) is investigated which originates from the atomic quantum optics. Here, it describes the interaction of a two-level system with a single-mode photon field with a fixed number of electrons [CTJDR92]. The photons only interact non-diagonally with the electronic system. The JCM is now applied to the non-diagonal LO phonon coupling. Therefore, the diagonal indices in Eqs. (10.8)-(10.10) are set to zero: $m = m' = 0$ and the non-diagonally coupled phonons play the role of the photons. Again, the external phonon bad is neglected and a small pure dephasing of $D = 0.4$ meV is considered. Also, the gap energy is on resonance with the LO phonon energy to enhance the interaction effects. Figure 11.2(left) shows the absorption spectrum for the model system for $T = 0$ K. Again, the initial condition for the phonon-assisted transition operator have been set to $\hat{T}^{0,0}_{0,0} = 0.5\mathbb{i}$ to model a delta pulse excitation. Now, the absorption spectrum exhibits two peaks instead of one peak around the gap energy. The double-peak indicates the formation of the polarons (in case of photons, the quasi-particles are called *polaritons*) with two new eigenenergies $\hbar\omega^{n_{\mathrm{LO}}}_{+/-}$, originating from the strong coupling between the electrons and the non-diagonally coupled LO phonons. The new eigenenergies of the system can be calculated with [SZ97]:

$$\hbar\omega^{n_{\mathrm{LO}}}_{+/-} = \hbar\omega_{\mathrm{LO}}(n_{\mathrm{LO}} + \frac{1}{2}) \pm \sqrt{\frac{1}{4}(\varepsilon_{\mathrm{gap}} - \hbar\omega_{\mathrm{LO}})^2 + g^2_{21}(n_{\mathrm{LO}} + 1)} \tag{11.1}$$

For $n_{\mathrm{LO}} = 0$ and $\varepsilon_{\mathrm{gap}} = \hbar\omega_{\mathrm{LO}}$, the energetic distance between the two main peaks equals $\Delta g_{21} = 2g_{21}$, also denoted as vacuum RABI splitting in the case of photons.

If the gap energy $\varepsilon_{\mathrm{gap}}$ is varied, the splitting vanishes for large detuning between $\varepsilon_{\mathrm{gap}}$ and the LO phonon energy $\varepsilon_{\mathrm{LO}}(= 36.4$ meV). This is shown in Fig. 11.2(right): Here, the dark red line corresponds to the spectrum in Fig. 11.2(left). For a negative detuning, that is $\varepsilon_{\mathrm{gap}} = 30$ meV $< \varepsilon_{\mathrm{LO}}$ (light blue line), the right peak shifts to higher energies and decreases in its signal strength while the left peak

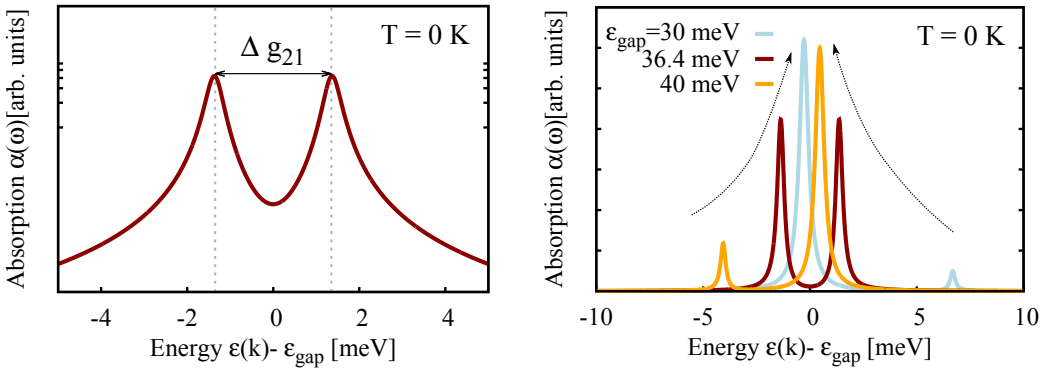

Figure 11.2 | Left: Absorption spectrum on a logarithmic scale for an ISL QD with only non-diagonal coupling for $T = 0$ K. The sublevel energy ε_{gap} is on resonance with the LO phonon energy ε_{LO}. The strong coupling leads to the formation of polarons and subsequently to a RABI splitting of the energy, equal to the Jaynes-Cummings model. The distance of the two peaks in the vacuum state is dependent on the FRÖHLICH coupling strength g_{21}. Right: Linear spectrum for varying sublevel gap energies. For increasing detuning, one peak increases and shifts to the sublevel gap energy. The second peak decreases.

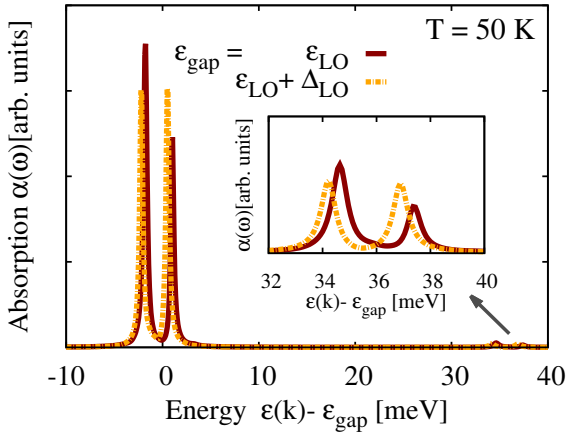

Figure 11.3 | Linear ISL QD absorption spectrum for a temperature of $T = 50$ K including all contributions, for two different sublevel gap energies. The spectrum shows the RABI splitting of the peaks. If the sublevel gap energy equals the polaronic eigenenergy (dotted light line), the RABI splitting is symmetric. Additionally, split STOKES peaks appear.

increases and shifts towards the sublevel gap energy. On the other hand, for a positive detuning ($\varepsilon_{\text{gap}} > \varepsilon_{\text{LO}}$), the splitting acts the opposite way, that is the right peak approaches $\varepsilon_{\text{gap}} = \varepsilon_{\text{LO}}$ and the left peak decreases (light orange line). In either way, for increasing detuning, one peak shifts to the sublevel energy while the second peak vanishes (indicated with the arrows), eventually exhibiting one main peak at the corresponding sublevel gap energy. Thus, the splitting is lifted for large detuning. This characteristic behavior is in the JCM also denoted as an anti-crossing. The comparison of Eq. (11.1) with the absorption spectrum Fig. 11.2, obtained with the induction method until sixth order, shows good agreement.

11.2 Full dynamics

After benchmarking the equations Eqs. (10.8)-(10.10) in the limit of solely diagonal (IBM) and solely non-diagonal coupling (JCM), the full dynamics of the ISL QD model is now investigated. The system is excited with a weak Gaussian-shaped pulse with $\sigma = 20$ fs and the pure dephasing is set to $D = 0.1$ meV.

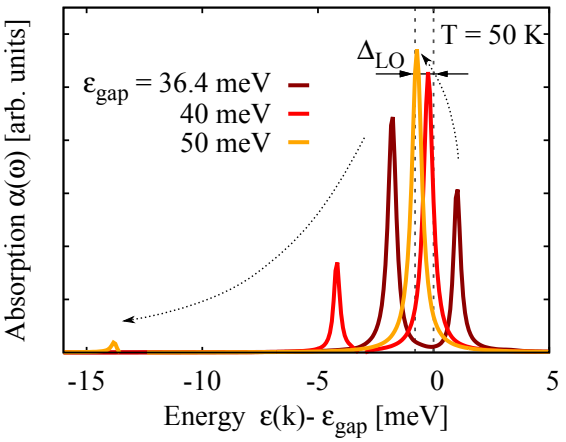

Figure 11.4 | ISL QD absorption spectrum of the main peak for three different gap energies for $T = 50$ K. The dark red curve corresponds to the spectrum in Fig. 11.3. The satellite peaks are not shown. For increasing gap energies, the left peak shifts to lower energies and decreases while the right peak approaches the polaronic eigenenergy.

Also, the external phonon bath is taken into account with an external bath temperature of $T = 50\ K$.[1]

Fig. 11.3 shows the spectrum including the full dynamics for two different sublevel gap energies. Here, signatures of both the diagonal and the non-diagonal coupling to the LO phonons can bee seen: The main peak around the gap energy is split due to the strong non-diagonal coupling, similar to the RABI splitting in the JCM. This indicates that (non-diagonal) polarons are formed. Additionally, one LO phonon energy above the main peak, the STOKES peak, originating from the diagonal coupling, is visible, see inset of Fig. 11.3. The satellite peak is split as well. The height of the satellite peaks is modulated due to the Poissonian relation of the peak height in the IBM. For a gap energy on resonance with the LO phonon energy (dark red line), the RABI splitting is asymmetric. This is caused by the diagonal *el-ph* coupling: Similar to the IBM, the gap energy is renormalized with the polaron shift Δ_{LO} of the diagonal polarons. Consequently, the RABI splitting is only symmetric if the polaron shift is considered. Hence, for $\varepsilon_{\mathrm{gap}} = \varepsilon_{\mathrm{LO}} + \Delta_{\mathrm{LO}}$ (dotted light line) the spectrum has a symmetric RABI splitting.

In the next step, the gap energy is detuned to larger energies between the levels. The resulting spectra are shown in Fig. 11.4, where the RABI splitting is plotted around the gap energy for three different gap energies $\varepsilon_{\mathrm{gap}} = 36.4$ meV 40 meV and 50 meV. The dark red line corresponds to the dark red line in the absorption spectrum of Fig. 11.4. Comparing the spectra for different $\varepsilon_{\mathrm{gap}}$, it can be seen that the height of one peak decreases for increasing gap energy and shifts to lower energies (indicated with the dotted arrow on the left). For $\varepsilon_{\mathrm{gap}} = 50$ meV (yellow line), the height of the low-energy peak is already strongly reduced (and shifted) compared to the main peak. For negative detuning, the peaks act vice versa (not shown here). This behavior is comparable to the anti-crossing the JCM. But unlike in the JCM, the eventual position of the main peak is shifted by the diagonal polaron shift Δ_{LO}. Thus, the absorption spectra show that the *el-ph* interaction strongly influences the ISL QD dynamics. While for a system in strong resonance with the LO phonon energy exhibits strong signatures of the non-diagonal coupling (the RABI splitting), the diagonal coupling is pronounced for an increasing detuning between the sublevel gap energy and the LO phonon energy (polaron shift).

11.3 Conclusions

In conclusion, the dynamics of an intersublevel quantum dot with strong electron-LO phonon coupling has been derived via the induction method. After benchmarking the method in the limit of solely diagonal and non-diagonal coupling, the full dynamics have been investigated in the linear regime. Both the diagonal and the non-diagonal coupling lead to different features, visible in the absorption spectra. For a sublevel gap energy near the LO phonon energy, a RABI splitting of the peaks occurs due to the non-diagonal electron-LO phonon coupling. Additionally, satellite peaks appear multiple LO phonon

[1] To check the dependence of the spectra on coupling to the external bath, the coupling values α, α' (see App. E) have been varied. However, the strength of the coupling to the external bath does not lead to a qualitative change of the spectra.

energies away from the main peak as a result of the diagonal electron-LO phonon coupling. For increasing detuning between the gap energy and the LO phonon energy, the splitting is lifted and one main peak arises around the gap energy, shifted by the diagonal polaron shift.

As a further outlook, it would be an interesting task to study the nonlinear effects of the strong electron-LO phonon coupling. Considering the nonlinear regime, the strong coupling could lead to further effects under strong field excitations such as the generation of coherent phonons. This is an aspect which should be considered for future investigations.

Part V

Epilogue

Chapter 12

Conclusion and outlook

In this work, the influence of the electron-electron- and electron-phonon coupling on the intersubband dynamics of low-dimensional semiconductor nanostructures has been investigated. Using the HEISENBERG equation of motion approach, the dynamics of intersubband quantum wells, bulk-surface dynamics and intersublevel dynamics in a quantum dot was calculated.

First, the intersubband dynamics of an *n*-doped GaAs/AlGaAs quantum well was studied. In a perturbative ansatz, first-order memory effects for the equilibrium ground state distribution were included. It could be seen that the COULOMB interaction leads to a renormalization of the equilibrium distribution, resulting in a small deviation from the generally used FERMI function. Although the deviation from the FERMI distribution lies only in the order of a few percent, the ground state correlations lead to a new physical scenario at low temperatures by providing new electron-electron scattering channels. This is directly visible in the absorption spectrum including electron-electron interactions. Consequently, the line width of the resulting absorption spectra including ground state correlations are broadened up to a factor of three (for $T = 1$ K) compared to the spectra neglecting ground state correlations. The inclusion of electron-phonon scattering rates as an additional dephasing constant strongly reduces the relative impact of the ground state correlations. However, to gain full insights into the impact of ground state correlations, the electron-electron- and electron-phonon coupling should be included on the same footing, since the ground state correlations must also be considered in the electron-phonon scattering.

Going to the non-equilibrium regime in quantum wells, the two-dimensional FOURIER transform spectroscopy was treated to investigate the intersubband dynamics with the focus on the electron-phonon interaction. To resolve relaxation processes, the 2D photon echo signal of an intersubband quantum well sample was calculated. The study of the free carrier dynamics shows that the lack of correlations is visible as a symmetric signal. With the inclusion of the electron-phonon interaction, the two-dimensional spectrum becomes asymmetric, revealing the main phonon-induced scattering channel from the upper to the lower subband. Since the two-dimensional FOURIER transform spectroscopy is not limited to relaxation processes but also allows insights into various many-body correlations, it would be a further interesting aspect to include electron-electron interactions and to investigate other signals such as the double quantum coherence signal.

Next, the bulk-surface dynamics in the silicon conduction band was examined. Calculating the relaxation of a hot carrier distribution, the equations of motion for the bulk and the surface were described within a relaxation rate approximation while the dominant dynamics of the LO phonon mode was calculated using a reduced PEIERLS equation. In agreement with recent experiments the theoretical simulations indicate that due to the emission of the dominant LO phonon mode during the relaxation of the carriers, the heated phonons couple back to the system and subsequently lead to a prolonged lifetime of heated carriers. To gain a more detailed insight into the coupling between the phonons and the non-equilibrium carrier distribution, further investigations should consider the inclusion of the full, momentum dependent PEIERLS equation.

In a zero-dimensional quantum dot, the intersublevel dynamics was studied. Here, a perturbative

approach was not possible due to the strong interactions between electrons and longitudinal optical phonons. By applying an induction method for the equations of motion, the electron-phonon interaction could be considered up to an arbitrary order. The resulting absorption spectrum showed that for a sublevel gap energy near the longitudinal optical phonon energy, the absorption line shape exhibits signatures from both, the diagonal and the non-diagonal electron-phonon coupling. Resulting from the diagonal coupling, STOKES peaks can be seen at multiples of the longitudinal optical phonon energy. Furthermore, as a result of the strong non-diagonal coupling, a splitting of the absorption peak is visible. These features weaken for an increasing detuning of the sublevel gap energy and the longitudinal optical phonon energy. As an outlook, the study of the strong electron-longitudinal optical phonon interaction should be expanded to the nonlinear regime. Here, the excitation with strong fields could lead to further interesting effects, such as the generation of coherent phonons.

Appendix A

Material parameters

Parameter	Symbol	Value	Unit
free electron mass	m_0	5.6857	$\mathrm{fs^2eV/nm^2}$
PLANCK constant	$\hbar$	6.582	eVfs
BOLTZMANN constant	k_B	$8.617 \cdot 10^{-5}$	eV/K
dielectric constant (vacuum)	ε_0	$5.526 \cdot 10^{-2}$	$\mathrm{e^2/(eVnm)}$
elementary charge	e_0	1	
speed of light	c	299.7925	nm/fs

Table A.1 | Natural constants.

Parameter	Symbol	Value	Unit
high frequency dielectric constant	ε_∞	10.9	
static dielectric constant	ε_s	12.53	
background dielectric constant	ε_bg	12	
bulk effective mass	m_eff	$0.067\,m_0$	$\mathrm{fs^2eV/\ nm^2}$
QD subband gap	$\hbar\omega$	0.03 - 0.05	eV
LO-phonon energy	$\hbar\omega_\mathrm{LO}$	0.0364	eV

Table A.2 | Numerical parameters for GaAs.

Well width L	subband gap energy ε_gap	lower subband effective mass m_1	upper subband effective mass m_2
5 nm	210.66 meV	$0.0777\ m_0$	$0.131\ m_0$
9 nm	114.09 meV	$0.0719\ m_0$	$0.0921\ m_0$
10 nm	98.54 meV	$0.0712\ m_0$	$0.0877\ m_0$

Table A.3 | Numerical parameters for the GaAs intersubband quantum well.

Parameter	Symbol	Value	Unit
surface state width	L_s	0.5	nm
fundamental gap (bulk-surface)	ε_CBM	0.45	eV
LO phonon energy	$\hbar\omega_\mathrm{LO}$	0.065	eV
initial electron density	n_init	0.01	nm^{-3}
effective bulk density of states mass	m_bulk	1.06 m_0	$\mathrm{fs}^2\mathrm{eV}/\mathrm{nm}^2$
effective surface mass	m_surf	0.19 m_0	$\mathrm{fs}^2\mathrm{eV}/\mathrm{nm}^2$
el-el intraband scattering time	$\tau^\mathrm{intra}_\mathrm{el,0}$	20	fs
el-LO intraband scattering time	$\tau^\mathrm{intra}_\mathrm{el\text{-}LO}$	180	fs
el-el interband scattering time	$\tau^\mathrm{inter}_\mathrm{el,0}$	20	fs
el-LO interband scattering time	$\tau^\mathrm{inter}_\mathrm{el\text{-}LO}$	100	ps
LO phonon lifetime	τ_LO	10	ps
D_down lifetime	τ_{D_down}	7	ps

Table A.4 | Numerical parameters for Si.

Appendix B

Scattering rates

B.1 Boltzmann scattering rates

The full linear equation including COULOMB interaction is:

$$
\begin{aligned}
\frac{d}{dt}\rho_{12,\mathbf{k}} = &-\frac{i}{\hbar}(\varepsilon_{2,\mathbf{k}}-\varepsilon_{1,\mathbf{k}})\rho_{12,\mathbf{k}} - i\Omega(t)(f_{2,\mathbf{k}}-f_{1,\mathbf{k}}) \\
(exchange) &+\frac{i}{\hbar}\sum_{\mathbf{q}\neq 0}\left[\left(V^{q}_{2222}-V^{q}_{2112}\right)f_{2,\mathbf{k}-\mathbf{q}} - \left(V^{q}_{1111}-V^{q}_{2112}\right)f_{1,\mathbf{k}-\mathbf{q}}\right]\rho_{12,\mathbf{k}} \\
(exciton) &-\frac{i}{\hbar}\sum_{\mathbf{q}\neq 0}\left[V^{q}_{1212}\rho_{12,\mathbf{k}-\mathbf{q}} + V^{q}_{2211}\rho_{21,\mathbf{k}-\mathbf{q}}\right]\left(f_{2,\mathbf{k}}-f_{1,\mathbf{k}}\right) \\
(depolarization) &+\frac{i}{\hbar}V^{0}_{2112}\sum_{\mathbf{q}\neq 0 s'}\left[\rho_{12,\mathbf{q}s'}+\rho_{21,\mathbf{q}s'}\right]\left(f_{2,\mathbf{k}}-f_{1,\mathbf{k}}\right) \\
(scattering) &-\left(\sum_{\mathbf{k}',\mathbf{q}}\Gamma_{\mathrm{diag}}\rho_{12,\mathbf{k}} + \sum_{\mathbf{k}',\mathbf{q}}\Gamma_{\mathrm{ndiag1}}\rho_{12,\mathbf{k}-\mathbf{q}} + \sum_{\mathbf{k}',\mathbf{q}}\Gamma^{*}_{\mathrm{ndiag1}}\rho_{21,\mathbf{k}-\mathbf{q}}\right).
\end{aligned}
\tag{B.1}
$$

Since in this model system the upper subband is assumed to be empty ($f_{2,\mathbf{k}}=0$), only a few scattering terms do not vanish:

$$
\begin{aligned}
\Gamma_{\mathrm{diag}} = &\\
&\frac{\gamma\cdot V^{\mathbf{q}}_{1111}(2\cdot V^{\mathbf{q}}_{1111}-V^{\mathbf{k}-\mathbf{q}-\mathbf{k}'}_{1111})}{\{\varepsilon_{1,\mathbf{k}'+\mathbf{q}}+\varepsilon_{1,\mathbf{k}-\mathbf{q}}-\varepsilon_{1,\mathbf{k}}-\varepsilon_{1,\mathbf{k}'}\}^2+\hbar^2\gamma^2}\left(f_{1,\mathbf{k}'}f^{-}_{1,\mathbf{k}'+\mathbf{q}}f^{-}_{1,\mathbf{k}-\mathbf{q}} + f_{1,\mathbf{k}-\mathbf{q}}f_{1,\mathbf{k}'+\mathbf{q}}f^{-}_{1,\mathbf{k}'}\right)\\
+&\frac{\gamma\cdot V^{\mathbf{q}}_{2121}(2\cdot V^{\mathbf{q}}_{2121}-V^{\mathbf{k}-\mathbf{q}-\mathbf{k}'}_{1221})}{\{\varepsilon_{1,\mathbf{k}'}+\varepsilon_{2,\mathbf{k}}-\varepsilon_{2,\mathbf{k}-\mathbf{q}}-\varepsilon_{1,\mathbf{k}'+\mathbf{q}}\}^2+\hbar^2\gamma^2}\left(f_{1,\mathbf{k}'}f^{-}_{1,\mathbf{k}'+\mathbf{q}}f^{-}_{2,\mathbf{k}-\mathbf{q}}\right)\\
+&\frac{\gamma\cdot V^{\mathbf{q}}_{2112}(2\cdot V^{\mathbf{q}}_{1221}-V^{\mathbf{k}-\mathbf{q}-\mathbf{k}'}_{2121})}{\{\varepsilon_{1,\mathbf{k}'}+\varepsilon_{2,\mathbf{k}}-\varepsilon_{1,\mathbf{k}-\mathbf{q}}-\varepsilon_{2,\mathbf{k}'+\mathbf{q}}\}^2+\hbar^2\gamma^2}\left(f_{1,\mathbf{k}'}f^{-}_{2,\mathbf{k}'+\mathbf{q}}f^{-}_{1,\mathbf{k}-\mathbf{q}}\right),
\end{aligned}
$$

$$
\begin{aligned}
\Gamma_{\mathrm{ndiag1}} = &\\
&-\frac{\gamma\cdot V^{\mathbf{q}}_{1111}(2\cdot V^{\mathbf{q}}_{2121}-V^{\mathbf{k}-\mathbf{q}-\mathbf{k}'}_{1221})}{\{\varepsilon_{1,\mathbf{k}'+\mathbf{q}}+\varepsilon_{2,\mathbf{k}-\mathbf{q}}-\varepsilon_{2,\mathbf{k}}-\varepsilon_{1,\mathbf{k}'}\}^2+\hbar^2\gamma^2}\left(f_{1,\mathbf{k}'+\mathbf{q}}f^{-}_{1,\mathbf{k}'}f^{-}_{2,\mathbf{k}}\right)\\
&-\frac{\gamma\cdot V^{\mathbf{q}}_{2121}(2\cdot V^{\mathbf{q}}_{1111}-V^{\mathbf{k}-\mathbf{q}-\mathbf{k}'}_{1111})}{\{\varepsilon_{1,\mathbf{k}'}+\varepsilon_{1,\mathbf{k}}-\varepsilon_{1,\mathbf{k}-\mathbf{q}}-\varepsilon_{1,\mathbf{k}'+\mathbf{q}}\}^2+\hbar^2\gamma^2}\left(f_{1,\mathbf{k}'+\mathbf{q}}f^{-}_{1,\mathbf{k}'}f^{-}_{1,\mathbf{k}} + f_{1,\mathbf{k}}f_{1,\mathbf{k}'}f^{-}_{1,\mathbf{k}'+\mathbf{q}}\right),
\end{aligned}
$$

$$\Gamma^{*}_{\text{ndiag1}} =$$
$$-\frac{\gamma\cdot V^{\mathbf{q}}_{2112}(2\cdot V^{\mathbf{q}}_{2211}-V^{\mathbf{k}-\mathbf{q}-\mathbf{k}'}_{2211})}{\{\varepsilon_{1,\mathbf{k}'+\mathbf{q}}+\varepsilon_{1,\mathbf{k}-\mathbf{q}}-\varepsilon_{2,\mathbf{k}}-\varepsilon_{2,\mathbf{k}'}\}^2+\hbar^2\gamma^2}\left(f_{1,\mathbf{k}'+\mathbf{q}}f^{-}_{2,\mathbf{k}'}f^{-}_{2,\mathbf{k}}\right)$$
$$-\frac{\gamma\cdot V^{\mathbf{q}}_{2112}(2\cdot V^{\mathbf{q}}_{2211}-V^{\mathbf{k}-\mathbf{q}-\mathbf{k}'}_{2211})}{\{\varepsilon_{1,\mathbf{k}'}+\varepsilon_{1,\mathbf{k}}-\varepsilon_{2,\mathbf{k}-\mathbf{q}}-\varepsilon_{2,\mathbf{k}'+\mathbf{q}}\}^2+\hbar^2\gamma^2}\left(f_{1,\mathbf{k}}f_{1,\mathbf{k}'}f^{-}_{2,\mathbf{k}'+\mathbf{q}}\right),$$

with the abbreviation $f^{-}_{i,\mathbf{k}}=(1-f_{i,\mathbf{k}})$. The other non-diagonal parts which are proportional to $\rho_{12,\mathbf{k}'}$ and $\rho_{12,\mathbf{k}'+\mathbf{q}}$ are neglected. Note that the COULOMB potential in the HARTREE-FOCK contribution is treated unscreened, whereas in the BOLTZMANN scattering terms screening is regarded (the tilde of $V^{\mathbf{q}}$ was dropped in the BOLTZMANN scattering terms).

B.2 Phonon scattering rates

In the following, the full dynamic equation, used in Chap. 6, and Chap. 7 is given. The subscript "corr" will not be indicated in the phonon-assisted density matrix elements (PADs), that is, $\sigma_{\text{corr}}=\sigma$. The full equations are :

$$-\imath\hbar\frac{\mathrm{d}}{\mathrm{d}t}f_{1,\mathbf{k}} = E(t)d_{12}\mathrm{Im}\{p_{12,\mathbf{k}}\}+2\sum_{\mathbf{q}}g^{11}_{\mathbf{q}}\mathrm{Re}\{\sigma^{11}_{\mathbf{k}+\mathbf{q}_{\parallel},\mathbf{q},\mathbf{k}}-\sigma^{11^{*}}_{\mathbf{k},\mathbf{q},\mathbf{k}-\mathbf{q}_{\parallel}}\} \tag{B.2}$$
$$+\sum_{\mathbf{q}}g^{12}_{\mathbf{q}}\left(\sigma^{21}_{\mathbf{k}+\mathbf{q}_{\parallel},\mathbf{q},\mathbf{k}}+\sigma^{12^{*}}_{\mathbf{k},\mathbf{q},\mathbf{k}-\mathbf{q}_{\parallel}}-\sigma^{12}_{\mathbf{k},\mathbf{q},\mathbf{k}-\mathbf{q}_{\parallel}}-\sigma^{21^{*}}_{\mathbf{k}+\mathbf{q}_{\parallel},\mathbf{q},\mathbf{k}}\right) \tag{B.3}$$

$$-\imath\hbar\frac{\mathrm{d}}{\mathrm{d}t}f_{2,\mathbf{k}} = -E(t)d_{12}\mathrm{Im}\{p_{12,\mathbf{k}}\}+2\sum_{\mathbf{q}}g^{22}_{\mathbf{q}}\mathrm{Re}\{\sigma^{22}_{\mathbf{k}+\mathbf{q}_{\parallel},\mathbf{q},\mathbf{k}}-\sigma^{22^{*}}_{\mathbf{k},\mathbf{q},\mathbf{k}-\mathbf{q}_{\parallel}}\} \tag{B.4}$$
$$+\sum_{\mathbf{q}}g^{21}_{\mathbf{q}}\left(\sigma^{12}_{\mathbf{k}+\mathbf{q}_{\parallel},\mathbf{q},\mathbf{k}}+\sigma^{21^{*}}_{\mathbf{k},\mathbf{q},\mathbf{k}-\mathbf{q}_{\parallel}}-\sigma^{21}_{\mathbf{k},\mathbf{q},\mathbf{k}-\mathbf{q}_{\parallel}}-\sigma^{12^{*}}_{\mathbf{k}+\mathbf{q}_{\parallel},\mathbf{q},\mathbf{k}}\right) \tag{B.5}$$

$$-i\hbar\frac{\mathrm{d}}{\mathrm{d}t}p_{12,\mathbf{k}} = (\varepsilon_{1,\mathbf{k}}-\varepsilon_{2,\mathbf{k}})p_{12}-E(t)d_{12}(f_{2,\mathbf{k}}-f_{1,\mathbf{k}})$$
$$+\sum_{\mathbf{q}}g^{11}_{\mathbf{q}}\sigma^{12}_{\mathbf{k}+\mathbf{q}_{\parallel},\mathbf{q},k}+g^{11^{*}}_{\mathbf{q}}\sigma^{21^{*}}_{k,\mathbf{q},\mathbf{k}-\mathbf{q}_{\parallel}}-g^{21}_{\mathbf{q}}\sigma^{11}_{k,\mathbf{q},\mathbf{k}-\mathbf{q}_{\parallel}}-g^{12^{*}}_{\mathbf{q}}\sigma^{11^{*}}_{\mathbf{k}+\mathbf{q}_{\parallel},\mathbf{q},k}$$
$$+g^{21}_{\mathbf{q}}\sigma^{22}_{\mathbf{k}+\mathbf{q}_{\parallel},\mathbf{q},k}+g^{12^{*}}_{\mathbf{q}}\sigma^{22^{*}}_{k,\mathbf{q},\mathbf{k}-\mathbf{q}_{\parallel}}-g^{22}_{\mathbf{q}}\sigma^{12}_{k,\mathbf{q},\mathbf{k}-\mathbf{q}_{\parallel}}-g^{22^{*}}_{\mathbf{q}}\sigma^{21^{*}}_{\mathbf{k}+\mathbf{q}_{\parallel},\mathbf{q},k}, \tag{B.6}$$

with the explicit equations for the phonon-assisted intersubband coherence:

$$-i\hbar\dot{\sigma}^{12}_{\mathbf{k},\mathbf{q},\mathbf{k}'} = (\varepsilon_{1,\mathbf{k}}-\varepsilon_{2,\mathbf{k}'}-\hbar\omega_{\text{LO}})\sigma^{12}_{\mathbf{k},\mathbf{q},\mathbf{k}'}$$
$$-g^{11^{*}}_{\mathbf{q}}\{-(1+n_{\mathbf{q}})p_{12,\mathbf{k}'}f_{1,\mathbf{k}}-n_{\mathbf{q}}(1-f_{1,\mathbf{k}})p_{12,\mathbf{k}'}\}$$
$$-g^{12^{*}}_{\mathbf{q}}\{(1+n_{\mathbf{q}})(1-f_{2,\mathbf{k}'})f_{1,\mathbf{k}}-n_{\mathbf{q}}(1-f_{1,\mathbf{k}})f_{2,\mathbf{k}'}\}$$
$$-g^{22^{*}}_{\mathbf{q}}\{(1+n_{\mathbf{q}})(1-f_{2,\mathbf{k}'})p_{12,\mathbf{k}}+n_{\mathbf{q}}p_{12,\mathbf{k}}f_{2,\mathbf{k}'}\}$$
$$-g^{21^{*}}_{\mathbf{q}}\{-(1+n_{\mathbf{q}})p_{12,\mathbf{k}'}p_{12,\mathbf{k}}+n_{\mathbf{q}}p_{12,\mathbf{k}}p_{12,\mathbf{k}'}\}, \tag{B.7}$$

$$-i\hbar\dot{\sigma}^{21}_{\mathbf{k},\mathbf{q},\mathbf{k}'} = (\varepsilon_{2,\mathbf{k}}-\varepsilon_{1,\mathbf{k}'}-\hbar\omega_{\text{LO}})\sigma^{21}_{\mathbf{k},\mathbf{q},\mathbf{k}'}$$
$$-g^{11^{*}}_{\mathbf{q}}\{(1+n_{\mathbf{q}})(1-f_{1,\mathbf{k}'})p_{21,\mathbf{k}}+n_{\mathbf{q}}p_{21,\mathbf{k}}f_{1,\mathbf{k}'}\}$$
$$-g^{12^{*}}_{\mathbf{q}}\{-(1+n_{\mathbf{q}})p_{21,\mathbf{k}'}p_{21,\mathbf{k}}+n_{\mathbf{q}}p_{21,\mathbf{k}}p_{21,\mathbf{k}'}\}$$
$$-g^{22^{*}}_{\mathbf{q}}\{-(1+n_{\mathbf{q}})p_{21,\mathbf{k}'}f_{2,\mathbf{k}}-n_{\mathbf{q}}(1-f_{2,\mathbf{k}})p_{21,\mathbf{k}'}\}$$
$$-g^{21^{*}}_{\mathbf{q}}\{(1+n_{\mathbf{q}})(1-f_{1,\mathbf{k}'})f_{2,\mathbf{k}}-n_{\mathbf{q}}(1-f_{2,\mathbf{k}})f_{1,\mathbf{k}'}\}, \tag{B.8}$$

and the phonon-assisted intersubband density:

$$\begin{aligned}
-i\hbar\dot{\sigma}^{11}_{\mathbf{k},\mathbf{q},\mathbf{k}'} = {} & (\varepsilon_{1,\mathbf{k}} - \varepsilon_{1,\mathbf{k}'} - \hbar\omega_{\mathrm{LO}})\sigma^{11}_{\mathbf{k},\mathbf{q},\mathbf{k}'} \\
& - g^{11^*}_{\mathbf{q}}\{(1+n_{\mathbf{q}})(1-f_{1,\mathbf{k}'})f_{1,\mathbf{k}} - n_{\mathbf{q}}(1-f_{1,\mathbf{k}})f_{1,\mathbf{k}'}\} \\
& - g^{12^*}_{\mathbf{q}}\{-(1+n_{\mathbf{q}})p_{21,\mathbf{k}'}f_{1,\mathbf{k}} - n_{\mathbf{q}}(1-f_{1,\mathbf{k}})p_{21,\mathbf{k}'}\} \\
& - g^{22^*}_{\mathbf{q}}\{-(1+n_{\mathbf{q}})p_{21,\mathbf{k}'}p_{12,\mathbf{k}} + n_{\mathbf{q}}p_{12,\mathbf{k}}p_{21,\mathbf{k}'}\} \\
& - g^{21^*}_{\mathbf{q}}\{(1+n_{\mathbf{q}})(1-f_{1,\mathbf{k}'})p_{12,\mathbf{k}} + n_{\mathbf{q}}p_{12,\mathbf{k}}f_{1,\mathbf{k}'}\},
\end{aligned} \tag{B.9}$$

$$\begin{aligned}
-i\hbar\dot{\sigma}^{22}_{\mathbf{k},\mathbf{q},\mathbf{k}'} = {} & (\varepsilon_{2,\mathbf{k}} - \varepsilon_{2,\mathbf{k}'} - \hbar\omega_{\mathrm{LO}})\sigma^{22}_{\mathbf{k},\mathbf{q},\mathbf{k}'} \\
& - g^{11^*}_{\mathbf{q}}\{-(1+n_{\mathbf{q}})p_{12,\mathbf{k}'}p_{21,\mathbf{k}} + n_{\mathbf{q}}p_{21,\mathbf{k}}p_{12,\mathbf{k}'}\} \\
& - g^{12^*}_{\mathbf{q}}\{(1+n_{\mathbf{q}})(1-f_{2,\mathbf{k}'})p_{21,\mathbf{k}} + n_{\mathbf{q}}p_{21,\mathbf{k}}f_{2,\mathbf{k}'}\} \\
& - g^{22^*}_{\mathbf{q}}\{(1+n_{\mathbf{q}})(1-f_{2,\mathbf{k}'})f_{2,\mathbf{k}} - n_{\mathbf{q}}(1-f_{2,\mathbf{k}})f_{2,\mathbf{k}'}\} \\
& - g^{21^*}_{\mathbf{q}}\{-(1+n_{\mathbf{q}})p_{12,\mathbf{k}'}f_{2,\mathbf{k}} - n_{\mathbf{q}}(1-f_{2,\mathbf{k}})p_{12,\mathbf{k}'}\}.
\end{aligned} \tag{B.10}$$

Appendix C

Phase cycling matrix

Restricting the incoming electromagnetic pulse sequence to the third order and regarding the dipole selection rules, where directional polarizations of even order vanish, 22 combinations remain:

$$
\begin{aligned}
&(\phi_1),(\phi_2),(\phi_3),(3\phi_1),(3\phi_2),(3\phi_3),(2\phi_1-\phi_2),(2\phi_1-\phi_3),(2\phi_2-\phi_1),\\
&(2\phi_2-\phi_3),(2\phi_3-\phi_1),(2\phi_3-\phi_2),(2\phi_1+\phi_2),(2\phi_1+\phi_3),(2\phi_2+\phi_1),\\
&(2\phi_2+\phi_3),(2\phi_3+\phi_1),(2\phi_3+\phi_2),(\phi_1+\phi_2-\phi_3),(\phi_1-\phi_2+\phi_3),(-\phi_1+\phi_2+\phi_3),(\phi_1+\phi_2+\phi_3).
\end{aligned}
\tag{C.1}
$$

The prefactor of the phases, i.e. $\{l\cdot\phi_1, m\cdot\phi_1, n\cdot\phi_1\}$ corresponds to the subindices in the directional polarizations $P_{l,m,n}$. Thus, 22 sets of phase combinations are needed to obtain the phase cycling matrix of the system. With the sets, given in Table 7.1, the matrix yields:

$$
\begin{pmatrix}
e^{i(0\cdot1+0\cdot0+0\cdot0)} & e^{i(0\cdot0+0\cdot1+0\cdot0)} & \cdots & e^{i(0\cdot3+0\cdot0+0\cdot0)}\\
e^{i(0\cdot1+0\cdot0+\frac{\pi}{2}\cdot0)} & e^{i(0\cdot0+0\cdot1+\frac{\pi}{2}\cdot0)} & \cdots & e^{i(0\cdot3+0\cdot0+\frac{\pi}{2}\cdot0)}\\
\vdots & \vdots & & \vdots\\
e^{i(\frac{3\pi}{2}\cdot1+\frac{\pi}{2}\cdot0+\pi\cdot0)} & e^{i(\frac{3\pi}{2}\cdot0+\frac{\pi}{2}\cdot1+\pi\cdot0)} & \cdots & e^{i(\frac{3\pi}{2}\cdot3+\frac{\pi}{2}\cdot0+\pi\cdot0)}
\end{pmatrix}
\begin{pmatrix}
P_{1,0,0}\\ P_{0,1,0}\\ P_{0,0,1}\\ P_{2,-1,0}\\ P_{2,0,-1}\\ P_{0,2,-1}\\ P_{-1,2,0}\\ P_{-1,0,2}\\ P_{0,-1,2}\\ P_{1,1,-1}\\ P_{1,-1,1}\\ P_{-1,1,1}\\ P_{1,1,1}\\ P_{2,1,0}\\ P_{2,0,1}\\ P_{0,2,1}\\ P_{1,2,0}\\ P_{1,0,2}\\ P_{0,1,2}\\ P_{0,0,3}\\ P_{3,0,0}
\end{pmatrix}
=
\begin{pmatrix}
\mathscr{P}(0,0,0)\\ \mathscr{P}(0,0,\frac{\pi}{2})\\ \mathscr{P}(\frac{\pi}{2},0,\pi)\\ \mathscr{P}(\frac{\pi}{2},0,\frac{\pi}{2})\\ \mathscr{P}(\pi,0,0)\\ \mathscr{P}(\pi,0,\frac{\pi}{2})\\ \mathscr{P}(\frac{3\pi}{2},0,\frac{3\pi}{2})\\ \mathscr{P}(0,0,\frac{3\pi}{2})\\ \mathscr{P}(0,0,\pi)\\ \mathscr{P}(\frac{\pi}{2},0,\frac{3\pi}{2})\\ \mathscr{P}(\frac{3\pi}{2},0,\pi)\\ \mathscr{P}(\frac{3\pi}{2},0,\frac{\pi}{2})\\ \mathscr{P}(0,\frac{3\pi}{2},0)\\ \mathscr{P}(0,\frac{\pi}{2},\frac{\pi}{2})\\ \mathscr{P}(\frac{\pi}{2},\frac{\pi}{2},\pi)\\ \mathscr{P}(\pi,\frac{\pi}{2},0)\\ \mathscr{P}(\pi,\frac{\pi}{2},\frac{\pi}{2})\\ \mathscr{P}(\frac{3\pi}{2},\frac{\pi}{2},\frac{3\pi}{2})\\ \mathscr{P}(0,\frac{\pi}{2},\frac{3\pi}{2})\\ \mathscr{P}(0,\frac{\pi}{2},\pi),\\ \mathscr{P}(\frac{\pi}{2},\frac{\pi}{2},\frac{3\pi}{2})\\ \mathscr{P}(\frac{3\pi}{2},\frac{\pi}{2},\pi)
\end{pmatrix}.
\tag{C.2}
$$

By inverting the matrix, the prefactors for the directional polarizations $P_{k,l,m}$ are obtained:

Appendix D

Calculations for silicon

D.1 Relaxation rate approximation of the electron-phonon scattering terms

D.1.1 The reduced Peierls equation

Starting from the PEIERLS equation, the equation can be split into a long term limit and a short term limit:

$$\begin{aligned} \dot{n_{\mathrm{LO},\mathbf{q}}} &= -\left(\frac{n_{\mathrm{LO},\mathbf{q}} - n_{\mathrm{Bose,\,300K}}}{\tau_{\mathrm{LO}}}\right) + \frac{2\pi}{\hbar}\sum_k |g_{\mathbf{k}(,\mathbf{q}_{\mathrm{LO}})}|^2 \delta(\varepsilon^{3\mathrm{d}}_{\mathbf{k}+\mathbf{q}_{\mathrm{LO}}} - \varepsilon^{3\mathrm{d}}_{\mathbf{k}} - \hbar\omega_{\mathrm{LO}})[n^+ f f^- - n f^- f] \\ &= \text{long time limit} + \text{short time limit}, \end{aligned} \tag{D.1}$$

with $n^+ = (n+1)$, $f^- = 1-f$. Now the short time term is evaluated:

$$\begin{aligned} &\frac{2\pi}{\hbar}\sum_k |g_{\mathbf{k}(,\mathbf{q}_{\mathrm{LO}})}|^2 \delta(\varepsilon^{3\mathrm{d}}_{\mathbf{k}+\mathbf{q}_{\mathrm{LO}}} - \varepsilon^{3\mathrm{d}}_{\mathbf{k}} - \hbar\omega_{\mathrm{LO}}) \\ &= \frac{2\pi}{\hbar}\frac{V}{8\pi^3}\int_0^{k_{\max}} \mathrm{d}k\, k^2 \int_0^{2\pi} \mathrm{d}\phi \int_0^{\pi} \mathrm{d}\theta |g_{\mathbf{k}(,\mathbf{q}_{\mathrm{LO}})}|^2 \sin(\theta)\delta(\varepsilon^{3\mathrm{d}}_{\mathbf{k}+\mathbf{q}_{\mathrm{LO}}} - \varepsilon^{3\mathrm{d}}_{\mathbf{k}} - \hbar\omega_{\mathrm{LO}}) \\ &\overset{\text{no } \phi\text{-dependence}}{=} \frac{2\pi}{\hbar}\frac{V}{4\pi^2}\int_0^{k_{\max}} \mathrm{d}k\, k^2 \int_0^{\pi} \mathrm{d}\theta |g_{\mathbf{k}(,\mathbf{q}_{\mathrm{LO}})}|^2 \sin(\theta)\delta(\varepsilon^{3\mathrm{d}}_{\mathbf{k}+\mathbf{q}_{\mathrm{LO}}} - \varepsilon^{3\mathrm{d}}_{\mathbf{k}} - \hbar\omega_{\mathrm{LO}}) \\ &= \frac{2\pi}{\hbar}\frac{V}{4\pi^2}\int_0^{k_{\max}} \mathrm{d}k\, k^2 \int_0^{\pi} \mathrm{d}\theta |g_{\mathbf{k}(,\mathbf{q}_{\mathrm{LO}})}|^2 \sin(\theta)\delta(\frac{\hbar^2}{2m_{\mathrm{b}}}[q^2 + 2kq\cos\theta] - \hbar\omega_{\mathrm{LO}}) \\ &\quad \rightarrow \cos\theta = \frac{m_{\mathrm{b}}\varepsilon_{\mathrm{LO}}}{\hbar^2 kq} - \frac{q}{2k} \\ &= \frac{2\pi}{\hbar}\frac{V}{4\pi^2}\int_0^{k_{\max}} \mathrm{d}k\, k^2 |g_{\mathbf{k}(,\mathbf{q}_{\mathrm{LO}})}|^2 \sin[\arccos(\frac{m_{\mathrm{b}}\varepsilon_{\mathrm{LO}}}{\hbar^2 kq} - \frac{q}{2k})] \\ &\overset{\text{Assuming equal coupling: } g_{k,q}\sim g}{=} \frac{2\pi}{\hbar}\frac{V}{4\pi^2} g^2_{\mathrm{const}} \int_0^{k_{\max}} \mathrm{d}k\, k^2 \sin[\arccos(\frac{m_{\mathrm{b}}\varepsilon_{\mathrm{LO}}}{\hbar^2 kq} - \frac{q}{2k})], \\ &\approx \frac{2\pi}{\hbar}\frac{V}{4\pi^2} g^2_{\mathrm{const}} \int_0^{k_{\max}} \mathrm{d}k\, k^2 \end{aligned} \tag{D.2}$$

$$\tag{D.3}$$

The approximation can be made due to a more numerical argument, since $k^2\sin[\arccos(\frac{m_{\mathrm{b}}\varepsilon_{\mathrm{LO}}}{\hbar^2 kq} - \frac{q}{2k})] \sim k^2$ for $q > 0.5\,\mathrm{nm}^{-1}$ and since $\arccos(0) = \frac{\pi}{2}$. The integrand is approximately: $k^2\sin[\arccos(\frac{m_{\mathrm{b}}\varepsilon_{\mathrm{LO}}}{\hbar^2 kq} - \frac{q}{2k})] \sim k^2 \quad \forall q,k$. This leads to an overestimation of the value for small q, but since n_q has to be considered in

$\dot{f}_{\mathrm{CB}} \propto \sum_q n_q \propto \int_q q^2 n_q$ the overestimation for small n_q is negligible. Hence:

$$\begin{aligned}\dot{n}_{\mathrm{LO},\mathbf{q}} &\approx -\left(\frac{n_{\mathrm{LO},\mathbf{q}} - n_{\mathrm{Bose,\,300K}}}{\tau_{\mathrm{LO}}}\right) + \frac{1}{\tau_{\mathrm{LO}}^{\mathrm{intra}}} \int_0^{k_{\max}} \mathrm{d}k\, k^2 [n^+ f_{\varepsilon_k+\varepsilon_{\mathrm{LO}}} f^-_{\varepsilon_k} - n f^-_{\varepsilon_k+\varepsilon_{\mathrm{LO}}} f_{\varepsilon_k}] \\ &= -\left(\frac{n^{\mathbf{q}}_{\mathrm{LO}} - n_{300}}{\tau_{\mathrm{LO}}}\right) + \frac{1}{\tau_{\mathrm{LO}}^{\mathrm{intra}}} \frac{\sqrt{2m^3_{\mathrm{bulk}}}}{\hbar^3} \\ &\times \int_0^{\varepsilon_{\max}} \mathrm{d}\varepsilon \sqrt{\varepsilon} \left[n^+_{\mathrm{LO}} f_{\mathrm{CB}}(t, \varepsilon + \hbar\omega_{\mathrm{LO}}) f^-_{\mathrm{CB}}(t,\varepsilon) - n_{\mathrm{LO}} f_{\mathrm{CB}}(t,\varepsilon) f^-_{\mathrm{CB}}(t, \varepsilon + \hbar\omega_{\mathrm{LO}})\right], \end{aligned} \tag{D.4}$$

with $\underline{\frac{1}{\tau_{\mathrm{LO}}^{\mathrm{intra}}} = \frac{2\pi}{\hbar} \frac{V}{4\pi^2} g^2_{\mathrm{const}}}$ and $[m_{\mathrm{b}}] = \mathrm{fs}^2\mathrm{meV}$. [1]

D.1.2 Derivation of the electron-longitudinal optical phonon rate equation

The microscopic equation is:

$$\begin{aligned}\dot{f}_{\mathbf{k},|\text{el-LO}} &= \frac{2\pi}{\hbar} \sum_{\mathbf{q}} |g_{\mathbf{k}(,\mathbf{q}_{\mathrm{LO}})}|^2 \delta(\varepsilon_{\mathbf{k}+\mathbf{q}_{\mathrm{LO}}} - \varepsilon_{\mathbf{k}} - \hbar\omega_{\mathrm{LO}}) \left[n^+_{\mathrm{LO}} f_{\mathbf{k}+\mathbf{q}_{\mathrm{LO}}} f^-_{\mathbf{k}} - n_{\mathrm{LO}} f^-_{\mathbf{k}+\mathbf{q}_{\mathrm{LO}}} f_{\mathbf{k}}\right] \\ &= \Gamma_{\mathrm{in}}(1 - f_{\mathbf{k}}) - \Gamma_{\mathrm{out}} f_{\mathbf{k}}. \end{aligned} \tag{D.5}$$

the subscript "CB" n f has been dropped. For long times, the distribution f differs from the equilibrium function f_0 with a small deviation: $f \approx f_0 + \delta f$.

$$\dot{f}_{\mathbf{k},|\text{el-LO}} = \Gamma_{\mathrm{in}}(1 - f_{0,\mathbf{k}} - \delta f_{\mathbf{k}}) - \Gamma_{\mathrm{out}}(f_{0,\mathbf{k}} + \delta f_{\mathbf{k}}) = -(\Gamma_{\mathrm{in}} + \Gamma_{\mathrm{out}})\delta f_{\mathbf{k}} = -\frac{1}{\tau_{\text{el-LO}}^{\mathrm{intra}}} \delta f_{\mathbf{k}}, \tag{D.6}$$

with the equilibrium assumption: $\Gamma_{\mathrm{in}}(1 - f_{0,\mathbf{k}}) = \Gamma_{\mathrm{out}} f_{0,\mathbf{k}}$. This can be applied to Eq. D.5:

$$\begin{aligned}\frac{1}{\tau_{\text{el-LO}}^{\mathrm{intra}}} &= \frac{2\pi}{\hbar} \sum_{\mathbf{q}} |g_{\mathbf{k}(,\mathbf{q}_{\mathrm{LO}})}|^2 \delta(\varepsilon_{\mathbf{k}+\mathbf{q}_{\mathrm{LO}}} - \varepsilon_{\mathbf{k}} - \hbar\omega_{\mathrm{LO}}) \left[n^+_{\mathrm{LO}} f_{0,\mathbf{k}+\mathbf{q}_{\mathrm{LO}}} + n_{\mathrm{LO}} f^-_{0,\mathbf{k}+\mathbf{q}_{\mathrm{LO}}}\right] \\ &\overset{\text{s.above}}{=} \overbrace{\frac{2\pi}{\hbar} \frac{V}{4\pi^2} g^2_{\mathrm{const}}}^{1/\tau_{\mathrm{LO}}^{\mathrm{intra}}} \int_0^{q_{\max}} \mathrm{d}q\, q^2 \int_0^{\pi} \mathrm{d}\theta \sin\theta\, \delta(\frac{\hbar^2}{2m_{\mathrm{b}}}[q^2 + 2kq\cos\theta] - \hbar\omega_{\mathrm{LO}})[n^+ f - n f^-] \\ &\to q_{1,2} = -k\cos\theta \pm \sqrt{k^2\cos^2\theta + 2\frac{m_{\mathrm{b}}}{\hbar^2}\varepsilon_{\mathrm{LO}}} \\ &= \frac{1}{\tau_{\mathrm{LO}}^{\mathrm{intra}}} \int_0^{\pi} \sin\theta (-k\cos\theta \pm \sqrt{k^2\cos^2\theta + 2\frac{m_{\mathrm{b}}}{\hbar^2}\varepsilon_{\mathrm{LO}}})^2 [n^+_{\mathrm{LO}} f_{0,\varepsilon_k+\varepsilon_{\mathrm{LO}}} - n_{\mathrm{LO}} f^-_{0,\varepsilon_k+\varepsilon_{\mathrm{LO}}}] \\ &\approx \frac{1}{\tau_{\mathrm{LO}}^{\mathrm{intra}}} \cdot [0.5 - 1.5], \end{aligned} \tag{D.7}$$

For $T_{\mathrm{phon}} \approx 350\,\mathrm{K}$, the integral equals 1. Thus, the scattering time in the reduced PEIERLS equation and in the *el-LO* intraband rate equation are approximately equal, that is, $\tau_{\text{el-LO}}^{\mathrm{intra}} \approx \tau_{\mathrm{LO}}^{\mathrm{intra}}$. Thus, it is:

$$\dot{f}_{|\text{el-LO}}(t,\varepsilon) \approx -\frac{1}{\tau_{\mathrm{LO}}^{\mathrm{intra}}} \delta f_{\varepsilon} = -\frac{f(t,\varepsilon) - f_{0,\mathrm{phon}}(t,\varepsilon)}{\tau_{\mathrm{LO}}^{\mathrm{intra}}}, \tag{D.8}$$

with the FERMI function $f_{0,\mathrm{phon}}$ with the phonon temperature T_{phon}: $f^{\mathrm{b,intra}}_{\text{el-LO}}[\varepsilon, T^{\mathrm{b}}_{\mathrm{LO}}, \mu^{\mathrm{b}}_{\mathrm{LO}}]$.

[1] Units: $[\hbar] = \mathrm{meVfs}$, $[m_0] = \frac{\mathrm{fs}^2\mathrm{meV}}{\mathrm{nm}^2}$, $[\varepsilon_0] = \frac{\mathrm{e}^2}{\mathrm{eV\,nm}}$ $[\sum_{\mathbf{k}_{3D}} = \frac{V}{(8\pi^3)} \int \mathrm{d}k\, k^2 \int \mathrm{d}\phi \int d\theta \sin^2(\theta)] = \frac{V}{(2\pi^2)} \int \mathrm{d}k\, k^2]$ = -, $[\delta()] = (\mathrm{meV})^{-1}$, $[g_{\mathbf{k}(,\mathbf{q})}] = \mathrm{meV}$.

D.2 Determination of local/global temperatures and the chemical potential

The calculations of the chemical potential μ and the temperature T are necessary for the description of the local distributions within the bulk and surface conduction band as well as the global equilibrium two band distribution.

D.2.1 Density of states

The electron density n_b, n_s and the energy density ρ_ε of the system is determined by summarizing over all k states and the spin. Therefore, the density of states of the different bands has to be considered:

$$\sum_{\sigma,k_{3\mathrm{d}}} = \sum_{\sigma,\underline{k}} = 2\sum_{\underline{k}} = \frac{V}{\pi^2}\int_0^\infty \mathrm{d}|\underline{k}|\,|\underline{k}|^2 \overset{\underline{k}\to\varepsilon}{=} \frac{V}{\pi^2\hbar^3}\sqrt{2m_\mathrm{bulk}^3}\int_0^\infty \mathrm{d}\,\varepsilon\sqrt{\varepsilon}, \tag{D.9}$$

$$\sum_{\sigma,k_{2\mathrm{d}}} = \sum_{\sigma,\mathbf{k}} = 2\sum_{\mathbf{k}} = \frac{A}{\pi}\int_0^\infty \mathrm{d}|\mathbf{k}|\,|\mathbf{k}| \overset{\mathbf{k}\to\varepsilon}{=} \frac{Am_\mathrm{surf}}{(\hbar^2\pi)}\int_0^\infty \mathrm{d}\,\varepsilon, \tag{D.10}$$

with $\varepsilon = \frac{\hbar^2k^2}{2m_\mathrm{bulk/surf}}$. In our case, it is more convenient to transform the k- into an ε- integral. In the Peierls equation, this transformation has already been applied.

D.2.2 Electron distribution in different dimensions

Within the relaxation rate approximation, the electron distribution is assumed to relax into a local Fermi distribution within the bulk ($f^{\mathrm{b,intra}}$) and the surface band ($f^{\mathrm{s,intra}}$), as well as into a global two band Fermi distribution function of the combined bulk and surface system (f^{tb}) with respective μ and T.

$$f^{\mathrm{b,intra}}[\varepsilon,T^\mathrm{b},\mu^\mathrm{b}] = \frac{1}{e^{\beta(T^\mathrm{b})(\varepsilon-\mu^\mathrm{b})}+1}, \tag{D.11}$$

$$f^{\mathrm{s,intra}}[\varepsilon,T^\mathrm{s}] = \left[\frac{e^{\beta(T^\mathrm{s})\varepsilon}}{(e^{\hbar^2\beta(T^\mathrm{s})\pi n_\mathrm{surf}/m_\mathrm{surf}}-1)}+1\right]^{-1}, \tag{D.12}$$

$$f^{\mathrm{tb}}[\varepsilon,T^\mathrm{tb},\mu^\mathrm{tb}] = \frac{1}{e^{\beta(T^\mathrm{tb})(\varepsilon-\mu^\mathrm{tb})}+1}, \tag{D.13}$$

with $\beta(T) = 1/(k_\mathrm{B}T)$, $f^{\mathrm{s,inter}} = f^{\mathrm{tb}}[\varepsilon,T^\mathrm{tb},\mu^\mathrm{tb}]$ and $f^{\mathrm{b,inter}} = f^{\mathrm{tb}}[\varepsilon+\varepsilon_\mathrm{gap},T^\mathrm{tb},\mu^\mathrm{tb}]$.

D.2.3 Energy density and electron density conservation

The electron density conservation is valid for all relaxation processes. For electron-electron processes, additionally the energy density is conserved. Hence, for each time step, one can determine μ and T by considering the particular conservation. Note that in the two-dimensional case, the density conservation

is already fulfilled for Eq. (D.12):

$$n_\mathrm{b} = \frac{2}{V}\sum_{\underline{k}} f_\mathrm{3d}(t_\mathrm{const},\varepsilon_k) \stackrel{!}{=} \frac{2}{V}\sum_{\underline{k}} f^{\mathrm{b,\ intra}}[\varepsilon_k, T^\mathrm{b}, \mu^\mathrm{b}], \tag{D.14}$$

$$\rho_\varepsilon = \frac{2}{A/V}\sum_{\mathbf{k}/\underline{k}} \varepsilon_k \cdot f_\mathrm{2d/3d}(t_\mathrm{const},\varepsilon_k) \stackrel{!}{=} \frac{2}{V}\sum_{\mathbf{k}/\underline{k}} \varepsilon_k \cdot f^{\mathrm{s/b,\ intra}}[\varepsilon_k, T^{\mathrm{s/b}}(,\mu^\mathrm{b})], \tag{D.15}$$

$$\begin{aligned} n_\mathrm{total} &= n_\mathrm{b} + \frac{1}{L_\mathrm{s}} n_\mathrm{s} = \frac{2}{V}\sum_{\underline{k}} f_\mathrm{3d}(t_\mathrm{const},\varepsilon_k) + \frac{2}{AL_\mathrm{s}}\sum_{\mathbf{k}} f_\mathrm{2d}(t_\mathrm{const},\varepsilon_k) \\ &\stackrel{!}{=} \frac{2}{V}\sum_{\underline{k}} f^{\mathrm{b,\ inter}}[\varepsilon_k, T^\mathrm{tb}, \mu^\mathrm{tb}] + \frac{2}{AL_\mathrm{s}}\sum_{\mathbf{k}} f^{\mathrm{s,\ inter}}[\varepsilon_k, T^\mathrm{tb}, \mu^\mathrm{tb}], \end{aligned} \tag{D.16}$$

$$\begin{aligned} \rho_{\varepsilon,\mathrm{total}} &= \rho^\mathrm{tb}_{\varepsilon,\mathrm{bulk}} + \frac{1}{L_\mathrm{s}}\rho^\mathrm{tb}_{\varepsilon,\mathrm{surf}} = \frac{2}{V}\sum_{\underline{k}} (\varepsilon_\mathrm{gap}+\varepsilon_k)\cdot f_\mathrm{3d}(t_\mathrm{const},\varepsilon_k) + \frac{2}{AL_\mathrm{s}}\sum_{\mathbf{k}} \varepsilon_k \cdot f_\mathrm{2d}(t_\mathrm{const},\varepsilon_k) \\ &\stackrel{!}{=} \frac{2}{V}\sum_{\underline{k}} \varepsilon_k \cdot f^{\mathrm{b,\ inter}}[\varepsilon_k, T^\mathrm{tb}, \mu^\mathrm{tb}] + \frac{2}{AL_\mathrm{s}}\sum_{\mathbf{k}} \varepsilon_k \cdot f^{\mathrm{s,\ inter}}[\varepsilon_k, T^\mathrm{tb}, \mu^\mathrm{tb}]. \end{aligned} \tag{D.17}$$

D.2.4 Determination of the temperature for the dominant phonon mode

For each time step, the LO phonon mode is assumed to be in quasi-equilibrium with a phonon bath. Thus the phonon temperature can be calculated for each time step via the boson distribution if the phonon occupation is known:

$$n_\mathrm{LO} = \frac{1}{\mathrm{e}^{\beta(T)\hbar\omega_\mathrm{LO}}-1} \Rightarrow \beta(T) = 1/k_\mathrm{B}T = \frac{1}{\hbar\omega_\mathrm{LO}}\ln\left(\frac{1+n_\mathrm{LO}}{n_\mathrm{LO}}\right) \tag{D.18}$$

D.2.5 Determination of the Gauss-convoluted bulk distribution

To adjust the resulting bulk relaxation $f_\mathrm{3d}(t_\mathrm{const},\varepsilon)$ for constant times to experimental data, $f_\mathrm{3d}(t_\mathrm{const},\varepsilon)$ (multiplied with the 3d density of states) is convoluted with a Gaussian pulse $G(\varepsilon)$:

$$\left[f_\mathrm{3d}^{t_\mathrm{const}} \circ G\right](\varepsilon) = \int_0^{\varepsilon_\mathrm{max}} \mathrm{d}\varepsilon'\, f_\mathrm{3d}^{t_\mathrm{const}}(\varepsilon') G(\varepsilon-\varepsilon')\cdot\sqrt{\varepsilon'} = \int_0^{\varepsilon_\mathrm{max}} \mathrm{d}\varepsilon' f_\mathrm{3d}^{t_\mathrm{const}}(\varepsilon') A_0 e^{\frac{(\varepsilon-\varepsilon')^2}{2(0.5\sigma)^2}}\sqrt{\varepsilon'}, \tag{D.19}$$

with the FWHM of the Gaussian $\sigma = 0.15$ eV and $\int_\infty^{-\infty} \mathrm{d}\varepsilon\, G(\varepsilon) = 1$. The convoluted distribution function is then shifted on the energy axis to the conduction band minimum at $\varepsilon = 0.27$ eV.

Appendix E

Dynamic equations of the quantum dot considering the external phonon bath

In the following, the EOM of the dynamics of the phonon-assisted electronic operators, $\frac{\mathrm{d}}{\mathrm{d}t}\langle\hat{O}\hat{B}^{l,m}_{l',m'}\rangle_{|\text{ph-ext}}$, are calculated with respect to the external phonon bath. The interaction with the other Hamiltonians have already been calculated in Sec. 10.2.3. The interaction of the system variables with the external phonon bath $\hat{H}_{\text{ph-ext}} = \sum_{\xi,\mathbf{q}} A^{\mathbf{q}}\hat{b}^{\dagger}_{\mathbf{q}}\hat{d}_{\xi} + \text{c. c.}$ has to be determined. Here, the coupling strength is assumed to be equal for all ξ-modes: $A^{\mathbf{q}(*)} = [\alpha(g^{22*}_{\mathbf{q}} - g^{11*}_{\mathbf{q}}) + \alpha' g^{21}_{\mathbf{q}}]^{(*)}$. The equations for the phonon-assisted values $\langle\hat{O}\hat{B}^{l,m}_{l',m'}\rangle$ of a two-electron operator $\hat{O} = \hat{a}^{\dagger}_i\hat{a}_j$ $(i,j \in \{1,2\})$ reads in second-order Born:

$$\begin{aligned}-\mathrm{i}\hbar\frac{\mathrm{d}}{\mathrm{d}t}\langle\hat{O}\hat{B}^{l,m}_{l',m'}\rangle_{|\text{ph-ext}} =& -m'\sum_{\xi}\alpha\langle\hat{d}_{\xi}\hat{O}\hat{B}^{l,m}_{l',m'-1}\rangle g^2_{\text{eff}} - l'\sum_{\xi}\alpha'\langle\hat{d}_{\xi}\hat{O}\hat{B}^{l,m}_{l'-1,m'}\rangle g^2_{21}\\ &+ m\sum_{\xi}\alpha^*\langle\hat{d}_{\xi}\hat{O}\hat{B}^{l,m-1}_{l',m'}\rangle g^2_{\text{eff}} + l\sum_{\xi}\alpha'^*\langle\hat{d}_{\xi}\hat{O}\hat{B}^{l-1,m}_{l',m'}\rangle g^2_{21}\end{aligned} \tag{E.1}$$

The dynamics for the external bath-assisted values has to be calculated as well:

$$\begin{aligned}-\mathrm{i}\hbar\frac{\mathrm{d}}{\mathrm{d}t}\langle\hat{d}_{\xi}\hat{O}\hat{B}^{l,m}_{l',m'}\rangle =& (\varepsilon_{\mathrm{R}(\hat{O})} - \varepsilon_{\xi})\langle\hat{d}_{\xi}\hat{O}\hat{B}^{l,m}_{l',m'}\rangle\\ &- \alpha^*\langle\hat{O}\hat{B}^{l,m}_{l',m'+1}\rangle - \alpha'^*\langle\hat{O}\hat{B}^{l,m}_{l'+1,m'}\rangle\\ &+ m\,\alpha^* n(\xi)\langle\hat{O}\hat{B}^{l,m-1}_{l',m'}\rangle g^2_{\text{eff}} + l\,\alpha'^* n(\xi)\langle\hat{O}\hat{B}^{l-1,m}_{l',m'}\rangle g^2_{21},\end{aligned} \tag{E.2}$$

$$\begin{aligned}-\mathrm{i}\hbar\frac{\mathrm{d}}{\mathrm{d}t}\langle\hat{d}^{\dagger}_{\xi}\hat{O}\hat{B}^{l,m}_{l',m'}\rangle =& (\varepsilon_{\mathrm{R}(\hat{O})} + \varepsilon_{\xi})\langle\hat{d}^{\dagger}_{\xi}\hat{O}\hat{B}^{l,m}_{l',m'}\rangle\\ &- m'\,\alpha^* n(\xi)\langle\hat{O}\hat{B}^{l,m}_{l',m'-1}\rangle g^2_{\text{eff}} - l'\alpha'^* n(\xi)\langle\hat{O}\hat{B}^{l,m}_{l'-1,m'}\rangle g^2_{21}\\ &+ \alpha^*\langle\hat{O}\hat{B}^{l,m+1}_{l',m'}\rangle + \alpha'^*\langle\hat{O}\hat{B}^{l+1,m}_{l',m'}\rangle,\end{aligned} \tag{E.3}$$

with the rotation energy $\varepsilon_{\mathrm{R}(\hat{a}^{\dagger}_i\hat{a}_i)} = [\mathrm{i}(l+l'+m+m')\gamma + (l-l'+m-m')\varepsilon_{\text{LO}}]$ and $\varepsilon_{\mathrm{R}(\hat{a}^{\dagger}_i\hat{a}_j)} = [\varepsilon_{\mathrm{R}\hat{a}^{\dagger}_i\hat{a}_i)} - \mathrm{i}D - \varepsilon_{\text{gap}}]$. $n(\xi)$ is the BOSE distribution function for an energy $\hbar\omega_{\xi}$. Expectation values such as $\langle\hat{O}\tilde{B}^{l,m}_{l'-i,m'+i}\rangle$ or $\langle\hat{O}\tilde{B}^{l+i,m-i}_{l',m'}\rangle$, $i = \pm 1$ are neglected since they represent higher orders than second-order Born. For the numerics, the constants α, α' are set to one.

Bibliography

[AHK99] V.M. Axt, M. Herbst, and T. Kuhn. Coherent control of phonon quantum beats. *Superlattices and Microstructures*, 26(2):117 – 128, 1999.

[AK04] V. M. Axt and T. Kuhn. Femtosecond spectroscopy in semiconductors: a key to coherences, correlations and quantum kinetics. *Rep. Prog. Phys.*, 67:433, 2004.

[All87] Philip B. Allen. Theory of thermal relaxation of electrons in metals. *Phys. Rev. Lett.*, 59(13):1460–1463, Sep 1987.

[AM10] Darius Abramavicius and Shaul Mukamel. Quantum oscillatory exciton migration in photosynthetic reaction centers. *J. Chem. Phys.*, 133(6):064510, 2010.

[APV+09] Darius Abramavicius, Benoit Palmieri, Dmitri V. Voronine, Frantisek Sanda, and Shaul Mukamel. Coherent multidimensional optical spectroscopy of excitons in molecular aggregates; quasiparticle vs. supermolecule perspectives. *Chem. Rev.*, 109:2350–2408, 2009.

[Bas81] G. Bastard. Superlattice band structure in the envelope-function approximation. *Phys. Rev. B*, 24:5693–5697, Nov 1981.

[BFC+88] P. C. Becker, H. L. Fragnito, C. H. Brito Cruz, R. L. Fork, J. E. Cunningham, J. E. Henry, and C. V. Shank. Femtosecond photon echoes from band-to-band transitions in gaas. *Phys. Rev. Lett.*, 61:1647–1649, Oct 1988.

[BFWK04] Stefan Butscher, Jens Förstner, Inès Waldmüller, and Andreas Knorr. Polaron signatures in the line shape of semiconductor ;intersubband transitions: quantum kinetics of the electron-phonon interaction. *Phys. Status Solidi B*, 241(11):R49–R51, 2004.

[BGH+00] D. Bimberg, M. Grundmann, F. Heinrichsdorff, N.N. Ledentsov, V.M. Ustinov, A.E. Zhukov, A.R. Kovsh, M.V. Maximov, Y.M. Shernyakov, B.V. Volovik, A.F. Tsatsulnikov, P.S. Kopev, and Zh.I. Alferov. Quantum dot lasers: breakthrough in optoelectronics. *Thin Solid Films*, 367(1-2):235 – 249, 2000.

[BGL99] D. Bimberg, M. Grundmann, and N. N. Ledentsov. *Quantum Dot Heterostructures*. John Wiley & Sons, Chichester, 1999.

[BHS+10] Carsten Brenner, Martin Hofmann, Maik Scheller, Mohammad Khaled Shakfa, Martin Koch, Iván Cámara Mayorga, Andreas Klehr, Götz Erbert, and Günther Tränkle. Compact diode-laser-based system for continuous-wave and quasi-time-domain terahertz spectroscopy. *Opt. Lett.*, 35(23):3859–3861, Dec 2010.

[Bim05] Dieter Bimberg. Quantum dots for lasers, amplifiers and computing. *J. Phys. D*, 38(13):2055–2058, 2005.

[BK06] Stefan Butscher and Andreas Knorr. "occurence of intersubband polaronic repellons in a two-dimensional electron gas". *Phys. Rev. Lett.*, 97:197401, 2006.

[BKSK07] N. Buecking, P. Kratzer, M. Scheffler, and A. Knorr. Theory of optical excitation and relaxation phenomena at semiconductor surfaces: linking density functional and density matrix theory. *Appl. Phys. A*, 88:505, 2007.

[BKSK08] N. Buecking, P. Kratzer, M. Scheffler, and A. Knorr. Linking density-functional and density-matrix theory: picosecond electron relaxation at the si(100) surface. *Phys. Rev. B*, 77:2333305, 2008.

[BLKW05] F. Banit, S.-C. Lee, A. Knorr, and A. Wacker. Self-consistent theory of the gain linewidth for quantum-cascade lasers. *Appl. Phys. Lett.*, 86(4):041108, 2005.

[BMH+07] S. Butscher, F. Milde, M. Hirtschulz, E. Malic, and A. Knorr. Hot electron relaxation and phonon dynamics in graphene. *Appl. Phys. Lett.*, 91(20):203103, 2007.

[BMS+03] I. V. Bondarev, S. A. Maksimenko, G. Ya. Slepyan, I. L. Krestnikov, and A. Hoffmann. Exciton-phonon interactions and exciton dephasing in semiconductor quantum-well heterostructures. *Phys. Rev. B*, 68:073310, Aug 2003.

[BMSF04] Tobias Brixner, Tomáš Mančal, Igor V. Stiopkin, and Graham R. Fleming. Phase-stabilized two-dimensional electronic spectroscopy. *J. Chem. Phys.*, 121(9):4221–4236, 2004.

[BTR+95] L. Banyai, D. B. Tran Thoai, E. Reitsamer, H. Haug, D. Steinbach, M. U. Wehner, M. Wegener, T. Marschner, and W. Stolz. Exciton - lo-phonon quantum kinetics: Evidence of memory effects in bulk gaas. *Phys. Rev. Lett.*, 75(11):2188, 1995.

[Bue08] Norbert Buecking. *Optical Excitation and Electron Relaxation Dynamics at Semiconductor Surfaces:A combined Approach of Density Functional and Density Matrix Theory applied to the Silicon (001) Surface*. PhD thesis, Technische Universität Berlin, 2008.

[But07] Stefan Butscher. *Many-Particle Effects in Two Dimensional Nanostructures: Semiconductor Intersubband Transitions and Graphene*. PhD thesis, Technische Universität Berlin, 2007.

[BW80] Max Born and Emil Wolf. *Principles of optics*. Pergamon Press, Oxford, 6 edition, 1980.

[CAH+96] F. X. Camescasse, A. Alexandrou, D. Hulin, L. Bányai, D. B. Tran Thoai, and H. Haug. Ultrafast electron redistribution through coulomb scattering in undoped gaas: Experiment and theory. *Phys. Rev. Lett.*, 77:5429–5432, Dec 1996.

[Cho08] Minhaeng Cho. Coherent two-dimensional optical spectroscopy. *Chem. Rev.*, 108(4):1331–1418, 2008. PMID: 18363410.

[CK99] Weng W. Chow and Stephan W. Koch. *Semiconductor-Laser Fundamentals: Physics of the Gain Materials*. Springer, Berlin, 1999.

[CK05] Weng W. Chow and Stephan W. Koch. Theory of semiconductor quantum-dot laser dynamics. *IEEE J. Quantum Electron.*, 41(4):495–505, 2005.

[CLSRP92] S. L. Chuang, M. S. C. Luo, S. Schmitt-Rink, and A. Pinczuk. Many-body effects on intersubband transitions in semiconductor quantum-well structures. *Phys. Rev. B*, 46(3):1897–1900, 1992.

[CMD+10] Alexander Carmele, Frank Milde, Matthias-René Dachner, Malek Bagheri Harouni, Rasoul Roknizadeh, Marten Richter, and Andreas Knorr. Formation dynamics of an entangled photon pair: A temperature-dependent analysis. *Phys. Rev. B*, 81(19):195319, May 2010.

[CPS+04] Pochung Chen, C. Piermarocchi, L. J. Sham, D. Gammon, and D. G. Steel. Theory of quantum optical control of a single spin in a quantum dot. *Phys. Rev. B*, 69(7):075320, 2004.

[CRCK10] Alexander Carmele, Marten Richter, Weng W. Chow, and Andreas Knorr. Antibunching of thermal radiation by a room-temperature phonon bath: A numerically solvable model for a strongly interacting light-matter-reservoir system. *Phys. Rev. Lett.*, 104:156801, Apr 2010.

[CT99] C. Cohen-Tannoudji. *Quantenmechanik*, volume 1. de Gruyter, 1999.

[CTJDR92] C. Cohen-Tannoudji and and Gilbert Grynberg Jacques Dupont-Roc. *Atom-Photon-Interactions*. John Wiley and Sons, Inc., 1992.

[CZB+09] Steven T. Cundiff, Tianhao Zhang, Alan D. Bristow, Denis Karaiskaj, and Xingcan Dai. Optical two-dimensional fourier transform spectroscopy of semiconductor quantum wells. *Acc. Chem. Res.*, 42(9):1423–1432, 2009. PMID: 19555068.

[Czy04] G. Czycholl. *Theoretische Festkörperphysik*. Springer, 2004.

[DJY+00] Scott A. Diddams, David J. Jones, Jun Ye, Steven T. Cundiff, John L. Hall, Jinendra K. Ranka, Robert S. Windeler, Ronald Holzwarth, Thomas Udem, and T. W. Hänsch. Direct link between microwave and optical frequencies with a 300 thz femtosecond laser comb. *Phys. Rev. Lett.*, 84:5102–5105, May 2000.

[DS08] I.A. Dmitriev and R.A. Suris. Quantum dot cascade laser: Arguments in favor. *Physica E: Low-dimensional Systems and Nanostructures*, 40(6):2007 – 2009, 2008. 13th International Conference on Modulated Semiconductor Structures.

[DV60] E. Daniel and S. H. Vosko. Momentum distribution of an interacting electron gas. *Phys. Rev.*, 120(6):2041–2044, Dec 1960.

[DWE+12] Thi Uyen-Khanh Dang, Carsten Weber, Sebastian Eiser, Andreas Knorr, and Marten Richter. Two-dimensional fourier spectroscopy applied to electron-phonon correlations in quantum well intersubband systems. *Phys. Rev. B*, 86(15):155306, Oct 2012.

[DWH74] R. Dingle, W. Wiegmann, and C. H. Henry. Quantum states of confined carriers in very thin $al_xga_{1-x}as$-gaas-$al_xga_{1-x}as$ heterostructures. *Phys. Rev. Lett.*, 33(14):827–830, Sep 1974.

[DWRK10] Thi Uyen-Khanh Dang, Carsten Weber, Marten Richter, and Andreas Knorr. Influence of coulomb correlations on the quantum well intersubband absorption at low temperatures. *Phys. Rev. B*, 82:045305, Jul 2010.

[EBW98] R. R. Ernst, G. Bodenhausen, and A. Wokaun. *Principles of Nuclear Magnetic Resonance in one or two dimensions*. Clarendon Press, Oxford, 1998.

[Eic10] Christian Eickhoff. *Zeitaufgelöste Zweiphotonen-Photoemission an der Si(001)-Oberfläche: Dynamik heißer Elektronen und zweidimensionaler Fano-Effekt*. PhD thesis, Freie Universität Berlin, 2010.

[Eke89] U. Ekenberg. Nonparabolicity effects in quantum well: Sublevel shifts, parallel mass, and landau levels. *Phys. Rev. B*, 40:7714, 1989.

[EO81] A. I. Ekimov and A. A. Onuschenko. Quantum size effect in three-dimensional microscopic semiconductor crystals. *JETP Lett.*, 34:375, 1981.

[FCS+94] J. Faist, F. Capasso, D. L. Sivco, C. Sirtori, A. L. Hutchinson, and A. Y. Cho. Quantum cascade laser. *Science*, 264:553–556, 1994.

[FDC+12] S. Fathololoumi, E. Dupont, C.W.I. Chan, Z.R. Wasilewski, S.R. Laframboise, D. Ban, A. Mátyás, C. Jirauschek, Q. Hu, and H. C. Liu. Terahertz quantum cascade lasers operating up to 200 k with optimized oscillator strength and improved injection tunneling. *Opt. Express*, 20(4):3866–3876, Feb 2012.

[Fri96] Jens Fricke. Transport equations including many-particle correlations for an arbitrary quantum system: A general formalism. *Ann. Phys.*, 252:479–498, 1996.

[FS90] E. Fick and G. Sauermann. *The Quantum Statistics of Dynamic Processes*. Springer, Berlin, 1990.

[GCSC01] C. Gmachl, F. Capasso, D. L. Sivco, and A. Y. Cho. Recent progress in quantum cascade lasers and applications. *Rep. Prog. Phys.*, 64:1533–1601, 2001.

[GGM+85] L. Goldstein, F. Glas, J. Y. Marzin, M. N. Charasse, and G. Le Roux. Growth by molecular beam epitaxy and characterization of inas/gaas strained-layer superlattices. *Applied Physics Letters*, 47(10):1099–1101, 1985.

[GHE01] Wilmut Gasser, Eberhard Heiner, and Klaus Elk. *Greensche Funktionen in Festkörper- und Vielteilchenphysik*. Wiley-Vch, 2001.

[GM31] Maria Göppert-Mayer. über elementarakte mit zwei quantensprüngen. *Annalen der Physik*, 401(3):273–294, 1931.

[GMB57] Murray Gell-Mann and Keith A. Brueckner. Correlation energy of an electron gas at high density. *Phys. Rev.*, 106:364–368, Apr 1957.

[GP94] J. R. Goldman and J. A. Prybyla. Ultrafast dynamics of laser-excited electron distributions in silicon. *Phys. Rev. Lett.*, 72:1364–1367, Feb 1994.

[GR86] Eberhard K. Gross and Erich Runge. *Vielteilchentheorie*. Teubner, 1986.

[GSKB00] S. Graf, H. Sigg, K. Köhler, and W. Bächtold. Direct observation of depolarization shift of the intersubband resonance. *Phys. Rev. Lett.*, 84:2686–2689, Mar 2000.

[GWS+09] D. Golde, M. Wagner, D. Stehr, H. Schneider, M. Helm, A. M. Andrews, T. Roch, G. Strasser, M. Kira, and S. W. Koch. Fano signatures in the intersubband terahertz response of optically excited semiconductor quantum wells. *Phys. Rev. Lett.*, 102:127403, Mar 2009.

[HAG+11] R. Huber, A. A. Anappara, G. Günter, A. Sell, S. De Liberato, C. Ciuti, G. Biasiol, L. Sorba, A. Tredicucci, and A. Leitenstorfer. Switching ultrastrong light–matter coupling on a subcycle scale. *J. Appl. Phys.*, 109(10):102418, 2011.

[Hai95] Richard Haight. Electron dynamics at surfaces. *Surface Science Reports*, 21(8):275 – 325, 1995.

[Hak93] Hermann Haken. *Quantenfeldtheorie des Festkörpers*. Teubner, 1993.

[Ham05] Peter Hamm. Principles of nonlinear optical spectroscopy: A practical approach. LECTURES OF VIRTUAL EUROPEAN UNIVERSITY ON LASERS, 2005.

[HBG+01] Robert Heitz, Harald Born, Florian Guffarth, Oliver Stier, Andrei Schliwa, Axel Hoffmann, and Dieter Bimberg. Existence of a phonon bottleneck for excitons in quantum dots. *Phys. Rev. B*, 64(24):241305, Nov 2001.

[HEC+89] M. Helm, P. England, E. Colas, F. DeRosa, and S. J. Allen. Intersubband emission from semiconductor superlattices excited by sequential resonant tunneling. *Phys. Rev. Lett.*, 63(1):74–77, 1989.

[HK04] H. Haug and S. W. Koch. *Quantum Theory of the Optical and Electronic Properties of Semiconductors*. World Scientific, Singapore, 2004.

[HTDF96] K. D. Hirschman, L. Tsybeskov, S. P. Duttagupta, and P. M. Fauchet. Silicon-based visible light-emitting devices integrated into microelectronic circuits. *Nature*, 384:338 – 341, nov 1996.

[HVL+97] Robert Heitz, Michael Veit, Nikolai N. Ledentsov, Axel Hoffmann, Dieter Bimberg, Viktor M. Ustinov, Petr Sergeevich Kop'ev, and Zhores Ivanovich Alferov. Energy relaxation by multiphonon processes in inas/gaas quantum dots. *Phys. Rev. B*, 56(16):10435–10445, Oct 1997.

[IKS+00] Norio Iizuka, Kei Kaneko, Nobuo Suzuki, Takashi Asano, Susumu Noda, and Osamu Wada. Ultrafast intersubband relaxation (<= 150 fs) in algan/gan multiple quantum wells. *Appl. Phys. Lett.*, 77(5):648–650, 2000.

[IR01] R. C. Iotti and F. Rossi. Nature of Charge Transport in Quantum-Cascade Lasers. *Phys. Rev. Lett.*, 87(14):146603, 2001.

[IT09] T. Ichibayashi and K. Tanimura. Ultrafast carrier relaxation in si studied by time-resolved two-photon photoemission spectroscopy: Intravalley scattering and energy relaxation of hot electrons. *Phys. Rev. Lett.*, 102:087403, Feb 2009.

[Jac99] John David Jackson. *Classical Electrodynamics*. John Wiley & Sons, New York, 3rd edition, 1999.

[Jon03] D. M. Jonas. Two-dimensional femtosecond spectroscopy. *Annu. Rev. Phys. Chem.*, 54:425–463, oct 2003.

[Kai00] R. A. Kaindl. *Ultrafast mid-infrared studies of low-energy excitations in solids*. PhD thesis, HU Berlin, 2000.

[Kam92] Van Kampen. *Stochastic processes in physics and chemistry*. North-Holland, 1992.

[KDT03a] M. Khalil, N. Demirdöven, and A. Tokmakoff. Coherent 2d ir spectroscopy: Molecular structure and dynamics in solution. *J. Phys. Chem. A*, 107(27):5258–5279, 2003.

[KDT03b] M. Khalil, N. Demirdöven, and A. Tokmakoff. Obtaining absorptive line shapes in two-dimensional infrared vibrational correlation spectra. *Phys. Rev. Lett.*, 90:047401, Jan 2003.

[KGF+10] I. Kuznetsova, N. Gögh, J. Förstner, T. Meier, S. T. Cundiff, I. Varga, and P. Thomas. Modeling excitonic line shapes in weakly disordered semiconductor nanostructures. *Phys. Rev. B*, 81:075307, Feb 2010.

[KK06a] M. Kira and S. W. Koch. Quantum-optical spectroscopy of semiconductors. *Phys. Rev. A*, 73(1):013813, 2006.

[KK06b] M. Kira and S.W. Koch. Many-body correlations and excitonic effects in semiconductor spectroscopy. *Prog. Quantum Electron.*, 30(5):155–296, 2006.

[KMCT07] I. Kuznetsova, T. Meier, S. T. Cundiff, and P. Thomas. Determination of homogeneous and inhomogeneous broadening in semiconductor nanostructures by two-dimensional fourier-transform optical spectroscopy. *Phys. Rev. B*, 76:153301, Oct 2007.

[KMS09] Jeongho Kim, Shaul Mukamel, and Gregory D. Scholes. Two-dimensional electronic double-quantum coherence spectroscopy. *Acc. Chem. Res.*, 42(9):1375–1384, 2009.

[KNR+09] K. Kempa, M. J. Naughton, Z. F. Ren, A. Herczynski, T. Kirkpatrick, J. Rybczynski, and Y. Gao. Hot electron effect in nanoscopically thin photovoltaic junctions. *Applied Physics Letters*, 95(23):233121 –233121–3, dec 2009.

[koudw12] S kei (original uploader) and Cepheiden (derivative work). Image: Schematics of calculated band structure of crystalline si, 2012. [Online; http://upload.wikimedia.org/wikipedia/commons/thumb/0/04/Band_structure_Si_schematic.svg/500px-Band_structure_Si_schematic.svg.png; accessed 19-November-2012].

[KRW+01] Robert A. Kaindl, Klaus Reimann, Michael Woerner, Thomas Elsaesser, R. Hey, and K. H. Ploog. Homogeneous broadening and excitation-induced dephasing of intersubband transitions in a quasi-two-dimensional electron gas. *Phys. Rev. B*, 63:161308, Apr 2001.

[KRW+11] W. Kuehn, K. Reimann, M. Woerner, T. Elsaesser, R. Hey, and U. Schade. Strong correlation of electronic and lattice excitations in GaAs/AlGaAs semiconductor quantum wells revealed by two-dimensional terahertz spectroscopy. *Phys. Rev. Lett.*, 107:067401, Aug 2011.

[KSR+12] Sandra Kuhn, Franz Schulze, Marten Richter, Andreas Knorr, and Alexander Carmele. Theory of phonon-assisted intraband transitions in semiconductor quantum dots. *Proc. SPIE, Ultrafast Phenomena and Nanophotonics XVI*, 8260:826004–8260048, 2012.

[KT01] Tsuyoshi Kato and Yoshitaka Tanimura. Multi-dimensional vibrational spectroscopy measured from different phase-matching conditions. *Chem. Phys. Lett.*, 341(3-4):329 – 337, 2001.

[Kuh98] Tilman Kuhn. Density matrix theory of coherent ultrafast optics and kinetics of semiconductors. In *Theory of Transport Properties of Semiconductor Nanostructures*. Chapman Hall, London, 1998. edited by E. Schöll.

[Kuh11] Sandra Kuhn. Theorie der elektron-phonon-kopplung optischer intrabandübergänge in quantenpunkten. Master's thesis, TU Berlin, 2011.

[Lan80] Lauri J. Lantto. Fermi hypernetted-chain calculations of the electron-gas correlations. *Phys. Rev. B*, 22:1380–1393, Aug 1980.

[Lau93] K.Y. Lau. *Dynamics of quantum well lasers*. Ed. Academic Boston, 1993.

[LCJ95] L. Lepetit, G. Chériaux, and M. Joffre. Linear techniques of phase measurement by femtosecond spectral interferometry for applications in spectroscopy. *J. Opt. Soc. Am. B*, 12(12):2467–2474, Dec 1995.

[LG97] S.-C. Lee and I. Galbraith. Multisubband nonequilibrium electron-electron scattering in semiconductor quantum wells. *Phys. Rev. B*, 55:R16025–R16028, Jun 1997.

[Liu94] Ansheng Liu. Local-field effect on the linear optical intersubband absorption in multiple quantum wells. *Phys. Rev. B*, 50:8569–8576, Sep 1994.

[LK88] M. Lindberg and S. W. Koch. Effective bloch equations for semiconductors. *Phys. Rev. B*, 38(5):3342, 1988.

[LN03] Jianzhong Li and C. Z. Ning. Interplay of collective excitations in quantum-well intersubband resonances. *Phys. Rev. Lett.*, 91:097401, Aug 2003.

[LN04] J. Li and C. Z. Ning. Effects of electron-electron and electron-phonon scatterings on the linewidths of intersubband transitions in a quantum well. *Phys. Rev. B*, 70:125309, 2004.

[LNC+12] V. Liverini, L. Nevou, F. Castellano, A. Bismuto, M. Beck, F. Gramm, and J. Faist. Room-temperature transverse-electric polarized intersubband electroluminescence from inas/alinas quantum dashes. *ArXiv*, page 1209.0139, Sept 2012.

[LV71] C. S. Lam and Y. P. Varshni. Energies of *s* eigenstates in a static screened coulomb potential. *Phys. Rev. A*, 4:1875–1881, Nov 1971.

[LZBC06] Xiaoqin Li, Tianhao Zhang, Camelia N. Borca, and Steven T. Cundiff. Many-body interactions in semiconductors probed by optical two-dimensional fourier transform spectroscopy. *Phys. Rev. Lett.*, 96(5):057406, Feb 2006.

[Mah00] G. D. Mahan. *Many-Particle Physics*. Kluwer Academic/Plenum Publishers, New York, 2000.

[MC84] José Menéndez and Manuel Cardona. Temperature dependence of the first-order raman scattering by phonons in si, ge, and α-sn: Anharmonic effects. *Phys. Rev. B*, 29:2051–2059, Feb 1984.

[ME00] S. Meyer and V. Engel. Non-perturbative wave-packet calculations of time-resolved four-wave-mixing signals. *Appl. Phys. B*, 71(3):293–297, 2000.

[Mes74] Albert Messiah. *Quantum Mechanics*. North-Holland Publ. Co., 1974.

[MK00] Volkhard May and Olivier Kühn. *Charge and Energy Transfer Dynamics in Molecular Systems*. Wiley-VCH Verlag, Berlin, 2000.

[MLR86] F. Malcher, G. Lommer, and U. Rössler. Electron states in gaas/ga(1-x)al(x)as heterostructures: Nonparabolicity and spin-splitting. *Superlattices and Microstructures*, 2(3):267 – 272, 1986.

[MMF+92] T. Mishina, Y. Masumoto, B. Fluegel, K. Meissner, and N. Peyghambarian. Observation of coherent optical phonons in bii_3. *Phys. Rev. B*, 46:4229–4232, Aug 1992.

[MR11] Shaul Mukamel and Marten Richter. Multidimensional phase-sensitive single-molecule spectroscopy with time-and-frequency-gated fluorescence detection. *Phys. Rev. A*, 83:013815, Jan 2011.

[MSN+09] F. Milota, J. Sperling, A. Nemeth, D. Abramavicius, S. Mukamel, and H. F. Kauffmann. Excitonic couplings and interband energy transfer in a double-wall molecular aggregate imaged by coherent two-dimensional electronic spectroscopy. *J. Chem. Phys.*, 131(5):054510, 2009.

[Muk95] Shaul Mukamel. *Principles of nonlinear optical spectroscopy*. Oxford University Press, New York, 1995.

[Muk00] Shaul Mukamel. Multidimensional femtosecond correlation spectroscopies of electronic and vibrational excitations. *Annu. Rev. Phys. Chem.*, 51(1):691–729, 2000.

[NAK99] B. Nottelmann, V.M. Axt, and T. Kuhn. Many-body effects in intersubband transitions of modulation-doped quantum wells. *Physica B: Condensed Matter*, 272(1 - 4):234 – 236, 1999.

[NIBS97] Dmitri E. Nikonov, Atac Imamoglu, Leonid V. Butov, and Holger Schmidt. Collective intersubband excitations in quantum wells: Coulomb interaction versus subband dispersion. *Phys. Rev. Lett.*, 79:4633–4636, Dec 1997.

[NIS99] Dmitri E. Nikonov, Atac Imamoglu, and Marlan O. Scully. Fano interference of collective excitations in semiconductor quantum wells and lasing without inversion. *Phys. Rev. B*, 59(19):12212–12215, 1999.

[Nol00] Wolfgang Nolting. *Grundkurs theoretische Physik 2: Analytische Mechanik*. Springer Verlag, 2000.

[OMOO07] K. Ohtani, Y. Moriyasu, H. Ohnishi, and H. Ohno. Above room-temperature operation of InAs/AlGaSb superlattice quantum cascade lasers emitting at 12 μm. *Appl. Phys. Lett.*, 90(26):261112, 2007.

[Oth98] Andreas Othonos. Probing ultrafast carrier and phonon dynamics in semiconductors. *Journal of Applied Physics*, 83(4):1789–1830, 1998.

[oudw12] Cepheiden (original uploader) and Doodle77 (derivative work). Image: Bandgap diagram for gaas, 2012. [Online; http://upload. wikimedia.org/wikipedia/commons/ thumb/6/67/ Bandstruktur_GaAs_en.svg/500px-Bandstruktur_GaAs_en.svg.png; accessed 19-November-2012].

[PDMK08] B. Pasenow, H.T. Duc, T. Meier, and S.W. Koch. Rabi flopping of charge and spin currents generated by ultrafast two-colour photoexcitation of semiconductor quantum wells. *Sol. State Comm.*, 145(1-2):61 – 65, 2008.

[PKA10] T. Papenkort, T. Kuhn, and V. M. Axt. Resonant generation of coherent lo phonons by charge oscillations in a biased quantum well. *Phys. Rev. B*, 81(20):205320, May 2010.

[PLL+07] L. Perfetti, P. A. Loukakos, M. Lisowski, U. Bovensiepen, H. Eisaki, and M. Wolf. Ultrafast electron relaxation in superconducting $bi_2sr_2cacu_2o_{8+\delta}$ by time-resolved photoelectron spectroscopy. *Phys. Rev. Lett.*, 99:197001, Nov 2007.

[Plo82] Klaus Ploog. Molecular beam epitaxy of iii-v compounds: Application of mbe-grown films. *Annual Review of Materials Science*, 12:123–148, aug 1982.

[PLW04] M. F. Pereira, S.-C. Lee, and A. Wacker. Controlling many-body effects in the midinfrared gain and terahertz absorption of quantum cascade laser structures. *Phys. Rev. B*, 69(20):205310, 2004.

[Ree08] Graham T. Reed. *Silicon Photonics: The State of the Art*. Wiley-Interscience, New York, NY, USA, 2008.

[RR90] S. Rudin and T. L. Reinecke. Electron–lo-phonon scattering rates in semiconductor quantum wells. *Phys. Rev. B*, 41:7713–7717, Apr 1990.

[RRA+88] M. A. Reed, J. N. Randall, R. J. Aggarwal, R. J. Matyi, T. M. Moore, and A. E. Wetsel. Observation of discrete electronic states in a zero-dimensional semiconductor nanostructure. *Phys. Rev. Lett.*, 60:535–537, Feb 1988.

[SAB07] Matthias Scholz, Thomas Aichele, and Oliver Benson. Single photons from single quantum dots - new light for quantum information processing. In *Adv. in Solid State Phys.*, volume 46. Advances in Solid State Physics, 2007.

[Sch64] T. D. Schultz. *Quantum field theory and the many body problem*. Gordon and Breach, 1964.

[Sch96] F. Scheck. *Analytische Mechanik*. Springer, 1996.

[SDW+11] E. Stock, M.-R. Dachner, T. Warming, A. Schliwa, A. Lochmann, A. Hoffmann, A. I. Toropov, A. K. Bakarov, I. A. Derebezov, M. Richter, V. A. Haisler, A. Knorr, and D. Bimberg. Acoustic and optical phonon scattering in a single in(ga)as quantum dot. *Phys. Rev. B*, 83:041304, Jan 2011.

[SKB+98] C. Sirtori, P. Kruck, S. Barbieri, P. Collot, J. Nagle, M. Beck, J. Faist, and U. Oesterle. GaAs/$Al_xGa_{1-x}As$ quantum cascade lasers. *Appl. Phys. Lett.*, 73(24):3486–3488, 1998.

[SKM94] J. Schilp, T. Kuhn, and G. Mahler. Electron-phonon quantum kinetics in pulse-excited semiconductors: Memory and renormalization effects. *Phys. Rev. B*, 50(8):5435, 1994.

[SKS+96] F. Steininger, A. Knorr, T. Stroucken, P. Thomas, and S. W. Koch. Dynamic evolution of spatiotemporally localized electronic wave packets in semiconductor quantum wells. *Phys. Rev. Lett.*, 77(3):550, 1996.

[SPD98] Theodore Sjodin, Hrvoje Petek, and Hai-Lung Dai. Ultrafast carrier dynamics in silicon: A two-color transient reflection grating study on a (111) surface. *Phys. Rev. Lett.*, 81:5664–5667, Dec 1998.

[SRW+05] T. Shih, K. Reimann, M. Woerner, T. Elsaesser, I. Waldmüller, A. Knorr, R. Hey, and K. H. Ploog. Nonlinear response of radiatively coupled intersubband transitions of quasi-two-dimensional electrons. *Phys. Rev. B.*, 72:195338, 2005.

[SSD95] Luis Seidner, Gerhard Stock, and Wolfgang Domcke. Nonperturbative approach to femtosecond spectroscopy: General theory and application to multidimensional nonadiabatic photoisomerization processes. *J. Chem. Phys.*, 103(10):3998–4011, 1995.

[SW02] Wilfried Schäfer and Martin Wegener. *Semiconductor Optics and Transport Phenomena*. Springer, Heidelberg, 2002.

[SZ97] M. O. Scully and M. S. Zubairy. *Quantum Optics*. Cambridge University Press, Cambridge, 1997.

[SZD+04] M. P. Semtsiv, M. Ziegler, S. Dressler, W. T. Messlink, N. Georgiev, T. Dekorsy, and M. Helm. Above room temperature operation of short wavelength (λ=3.8 μm) strain-compensated $In_{0.73}Ga_{0.27}As$-AlAs quantum-cascade lasers. *Appl. Phys. Lett.*, 85(9):1478–1480, 2004.

[Tan08] Howe-Siang Tan. Theory and phase-cycling scheme selection principles of collinear phase coherent multi-dimensional optical spectroscopy. *J. Chem. Phys.*, 129(12):124501, 2008.

[TIT09] S. Tanaka, T. Ichibayashi, and K. Tanimura. Dynamics of bulk-to-surface electron transitions on $Si(001)$-(2×1) studied by time-resolved two-photon photoemission spectroscopy. *Phys. Rev. B*, 79:155313, Apr 2009.

[TKSW03] Peifang Tian, Dorine Keusters, Yoshifumi Suzaki, and Warren S. Warren. Femtosecond Phase-Coherent Two-Dimensional Spectroscopy. *Science*, 300(5625):1553–1555, 2003.

[TM93] Yoshitaka Tanimura and Shaul Mukamel. Two-dimensional femtosecond vibrational spectroscopy of liquids. *J. Chem. Phys.*, 99(12):9496–9511, 1993.

[TY91] Yasutami Takada and H. Yasuhara. Momentum distribution function of the electron gas at metallic densities. *Phys. Rev. B*, 44(15):7879–7887, Oct 1991.

[UAS+97] C. Ulrich, E. Anastassakis, K. Syassen, A. Debernardi, and M. Cardona. Lifetime of phonons in semiconductors under pressure. *Phys. Rev. Lett.*, 78:1283–1286, Feb 1997.

[vD79] H. M. van Driel. Influence of hot phonons on energy relaxation of high-density carriers in germanium. *Phys. Rev. B*, 19:5928–5932, Jun 1979.

[VK91] John L. Vossen and Werner Kern. *Thin Film Processes II*. Gulf Professional Publishing, 1991.

[VN68] John Von Neumann. *Mathematische Grundlagen der Quantenmechanik*. Springer, 1968.

[Vor00] L. E. Vorobjev. Mid infrared range laser based on intersubband transitions and resonant auger processes in quantum wells. *8th International Symposium: Nanostructures: Physics and Technology*, FIR.04, 2000.

[VVA+09] M. Vogel, A. Vagov, V. M. Axt, A. Seilmeier, and T. Kuhn. Spin-sensitive intersubband dynamics of optically generated carriers in semiconductor quantum wells. *Phys. Rev. B*, 80(15):155310, 2009.

[VWW01] W. Vogel, D. Welsch, and S. Wallentowitz. *Quantum Optics An Introduction*. WILEY-VCH, Berlin, 2nd edition edition, 2001.

[Wal02] Inès Waldmüller. Many particle theory of the optical gain of interssuband transitions. Master's thesis, TU Berlin, 2002.

[Wal04] Inès Waldmüller. *Intersubband Dynamics in Semiconductor Quantum Wells*. PhD thesis, Technische Universität Berlin, 2004.

[WCYW06] I. Waldmueller, W. W. Chow, E. W. Young, and M. C. Wanke. Nonequilibrium many-body theory of intersubband lasers. *IEEE J. Quantum Electron.*, 42(3):292–301, 2006.

[WE77] A. Wokaun and R.R. Ernst. Selective detection of multiple quantum transitions in nmr by two-dimensional spectroscopy. *Chem. Phys. Lett.*, 52(3):407 – 412, 1977.

[Wey25] H. Weyl. Theorie der darstellung kontinuierlicher halb-einfacher gruppen durch lineare transformationen. i. *Mathematische Zeitschrift*, 23:271–309, 1925. 10.1007/BF01506234.

[WFL+04] I. Waldmüller, J. Förstner, S.-C. Lee, A. Knorr, M. Woerner, K. Reimann, R. A. Kaindl, T. Elsaesser, R. Hey, and K. H. Ploog. Optical dephasing of coherent intersubband transitions in a quasi-two-dimensional electron gas. *Phys. Rev. B*, 69(20):205307, 2004.

[Wil07] B. S. Williams. Terahertz quantum-cascade lasers. *Nature Photonics*, 1:517, 2007.

[WKFR04] M. Weinelt, M. Kutschera, T. Fauster, and M. Rohlfing. Dynamics of exciton formation at the Si(100) $c(4 \times 2)$ surface. *Phys. Rev. Lett.*, 92:126801, 2004.

[WRW+05] Z. Wang, K. Reimann, M. Woerner, T. Elsaesser, D. Hofstetter, J. Hwang, W. J. Schaff, and L. F. Eastman. Optical phonon sidebands of electronic intersubband absorption in strongly polar semiconductor heterostructures. *Phys. Rev. Lett.*, 94:037403, 2005.

[WRW+06] Z Wang, K Reimann, M. Woerner, T. Elsaesser, D. Hofstetter, E. Baumann, F. R. Giorgetta, H. Wu, W. J. Schaff, and L. F. Eastman. Ultrafast hole burning in intersubband absorption lines of gan/aln superlattices. *Appl. Phys. Lett*, 89:151103, August 2006.

[WSSD97] Brigitte Wolfseder, Luis Seidner, Gerhard Stock, and Wolfgang Domcke. Femtosecond pump-probe spectroscopy of electron-transfer systems: a nonperturbative approach. *Chem. Phys.*, 217(2-3):275 – 287, 1997.

[WWFK03] Inès Waldmüller, Michael Woerner, Jens Förstner, and Andreas Knorr. Theory of the lineshape of quantum well intersubband transitions: optical dephasing and light propagation effects. *Phys. Status Solidi B*, 238(3):474–477, 2003.

[WWK09] C. Weber, A. Wacker, and A. Knorr. Density-matrix theory of the optical dynamics and transport in quantum cascade structures: The role of coherence. *Phys. Rev. B*, 79(16):165322, 2009.

[YT09] Suxia Yan and Howe-Siang Tan. Phase cycling schemes for two-dimensional optical spectroscopy with a pump - probe beam geometry. *Chem. Phys.*, 360(1):110 – 115, 2009.

[ZGC+09] E. A. Zibik, T. Grange, B. A. Carpenter, N. E. Porter, R. Ferreira, G. Bastard, D. Stehr, S. Winnerl, M. Helm, H. Y. Liu, M. S. Skolnick, and L. R. Wilson. Long lifetimes of quantum-dot intersublevel transitions in the terahertz range. *Nature Materials*, 8:803 – 807, 2009.

[ZHH+04] W. M. Zheng, M. P. Halsall, P. Harmer, P. Harrison, and M. J. Steer. Effect of quantum confinement on shallow acceptor transitions in δ-doped gaas/alas multiple-quantum wells. *Appl. Phys. Lett.*, 84:735, 2004.

[Zim92] J. M. Ziman. *Prinzipien der Festkörpertheorie*. Verlag Harri Deutsch, Frankfurt/Main, 1992.

[ZWLF98] R. Zimmermann, J. Wauer, A. Leitenstorfer, and C. Fürst. Observation of memory effects in electron-phonon quantum kinetics. *J. Lumin*, 76(7):34–37, 1998.

Danksagung

Für das Gelingen meiner Projekte, die in dieser Doktorarbeit zusammengefasst sind, möchte ich vielen Menschen danken. Als erstes danke ich meinem Doktorvater Andreas Knorr für seine sehr gute Betreuung sowie seine Unterstützung und Hilfe während der ganzen Promotionszeit. Ein ganz besonderer Dank gebührt Marten Richter, der an nahezu allen Projekten mit Wissen, Rat und Tat beteiligt war und ohne den diese Arbeit nicht möglich gewesen wäre. In dieser Hinsicht geht auch ein ganz großes Dankeschön an Carsten Weber, mit dem zusammen das Projekt der Grundzustandskorrelationen erfolgreich zu Ende geführt wurde und das Silizium Projekt entstanden ist. Desweiteren bedanke ich mich sehr bei Christian Eickhoff und Martin Weinelt vom Max-Born Institut für die Zusammenarbeit an dem Silizium Projekt. Weiterer Dank geht an Sandra Kuhn für das Quantenpunkt Projekt und Sebastian Eiser für das 2D Spektroskopie Projekt.
Mein Dank geht auch an Herrn Prof. Manfred Helm für die Überhahme des Zweitgutachtens und an Frau Prof. Birgit Kanngießer für die Überhahme des Vorsitzes.
Für das Korrekturlesen meiner Arbeit bedanke ich mich bei Mario Schoth, Matthias-René Dachner, Torben Winzer, Sandra Kuhn, Marten Richter, Carsten Weber und ganz besonders Frank Milde.
Durchweg während der ganzen Promotionszeit habe ich mich in unserer Arbeitsgruppe sehr wohl gefühlt. Die tolle Arbeitsatmosphäre ist der ganzen AG geschuldet, mit denen es nie langweilig wurde. Die Mensagänge mit den lieben Kollegen aus dem 1. Stock (Felix mit inbegriffen!) und den Graphen-Leuten sowie die etwas ausgefalleneren Essensgänge zur Mathekantine/Thai/Indisch/Koreanisch mit den Kollegen aus dem 7. Stock waren immer eine erhol- und unterhaltsame Pause während der Arbeitszeit! Auch unsere gelegentlichen abendlichen (leider doch zu seltenen) AG-Ausflüge waren eine schöne Sache. Zur AG zählen auch Peter Orlowski, durch dessen unermüdlichen EDV-Einsatz die Rechner (fast) immer das taten, was sie tun sollten, und Frau Kristina Ludwig, die in allen verwaltungstechnischen Belangen stets eine kompetente, geduldige und liebe Hilfe war. Ihnen beiden auch ein großes Danke!
Ganz herzlich bedanke ich mich bei Anni und Klaus, für ihre helfenden Hände und für das leckere Essen, mit dem sie mich das ein oder andere Mal zu Hause beglückt haben. Auch danke ich meiner Schwester Lilly dafür, dass sie immer ein offenes Ohr für mich hat; Und natürlich bin ich meinen Eltern unglaublich dankbar für ihre Unterstützung und ihren Glauben an mich. Ohne sie wäre ich nicht da, wo ich jetzt bin! Dankend erwähnen möchte ich auch meine Bgirls. Durch unser gemeinsames Training konnte ich auch während meiner heißen Endphase für ein paar Stunden richtig abschalten und neue Kraft tanken.
Am allermeisten jedoch möchte ich Frank danken - und da könnte ich abertausende Sachen aufzählen. Angefangen damit, dass er nicht nur den grössten Teil meiner Arbeit korrekturgelesen, alles kritisch hinterfragt hat und über unzählige Dinge mit mir fachlich diskutiert hat. Aber am meisten bin ich ihm dafür dankbar, dass wir uns blind verstehen, dass er mich immer bestärkt und beruhigt hat wenn ich Zweifel hatte und dass ich in jeder Hinsicht bedingungslos von ihm unterstützt werde. Ohne ihn wäre ich nicht so glücklich wie ich es heute bin, und dafür gibt es keine Worte, die meine Gefühle für ihn auch nur annähernd ausdrücken könnten!